Graz University of Technology

Aerodynamic Design and Investigation of an Embedded Concept for Turning Mid Turbine Frames

Author:
Rosario Spataro

Supervisor:
Dr. Emil Göttlich

A thesis submitted in fulfillment of the requirements for the degree of Doctor of Philosophy

at the

Institute for Thermal Turbomachinery and Machine Dynamics
Graz University of Technology

November 2013

Declaration of Authorship

I declare that I have authored this thesis independently, that I have not used other than the declared sources/resources, and that I have explicitly marked all material which has been quoted either literally or by content from the used sources.

Graz, 07. 11. 2013 

Date Signature

Ich erkläre an Eides statt, dass ich die voliegende Arbeit selbständig verfasst, andere als die angegebenen Quellen/Hilfmittel nicht benutzt, und die den benutzten Quellen wörtlichen und inhaltlich entnommenen Stellen als solche kenntlich gemacht habe.

Graz, 07. 11. 2013 

Datum Unterschrift

"Larga la foglia, stretta la via, dite la vostra che ho detto la mia."

Pietro l'Aretino

Abstract

Aerodynamic Design and Investigation of an Embedded Concept for Turning Mid Turbine Frames

by Rosario Spataro

This thesis discusses the aerodynamics of two advanced setups for intermediate turbine ducts. Connecting the high pressure and the low pressure turbines, such components play a critical role in the design of modern and next generation aero engines. An integrated concept called turning mid turbine frame (TMTF) constitutes the baseline setup for this work. In a TMTF architecture, aerodynamically optimised struts replace the state-of-the-art configuration (strut followed by the first low pressure (LP) vane row). The thesis presents the design of a new stage where an embedded concept was applied to the baseline TMTF. This means that two smaller splitter vanes were added (embedded) into the strut passage in order to improve the flow. The aerodynamic comparison between the two setups was performed testing both stages under similar flow condition in a two-stage two-spool counter-rotating turbine rig. This work shows that by a proper use of an embedded concept it is possible to sensibly improve the time-mean and the time-resolved inflow of a following LP rotor.

Diese Arbeit diskutiert die Aerodynamik von zwei verschiedenen fortschrittlichen Geometrien für Turbinen-Zwischenkanäle. Der Zwischenkanal verbindet die Hochdruck- und die Niederdruckturbine, und spielt eine kritische Rolle im Entwurf aktueller und zukünftiger Flugtriebwerke. Ein integriertes Konzept namens “Turning Mid Turbine Frame” (Umlenkendes Turbinen-Zwischengehäuse, TMTF) bildet den Ausgangspunkt für diese Arbeit. Während in aktuellen Konfigurationen , die dem Stand der Technik entsprechen, auf nicht umlenkende Streben umlenkende Niederdruckturbinen-Statoren folgen, werden in einem derartigen TMTF aerodynamisch optimierte umlenkende Streben verwendet. Diese Arbeit präsentiert einen Entwurf einer Turbinenstufe, in der ein neuartiges, sogenanntes “embedded” Designkonzept auf ein bestehendes TMTF angewandt wird. Das bedeutet, dass zwei zusätzliche kleinere Splitterschaufeln in den Kanal zwischen zwei Stützschaufeln eingebettet werden, um die Strömung zu verbessern. Die beiden Konfigurationen wurden unter ähnlichen Strömungsbedingungen in einem Zwei-Wellen Prüfstand mit gegenläufig drehenden Turbinenstufen untersucht und die Aerodynamik der beiden Stufen wird verglichen. Die Arbeit zeigt, das durch die vernünftige Anwendung eines “Embedded Design” Konzeptes sowohl die stationäre als auch instationäre Zuströmung des folgenden Niederdruckrotors massgeblich beeinflusst und optimiert werden können.

Acknowledgements

This thesis represents not only a discussion on advanced design techniques for turbomachinery, but encloses also three years of my life spent at the Institute. Here in Graz, I found a lot of friends from the professors to the students that I will never forget in the years ahead.
Therefore, I would like to start thanking my supervisor Emil Göttlich for the very constructive discussions we had and for his continuous trust in me during the thesis development.
Similarly, I want to address my deepest thanks to Franz Heitmeir, for his kindness and for his continuous support (especially in terms of funding!!).
A very very special thanks goes to Davide "Lenga" Lengani, who has been for me more than a mentor and more than a friend. Thanks Davide for having represented part of my family in these three years.
Further, I want to thank Christian "Fausty" Faustmann and Andreas Ampferer for the help in assembling the stage and operating the machine but especially for your friendship.
I can't forget to name the old crew: Cornelia "Conny" Santner, Sergej Alexandrovic Josef Hubinka also named "Josip" and Berardo "Bera" Paradiso. Thanks guys for your affection and for all the fun we had together.
Another special Dankeschön is for Wolfgang Sanz for being decisive for my professional future and for being a good friend. Thank you!!
I want to thank Bianca for being the best-secretary-ever, Peter Pirker for his never ending enthusiasm, Andreas Marn, Thorsten Selic, Bernd Schlegl, Thomas Leitgeb, Christoph Henning, Bugra Akin, Johannes Peterleithner, Jakob Woisetschläger and Johannes Fritzer.
Thanks to Davide Roveda for every coffee break where the mood was set back on the trails.
I need then to apologize to all the people who were not listed above for forgetfulness. They deserve as much as the others to be mentioned since all of them contributed to my growing up as a person as well as an engineer.

The first persons I want to acknowledge outside of the Institute are my parents who definitely deserve to have this work dedicated to them. Thanks for having turned in friends and for your constant presence whenever this was asked for.
Thanks also to my sister Annalisa, to Enrico and to the little Francesco.
What to say to my grandmother? Grazie nonna Maria di esserci sempre stata!
Another special acknowledgment is addressed to Federico for having been another piece of my small family during my time in Austria.

In the same way, I want to thank all the rest of my family.
I can't forget all my friends who live disseminated all around Europe but it would take forever to name all of them. Thank you for you friendship and your support.
Last but not least, I want to thank Filomena for her love and her close presence.

Contents

List of Figures

List of Tables

Abbreviations

AIDA	**A**ggressive **I**intermediate **D**uct **A**erodynamics
AMA	**A**zimuthal **M**odal **A**nalysis
BPF	**B**lade **P**assing **F**requency
BPP	**B**lade **P**assing **P**eriod
CP	**C**locking **P**osition
CRT	**C**ounter **R**otating **T**urbine
DREAM	valid**D**ation of **R**adical **E**ngine **A**richitecture syste**M**s
FHP	**F**ive **H**ole **P**robe
FRAPP	**F**ast **R**esponse **A**erodynamic **P**ressure **P**robe
CFD	**C**omputetional **F**luid **D**ynamics
HP	**H**igh **P**ressure
HPV	**H**igh **P**ressure **V**ane
ITTM	**I**nstitute for **T**hermal **T**urbomachinery and **M**achine dynamics
LP	**L**ow **P**ressure
LPV	**L**ow **P**ressure **V**ortex
LDV	**L**aser **D**oppler **V**elocimetry
PIV	**P**article **I**mage **V**elocimetry
PS	**P**ressure **S**ide
REV	rotor **REV**olution period
RMS	**R**oot **M**ean **S**quare
RSA	**R**otor **S**ynchronic **A**nalysis
RWTH	**R**heinisch **W**estfaelische **T**echnische **H**ochschule
sec	**sec**ondary flows
SS	**S**uction **S**ide
SV	**S**hed **V**ortex

TLV	**T**ip **L**eakage **V**ortex
TMTF	**T**urning **M**id **T**urbine **F**rame
VG	**V**ortex **G**enerator

Symbols

A	amplitude	Pa
C	strut axial chord	m
C_p	static pressure coefficient	$-$
C_{pT}	total pressure coefficient	$-$
f	frequency	Hz
H	normalized channel height	$-$
M	Mach number	-
m	azimuthal mode	$-$
$m_{r,in}$	reduced mass flow	$kg/s \cdot \sqrt{K}/(bar)$
n	rotation speed	rpm
p	static pressure	Pa
p_t	total pressure	Pa
$n_{r,in}$	reduced rotational speed	$rpm/\sqrt{K}$
r	radius	m
S_{REF}	reference static entropy	J/K
U	tangenzial velocity	m/s
V	absolute velocity	m/s
x	axial coordinate	m
α	yaw angle	deg
β	metallic blade angle	deg
γ	pitch angle	deg
ι	blade turning coefficient	$-$
θ	tangential coordinate	deg
ρ	density	kg/m^3
ω	vorticity	$1/s$

To my father Giovanni and to my mother Teresa

Chapter 1

Introduction

Civil turbofan engines are among the most complicated and fascinating machines in terms of applied technology as well as engineering challenges. The state of the art of such machines reflects the extensive research carried out over the last century.

The basic layout of the modern gas turbine engine goes back to 1930 when Frank Whittle was granted his first patent for using a gas turbine to produce a propulsive jet, but it took still eleven years to complete its first flight [68].

In 1935 Hans von Ohain started work on a similar design in Germany, apparently unaware of Whittle's work [30]. The first centrifugal engine named Heinkel HeS-1 was running in September 1937. Unlike Whittle's design, Ohain used hydrogen as fuel, supplied under external pressure. Further designs culminated in the gasoline-fuelled HeS 3 of 1,100 lbf (5 kN), which flew in the early morning of August 27, 1939. Such engine powered the world's first jet plane, the Heinkel He 178 [90].

History of thermal turbomachinery tells us that, even if pioneer works on jet-engines were carried out during World War II, the time for first large gas turbine development programs for aeronautical application came in the years of the Cold War by the middle of the 20th century, where military projects were considerably more founded than civil research projects.

The development of the first by-pass jet engine in the world (Rolls-Royce RB-80 Conway) started in the 1940s, but it was used only briefly in the late 1950s and early 1960s before other turbofan designs were introduced. Such an engine was characterized by a maximum thrust of 17,150 lb (76.3 kN) and a bypass ratio of 0.25.

On 20th of May 1955, the General Electric J79 turbojet engine had his first flight [4]. This was the first engine with movable stator vanes which helped the compressor cope with the huge internal variations in airflow from takeoff to high supersonic speeds.

The addition of a fan to the rear of the CJ805 (a modified version of the J79 engine) created the first turbofan engine for commercial service which was used to power the

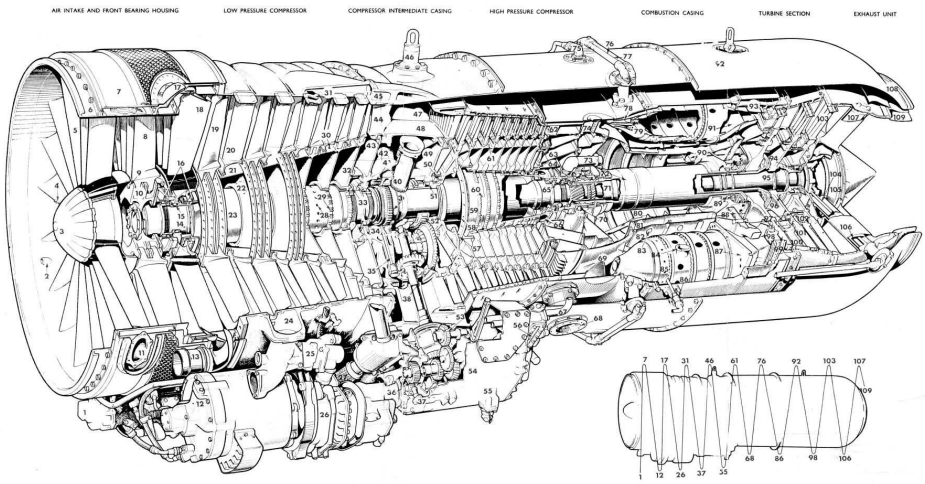

FIGURE 1.1: Rolls Royce Conway (http://www.turbineel.net)

Convair 990. Such an engine had a maximum thrust of 11,200 lbf (49.8 kN), a bypass ratio of 1.46 and a thrust-to-weight ratio of 3.93 [91].

In the middle of the '60s, the Lockheed C-5 Galaxy military transport aircraft was powered with the world's first high bypass turbofan (General Electric TF39). A civil derived version of the TF39, the CF6 engine, was used to power the Lockheed L-1011 and McDonnell Douglas DC-10. In 2011, the CF6 celebrated 40 years in service.

Since the '90s, after the collapse of the USSR, new factors such as a strong need of globalized economies led to a more interconnected world, where the aerospace traffic played a major role (nowadays studies forecast a doubling factor over the next 15 years [1]). Despite the huge turnover of companies operating in this field, the arising cost of fossil fuel to power the civil engines shorted considerably the revenue rates turning the aerospace sector in one of the most delicate financial businesses in the world.

The 21st century drew a new scenario for the aerospace industry, where military investment spendings on new acquisition and R&D could decline, recent studies say [82], from US $253 billion in 2008 to as low as $150 billions in 2016. On the other hand, in commercial aviation the industry faces a renewed growth, where the Boeing-Airbus duopoly has to face emerging airframe competitors whose growth is expected to get 3.6 percent annual rate for the next 20 years. The shortening of the innovation cycle and an increase in R&D spending involves airplanes manufactures as well as suppliers like aero engines companies. Therefore, the present context can been seen offering significant opportunities with the strongest capabilities in research and innovation.

The standard layout of modern large civil aero engines is constituted by multishaft turbofan architectures. More recent large high-bypass turbofans include the Pratt & Whitney PW4000, the three-shaft Rolls-Royce Trent, the General Electric GE90/GEnx and the GP7000, produced jointly by GE and P&W [93].

Besides, a lot of research programs (i.e. the EU-projects DREAM, CLEAN Sky, etc.)

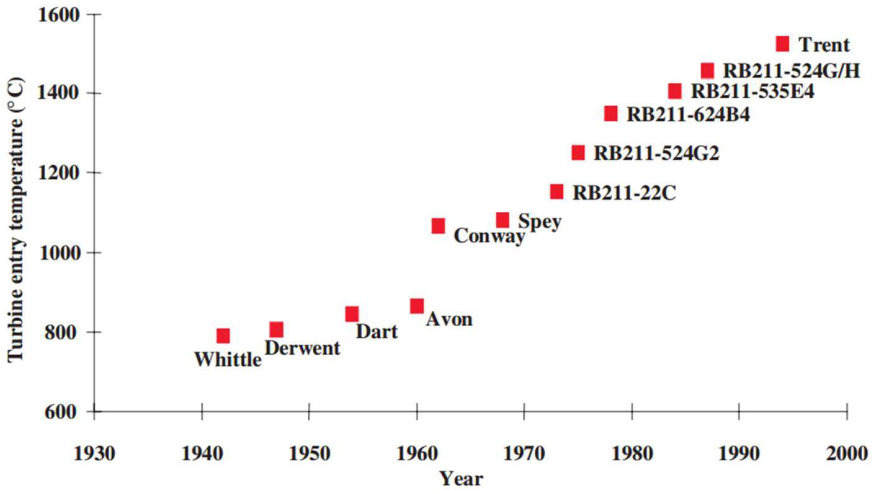

FIGURE 1.2: Turbine Inlet Temperatures trend of Rolls-Royce engines (Spittle [81])

tried to explore alternative configurations such as the *open-rotor technology* or the *geared turbofan* with the intention to combine the advantages of a propeller in terms of efficiency with the high thrust-to-power ratio of the turbojet propulsion. The studies are currently facing problems like for example the aeroelastic interaction between the propeller and structures (wings, pylon, fuselage, etc.), thus leading to vibrational mechanical fatigue as well as induced noise emission.

1.1 The research on Mid Turbine Frames

The increase in the cycle maximum temperature (TIT - Turbine inlet temperature), overall pressure ratio (OPR) and bypass ratio lead to an improvement of the propulsion efficiency which is vital in such a business.
Figure 1.2 and Figure 1.3 show the historical trend for jet engines TIT and OPR.
Table 1.1 shows examples for modern high bypass jet engines. In this context, the trend to set up high power engines in multi-shaft architecture (up to 3 shafts in Rolls Royce

TABLE 1.1: Examples of modern civil turbofans bypass ratios (Wikipedia website, http://www.wikipedia.org/)

Manufacturer	**Aircraft**	**Bypass ratio**
PowerJet SaM146	Sukhoi Superjet 100	4.43:1
Pratt & Whitney PW2000	Boeing 757, C-17 Globemaster III	5.9:1
Progress D-436	Yak-42M, Beriev Be-200, An-148	6.2:1
Rolls-Royce Trent 900	Airbus A380	8.7:1
General Electric GE90	Boeing 777	9:1
Rolls-Royce Trent 1000	Boeing 787	10:1
General Electric GEnx	Boeing 787	8.5:1

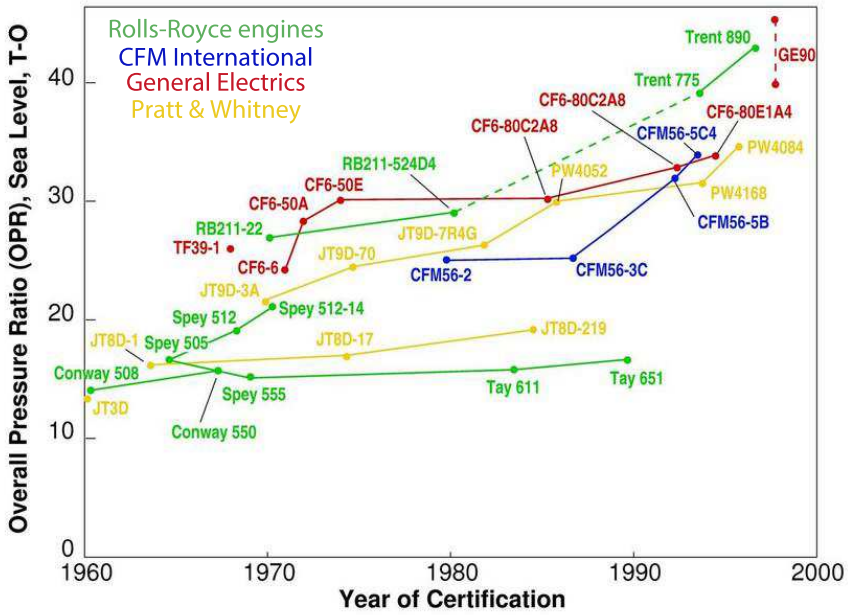

FIGURE 1.3: Total Pressure Ratio trend
(Take Off (T-O) condition, Massachusetts Institute of Technology website, http://web.mit.edu)

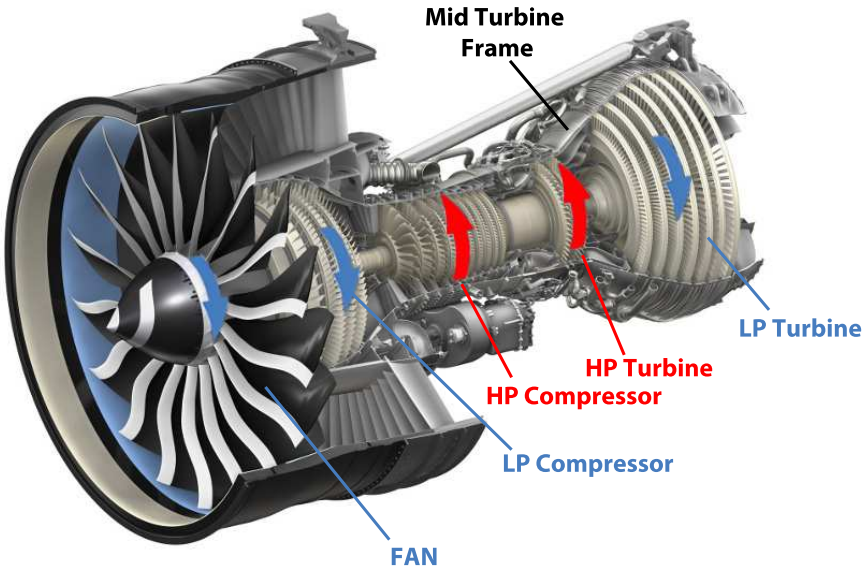

FIGURE 1.4: A modern high bypass civil turbofan
(General Electrics Aviation website, http://www.geaviation.com)

engines family) is necessary in order to maximize the pressure ratio at a fixed number of stages and to assign adequate rotational directions of the spools. In particular, counter-rotating shaft setups can be used to compensate the gyroscopic effect of the rotating

masses as well as to minimize the aerodynamic losses in the intermediate stage [80] (i.e. General Electric GEnx, Rolls Royce TRENT 1000, Pratt & Whitney PW1500).
The fan tip velocity is a design constrain proportional to the maximum stress in the component and which imposes the engine noise emission limit. Since the turbofan front section and hence the fan radii have to be enlarged in order to maximize the engine bypass-ratio and therefore the propulsion efficiency, lower LP-shaft rotational speed is required. On the other hand, the rotational speed of the high pressure stage has to be increased in order to reach higher maximum cycle pressure.
The resulting larger difference in the shafts rotational speeds leads to an increasing difference in the components diameters (compressors and turbines). Therefore the resulting S-shaped design of the transition duct between the HP and LP systems is quite important for the optimisation of the overall engine aerodynamic performance.
For example, in modern engines bulky struts are located within the turbine transition duct (Figure 1.5 (a)) in order to support the engine shaft and to lead throught service pipe lines (Figure 1.6). The size of such wide chord vanes induces an obstacle for the fluid flowing towards the LP turbine causing higher losses in this part of the machine. Recently, Göttlich [24] published a review on the present state of the research on these components.
Among the different solutions aimed to shorten the transition duct, an integrated concept such as the turning mid turbine frame (TMTF) (Figure 1.5 (b)) represents a remarkable example. Such architectures have been studied in a one-and-a-half stage [50, 53] and in a two stages configuration [59, 72]. Here, the idea was to integrate the function of the first LP vane row into aerodynamically optimised turning struts.
The operation of such setups showed that the LP rotor inlet flow is characterized by large structures such as thick wakes and big secondary flows generated by the struts. These structures on the one hand contribute to reduce the performance of the rotor, while on the other hand they represent a potential source of vibration for the rotor blades.
A further problem in shortening the components is that the engine performance is highly affected by the blade row interaction. In particular for the mid turbine frame, the extent of the unsteadiness at the outlet of the duct, downstream of the first LP rotor, is critical for the aerodynamic performances, vibrations and acoustic emissions of the successive LP stages, and, therefore, need a careful analysis. The pressure fluctuations from the stage upstream of the duct contribute considerably to the overall pressure fluctuations at the exit of the second stage, downstream of the diffusing duct (Lengani et al. [45]).
The application of an embedded design concept in the design of such components could represent a step forward in the development of mid turbine frames(Figure 1.5 (c)). For the first time, during this work, this last architecture was investigated in a transition duct connecting counter-rotating turbines.

1.2 Motivation and tasks of the doctoral thesis

This thesis would like to be pioneer study for evaluating alternative architectures for the future turbine transition ducts. The work was developed after experimental and numerical investigations on the aerodynamics of two setups. The publications related to this thesis show the transversal character of the research work. Therefore, it was important to create a plot for the reader reflecting the development of the dissertation.

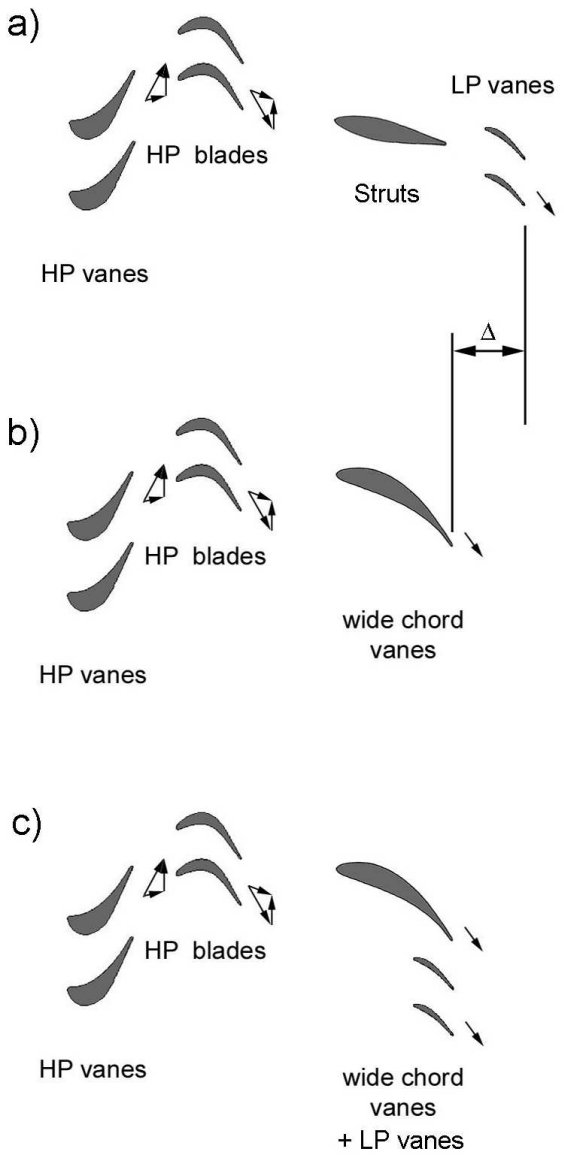

FIGURE 1.5: Different architectures for Mid-Turbine-Frames placed between counter-rotating HP and LP stages (Göttlich [24])

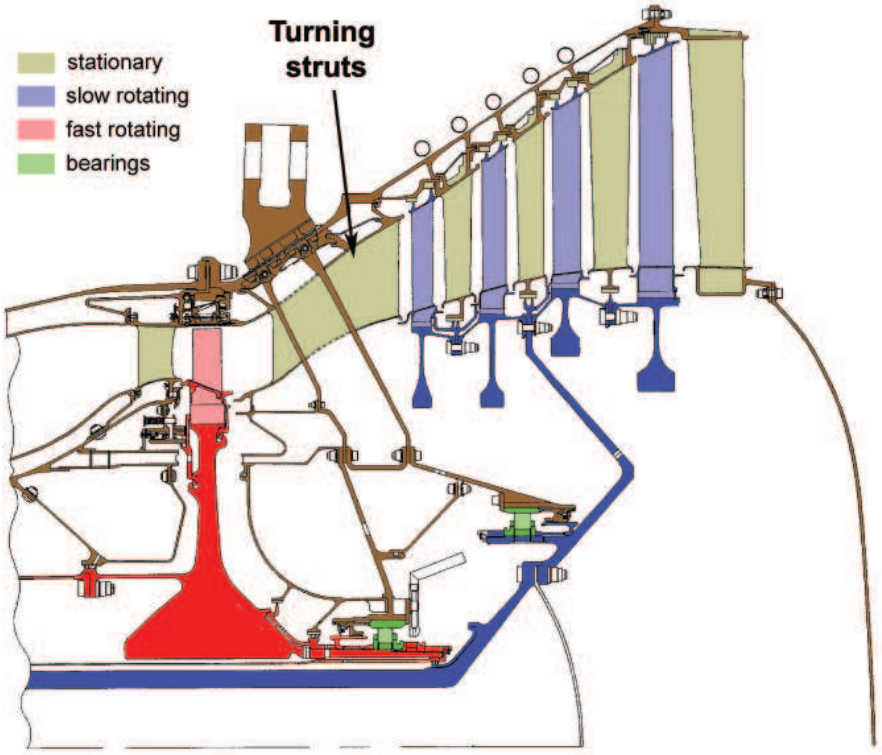

FIGURE 1.6: Meridional section of a future multishaft turbofan turbine (Göttlich [23])

1.2.1 Studies on the baseline TMTF stage

At the beginning of this dissertation, the author performed an extensive numerical investigation on one TMTF configuration tested during of the EU-project DREAM. Such setup constituted also the Baseline case in order to compare the new embedded design concept. Moreover, the author implemented a special post-processing procedure in order to properly analyze the unsteady measurements data acquired downstream of the two-stage turbine. Such a procedure is called Rotor Synchronic Averaging (RSA, see Section 5.2) which was presented in Lengani et al. [44]. The application of such procedure to the unsteady data of the baseline configuration was published in Lengani et al. [45].
A detailed analysis on the time-averaged (Spataro et al. [80]) and on the time-resolved flow field (Spataro et al. [79], Lengani et al. [46]) of the baseline configuration is reported in Section 6.1.

1.2.2 Studies on the multisplitter TMTF stage

The second part of the work (Section 6.2) was performed within a national funded project. Here, the task consisted in transferring the knowledge acquired on the fluid dynamics of the baseline stage into the design of a new stage intended to improve the

performance of the TMTF.
Therefore, the author designed two splitter vanes embedded into the TMTF strut passage. He was also responsible for the CAD drawings of the new setup which was then delivered to the Institute by the manufacturing company HELDECO Gmbh. After manufacturing, the new stage was instrumented and made ready for testing.
The design goal for the new configuration was to reduce the strength of the strut wakes and the secondary flows observed in the baseline setup at the LP rotor inlet as well as to reduce the unsteady interaction observed in the time-resolved flow field downstream of the stage.
After the new stage was manufactured and instrumented, the author started an experimental campaign which involved the use of steady and unsteady measurements techniques. The results of this campaign have been published in Spataro et al. [77], Spataro et al. [78] and Faustmann et al. [18] where it is discussed how the splitters influence the homogeneity of the flow field, leading to a more suitable condition for the LP rotor.

Chapter 2

Literature review

This thesis deals with the aerodynamics of intermediate turbine diffusers placed between a transonic high pressure turbine and a low pressure turbine. Therefore, in the remainder of this chapter, studies on the aerodynamics of these engine components were selected and are here briefly reviewed.

2.1 High pressure turbine

The relative motion of moving turbine rotor blades and stationary vanes introduces two forms of unsteadiness into the flow [55]: random fluctuations such as turbulence and deterministic time–resolved fluctuations such as blade wakes and shock waves. When the flow unsteadiness experienced by a blade occurs at frequencies close to the blades natural frequencies a significant vibration can occur. Over time this can cause high cycle fatigue (HCF) and eventually, if not identified, to a catastrophic blade failure. A detailed understanding of the unsteady flow physics within turbine stages is thus clearly of great importance to engine manufacturers.

The transonic flow leaving the vane of a high-pressure turbine interacts with the downstream rotor being characterized by a combination between direct and reflected shocks and wakes, the first being predominant (Figure 2.1). The large pressure gradients associated with the shock wave affect not only the aerodynamics of the flow in the rotor passage, but also the heat transfer [22]. Blades are submitted to unsteady lift that causes vibrations while unsteady heat transfer increases thermal fatigue. The understanding of such complex interactions was necessary to improve the blade design and the flow field prediction as well as the evaluation of mechanical and thermal fatigue. As a result of an experiemental and numerical investigating on the flow field of the transonic test facility at VKI, Denos et al. [11] found that the rotor relative inlet total pressure is submitted

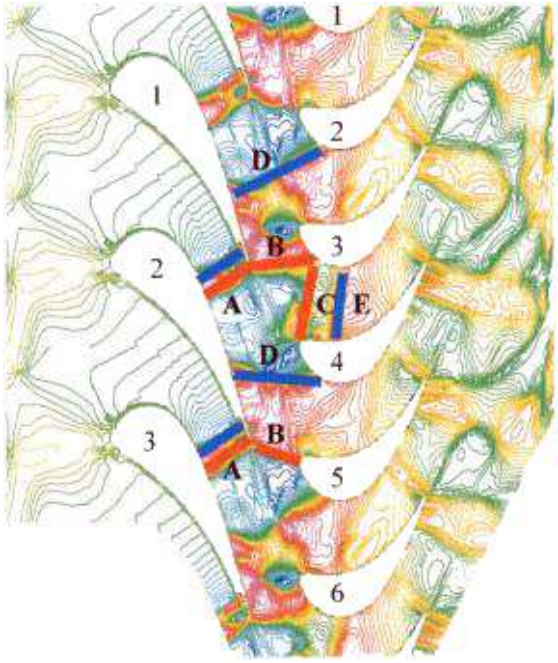

FIGURE 2.1: Computed shock pattern in a transonic field of the high pressure turbine at the Von Karman Institute (Denos et al. [11])

to fluctuations with an amplitude of 10 percent of its mean value. It is clear that the trailing edge shock imposes a strong static pressure discontinuity, which is largely felt in the relative total pressure. The wake has a less strong effect but the computations show how it interacts with the shock and how it is distorted.

The unsteady rotor surface pressure field was found being dominated by the strong gradient imposed by the vane trailing edge shock on the front suction side. The shock-sweeping phenomenon from the crown toward the leading edge was clearly identified, associated with fluctuations up to 40 percent of the design relative total pressure. The decrease of the fluctuation amplitude from the crown to the leading edge is explained by the decreasing strength of the shock caused by the increasing local static pressure.

The periodic apparence of a reflected shock was highlighted. The amplitude of the fluctuations decreases strongly on both the rear suction side and pressure side, where the shock has no direct impact. On the first, random fluctuations of increasing amplitude appear while on the second, the fluctuations remain strongly correlated with the blade passing events. The computations reveal that the path of the wake is highly distorted, not only due to a local velocity deficit in the main stream but also due to its interaction with the shock

Miller et al. [55, 56] investigated the time-resolved flow field by means of unsteady sensors placed on one rotor blade of the test turbine located at the University of Oxford. Such configuration (Figure 2.2) is similar to the one investigated during this thesis, but the wide chord vane in that case was designed to lead the flow towards a co–rotating

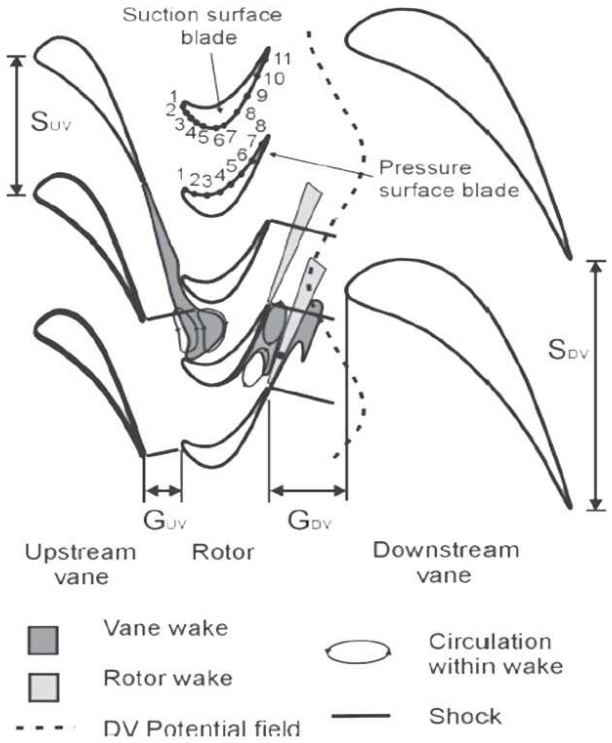

FIGURE 2.2: Vane–Rotor and Vane–Vane interaction in a transonic low aspect ratio turbine (Miller et al. [56])

second rotor. Unsteady calculations were performed in order to improve the understanding of the investigated phenomena. The test rig consisted of a transonic turbine set in 1.5 stage configuration. In their paper, the authors investigated rotor–vane as well as vane–vane interactions. The schematic view in Figure 2.2 shows that upstream of its crown the rotor suction surface pressure field is dominated by the upstream vanes potential field and shock. The authors found out that as the vane trailing edge approaches the rotor leading edge an effective throat is set up between the two blades causing the vane trailing edge shock to strengthen. This effect reduces in strength as the vane shock moves around the surface of the rotor. As the vane trailing edge shock approaches the rotor leading edge a second stronger shock is observed to occur.

One of the conclusions showed by Miller in [56] was that in transonic turbine stages wake interaction has been shown not to cause a significant change in the rotor surface pressure field and, therefore, it may be ignored from an aeroelastic perspective. The presence of the downstream vane does not affect the pressure field around the suction surface leading edge or the pressure surface. The presence of the downstream vane causes a change in the pressure field downstream of the rotor's geometric throat. The size of this effect was found comparable with that caused by the upstream vane.

Gaetani et al. [20, 21] investigated the stator–rotor axial gap variation between $x/b_s =$

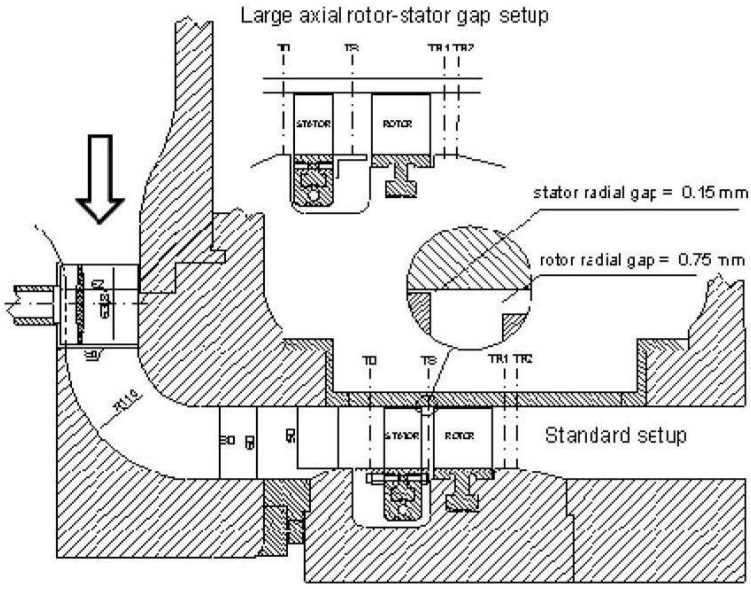

FIGURE 2.3: Investigation on the Stator–Rotor axial gap variation in the transonic high pressure turbine at Politecnico di Milano (Gaetani et al. [20])

0.16 and $x/b_s = 0.60$ (where x/b_s indicated the axial coordinate normalized on the stator axial chord) of the transonic turbine in one–and–half stage configuration located at Politecnico di Milano. The rotor hub region was found to be most affected by the stator flow. On the contrary, the rotor flow in the outer part of the channel above 60% span remains almost unaffected by the stator incoming flow, since the stator vortices and wake were found almost mixed out for the two investigated gaps. Moreover, the authors reported that the dependence of the stage performances on the stator-rotor axial gap is the result of a trade-off between the mixing losses downstream of the stator and the rotor performances under unsteady inlet boundary conditions.

The stages investigated during this thesis were set with a the stator-rotor axial gaps of $x/C_{HPV} = 1$ (C_{HPV} is the HP vane axial chord) and $x/C_{Strut} = 0.3$ (C_{Strut} is the strut axial chord)for the transonic stage and for the low pressure turbine respectively. This means that the HP stage is expected to be characterized by high mixing losses downstream the HP vanes, while the LP rotor being affected by unsteady inlet boundary conditions.

Göttlich et al. [26] investigated the unsteady flow field in a transonic turbine by means of LDV, PIV as well as unsteady CFD analysis. During their work, the authors pointed out that the vane suction side shock extends across the interface between stator and rotor towards the axial direction (see Figure 2.4 thick line at $t/\tau = 0.14$). This shock is periodically reflected at the surface of the passing rotor blades. Reflected pressure waves move upstream toward the vane suction side (Figure 2.4, dashed lines) and impinge on the trailing edges (see Figure 2.4, $t/\tau = 0.35$). There, it enforces a vortex separation (Figure 2.4, arrow). From then on the wake is shedding undisturbed, until the next

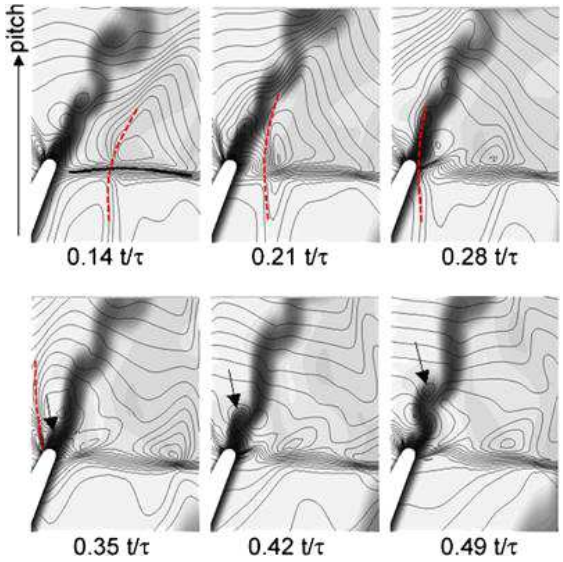

FIGURE 2.4: Investigation on vortex shedding mechanism triggered by the shock wave propagation in the transonic facility at Graz University of Technology (Göttlich et al. [26])

reflected shock wave triggers it again.

So, the pressure wave is reflected on the vane suction side after traveling upstream, and then starts to move downstream through the rotor passages to the trailing edge influencing the boundary layers and the vortex shedding in a similar way there.

The transonic stage investigated during this thesis is also characterized by a shock system similar to the one investigated by Göttlich et al. [26] and similar features are expected to occur.

Schennach et al. [74] studied the three dimensional clocking effects in the same test facility. The high pressure turbine was extended to a one–and–half stage configuration by a second vane row with the same blade count, a cross sectional view can be seen in

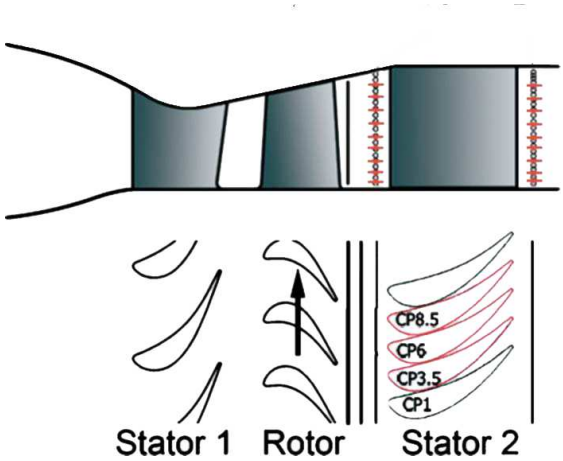

FIGURE 2.5: Investigation on the clocking effects in the transonic high pressure turbine at Graz University of Technology [74]

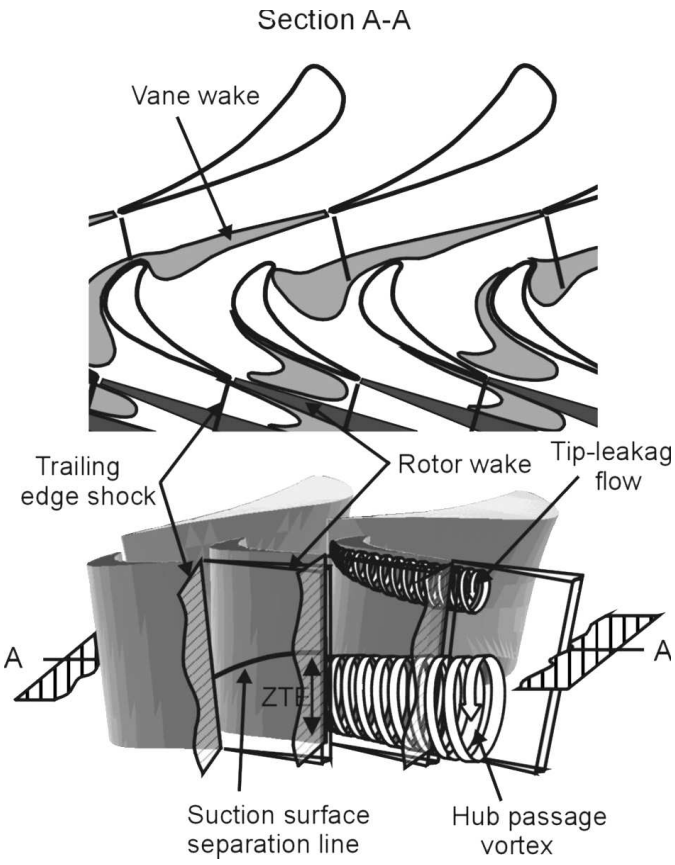

FIGURE 2.6: Flow structures at the high pressure turbine outlet (Miller et al. [54])

Figure 2.5. The authors studied the modulation of the second vane aerodynamics due to the first vane-rotor interaction effects. It was evidenced that the highly unsteady rotor hub passage vortex interacts with the second stator in different ways depending on the indexing; in particular, for one clocking position (CP1 in Figure 2.5) this vortex reaches its maximum magnitude when entering the second vane channel close to the suction side of the airfoil, while in position CP6 this occurs when entering close to the airfoil pressure side.

The turbine setup investigated during this thesis has a wide-chord vane placed downstream of the transonic stage: the three dimensional clocking effects are expected to play a major role in the two stage performance similarly as in [74].

2.1.1 HP rotor exit flow

In this thesis the main focus was concentrated on the mid turbine frame, whose engine–like inlet condition is represented by the flow leaving an upstream high pressure stage. Therefore, in this section the main features which characterize an unshrouded transonic turbine exit flow are presented. Miller et al. [54] provided a very comprehensive study performed on the Oxford transonic facility, where structures and vane–rotor phenomena

at the turbine exit flow have been summarized and presented (Figure 2.6). In particular, the authors observed the HP stage outflow being dominated by four flow features: the rotor tip-leakage flow, the rotor hub secondary flow the rotor trailing edge shock and the rotor wake. Moreover, two significant vane periodic changes in the rotor exit flowfield have been identified. The first and most severe was found to occur close to the hub wall while the second was found to occur close to the rotor suction surface at all radial heights. The main features of these interaction mechanism are as follows:

- Hub interaction, which is thought to be caused by the pooled vane wake segments aided to a lesser extent by vane secondary flow.
- Two-dimensional interaction, which is thought to be caused by vane-rotor shock and potential flow interaction in addition to the remnants of the vane wake that has not pooled onto the hub wall upstream of the rotor leading edge. The interaction was found to result in a change in Mach number and total pressure at the same rotor and vane relative phase at all radial heights.

Moreover, the authors [54] pointed out the Time-Resolved Behavior of the Rotor Wake and of the Tip-Leakage Flow:

Rotor Wake The semiwake width of the wake was found to change by 50% and the rotor relative phase of the wake was found to change by 10%. The change in the wake characteristic caused by vane-rotor interaction was found to be much greater than has been reported for subsonic stages.

Tip-Leakage Flow The tip leakage flow was found to be largely unaffected by vane-rotor interaction

A special focus on the tip leakage flow was, then, put by Marn et al. [51] and Göttlich et al. [25] investigating the influence of the rotor tip gap on the flow evolution through an intermediate turbine duct place downstream of a high pressure turbine located at Graz University of Technology. (Figure 2.7) The authors observed the flow behavior for different clearance sizes and simulated the behavior also for the zero-gap case (Sanz et al. [73]). Focusing on the critical outer endwall at the first bend of an aggressive and superaggressive duct, they observed a beneficial effect of the tip leakage flow which re-energizes the boundary layer. The flow detachment was found less extended for the larger gap. On the other side, at the hub the duct was found to be close to separation at different circumferential positions for the large gap.

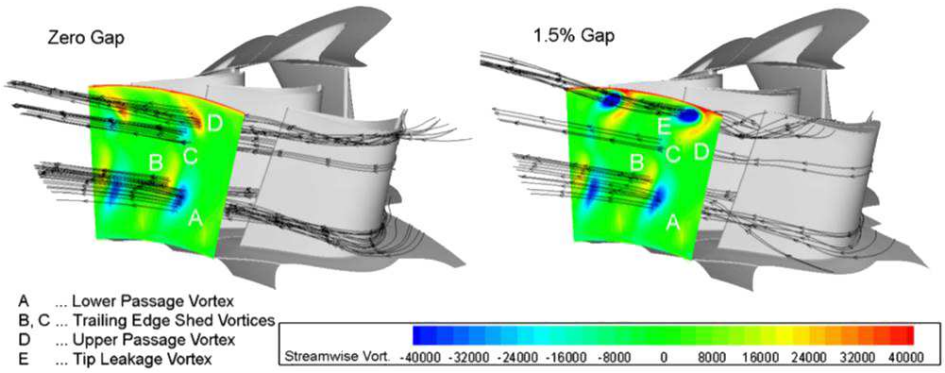

FIGURE 2.7: Flow structures at the inlet of an intermediate turbine diffuser (Göttlich et al. [25])

2.2 Interturbine diffusers

This thesis deals with advanced architectures for the turbine transition duct (also referred as mid turbine frame (MTF)). Therefore, this section is central in order to understand the basic fluid dynamic of an S-shaped diffuser as well as to have an overlook on advanced design techniques already investigated for the flow control through this component.

The fundamentals of the aerodynamic of such component is presented in Section 2.2.1, while in the Sections 2.2.2, 2.2.3 advanced techniques such as 3D endwall contouring or active/passive flow control systems will be presented. Finally, in Section 2.2.4 a previous study on the application of embedded concepts in the design of such components is presented.

2.2.1 Fundamentals

The fundamental work on swan-necked diffusers by Dominy et al. [14] identified the influence of the cross-passage pressure gradients in S-shaped ducts [80]. In particular, experimental and numerical data revealed clearly the effects of the two bends on the generation of secondary flows as the flow develops through the diffuser. The pressure distribution in an S-shaped diffuser depends not only on the area change such as in straight-walled channels, but also upon the curvature of the endwalls and hence of the streamlines [24]. The effective local curvature is also linked to the boundary layer growth at the surfaces. If the flow is turned from the axis-parallel direction radially outward in the first bend of an S-shaped duct, a pressure gradient from the casing (low pressure) to the hub (high pressure) will be created according to the radial equilibrium within the flow field. This cross-passage pressure gradient is superimposed to the adverse pressure gradient, evoked by the diffusion due to an increase in flow area [24].

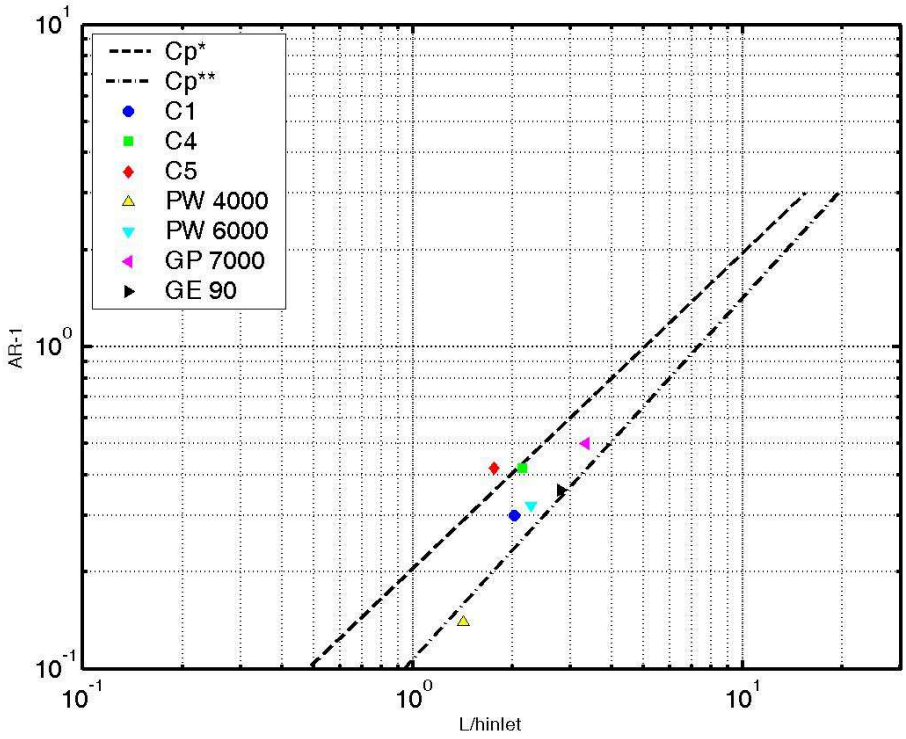

FIGURE 2.8: Performance chart for straight-walled annular diffusers after Sovran and Klomp with optimum lines for maximum pressure recovery coefficient at fixed non-dimensional duct length (C_p*) or duct area ratio (C_p**) ([76])

An optimized design of the endwall curvature can help to control these pressure gradients, but both of them play a significant role in an aggressive intermediate turbine diffuser. At the end of the duct the flow has to be turned back towards the engine axis in order to match the channel shape with the inflow of the following LP turbine stage in a real engine or with the rig exit section of an individual test setup. This will cause a cross-passage pressure gradient but now with the higher pressure at the casing and the lower pressure at the hub. The pressure distribution in an S-shaped diffuser has a major effect on the boundary layer behavior at the endwalls, which is most critical due to the strongest adverse pressure gradients right after strong wall curvatures [24].

The performance chart for straight-walled annular diffusers (Figure 2.8) provided by Sovran and Klomp in 1967 [76] is still used as a reference to classify intermediate turbine diffusers regarding their criticality [24]. In the diagram, designs of intermediate turbine diffusers of selected aero engines and rig test setups recently investigated at Chalmers University of Technology (C1) and Graz University of Technology (C4 and C5) are compared. The optimum lines for maximum pressure recovery coefficient at fixed non-dimensional duct length (C_p*) or duct area ratio (C_p**) taken from [76] are plotted [24].

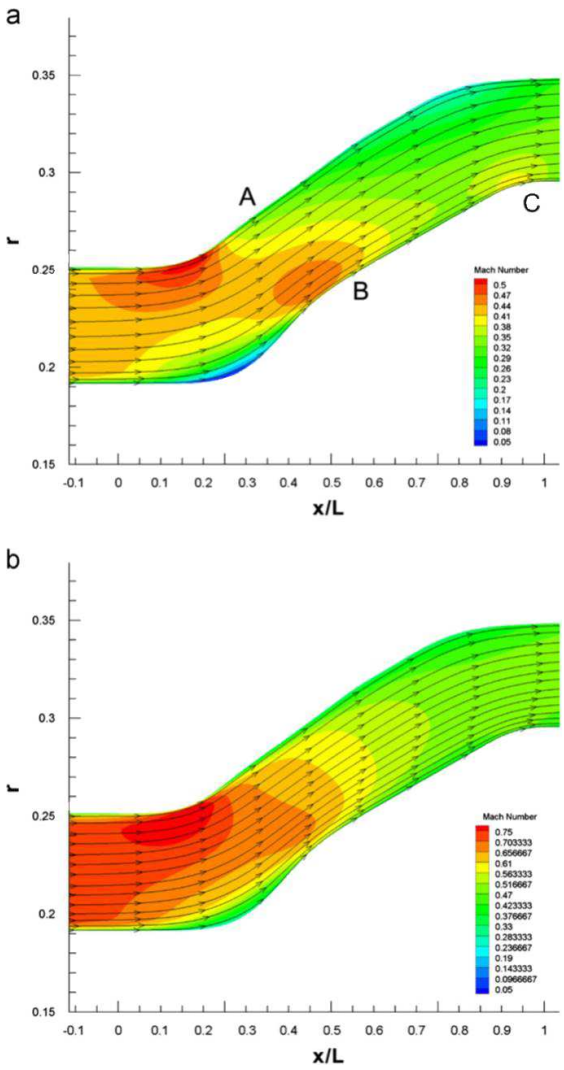

FIGURE 2.9: Mach number distribution in a typical S-shaped diffuser without (a)and with (b) swirl (Göttlich [23])

A diffuser design described by the non-dimensional duct length (L/h_{in}) and the area ratio ($AR = A_{out}/A_{in}$), which is between these lines can be seen as optimal, while a layout below and above is classified as conservative and aggressive, respectively. However, this can only be a rough assessment since the effects of curvature, flow swirl and inlet wakes occurring in a real S-shaped intermediate duct are not considered in the investigations of Sovran and Klomp [76]. It can be seen that the engine manufactures placed their designs within or close to the optimal region but rather tight to the conservative border [24].

Swirl was found to influence the character of the flow [13] particularly through the skewing of the wakes. Figure 2.9 shows an example for the flow through an S-shaped duct without swirl (a) and other inlet distortions (b).

These effects on the flow are discussed and summarized by Dominy et al. [14] with

a comparison of their measurements to CFD and to results from an intermediate turbine diffuser arranged downstream of a single-stage LP turbine stage [24]. The early preliminary design phase of an intermediate turbine duct is often done with the help of experimentally generated standard diffuser performance maps like the well known Sovran and Klomp diagram [76] which is used, beside the classification of the aggressiveness, to correlate a pressure rise coefficient C_p for a given area ratio AR and a non-dimensional duct length L/h_{in}. But it is only valid for non-swirling flows. Also the theoretical maximum pressure recovery represented by $C_{p,ideal} = 1 - AR^2$ which is only a function of AR does not consider swirl. On the other hand, an intermediate turbine duct downstream of a turbine stage usually works with a significant inlet swirl and is equipped with struts. Therefore the total pressure loss of such a design has to be estimated with the help of a database where parameters like swirl angle, duct blockage and strut losses have been added and which is usually gained by a systematic computational study.

2.2.2 3D endwall contouring techniques

In order to reduce the cross passage pressure gradient one possible solution is to design the duct endwalls using non-axisymmetric shape optimization techniques. In Wallin and Eriksson [88] non-axisymmetric endwall contouring has been applied at the diffuser hub endwall in order to reduce the effects on secondary flows, distortion and local separations. The same parameterization with perturbations to a baseline design like in [87] was applied to maintain an axisymmetric inlet and outlet. The non-axisymmetry was obtained by adding circumferential cosine and sine perturbation functions in the strut area of interest (Figure 2.10).

2.2.3 Flow-controlled intermediate turbine diffusers

Flow control enables the designer to generate more aggressive transition duct geometries with larger radial offsets as suggested, for example, by Lord et al. [47]. Flow separation can be suppressed by active or passive flow control measures. The first type can either be the energization of the boundary layer by injection of high energy fluid or the removal of low energy fluid from the critical wall regions (see Figure 2.11)
The injection of high-energy fluid by means of wall jets in order to eliminate flow separation within aggressive intermediate turbine diffusers is demonstrated by Florea et al. [19]. It was shown that flow control alone might not be sufficient to eliminate flow separation and to obtain the ideal flow quality for the following turbine stage. Therefore a novel methodology for designing flow–control–enabled turbine transition ducts coupled with shape optimization was presented.

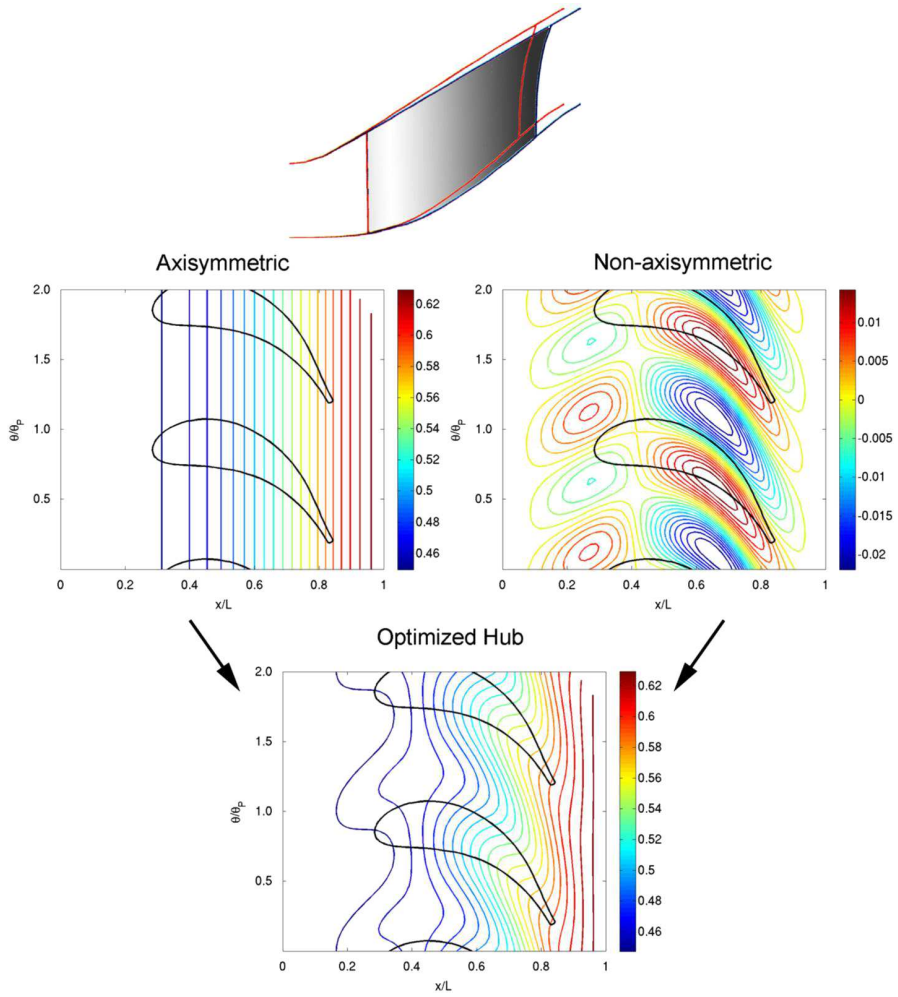

FIGURE 2.10: Baseline and shortened duct (top), hub modification procedure (mid), non-axisymmetric optimized hub (bottom), blue contour lines represent a radius decrease and red a radius increase (Göttlich [24])

In contrast to active flow control the application of passive flow control is less complex because there is no need for handling additional fluid streams possibly at unsteady flow rates. The installation of fixed components in order to reenergize the boundary layer in critical areas would be very beneficial (see Figure 2.11). For that reason one work package of the EU project AIDA ("Aggressive Intermediate Duct Aerodynamics") was installed to evaluate the application of passive flow control devices in compressor as well as in turbine transition ducts. Numerical and experimental investigations have been conducted in order to assess their performance. On the turbine side low-profile vortex generators have been designated as the most promising candidate for going into a rig test in an engine representative turbine transition duct environment.

The application and the performance of a low-profile vortex generator installation within a super-aggressive (very high diffusion) intermediate turbine diffuser have been investigated experimentally by Santner et al. [70] within the AIDA project.

The main parameters of the installation, which have a high influence on the efficiency

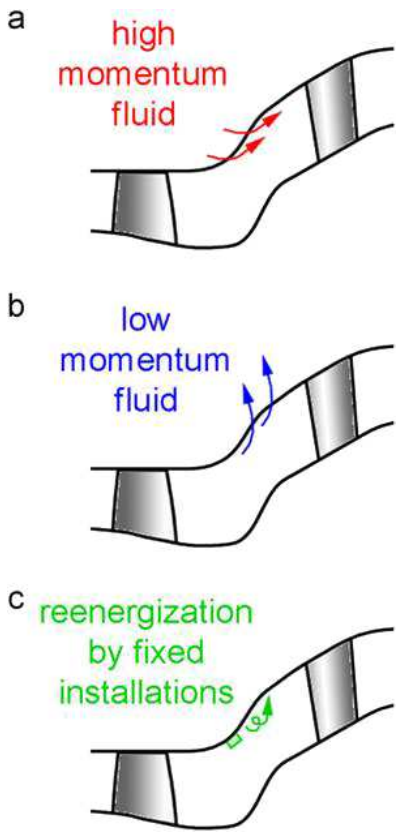

FIGURE 2.11: Flow control mechanism: active (a and b) and passive (c) measures for re-energization of boundary layer. (Göttlich [24])

of these low-profile vortex generators, are the angle of attack and the position relative to the separation according to Wallin and Eriksson [89]. In this test vortex generator geometries with low-profile vanes similar to those defined in the work of Canepa et al. [6] together with an angle of attack of 25 degrees were used.

On one side the results presented in the paper showed that the investigated low-profile VGs were able to decrease an existing separation in an s-shaped rectangular duct with strong curvature, high Mach-number and steady inflow conditions. The onset of the separation has been moved about 10 mm further downstream and the pressure recovery has been increased significantly.

On the other side the VGs applied within the superaggressive intermediate turbine duct downstream the transonic HP-turbine could not decrease the separation at the casing. On the contrary they even increased the losses through the duct. It was assumed that this is mainly a result of the wakes emanating from the HP-blades which preclude the VGs to develop vortices. Further the strong tip leakage flow already energizes the flow at the casing and with the vortex generators installed this effect is decreased and as a result the diffuser efficiency becomes even worse.

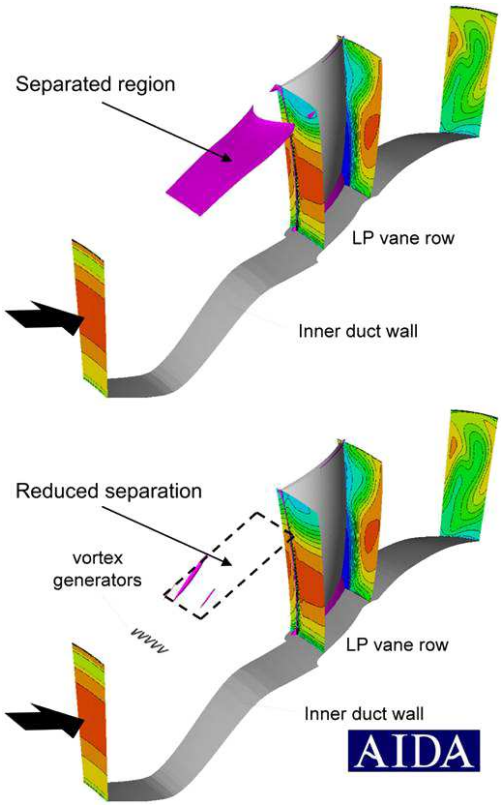

FIGURE 2.12: Steady CFD simulation of AIDA C5 duct without (top) and with (bottom) vortex generators (Göttlich [23])

The authors concluded that the investigated low-profile VGs at the defined axial position within the annular duct were not effective in stabilizing the flow through a three-dimensional ITD with a highly unsteady three-dimensional flow field although they showed promising results in the 2D S-shaped duct.

Within the cooperation of AIDA Wallin performed a variety of steady CFD simulations of the duct and the LP vane row but without the upstream turbine stage in order to define the optimal vortex generator position and height (Figure 2.12). The optimum was found for a counter-rotating vortex generator installation with a height of 0.7 mm and a length of 5 mm leading to 240 vane pairs around the circumference at approximately one vortex generator length upstream of the separation line of the clean duct.

Figure 2.12 shows a comparison between the baseline duct (no vortex generator) and the optimal vortex generator arrangement out of Wallins pre-test simulations. Besides the contours of stagnation pressure (low pressure in blue, high pressure in red) an iso-surface of negative axial velocity (in purple) is shown for each configuration.

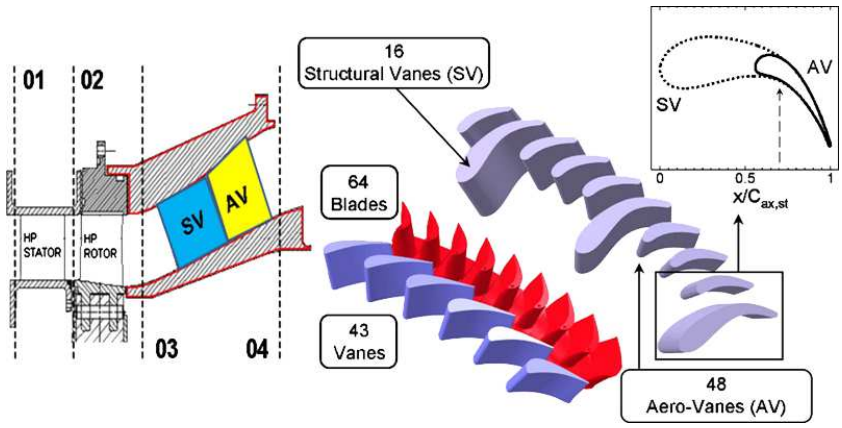

FIGURE 2.13: Investigation of the aerodynamics of a turning mid turbine frame designed with an embedded concept and tested in one–and–half stage configuration at the Von Karman Institute (Lavagnoli et al. [42])

2.2.4 Embedded concept for the turning mid turbine frame

A step forward in the design of mid turbine frames could be represented by the application of an embedded design concept. This architecture constitues the layout of the new stage developed and investigated during this thesis.
The basic idea is to merge the strut and the LP vanes in one embedded component. Such a concept was already investigated by Lavagnoli et al. [42] and Yasa et al. [94] in the one and half stage short duration test facility located at the Von Karman Institute (VKI). In that facility, starting from a pre-existing LP vane row, the bulky struts were shaped extending every fourth vane, while, similarly than in this thesis, the meridional flow path was kept the same (see Figure 2.13). In their comparison, the authors observed the struts causing an evident blockage effect and worsening the circumferential non-uniformity of the aerovane inlet flow field. The combined effect of multisplitter configuration and clocking was found to modify the spatial periodicity of the unsteadiness structure shed by the upstream stage. On the other hand no dramatic influence of the strut was found on the global unsteady performance.

2.3 Low Pressure Turbines

Low pressure turbine are conventionally made of high aspect ratio blades, that means secondary effects are confined to the endwall regions and, therefore, their contribution to the loss generation is less important than than in high pressure turbine.
Apart the potential effects which extends upstream and downstream the blade rows, the most relevant blade row interaction mechanism for these stages is normally the wake convection which has a 2D nature. Therefore, the studies provided in literature on the

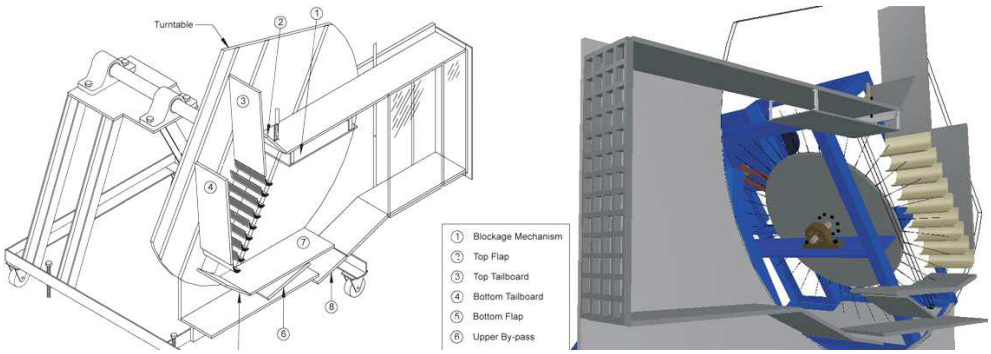

FIGURE 2.14: A view of the test section with the wake-generator rig (Mahallati et al. [48, 49])

unsteady aerodynamics of such turbines often refers to investigations in straight cascades where wake generators as rotating bars where used (see for example Figure 2.14). Whenever the aircraft climb to high-altitude cruise conditions [49], one of the problems which affects the low pressure turbine blades is the large drop in Reynolds number which they experience. There, the kinematic viscosity of gas is significantly higher than the corresponding sea level values. Therefore, modern turbines designed with high-lift LP blades have considerable regions of laminar boundary layers that are prone to separation at low Reynolds numbers even if the free stream has high levels of turbulence.

It was observed [32] that periodic wakes from the upstream blade-rows influence the location of boundary layer transition and reattachment, and the wake-blade interaction can in fact improve the performance of LP turbines. These investigations resulted in decreasing the losses while decreasing the number of blades of the rotor (High-Lift and Ultra-High-Lift blades) [29, 31].

In an experimental study of attached flows, Pfeil et al. [63] proposed that increasing the wake passing frequency prevents natural transition by the "calmed region" of the wake-induced turbulent spots, and the onset of wake-induced transition was independent of the wake-passing frequency.

Orth [58] arrived at similar conclusions and also found that transition onset is strongly controlled by the wake turbulence. One of the first surface–mounted hot–film measurements in unsteady turbomachinery flows was reported by Dring et al. [15], followed by Hodson [62]. Hodson reported that the higher wake-passing frequency produced higher profile losses due to higher turbulent wetted area on the surface of the blade.

Although wake-induced transition has been described by a number of authors, perhaps the experimental study of Halstead et al. [29] was a milestone in understanding the wake–induced transition in LP turbines and compressors. Their study showed that the calmed region, followed by turbulent spots in the wake path, was effective in suppressing flow separation at low Reynolds numbers. With increased blade loading, the onset of wake-induced transition moved upstream, closer to the leading edge.

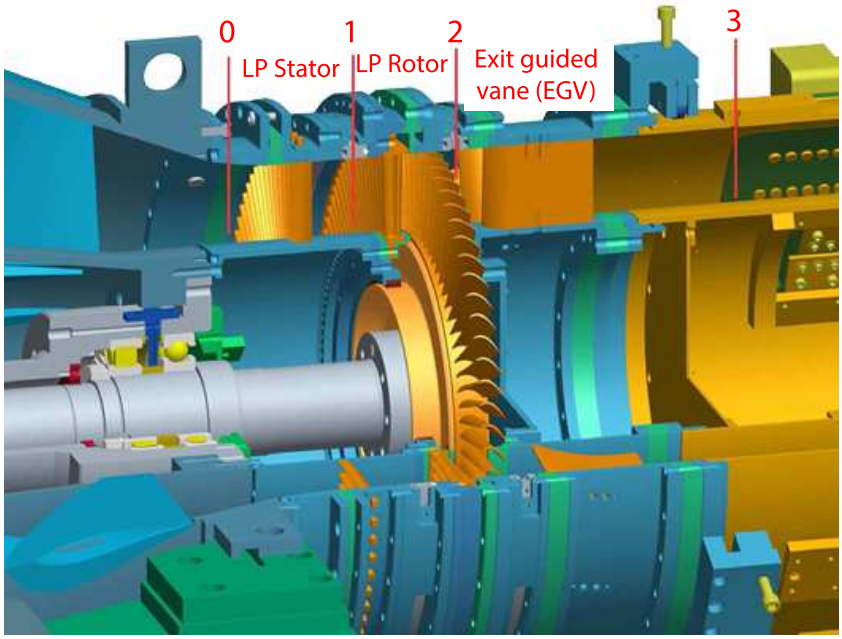

FIGURE 2.15: Subsonic test rig at Graz University of Technology for the investigation of the noise emitted by an engine-like low pressure turbine (Lengani et al. [43])

2.3.1 LP turbine exit flow

Modern civil aero-engines have to be designed in order to minimize the environmental impact also in term of acoustic emissions. Therefore, the study of the unsteady flow field downstream of the low pressure turbine is particularly interesting. In fact, the flow stream exiting the last stage of the LP turbine is (together with the Fan, LP compressor, combustion chamber and the jet flow) between the main sources of engine noise emission.

As already briefly introduced, the potential flow interaction of each blade/vane row extends upstream and downstream, as a mutual interaction between adjacent rows, whose relative influence on the flow fields depends on the ratio of stator to rotor pitches [40]. The potential flow field cuts into the wakes propagating from upstream, and the wakes are bowed and stretched as they convect through the rotor blade passages.

In state-of-the-art aero engines, LP turbine outflow is characterized by the presence of structural exit vanes aimed to support the rear bearing of the LP rotor shaft. Lengani et al. [43] described the development of the unsteady flow downstream of LP turbine rotor in one-and-a-half stage representative of a last stage turbine exit case of a modern LP turbine (Figure 2.15).

The time resolved measurements have been used to discuss in detail the features that characterize the unsteady flow field. The tip-leakage vortex, hub secondary flow, rotor wake and potential effects from the downstream exit guided vane (EGV) have been identified on the rotor outlet flow. All these features are influenced by the viscous and

potential interactions of the upstream stator. Hence, as the rotor moves each blade passage experiences variations in the wake and secondary flow extension.
Furthermore, in such a configuration designed with an uneven blade/vane count in order to reduce the tonal noise propagation, the superposition of perturbations from the stator and rotor blade row generates rotating patterns. The characteristics of the spinning modes, lobed structures and spinning rotational speeds directly depend, according to the aeroacoustic theory, on the blade to vane count ratio. The fluctuations of the flow quantities within a cycle of this periodic pattern are related to the stator/rotor mutual potential interaction and may influence the aerodynamic behaviour of the downstream rows.

2.3.2 Note to this thesis

The test setup used for this thesis adopts a low pressure turbine in a simplified configuration. Such a turbine, in a real engine, would represent just the first rotor of several stages which form a real LP turbine. In fact, the absence of a deswirler downstream of the two–spool rig second rotor does not allow a proper exit angle distribution reducing the turning of the flow across the rotor.
On the other hand, the measurements performed downstream of the second rotor allow to have a proper estimation of the impact of the structures generated through the turning mid turbine frames (object of this work) on the downstream low pressure turbine. In particular, the acoustic measurements reported in Faustmann et al. [18] can be used to estimate the propagation of the acoustic field through the successive blade rows.

Chapter 3

Test turbine facility description and modeling

In the remainder of this chapter, the facility used for the experimental investigation is introduced.
Moreover, the design of the new stage developed during the thesis is described.
Finally, the rig instrumentation is briefly presented.

3.1 Facility overlook

The transonic test turbine facility is a continuously operating two-stage cold-flow open-circuit plant, which consists of a transonic HP stage and a counter-rotating LP stage (marked with a red rectangle in Figure 3.1). This unique configuration allows the testing of rig inserts under engine representative conditions. The power output of the HP stage is used to drive a three-stage radial brake compressor (BC), while the power of the LP turbine is absorbed by a water brake (WB) with a maximum power of 700 kW. Both turbines are designed with overhung-type turbine shafts and additionally the LP turbine is mounted on an axially movable frame. This allows easy disk assembly without dismantling the bearings and the simple application of transition ducts and TMTF designs with different axial lengths. The facility is driven by pressurized air delivered by a separate 3 MW compressor station shown in Figure 3.1 and located in the second basement of the building.
Further information regarding the original test facility (1999) and the compressor station can be found in [17] and Pirker et al. [64].
During the DREAM project, the test facility consisting of the HP shaft was expanded by a single-stage counter-rotating low pressure turbine (LPT) in order to allow more engine

realistic investigations of different turbine mid structures. Anyway, the facility can be operated also in case of two co-rotating stage setup. Both turbines are designed with overhung-type turbine disks and additionally the LPT is mounted on an axially movable frame. This unique configuration allows the testing of rig inserts with a diameter of up to 800 mm with different axial lengths. It also enables a quite fast and simple exchange of different TMTF setups and an easy rotor disk assembly without the need of dismantling the bearings. For the design and operation of the LP-stage together with the TMTF see Hubinka et al. [36, 37].

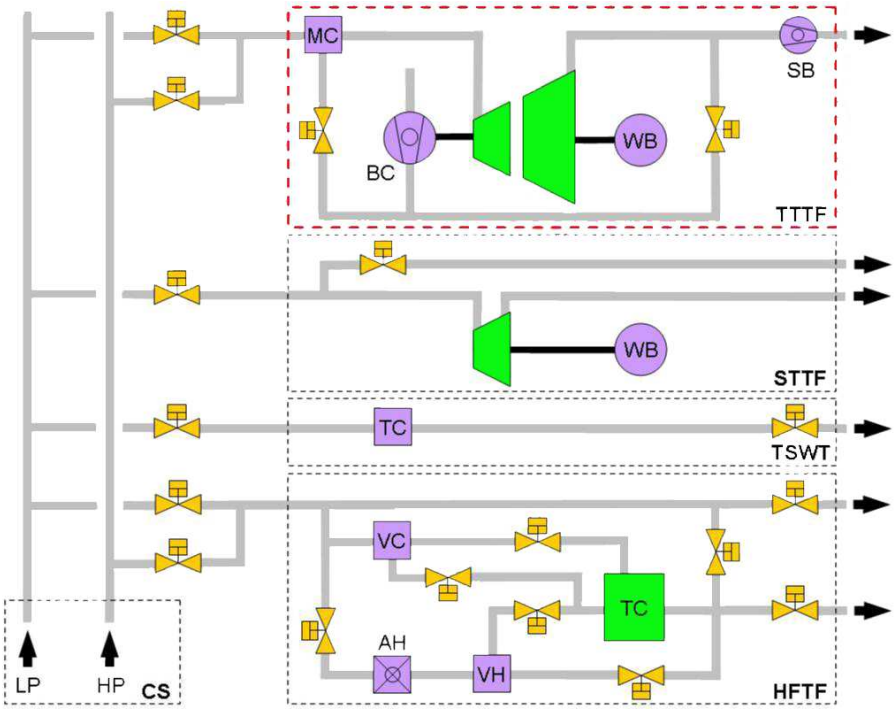

FIGURE 3.1: Compressor station

TABLE 3.1: Blading parameters and operating conditions.

Blading parameters						
		HP vane	HP blade	Struts	Splitters	LP blade
Vane/ blade no.		24	36	16	24	72
h/c_{ax}		1.15	1.37	0.53	3.5	2.94
Re(10^6)		2.38	1.1	1.86	0.4	0.46
Tip gap		-	unshrouded	-	-	shrouded
Operating conditions						
			HP stage		LP stage	
$n_{r,in}$ $[rpm/\sqrt{K}]$			524.4		195.3	
$m_{r,in}$ $[kg/s \cdot \sqrt{K}/(bar)]$			81.2		214.6	
Baseline	Stage p_t ratio		3		1.3	
Baseline	Power [kW]		1710		340	
with Splitters	Stage p_t ratio		2.83		1.36	
with Splitters	Power [kW]		1425		353	

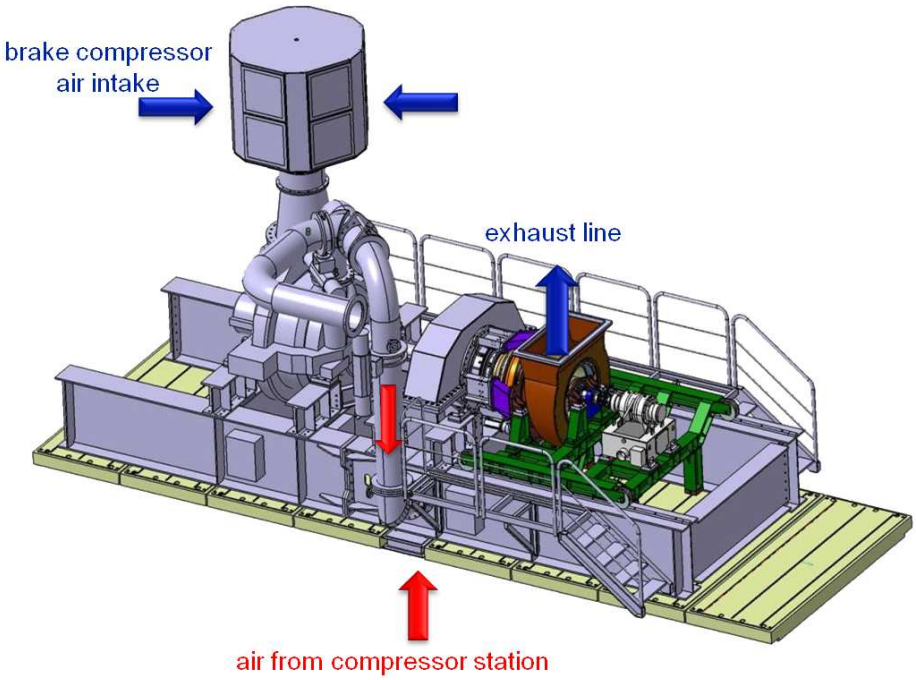

FIGURE 3.2: three dimensional view of the TTM Two stage - two spool test facility

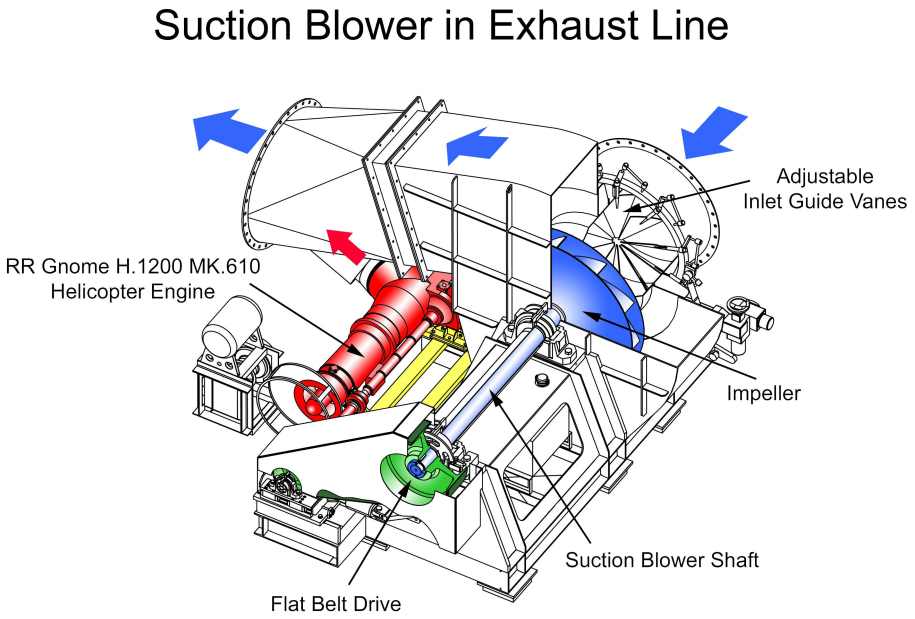

FIGURE 3.3: Suction Blower

The redesigned test facility is depicted in Figure 3.2 where the colored parts indicate the new stage. The arrows in the figure outline the air flow through the rig. The two mass flows originating from the compressor station and the brake compressor, respectively, are merged in a complex system consisting of a mixer and a tandem cascade at the inlet of the mixing chamber. The system was aerodynamically optimized by Bas and Mooren [5] using numerical investigations in order to obtain a quite homogenous mass flow and temperature distribution at the test section inlet.

Furthermore, the inlet temperature can be adjusted by cooling the air coming from the compressor station. However, the boundaries for the temperature control are limited due to the fact the mass flow provided by the brake compressor cannot be cooled. As already mentioned, the additional mass flow of the brake compressor an overall mass flow of up to 22 kg/s can be achieved.
The inlet pressure is limited to 4.5 bar absolute due to the design of the mixing chamber. The testing of the embedded design setup needed to increase the overall pressure ratio (Table 3.1). Therefore, the only possibility was to reduce the rig backpressure by operating a suction blower to reduce the external pressure down to 200 mbar below ambient pressure (SB in Figure 3.1). This device allows to run the test turbine facility with stable operating conditions without day-to-day variations. The suction blower showed in Figure 3.3 uses a Rolls Royce Gnome helicopter engine via a flat belt drive as power source and allows a very precise adjustment of the turbine exhaust pressure by means of speed control. The maximum rotational speed of the HPT stage is limited by the brake compressor to 11550 rpm and depending on the stage characteristic a maximum coupling power of 2.8 MW can be reached. The power of the LPT is absorbed by a waterbrake with a maximum power of 700 kW and a maximum rotational speed of 4500 rpm. Detailed descriptions of the design, the possibilities and the operation of the adapted TTTF can be found in Hubinka [36].
Figure 3.4 depicts a cross-sectional view of the test setup with the flow going from left to right. The air enters the rig through the mixing chamber and is then guided to the inlet of the test section which consists of the transonic HP stage, an S-shaped TMTF and a counter-rotating shrouded LP turbine. The flow leaves the test section through support struts with a simple straight airfoil shape and a diffuser to recover some pressure before entering the exhaust casing. Within this thesis two TMTF setups (baseline and multisplitter designs) have been investigated using the same HP stage and LP rotor.

3.2 The turning mid turbine frame

High pressure and low pressure stage are connected via a Turning Mid Turbine Frame. The discussion carried out through this thesis is based on the aerodynamic investigation and comparison of two TMTF setups.

3.3 Baseline case: turning mid turbine frame (TMTF)

The aerothermal design of the baseline configuration was designed by MTU Aero Engines. The experimental setup of this stage was already presented in the PhD thesis of

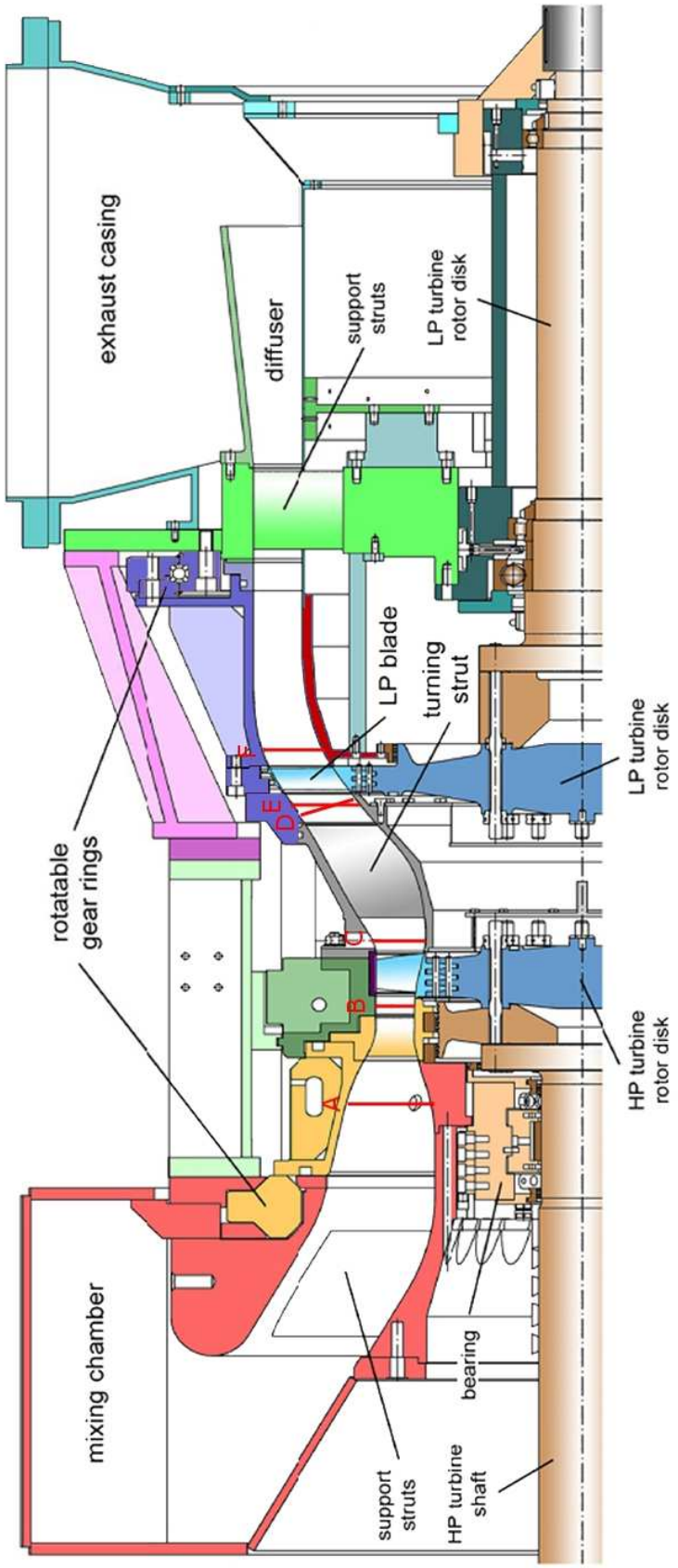

FIGURE 3.4: Cross section of the TTM Two stage - two spool facility

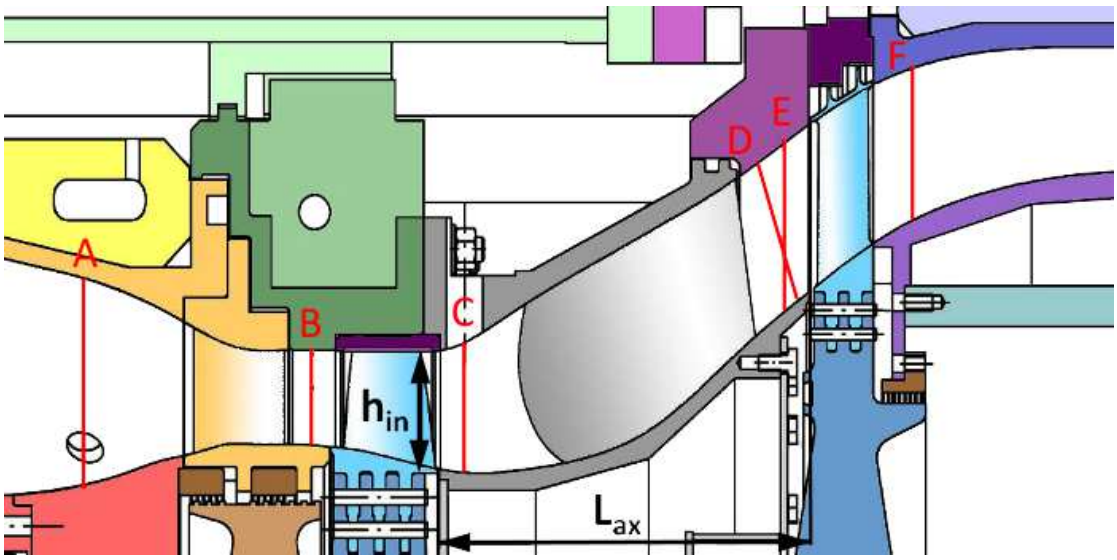

FIGURE 3.5: Cross section of the Baseline mid turbine frame

Santner [69]. It consists of 16 turning struts, has a non-dimensional axial duct length of about 3.5 (L_{ax}/h_{in}, see Figure 3.5) and an area ratio of 2. Figure 3.5 represents a cross-sectional view of this setup. The baseline configuration was designed using a quite complex three-dimensional design of the TMTF strut and keeping rotationally symmetric endwall contours. The struts have a maximum thickness to chord ratio of 22% at about 25% of the axial chord length to provide enough space for service lines like oil pipes and for load carrying structures which results in a radial insertability of 18%.

3.4 Embedded concept setup (S-TMTF): turning mid turbine frame with embedded splitter vanes - S-TMTF

The design process of the splitter vanes was based on numerical investigations performed on the baseline configuration [79, 80].

Figure 3.6 shows that, for the new stage, the meridional flow path was kept as in the baseline case. The axial extension of the splitters as well as the splitters count were decided after a compromise between aerodynamic effectiveness and solid blockage. In order to increase the uniformity of the flow field downstream of this stage, the position of the new wakes should be equi-spaced along the strut pitch. Therefore, the two splitters axes have been located at $P = 0.33$ and $P = 0.67$.

Since the design target was to reach a zero-incidence zero-lift for each of the two vanes, it was important to control the profile parameter along the span. Therefore, Figure 3.6 plots the positions of seven control sections chosen at different spanwise locations (H=0.00, H=0.05, H=0.25, H=0.50, H=0.75, H=0.95, H=1.00).

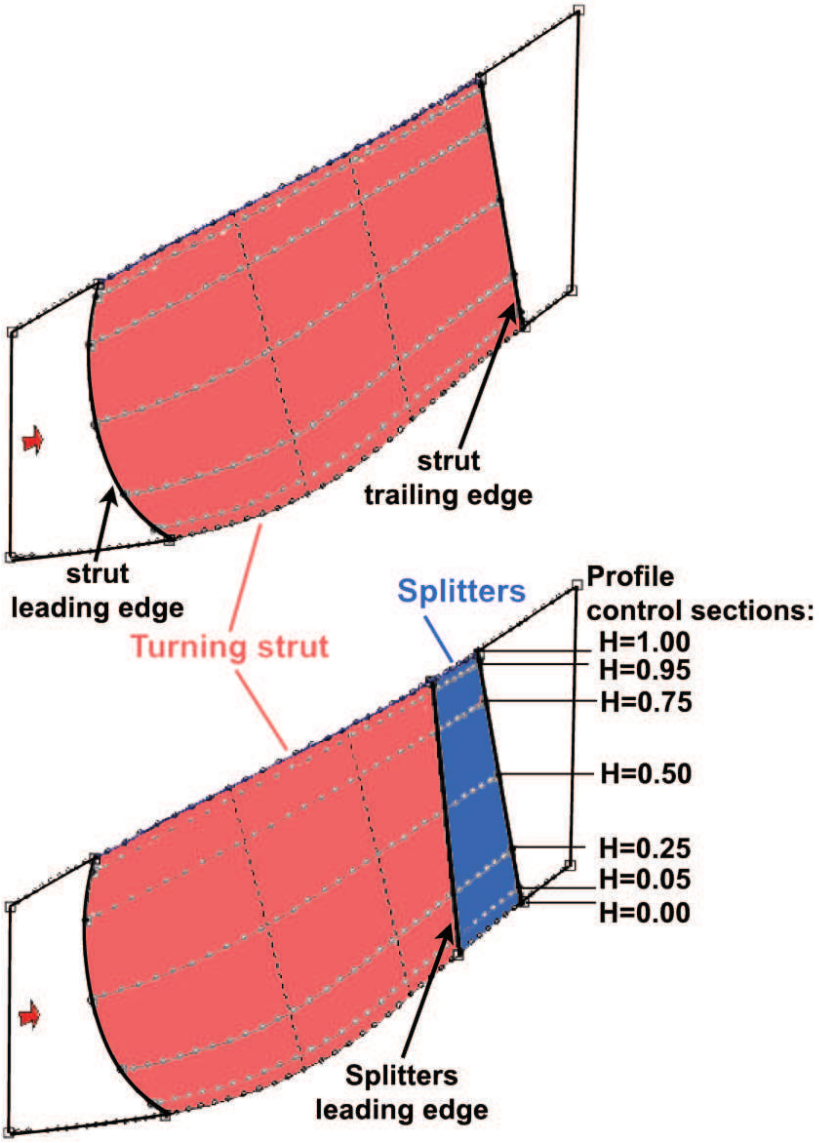

FIGURE 3.6: Meridional view

Figure 3.7 shows that the metallic angle and the thickness distributions at the splitter trailing edge were kept the same as the struts, while, at the splitter leading edge the vane inlet angle was iteratively turned targeting to a zero-incidence condition.
The vanes were finally shaped by means of a hyperbolic interpolation the single layouts over the span in order to obtain a full 3D design (see Figure 3.8) The generation and evaluation of several designs defined the final shape which was manufactured and tested.

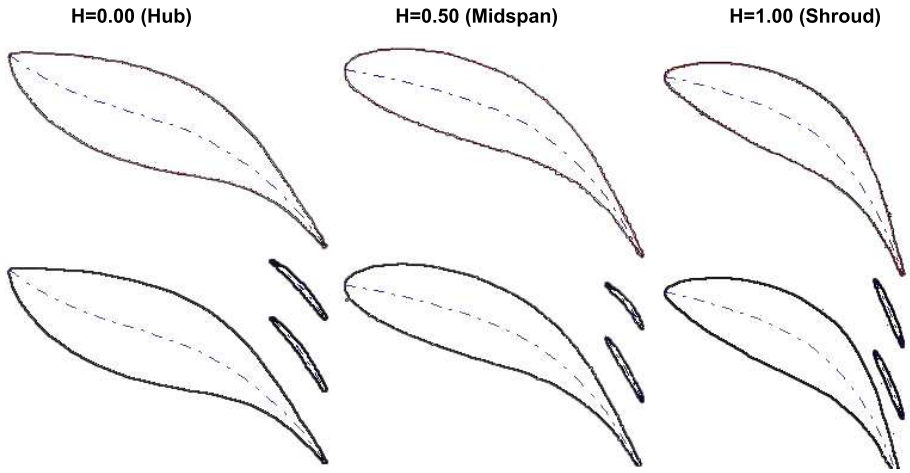

FIGURE 3.7: Blade to Blade view at three different span positions: H=0.00, H=0.50, H=1.00

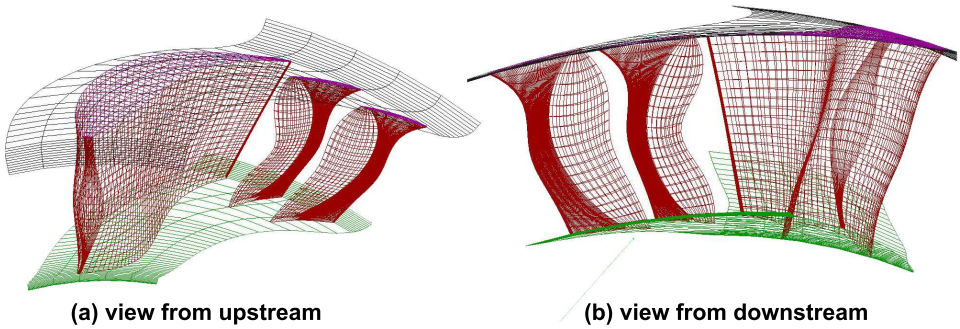

FIGURE 3.8: 3D view of the embedded concept

3.5 Design and manufacturing

Figure 3.9 shows the machine cutaway where the component with turning struts and embedded splitters (S-TMTF) is placed between the two turbines. The CAD design was optimized to allow an easy assembly of the component.
The splitters have been milled out of one piece generating a bladed ring (*bling*). Security reasons for the operation of the facility required a crack testing of this component by means of leak liquids (Figure 3.10).

3.6 Rig Instrumentation

In order to ensure the repeatability of the test runs to obtain comparable measurement results the test rig is instrumented with several sensors and total pressure and temperature rakes to be able to adjust and to monitor the operating conditions. The equipment and the positions of the applied techniques will be explained in this part just briefly

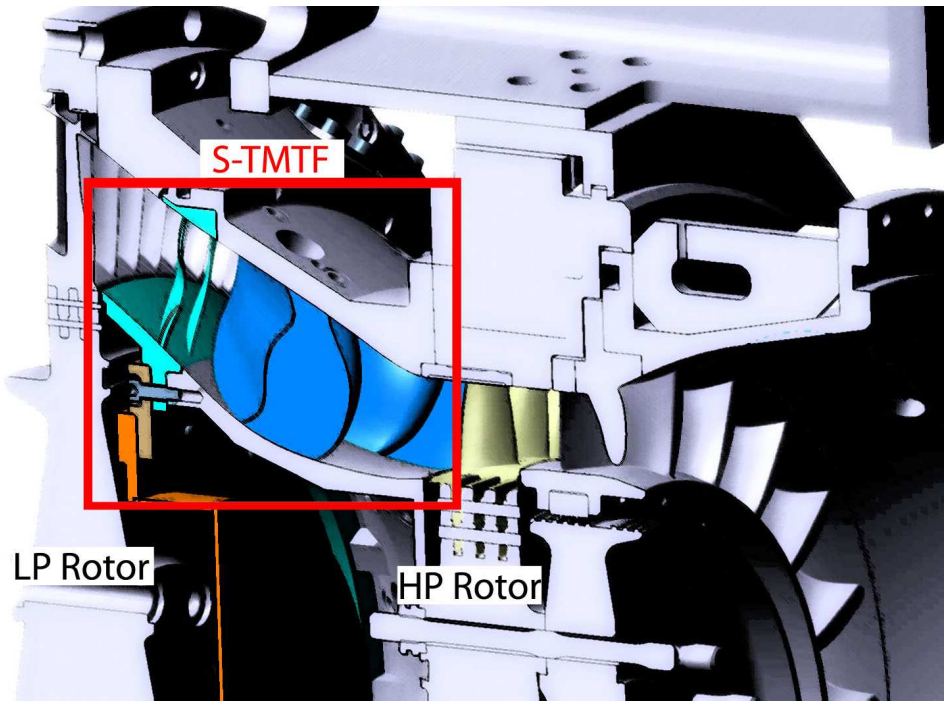

FIGURE 3.9: 3D view of the embedded concept

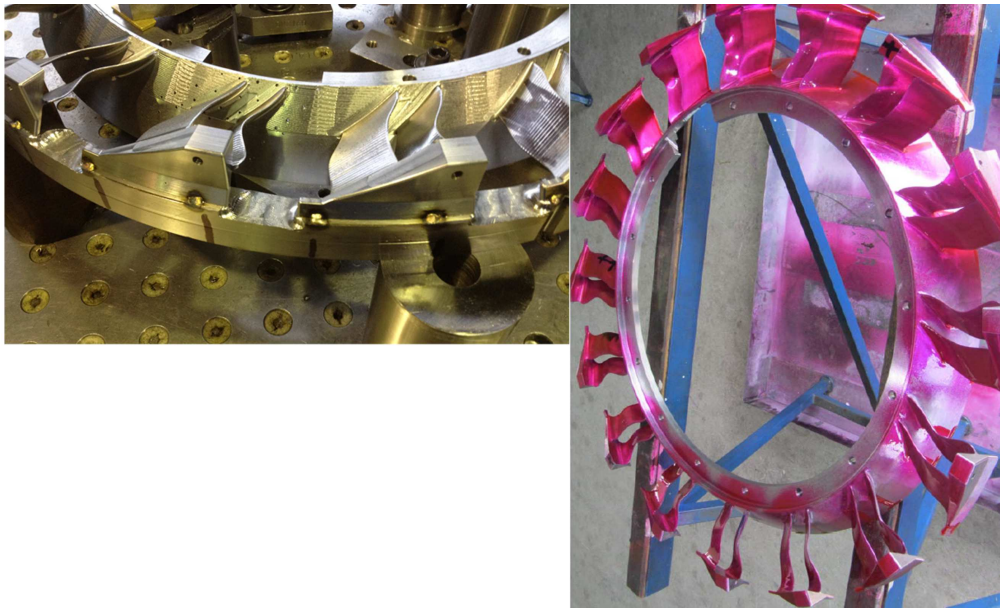

FIGURE 3.10: Manufacturing and integrity checkup of the splitter bladed ring

whereas detailed information of the applied instrumentation can be found in Hubinka [35].

3.6.1 Measurement devices

The permanent instrumentation of the rig consists of:

1. Pressure scanner modules PSI 9016 with 16 channels and an accuracy of 0.05% full scale to measure total and static pressure
   - 4 x ± 0.35 bar
   - 1 x ± 2.1 bar
   - 1 x ± 2.1 bar (12 channels) and ± 3.5 bar (4 channels)
2. National Instruments Field Point modules for temperature measurements
   - 2 x resistance thermometer input modules FP-RTD-122
   - 4 x thermocouple input modules FP-TC-120
3. National Instruments Field Point modules for all sensors
   - 5 x analogue input modules FP-AI-110
4. Bently Nevada shaft monitoring system to detect and record (ADRE box) the shaft data like rotational speeds, power output, vibrations and radial displacement

3.6.2 Total Pressure and Total Temperature Rakes

Total pressure and temperature rakes are used to acquire the operating conditions. Therefore, a total pressure and total temperature rake have been applied at HP stage inlet (plane A), TMTF inlet (plane C) and LP stage exit (plane F); positions see Figure 3.5.

The rakes in plane A and F are mounted in the rotatable HP vane ring and the rotatable outer LP casing, respectively, which enables 360 degree traverses to acquire the rig inlet and exit flow distributions. Due to the rig design the rakes in plane C are mounted in the fixed part of the TMTF and cannot be moved in circumferential direction but by moving the HP vane ring the total pressure and total temperature distribution over one HP vane pitch can be acquired. Further informations about the positioning can be found in Santer [69].

A Kiel-hole probe design was applied for total pressure as well as total temperature measurements because it is insensitive to flow angle variations up to ±30 deg. The pressure was acquired with the pressure scanner modules PSI 9016.

The total temperature rakes were equipped with type K thermocouples connected to the National Instruments field point modules (FP-TC-120). Area averaging was performed to obtain the mean total Experimental Setup 18 pressure and total temperature in each plane. More information about the design and the calibration of the rakes can be found in Hubinka [35].

3.7 Total Pressure and Total Temperature Rakes

The intention of the measurements was to investigate the TMTF under engine realistic conditions. Therefore, the aero design point was chosen in order to simulate cruise operating conditions like in a modern jet engine with a single stage HPT. Due to the fact that the facility is a cold flow facility with temperatures around 440 K (compared to about 1700 K in turbofan engines) the Mach number similarity was chosen as criterion. Table 3.1 displays the main parameters of the investigated operating point. Non-dimensional and/or reduced parameters were defined to guarantee the same conditions and to obtain comparable results.

$$m_{red} = m\frac{\sqrt{T_{t,in}}}{p_{t,in}} \tag{3.1}$$

$$n_{red} = \frac{n}{\sqrt{T_{t,in}}} \tag{3.2}$$

$$\Pi_{tot} = \frac{p_{t,A}}{p_{t,F}} \tag{3.3}$$

Baseline and multisplitter cases were both operated keeping the same reduced massflow (Equation 3.1) and reduced speed (Equation 3.2) for both the HP and the LP stages. As already stated, the embedded design required the use of a suction blower to increase the overall pressure ratio. The effect of the blockage due to the splitters lead to a redistribution of the pressure ratio of both the turbines. Across the HP stage the pressure ratio dropped from 3 to 2.83 (the HP stage was then still transonic), while the pressure ratio raised from 1.3 up to 1.36 through the LP stage. The overall pressure ratio defined in Equation 3.3 (where the pedix A and F are referred to the measurement planes in Figure 3.5) raised from 4 up to 4.09.

Chapter 4

Numerical setup

A central part of this thesis concerns the analysis of numerical prediction results. Therefore, this chapter is aimed to present the different setups used to model the flow field within the two-stage two-spool facility.
The baseline setup (without splitters) was simulated by means of both steady and unsteady schemes. The interpretation of the time-averaged field within the TMTF passage is reported in Spataro et al. [80] where the LP stage was simulated.
On the other hand, both the high pressure and low pressure stages have been modeled and simulated comparing different CFD setups in order to analyse the performance prediction of different interface schemes. These results are discussed in Spataro et al. [79] where experimental data were compared with numerical results.
All the meshes presented in the followings undertook a grid independence study as assumption for the numerical investigation.

4.1 Steady simulation of the low pressure stage

Numerically, the time-averaged flow field of the LP stage was investigated calculating the TMTF and the LP rotor passages with five-hole probe measurements in Plane C (downstream of the HP rotor) as 3D inlet boundary. The probe was traversed in this plane over one HP vane pitch (15 deg). To obtain the full HP vane strut periodicity of 45 degree the plane was triplicated in circumferential direction.
A mixing plane interface between turning struts (stationary domain) and LP rotor (rotating domain) was applied. The outlet condition of static pressure in a plane located at an axial distance of 6 times the LP blade axial chord length downstream of the LP rotor trailing edge where a row of pressure taps is located.
Figure 4.1 shows the domain boundaries and the interface location for the simulation of

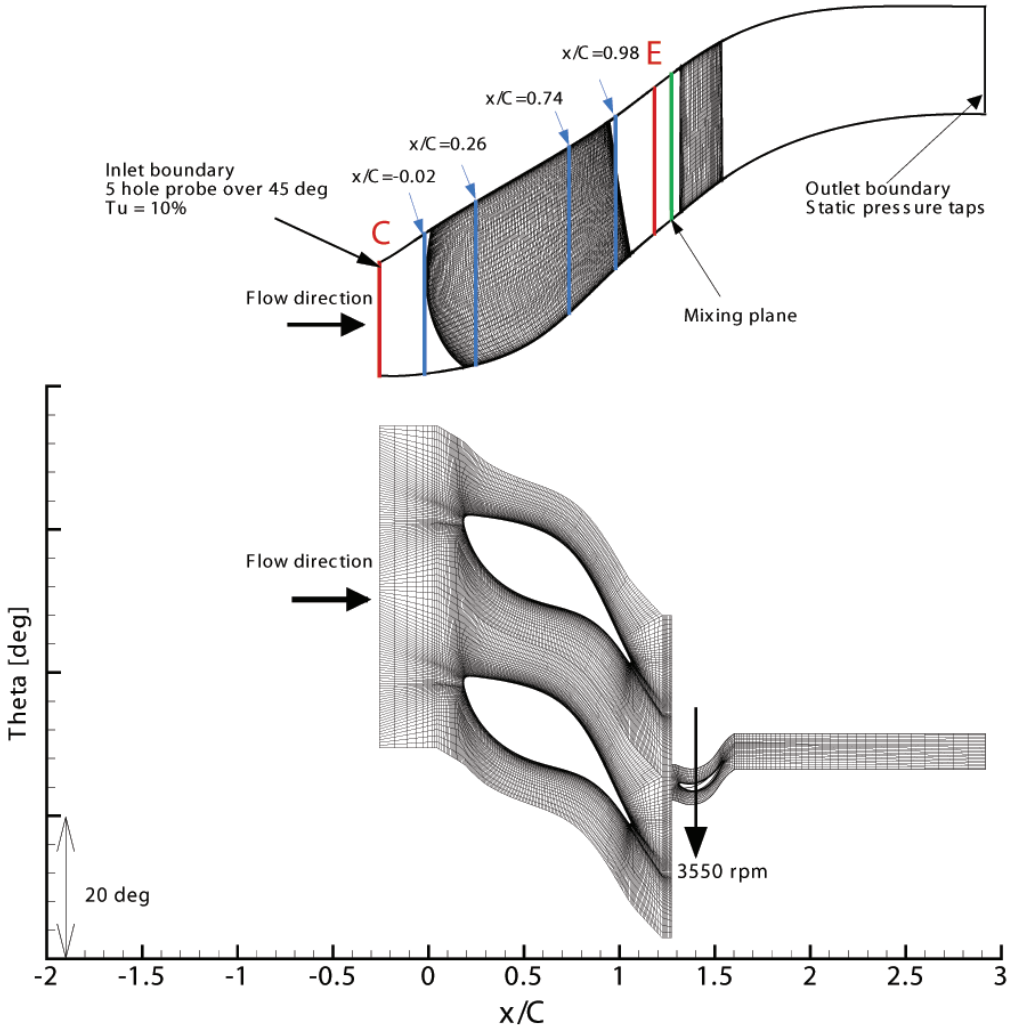

FIGURE 4.1: Numerical setup for the steady computation performed on the low pressure stage (Spataro et al. [80])

the LP stage.

The mesh consists of 2.5 Millions elements, while the y^+ was limited to 1 next to the blade surface and to 2 next to the endwalls. A commercial CFD code (Ansys CFX©v12.1) was used as solver.

The code solves the Navier Stokes equation system with first order accuracy in areas where the gradients change sharply to prevent overshoots and undershoots and maintain robustness, and second order in flow regions with low variable gradients to enhance accuracy [3]. The turbulence was modeled using a k-ω SST turbulence model (Menter [52]).

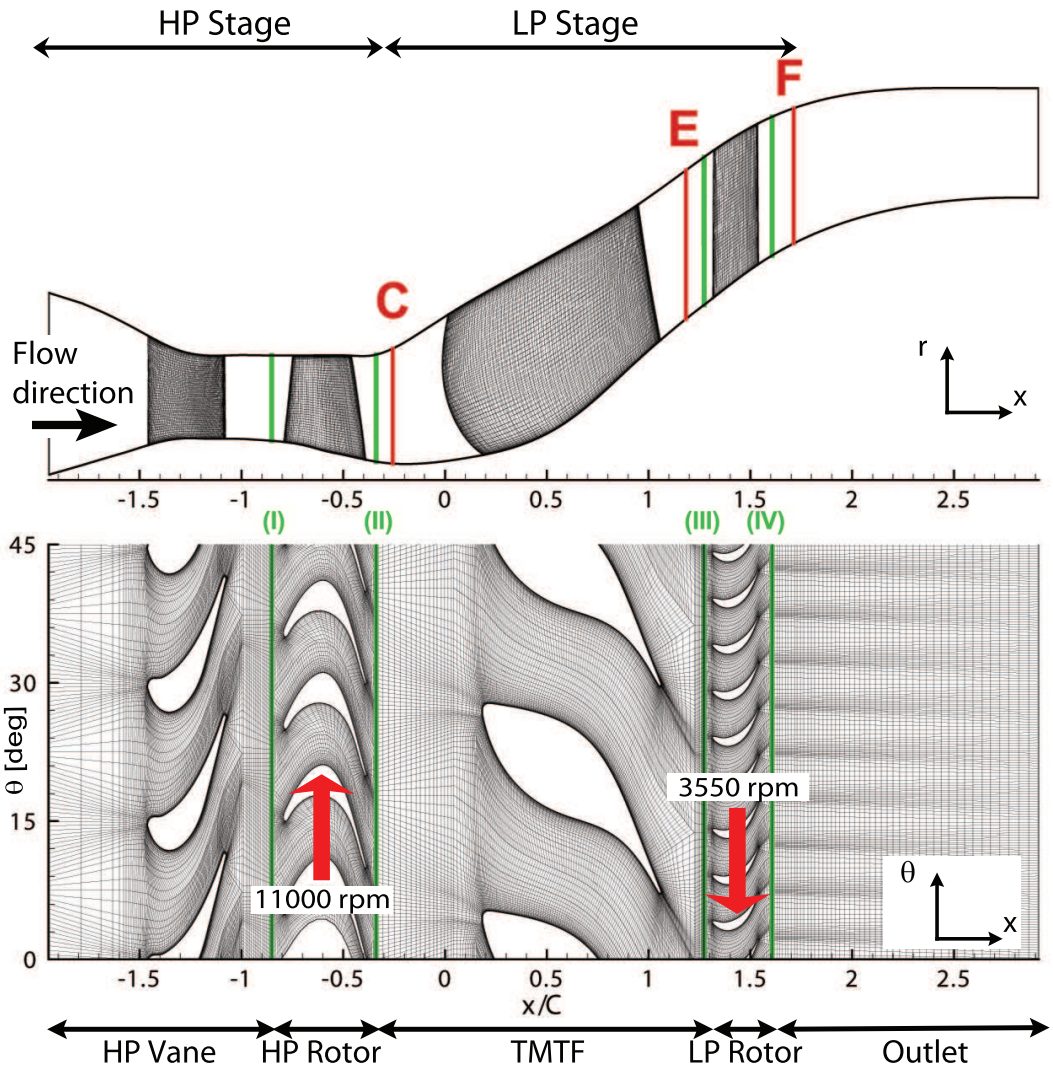

FIGURE 4.2: Numerical setup for the simulation of the whole machine (Spataro et al. [79])

4.2 Steady and unsteady simulation of the whole machine

Several numerical simulations of a two-stage two-spool transonic turbine with the baseline setup were undertaken. Figure 4.2 shows the computational domain for this investigation. Before proceeding with the discussion of the results, it is important to present the differences between the setups (Table 4.1):

Case A In this simulation each domain consists of one blade passage mesh. The outlet domain has a pitchwise extension of 5 degrees of pitch extension (the same as the LP rotor's mesh). All interfaces (I, II, III, IV) are mixing planes.

Case B Interfaces II and IV were changed to frozen rotors. Therefore, the same periodicity is required for the HP rotor and the TMTF (90 degrees), and for the LP

TABLE 4.1: CFD Setups.

Mesh passage per domain and Mesh size (in million of nodes)						
	HP Vane	HP Rotor	TMTF	LP Rotor	Outlet	Tot Mesh size
Mesh size	0.67	0.39	1.03	0.23	0.06	
Case A	1	1	1	1	1	2.38
Case B	1	9	4	1	1	8.59
Case C	1	1	1	1	1	2.38
Case D	1	1	1	1	1	2.38
Unsteady	6	9	4	18	18	16.7

Domain Interfaces for different numerical setups				
	(I)	(II)	(III)	(IV)
Case A	Mix pl	Mix pl	Mix pl	Mix pl
Case B	Mix pl	Frz rot	Mix pl	Frz rot
Case C	Mix pl	Mix pl	Mix pl	Frz rot
Case D	Mix pl	Mix pl	Mix pl	– (*)
Unsteady	Slide	Slide	Slide	Slide

(*) counter rotating endwalls for the downstream domain

rotor and the outlet domain (5 degrees). Interfaces I and III were kept as mixing planes.

Case C The mesh setup for this case is the same as for Case A: interfaces I, II and III are mixing planes, while interfaces IV was turned to frozen rotor.

Case D For this case the mesh of the outlet domain and the one of the LP rotor were merged together removing interface IV. This leads to one rotational domain (LP rotor + Outlet) where counter rotating wall velocity was assigned to the hub and shroud endwalls in order to fix them in the absolute frame. Interfaces I, II and III are mixing planes.

Unsteady In order to simulate the time-resolved flow, an unsteady CFD was performed using sliding interfaces. Therefore it was required to satisfy the machine full periodicity computing 90 degrees pitch for each domain. This leads to a quite heavy calculation where the mesh refinement was constrained by the server maximal memory (32 GB). The timestep was set to 1/100 of the HP rotor blade passing period ($t_s = 1.5e-6s$). The numerical scheme is time marching where the code solves second order backward equations.

Chapter 5

Instrumentation and Measurements techniques

The study of the flow field through a transonic two-stage two-spool turbine requires the use of the most advanced instrumentation and measurement techniques in order to properly catch the time-mean as well as the time-resolved flow field.
Despite the analysis of steady measurements still represents the basis for proper machine characterization, unsteadiness plays a major role in turbines, especially in the case of a rig meant to test shortening solutions where blade rows interaction is critical. This is particularly true for the evaluation of the aerodynamics as well as of the acoustics of the two turbine transition duct configurations investigated in this thesis.
Therefore, in order to properly reconstruct a time-dependent signal of the flow field downstream of the LP turbine where the unsteadiness content is due to both rotors, a new post processing procedure called Rotor Synchronic Average (RSA) was implemented by the author and presented in Lengani et al. [44].
Moreover, the modal theory by Tyler and Sofrin [86] originally used to describe the sound generation mechanisms downstream of a compressor stage, was applied during this work to investigate the flow field downstream of the two-spool turbine rig.
Applying such a theory, a variable is decomposed in time and space at any circumferential positions downstream of a turbine stage. Since one of the assumptions of the Modal Theory is the full time-space periodicity of the processed signal, for the aerodynamic analysis, this decomposition could be applied just to the numerical results after unsteady simulation [46], while, for the acoustic analysis, also to the microphones data [18]. Therefore, for the unsteady-CFD simulation, the full machine spacial periodicity (90 degrees) was modeled, while the traversable microphone array allowed full traversing over 360 degrees. In fact, the limited aerodynamic probe traversing (maximum range 22.5 degrees in circumferential direction) did not allow the application of such Theory

to fast response probe (FRAPP) data.
The first part of this chapter presents the measurement setups, while, afterwards, advanced post processing tools for unsteady data reduction (RSA procedure and Modal Theory analysis) are presented.

5.1 Instrumentation

For the steady investigations the test section was equipped with static pressure taps at several positions and five-hole probe (FHP) measurements have been performed at TMTF inlet and exit as well as at the LPT exit.
Furthermore, oil flow visualization was applied to obtain a qualitative insight of the flow evolution. The unsteady effects and interactions of the components were investigated using a fast response aerodynamic probe (FRAP) and a microphone array traversed at the turbine exit duct. In the remainder of this section, the instrumentation is presented.

5.1.1 Wall pressure measurements

The test rig was equipped with pressure taps at each measurement plane (A to F, see Figure 3.5) at hub and casing at four positions over the circumference. One strut passage of each setup was fully instrumented with five lines of pressure taps located at 10%, 25%, 50%, 75% and 95% pitch over the hub and shroud endwalls.
The pressure taps rows for the baseline setup are shown in Santner [69], while Figure 5.1 reports the taps positions for the multisplitter stage which was instrumented during this thesis. Within this configuration, two more lines where added at the hub endwall of the central splitter passage (35%, 65%). Instead, the assembly design of the turning mid turbine frame with embedded splitters did not allow the placement of pressure taps within the splitter passage at the casing.
Moreover, one of the struts was instrumented with pressure taps along five lines located at 10%, 25%, 50%, 75% and 90% span (see Figure 5.2). All measurement positions along the endwalls were realized with an inner diameter of 0.8 mm. The struts were equipped with metal pipes with a smaller diameter in order to avoid the disturbance of the flow along the surface. All pressure taps were connected to the pressure scanner modules PSI 9016 via silicone tubes. The measurement accuracy of the pressure taps was around ± 1 mbar.

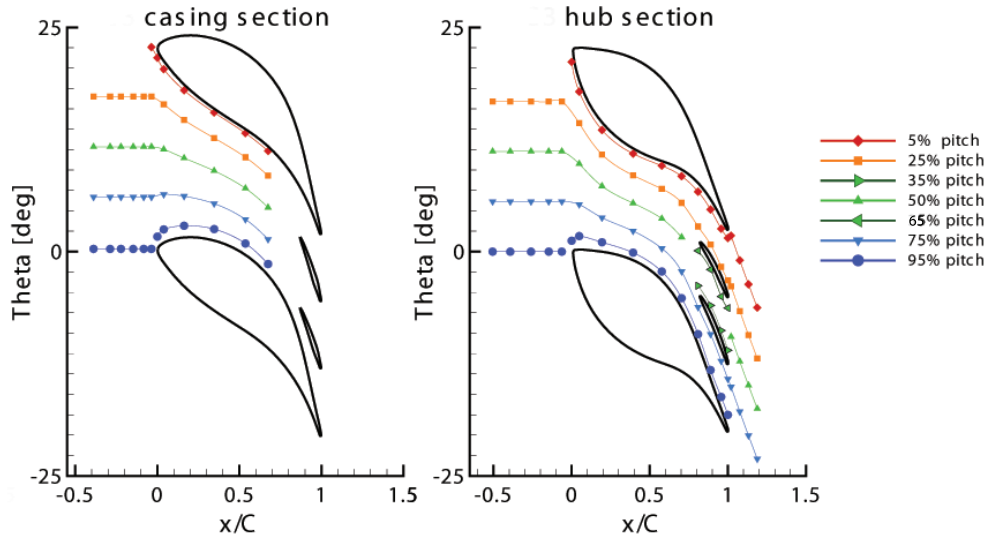

FIGURE 5.1: Location of pressure taps on the duct inner and outer endwalls

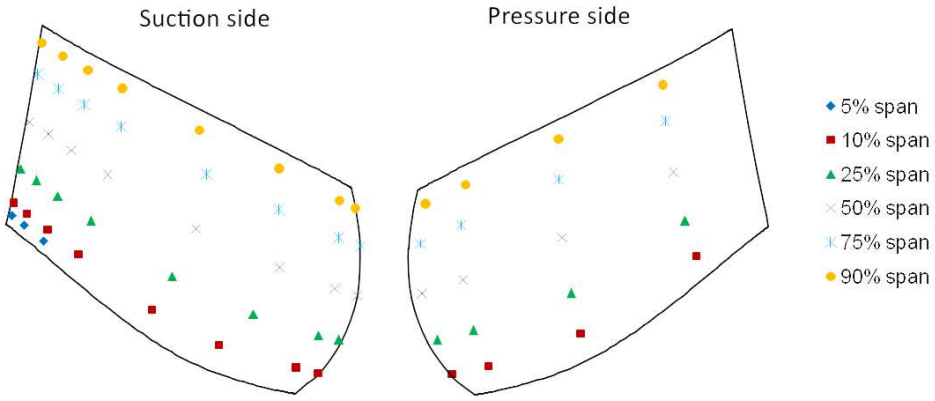

FIGURE 5.2: Location of pressure taps on the strut suction and pressure sides

5.1.2 Five hole probe measurements

Among the steady measurements, five hole probes were traversed in three measurement planes (Plane C, E and F according to Figure 3.5). In Plane C a probe was traversed radially over 85% of the blade height and over one HP-vane pitch which corresponds to one third of two struts pitches. In each measurement point, the probes were turned into the flow to reach the highest accuracy and to ensure to be always within the calibration range of the probe. During the probes rotation around their axis, the probe head remains aligned with the axis in order to avoid tangetial and axial displacements of the measurement position. Due to the uncommon flow direction relative to the measurement location, in some planes (D, E and F in Figure 3.5) special developed five-hole-probes (IST, RWTH Aachen) with an inclined probe head of 2.5mm diameter were applied. The probes were calibrated for Mach numbers between 0.1 and 0.8, yaw angles between -20 deg and +20 deg as well as pitch angles between -16 deg and +20 deg. The uncertainty

of the Mach number is 0.005, while for the yaw and pitch angle the measurement error is ±0.3 and ±0.5 degrees respectively. Negative values of the yaw angle indicate a counter-rotating flow (with respect to the HP rotor circumferential speed) and negative values of the pitch angle indicate the flow direction towards the machine axis.
The correlation between the calibration characteristic and the value to be measured is given by a multi-parameter approximation.

5.1.3 Aerodynamic unsteady measurement techniques

Unsteady flow measurements were performed by means of two different fast-response aerodynamic pressure probes. In the former studies with the baseline configuration [44, 46], a 2-sensor probe, operated as a virtual four sensor probe for 3D aerodynamic measurements [41], has been used.
The results presented in this thesis are obtained by a cylindrical one sensor probe, see Persico et al. [61] for more details. Unsteady measurements with the one sensor probe have been repeated in the baseline setup and provided results in very good agreement with the 2-sensor probe. The one-sensor probe works as a virtual 3-hole probe by performing three acquisition at three different positions around probe axis.
Limits of the one sensor probe have been observed in regions of the measurement plane with large radial components, where the error on static pressure increases when compared with the 2-sensor probe. It has to be noted that also the 2-sensor probe is at the limits of the pitchwise calibration range in the same regions. Otherwise, for both probes, the extended uncertainty is in the order of ±0.5% of the kinetic head for the pressure measurements and of ±0.3 deg for the flow angles.
The fast response probes were traversed in annular sectors in planes D and F (marked in Figure 3.5 and Figure 5.3(a)). Plane D is a conical surface which, in the meridional view, results inclined by 110 deg measured from the machine axis direction and, at midspan. Its distance from the vane trailing edge is 14% of the strut axial chord; whereas, plane F is perpendicular to the machine axis and is located at 77% of the LP rotor chord downstream of the LP blade trailing edge.
Data is acquired at 200 kHz for 2 s, it corresponds to more than 100 revolutions of the LP turbine and more than 350 of the HP turbine.
The full area traverses were performed over one strut pitch (22.5 deg) up-and downstream of the LP rotor. The measurement grid consists, for both planes (D and F) and both configurations, of 19 positions along the blade span and of 46 positions over one pitch of the strut ($\Delta\theta_{strut}$).

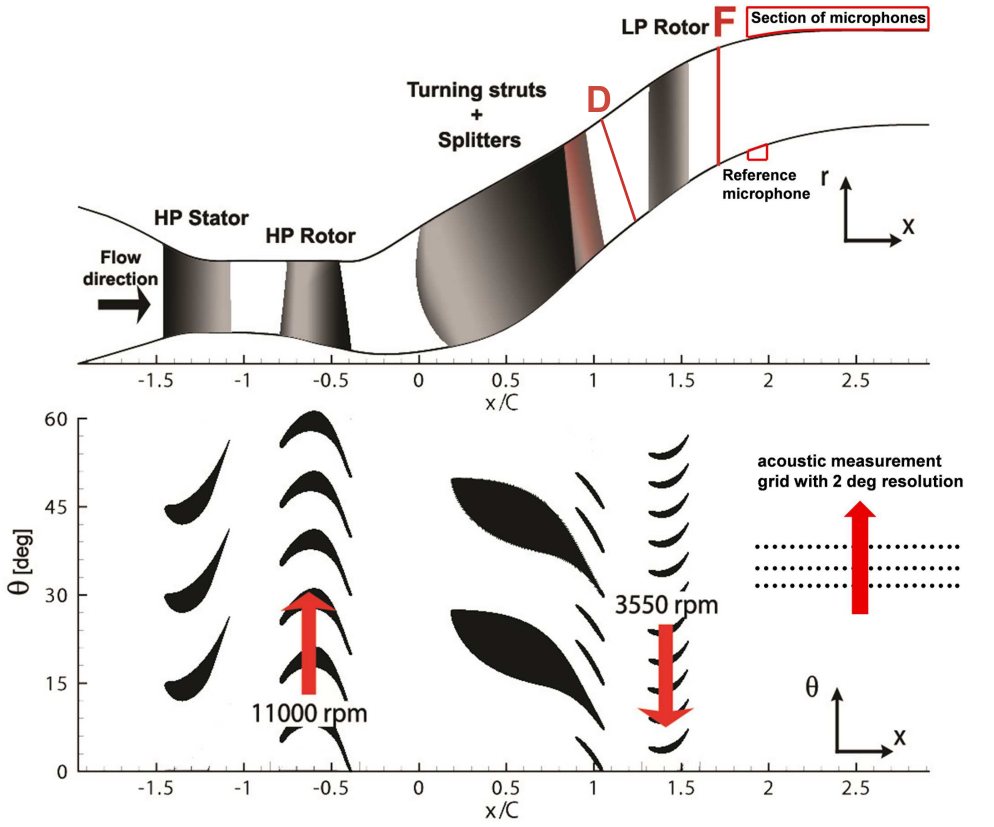

(a) Measurement section traversing

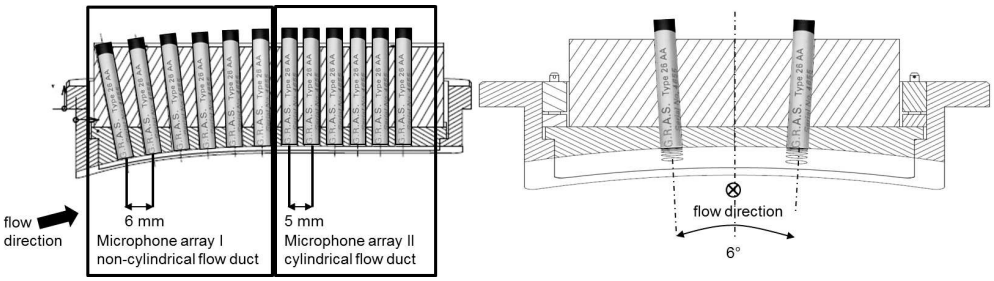

(b) Microphone array at the rig exit duct

FIGURE 5.3: Acoustic measurement setup

5.1.4 Acoustic measurement setup

The measurement setup installed to perform acoustic investigation on the noise generation and propagation is presented in detail in Faustmann et al. [18]

The microphone array, which was used to instrument the rig, consists of 24 microphones type 40DB from the company G.R.A.S.. This type of microphone is a 1/4-inch prepolarized pressure microphone with a dynamic range upper limit of 170 dB and a frequency response from 10 Hz to 25 kHz (1 dB). The preamplifier type 26AC has a very low inherent noise level as well as a dynamic range and a frequency response from below 2 Hz to 200 kHz (0.2 dB). Pressure microphones have a so called sphere characteristic,

which means, that every sound wave, independent from the angle of impingement on the diaphragm, has nearly the same intensity. There are two ways of mounting the microphone for acoustic investigations in flow ducts, either mounting a microphone rake in the flow [16], or with flush mounted microphones on the wall [57]. A study was done for aligning the microphones behind the LP turbine in one of four exchangeable wall plates (see Figure 5.3(a)). In total 25 microphones are used, one as reference microphone at the hub, which is fixed, and 24 microphones staggered and flush mounted at the outer casing downstream of the LP turbine, which are fully circumferentially movable. The angular displacement between the microphones is 6 deg and can be seen in Figure 5.3(b). The first 12 microphones are placed in the non-cylindrical part of the flow duct with an axial displacement of 6 mm with respect to the center of the diaphragm.
The acoustic measurement data out of this region will be used to widen out the post processing also for non-cylindrical ducts. Since the established acoustic post processing tools are developed for flows in cylindrical ducts (e.g. [57] and [85]), it was important to maximize the microphone number in the straight part of the measurement section (Figure 5.3(b)).
The results presented in this thesis are taken from microphone array II. Due to the desired frequency resolution and the space limitations the distance between the microphones is 5 mm (see Figure 5.3(b)). For the data acquisition National Instruments equipment is used. The sampling frequency is 60 kHz. The post processing is done up to a frequency of 15 kHz. 26 of 32 channels are allocated to the 24 microphones plus 1 reference microphone as well as the HP- and the LP-trigger. The trigger signal was used to reconstruct the unsteady sound field by the rotor phase. The microphone array is traversed in steps of 2 deg. The signal from every channel is contemporary acquired and stored. The data acquisition period is 20 seconds per measurement point. It corresponds to more than 1000 revolutions of the LP turbine and more than 3500 of the HP turbine. In total 180 measurement positions are recorded in one and a half hours. During this time the operating condition is maintained perfectly stable.

5.1.5 Oil flow visualization techniques

A mixture of synthetic motor oil and titanium oxide is used to visualize the trajectory of the shear stress at the walls. The mixture has been uniformly painted in the whole passage surfaces of different exit guide vanes in order to verify the periodicity of the flow and the reliability of the results. The applied oil film was exposed to the flow for approximately one hour after reaching the stable operating condition.

5.2 Data reduction tools: Rotor Synchronic Averaging

In the last 10 years, different research groups, in particular GE Aircraft Engines [39, 92] and Pratt and Whitney [27, 84], have performed unsteady measurements in two-spool test rigs. Similarly, different numerical studies have been recently performed, see for example Qingjun et al. [66]. Most of these works, in particular Keith et al. [39] and Praisner et al. [84], concluded that the level of unsteadiness and frequency contents in a counter-rotating turbine is very high and may not be predicted from classical considerations. There is still a lack of systematic analyses which accounts for the different sources of unsteadiness in configurations relevant for current and new engine architectures.
In such a case, in fact, the adoption of a classical post processing decomposition, developed for unsteady flows in the 1970s (see for example Hussain and Reynolds [38]), does not provide a global view of the phenomena because normally takes into account the presence of one main unsteady perturbation. Using such procedure, it is possible then to isolate just the fluctuations induced by one of the two rotors once a time by means of a phase averaging procedure based on the rotor shaft encoder (e.g. [75, 83]). A classical decomposition of the variable p is the so-called triple decomposition procedure [38]:

$$p(t) = \overline{p} + < p(t) > + p'(t) \tag{5.1}$$

where $< p(t) >$ is the purely periodic component associated with a coherent periodic structure and $p'(t)$ is the random fluctuation associated mainly with turbulence. This decomposition is valid when a single source of periodic unsteadiness is characterizing the flow.
In a virtual 3 hole probe (one sensor probe), the determination of the flow properties is made possible after phase averaging: the periodic fluctuations of velocity, pressures and flow angles are determined at each phase from the phase averaged values of the three rotations of the probe [65].
Phase averaging is commonly performed in rotating machinery by means of one pulse per revolution obtained from a shaft encoder (see for example the early papers from Sharma et al. [75] and Suder et al. [83]). This pulse is used to determine the beginning of each revolution, which represents also the end of the previous one. In the present thesis each revolution is resampled to a fixed number of samples in order to correct the small speed variations of the turbine shafts [10].
The phase averaged values are then computed as the average of the samples at the same phase. Such procedure is very well established and allows the identification of the structures correlated to the rotor rotational speed. However, for the present experiments it was not sufficient, because it does not provide any informations about rotor-rotor interactions. Since the two rotors are counter-rotating and their rotational speeds are

uncorrelated, a phase locked average based on the phase of one of the two rotors removes completely the fluctuations of the flow quantities induced by the other rotor.
To take into account for the full unsteadiness, hence the interactions at the frequencies $i \cdots BPF_{HP} + k \cdots BPF_{LP}$ (with i and k integer numbers), a special phase averaging procedure has been studied. Considering the presence of two rotors at uncorrelated frequencies (2 uncorrelated coherent periodic structures) the decomposition in Equation 5.1 may be rewritten:

$$\begin{aligned} p(t) &= \overline{p} + < p(t) >_1 + \\ &\quad + < p(t) >_2 + < p(t) >_{1,2} + p'(t) \end{aligned} \tag{5.2}$$

where the two distinct purely periodic components $< p(t) >_1, < p(t) >_2$ have their own period and frequency, and $< p >_{1,2} (t)$ indicates the cross-interactions which generate the frequency peaks at $i \cdot BPF_{LP} + k \cdot BPF_{HP}$ (with i and k not zero). The Rotor Synchronic Average (RSA) provides the following time resolved distribution:

$$\tilde{p}(t)_{RSA} = \overline{p} + < p(t) >_1 + < p(t) >_2 + < p(t) >_{1,2} \tag{5.3}$$

5.2.1 Ideal case

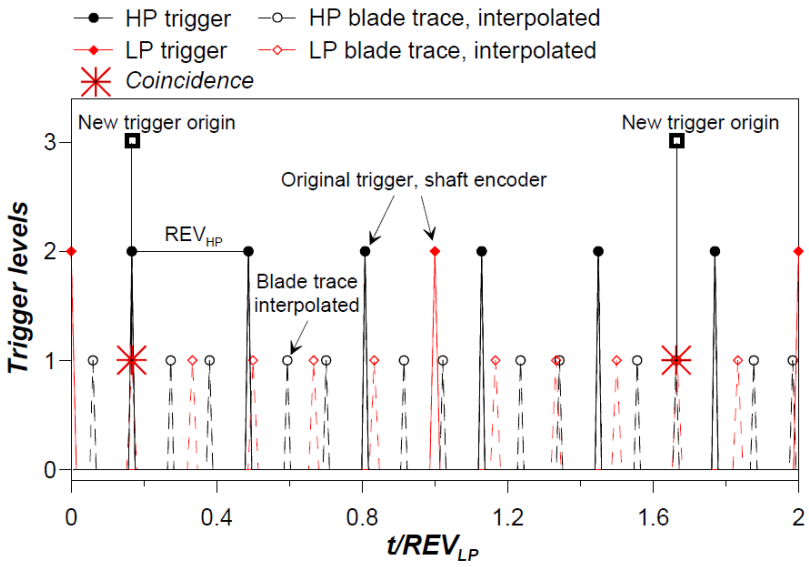

FIGURE 5.4: Schematic representation of trigger post-processing

Figure 5.4 shows a schematic representation of the shaft triggers. The time made non-dimensional by the revolution period of the LP turbine (REV_{LP}) is plotted on the abscissa, and the trigger level is plotted on the ordinate. The trigger level is a symbolic number associated to different origins of the trigger. A trigger level equal to 2

corresponds to the shaft encoder signals and identifies the beginning and the end of the revolutions of each rotor, red filled diamonds for the LP turbine and black filled dots for the HP turbine (the label REV_{HP} superimposed to the plot helps the identification of a revolution of the HP rotor, while the revolution period of the LP turbine may be read on the x-axis). The trigger level equal to 1 corresponds to the identification of the blades within the revolution, namely every revolution is divided into equi-distant intervals corresponding to the trace of the blade passing period. For readability of the graph the HP rotor has been simplified to 3 blades (hollow black circles), 3 constant blade period within one revolution, and 6 blades for the LP turbine (hollow red diamond) maintaining the original HP blade to LP blade count ratio (36 to 72). As marked over the picture such blade triggers are interpolated. The identification of equidistant period has the only assumption that within one revolution the rotational speed of the rotor remains constant. Considering the very high rotational speed this hypothesis may be considered always verified. A simple algorithm is then written with the purpose of identifying positions of coincidence between the triggers of the two rotors at levels 1 and/or 2. The coincidence is considered as the origin of a new trigger, indicated as "level 3" in the picture.
From this idealized scheme, it may be shown that the periods identified with the coincidence positions may be directly correlated to the different sources of unsteadiness. The time interval Δt between two successive "level 3" triggers is a multiple of the blade passing periods of the HP and LP rotor. It may be written that:

$$\Delta t = mT_{HP} = nT_{LP} \tag{5.4}$$

with m, n non-zero and positive integer numbers. Hence, the unsteadiness due to the single rotor(BPF_{LP} and BPF_{HP} and their multiples) is correctly resolved. Furthermore, as previously observed, the rotor-rotor interactions may be identified for the frequencies $f_{HP,LP} = i \cdot BPF_{LP} + k \cdot BPF_{HP}$ with i and k non-zero integer numbers. This frequency may be rewritten considering the blade passing periods of the HP and LP rotor and their link ($T_{LP} = m/nT_{HP}$) observed from eq. 5.4:

$$f_{HP,LP} = \frac{i}{T_{LP}} + \frac{k}{T_{HP}} = \frac{i}{(m/n)T_{HP}} + \frac{k}{T_{HP}} \tag{5.5}$$

Rearranging and considering eq. 5.4, the frequency $f_{HP,LP}$ of the rotor-rotor interactions results:

$$f_{HP,LP} = \frac{i \cdot n + k \cdot m}{mT_{HP}} = \frac{i \cdot n + k \cdot m}{\Delta t} \tag{5.6}$$

with $(i \cdot n + k \cdot m)$ a positive integer number. Equation 5.6 proves that the interaction frequency $f_{HP,LP}$ is always a multiple of the new trigger frequency $1/\Delta t$.

5.2.2 Real case

As observed from eq. 5.4 and 5.6, the energy content at the blade passing frequencies of the two rotors and their combined interactions is directly linked to this phase averaging procedure. Hence, the RSA preserves the frequency content of all coherent structures of the original signal.
A further reconstruction of the signal is also proposed. Even in such complex flow, the contributions of the time-mean and of one purely periodic part (e.g. $< p(t) >_1$) give the phase locked average quantity $\tilde{p}$ within the phase of the period of the phenomenon "1":

$$\tilde{p}(t)_1 = \overline{p} + < p(t) >_1 \tag{5.7}$$

When such average is performed over a sufficiently high number of periods of the phenomenon "1" the effects of the fluctuations $< p(t) >_2$, the random unsteadiness $p'(t)$ as well as the combined interactions $< p >_{1,2} (t)$ are removed. In the present case, such operation is the classical phase average performed considering the shaft encoder of one of the two rotors. To resolve the unsteadiness of the flow it may be thought to sum the results of the classical phase averaging procedures. In detail, the purely periodic fluctuations $< p(t) >_1$ and $< p(t) >_2$ may be obtained from eq. 5.7 as difference of the phase average and the time mean value. Then, $< p(t) >_1$ and $< p(t) >_2$ may be added to the time mean value $\overline{p}$ in order to obtain the following time resolved distribution:

$$\tilde{p}(t)_{sum} = \overline{p} + < p(t) >_1 + < p(t) >_2 \tag{5.8}$$

However, this distribution resolves partially the unsteadiness of the flow, it does not account for the rotor-rotor interactions ($< p >_{1,2} (t)$) when compared to eq. 5.3. It has to be noted that $\tilde{p}(t)_{sum}$ is periodic for the least common multiple of the two periods in analogy with eq. 5.4 which is resolved by the RSA, but it does not capture the terms observed in eq. 5.6.
The classical phase averages (LP and HP shaft encoder) and consequently their sum have been further post-processed. Thus the average among the 72 (LP rotor) or 36 (HP rotor) blade passages has been computed. Due to the high number of blade passing periods, it is possible to compute the average-representative blade passing period increasing the temporal resolution. The sum of the phase averages was then reconstructed as the sum of the averages on the blade passing periods of the 2 rotors.
In the exemplification of Fig. 5.4 the ratio of the revolution period of the two rotors is kept constant and equal to the real one and two coincidence positions may be identified ($t/REV_{LP} = 0.165, 1.66$ in Fig. 5.4). In the real case there are 12 times more blades and then more coincidence positions. However, in the real case the rotational speed of the rotors may be kept constant within a certain accuracy, $\pm 1.5/1000$ for both rotors in

this facility. Even if such variations are really small, they are taken into account, since the signals of the two shafts are acquired at a very high frequency. At the same time, an accuracy for the coincidence of the triggers has to be chosen. In the present work the triggers have been considered to have a coincidence when their time difference was below 1/1000 of the blade passing period of the HP rotor (the lowest among the two rotors). Under such conditions, for the 2 seconds of acquisition time, there are around 600 coincidences, and the variation of such number is within ±2% for all the measurement positions.

Nevertheless, the small variations of the rotational speed of the two rotors, unlike the example of Figure 5.4, lead to intervals between each coincidence position that are not constant. To perform a phase averaging procedure like explained in the beginning of this section a start and an end of the periodic phenomena has to be chosen (it is commonly the shaft encoder signal when phase averaging on the revolution period of a rotor). In the present case, where the phase averaging is meant to be performed out of synchronic positions of the rotor, the beginning of the phase is obtained as previously explained while the end is chosen following these two criteria:

1) a fixed number of LP blades is counted after the coincidence position, this is automatically done as the "level 1" trigger is interpolated;

2) within this time interval the ratio of HP blade periods to LP blade periods is computed, if the ratio is different from the theoretically predicted (see eq. 5.4) for more than a fixed uncertainty the period is discarded.

The very stable operating conditions of the facility allowed the evaluation of 7 LP blade passing periods without discarding any interval, since the computed blade ratio has variations below 0.5%.

With this procedure the relative position of the HP rotor blades and the LP rotor blades, in the absolute frame of reference, is coherently preserved at any phase of the newly derived averaging period. Basically, the positions of the rotors are re-synchronized within the period of this new phase averaging that will be referred as rotor synchronic averaging (RSA) in the followings.

Further, it has to be noted that the parameters discussed up to now, in particular the accuracy of the coincidence and the accuracy of the ratio of BPP_{HP} and BPP_{LP} within one averaging period, are the only ones to affect the RSA procedure. For example, there is no need to assume that the blades of the rotors are identical. In fact, when the RSA is performed over a very large number of periods (600 periods in the present case) derived from random combinations of HP and LP blades, the averaging removes the unsteadiness at low frequencies due to the rotor geometrical asymmetries. From the spectral analysis of the classically phase averaged signal (shown in Lengani et al. [44]) it emerged that almost the whole signal energy is included at the blade-passing frequency and its harmonics for the LP rotor.

5.3 Data reduction tools: Modal theory

Tyler and Sofrin [86] provided an apparently different decomposition of a variable than Equation 5.1, this time in time and space. In order to describe the sound generating mechanisms, they wrote the pressure fluctuations at any circumferential positions downstream of a compressor stage as a sum of harmonics. The theoretical model that they proposed has been verified by numerous aeroacoustic experimental investigations, and it is valid also for turbines (e.g. [57]). In particular, for an ideal rotor with identical blades the pressure fluctuations at a circumferential position θ may be written as a Fourier series [67]:

$$p(\theta, t) = \sum_{n=-\infty}^{\infty} \sum_{m=-\infty}^{\infty} A(m, n) e^{inB_n\Omega t - im\theta} \tag{5.9}$$

where n is the harmonic index (1 for the BPF, 2 for the 2*BPF, etc.), Ω the rotor angular velocity, $A(m, n)$ the coefficient of the Fourier series for each harmonic n and for each circumferential mode m.

The pressure field may be interpreted as a superposition of an infinite number of rotating patterns, where the number of lobes is given by successive values of m. Each m-lobed pattern rotates at the speed $\frac{nB_n}{m}\Omega$ required to generate the n^{th} multiple of the BPF. According to this convention, positive modes correspond to pattern rotating with the rotor direction, while, negative modes are related to pattern rotating in the opposite direction. Furthermore, Tyler and Sofrin [86] showed that the mode m of the spatial Fourier decomposition is restricted just to some particular values:

$$m = nB_n + kV_n, \quad with \quad k = ..., -1, 0, 1, ... \tag{5.10}$$

where a simple stator-rotor interaction is considered, B_n is the number of rotor blades and V_n is the number of stator blades.

The interactions of the rotor with a complete vane assembly may be extended by superimposing the effect of a single events. For example, in a turbine, a mode m^* generated by a stator-rotor interaction will be scattered in the modes $m = m^* + kV_{n2}$, $with$ $k = ..., -1, 0, 1, ...$ by the following stator rows. Hence, for a stator-rotor-stator assembly the following mode may be predicted:

$$m = nB_n + k_1V_{n1} + k_2V_{n2}, \quad with \quad k_1, k_2 \quad integer \tag{5.11}$$

where V_{n1} and V_{n2} are the number of vanes of the first and second stator row, respectively. A further extension of the present theory was provided by Holste and Neise [34]. They described the possible modes which may propagate in case of rotor-rotor interaction

with different rotational speed, counter or co-rotating.

5.3.1 Modal decomposition of the flow field

The modal theory has been developed for the pressure field. However, as experimentally observed by Lengani et al. [43], rotating patterns characterize all the aerodynamic quantities, the components of the velocity, the flow angles, and the pressure fluctuations. Hence, the decomposition of eq. 5.9 may be applied to the aerodynamic field. For example, Hall et al. [28], represented the flow variables as a Fourier series in time with spatially varying coefficients in order to satisfy the temporal periodicity of the flow in a time-harmonic balance computational method.
On the basis of the modal theory, a double Fourier decomposition method was developed by Courtiade et al. [9]. They perform a spatial Fourier decomposition of a generic flow quantity q in space in order to obtain a spatial mode for different time steps. Then, they apply a second Fourier transform in time of the spatial modes. The information obtained from the first decomposition is the structure of the spatial lobes. The second transformation is then necessary to understand the rotational speed of the lobes and the stator/rotor interactions which generate the mode.
The similar double Fourier decomposition adopted for this dissertation was in Lengani et al. [46]. However, the order of the decompositions is the opposite of the method of Courtiade et al. [9]. For every radial and circumferential position of the measurement mesh a discrete Fourier transform is applied to the phase averaged generic flow quantity q (normalization factor are voluntary omitted in the formulation):

$$q(f)_{\theta,r} = \sum_{n_t} q(t)_{\theta,r} e^{-in_t f} \tag{5.12}$$

where the limit of the integration are defined by the number of points n_t within the revolution period, obtained from the phase averaging procedure. This is the classic discrete Fourier transform in time which reveals the frequencies that characterize the flow field.
Thereafter, a discrete Fourier transformation in the circumferential direction is applied to the complex number $q(\theta, r, f)$:

$$A(m)_{r,f} = \sum_{n_c} q(\theta)_{r,f} e^{in_c m} \tag{5.13}$$

where the limit of the integration are defined now by the number of points n_c in the circumferential direction. The operation is performed at any fixed frequency f and radius r and now the variable $q(\theta)_{r,f}$ is integrated over the circumferential position θ. The

Fourier coefficients $A(m)_{r,f}$ are, then, a set of complex numbers which are function of the frequency and of the radius at which the data are obtained.
In this last formulation the fluctuations of the generic variable $q(\theta)_{r,f}$ are written as complex numbers in the frequency domain. According to the Fourier transform theory a transformation of complex numbers leads to values of $A(m)_{r,f}$ which are not symmetric with respect to the spatial frequency (namely, the modes m). Modes, as predicted by the modal theory, may be, then, positive or negative, spinning in the same direction or in the opposite direction of the rotor, respectively, following the convention previously adopted.
Equation 5.13 may be applied to different circumferential boundaries, where the spatial extension of the boundaries defines the minimum mode computable. In fact, the minimum mode computable, except for the mode 0, is directly proportional to the circumferential arc adopted in the decomposition. For example, measurements across a sector of 15 deg will lead to a minimum computable mode equal to 24. Similarly, the number of circumferential points define the maximum mode computable. Therefore, it is easy to demonstrate that all the modes of interest may be computed when eq. 5.13 is applied to the blade/vane count periodicity condition of a test rig.

5.3.2 Analogy with conventional decomposition

At any frequency and radial position a set of coefficients $A(m)_{r,f}$ is defined. Comparing eq. 5.9 and eq. 5.13, it comes out that the contribution to the deterministic unsteadiness may be observed at the multiple of the blade passing frequency. This set of coefficients may be considered, performing an analogy with the Adamczyk's decomposition [2], as the sum of different contributions:
1) the frequency 0 (time mean value) and circumferential mode 0 corresponds to the axisymmetric term;
2) the frequency 0 (time mean value) and circumferential mode different from zero corresponds to the average stator to stator flow field;
3) the unsteadiness due to the rotor and its interactions with the stator rows correspond to the sum of the modes $A(m)_{r,f}$ at all the multiple of the blade passing frequency.
This last contribution may be further decomposed, considering eq. 5.11, in the following two terms:
3') for k_1, k_2 equal to zero: the modes $m = nB_n$ at the rotational speed $\frac{nB_n}{m}\Omega$ correspond to the average rotor blade passage flow. For example, at the BPF a mode corresponding to the blade number is observed, at 2 times the BPF a mode corresponding to 2 times the blade number may be observed and so on. All this modes rotates at the rotational speed of the rotor (eq. 5.9), therefore, they are the trace of the rotor signal.

3") for k_1, k_2 not zero: all the lobed structures arising from the rotor/stator interactions may be found. In fact, due to the rotor/stator interaction, the flow field can be considered a superimposition of spinning modes rotating at multiples of the blade passing frequency both co- and counter-rotating with the rotor angular direction.

Chapter 6

Results and discussion

This chapter constitutes the central part of this dissertation. The reader will be led through a summary of the research carried out by the author. All the details are given in Spataro et al. [80], Spataro et al. [79], Spataro et al. [77], Spataro et al. [78] and in Lengani et al. [46], Lengani et al. [45], Lengani et al. [44] and Faustmann et al. [18].
The analysis of the Baseline configuration and of the TMTF with embedded splitters will be presented in the Sections 6.1 and 6.2 respectively.
In the remainder of this chapter, total and static pressure will be discussed in terms of normalized coefficients. Therefore, the total pressure coefficient was defined as:

$$C_{pT} = \frac{p_T - \hat{p}_{T,C}}{\hat{p}_{T,C} - \hat{p}_C} \tag{6.1}$$

where $\hat{p}_{T,C}$ and $\hat{p}_C$ represent the averaged total and static pressure in Plane C respectively. For the position of the measurement planes, please refer to Figure 3.5.
In a similar way, the static pressure was normalized as:

$$C_p = \frac{p - \hat{p}_C}{\hat{p}_{T,C} - \hat{p}_C} \tag{6.2}$$

6.1 Flow evolution through the Baseline Configuration

6.1.1 Flow field upstream of the Mid Turbine Frame

This chapter is particularly important for the analysis of the two configurations presented in this thesis, since both stages have the same kind of inflow. In this section, the time-mean as well as the time-resolved flow at the transition duct inlet are presented and discussed.
Such a flow field is characterized by the typical structures normally observed downstream

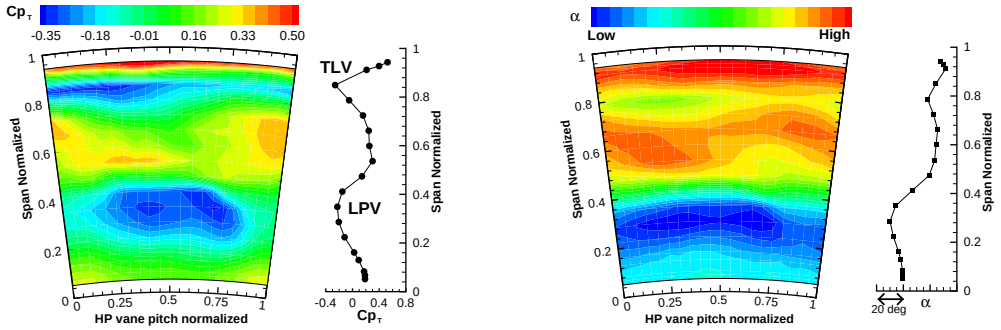

(a) Total pressure

(b) Yaw angle

FIGURE 6.1: Five hole probe measurements in Plane C - TMTF inlet flow: contour plots and circumferentially averaged values (Spataro et al. [80])

of a HP turbine (Section 2.1.1).

The main flow features which dominate the time-resolved exit flow of such stages are secondary flows.

Considering also the effect of the downstream strut, a series of stator–rotor, rotor–stator and stator–stator interaction mechanisms take place. The convection of viscous effects (i.e. wakes and vortices transport) through the TMTF is mainly driven by potential effects. From the five hole probe measurements in Figure 6.1, it is possible to observe changes in the spanwise total pressure and mean flow angle distributions due to these structures. Previous studies on a very similar stage investigated in this facility (Marn et al. [51], Sanz et al. [73]) have showed that the work coefficient ($\Delta H/U^2$) increases moving from the rotor tip toward the hub. Therefore, lower levels of total pressure at the hub should be read mainly due to more extracted work. On the other hand, the analysis of the rotor time-resolved field [73] showed that the presence of the rotor tip leakage vortex (TLV) and of rotor lower passage vortex (LPV, in literature also referred as Hub Passage Vortex) were located where sharp changes in the time mean flow angle and in the total pressure spanwise distributions were observed.

Starting from these considerations, it might be possible to assume the locations the consequences of the TLV at $H = 0.8$ and of the LPV at $H = 0.4$ (co-rotating with the TLV [54]). Any visible circumferential variation of these features in the contour plots derives mainly from the stator-rotor interaction between the HP vanes and the HP rotor. Anyway, the location of these structures in this turbine stage is confirmed by the analysis of the time-resolved field presented in the following of this section (see Figure 6.5).

Figure 6.2 reports the time-averaged flow simulated by means of an unsteady CFD simulation. Looking at these results, similar considerations as for the five-hole probe measurements can be done. The horizontal stripes indicate the time-mean effect of the rotor structures. Looking at the total pressure contour plots, the effects of the HP vanes (orange dashed lines named V) are sensibly visible in the lower half of the channel where

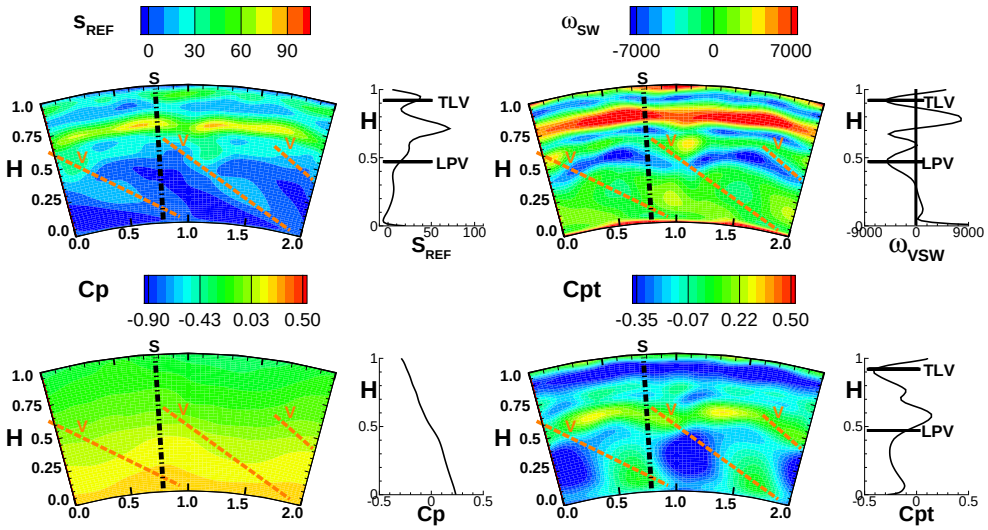

FIGURE 6.2: Unsteady CFD - TMTF inlet flow: time-averaged quantities (view from downstream)

the stator-rotor interaction has a considerable impact, while its influence is negligible in the upper half. From the static pressure contour plot (C_p) it is possible to notice that the strut potential field (black dash-dotted line named S) extends far upstream (this plane is located at $x/C = -0.26$ where C is the strut axial chord at midspan).

In a conventional axial turbine, the spanwise distribution of the discharged flow is characterized by the influence of a radial equilibrium gradient induced by the swirl effect,

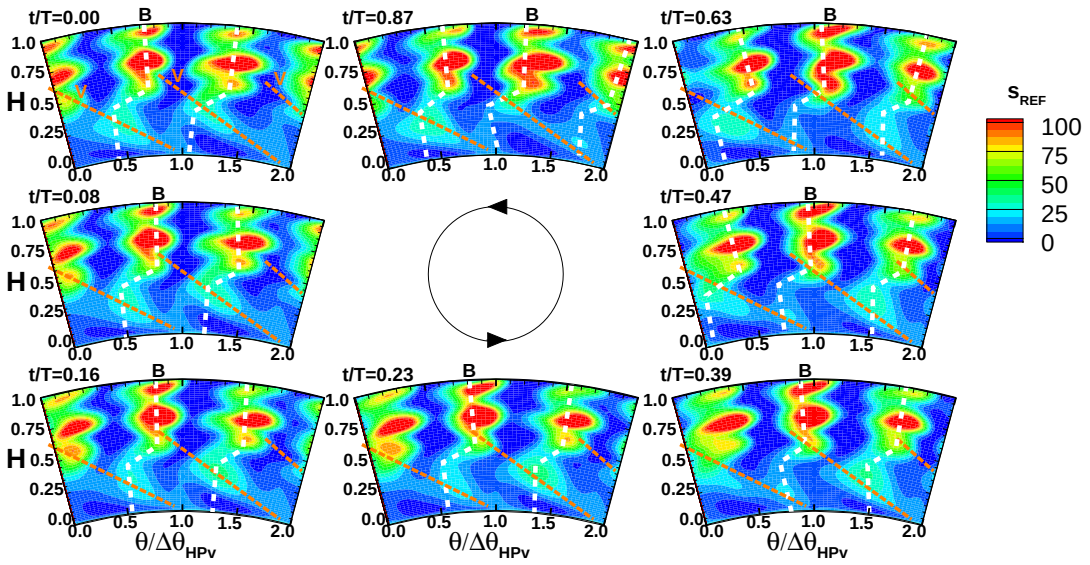

FIGURE 6.3: Unsteady CFD - TMTF inlet flow: time-resolved entropy (view from downstream)

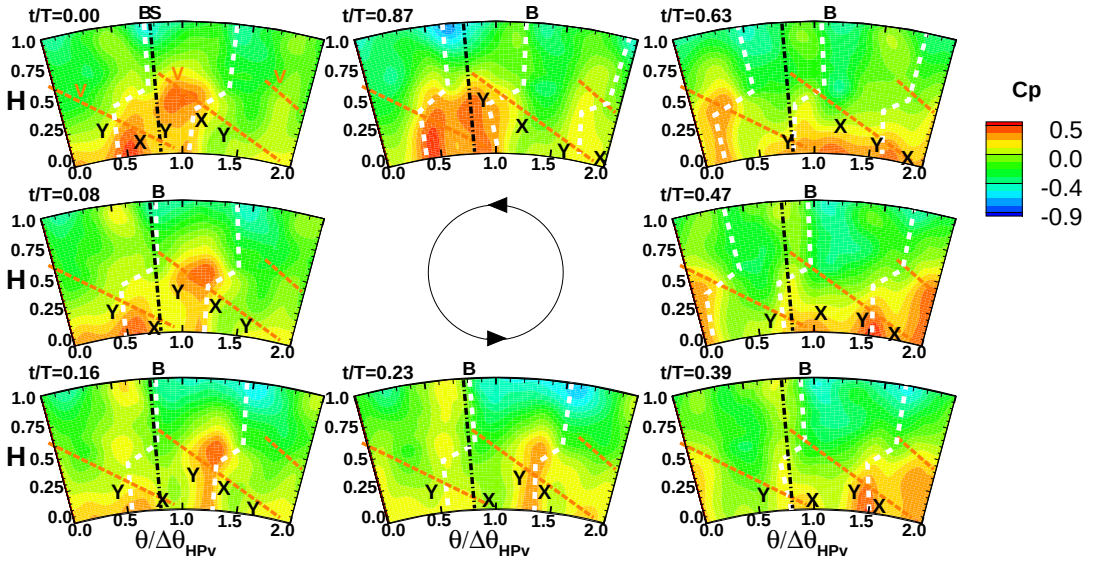

FIGURE 6.4: Unsteady CFD - TMTF inlet flow: time-resolved pressure (view from downstream)

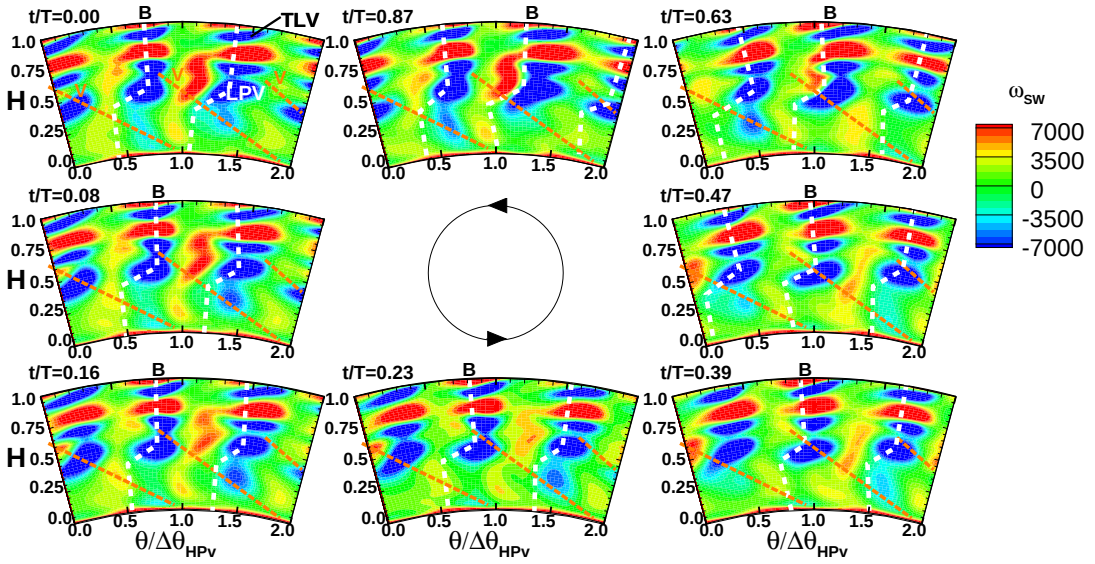

FIGURE 6.5: Unsteady CFD - TMTF inlet flow: time-averaged streamwise vorticity (view from downstream)

which pushes the flow field towards the hub. In this case, the presence of the downstream bend of the channel plays a major role: from the C_p distribution in Figure 6.2 it is possible to observe a pressure gradient oriented from the shroud to the hub (counter acting the swirl effect). In this plane, the flow is then pushed towards the casing where higher flow velocities, higher Mach number and higher total pressure levels can be observed (the LPV is observed being pushed up to $H = 0.4$). Figure 6.3 shows the time–resolved entropy distribution extracted over two HP stator pitches. In this figure, it is easy to

identify the main structures such as the wakes of the rotor blades (white lines named B) and the effect of the rotor vortices on the losses distribution. The traces of the skewed and chopped wake segments convected from the upstream HP vanes (orange lines V) are still visible.

Figure 6.4 shows the time–resolved static pressure field at the transition duct inlet. The plots show that, while the presence of the bend is responsible for the shroud-to-hub radial pressure gradient, the main fluctuations in circumferential direction are related with the rotor blade passing period. The sharp pressure gradients in circumferential direction are representative of the rotor trailing edge and suction side shocks. Figure 6.4 shows how the intensity of the rotor shocks (X and Y) is modulated in the lower half of the channel by the stator-rotor interaction (structures V).

Moreover, as already observed in Figure 6.2, a time–constant pitchwise increment of pressure at $\vartheta/\Delta\vartheta_{HPv} = 0.8$ (black dashed line called S) indicates the modulation due to the strut potential field. The streamwise vorticity contour plots at the duct inlet presented in Figure 6.5 confirms what already observed in the time–mean flow analysis. The main vorticities representing the low passage and tip leakage vortices (LPV and TLV, respectively) can be seen co-rotating, while the upper passage is counter–rotating. Figure 6.5 confirms also how the structures at high vorticity and low energy subdue the radial pressure gradient being pushed towards the shroud.

6.1.2 Flow field through the Mid Turbine Frame

Moving downstream the HP stage, the flow is convected towards the strut passage. In the investigated case, such a convection process is atypical for conventional turbine application. In fact, the strut is designed to lead the flow towards a counter-rotating turbine.

Defining β the blade angle and θ the tangential coordinate both positive in the turbine rotating direction, the blade turning coefficient can be written as:

$$\iota = \int_{x=LE}^{x=TE} \int_{\theta=LE}^{\theta=TE} \frac{d^2\beta}{d\theta^2} d\theta dx \tag{6.3}$$

In a classical stator-rotor configuration, the vanes have to generate the required swirl to make the turbine rotate. Therefore, the stage will be designed with opposite signs for the stator and the rotor turning coefficient ($\iota_{vane} > 0$ and $\iota_{blade} < 0$). In case of a multi-stage turbine with co-rotating rotors, all the stages will be designed with similar design configuration ($(\iota_{vane} > 0)_i$ and $(\iota_{blade} < 0)_i$ with $i = 1, .., N_{stages}$).

In case of counter-rotating turbines designs, the intent is to use the residual swirl downstream of the first stage to have a pre-swirled flow for the following stage and minimize the turning required to the second stage vane. Therefore, two successive stages will be

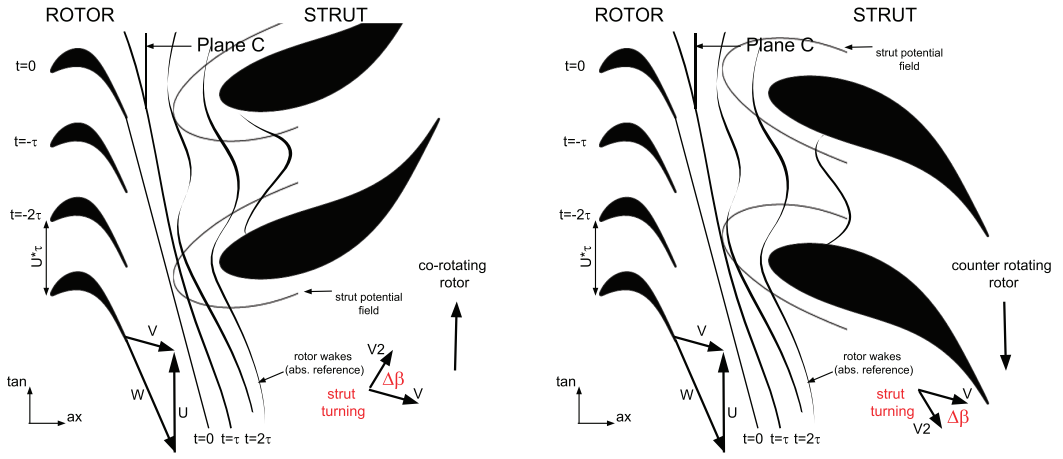

(a) Rotor structures convection and decay in the strut passage (co–rotating turbine configuration)

(b) Rotor structures convection in the strut passage (counter–rotating turbine configuration)

FIGURE 6.6: Schematic representation of rotor structures evolution through the TMTF

designed with:

$$(\iota_{vane} > 0)_1 \quad (\iota_{blade} < 0)_1 \tag{6.4}$$

$$(\iota_{vane} < 0)_2 \quad (\iota_{blade} > 0)_2 \tag{6.5}$$

where 1 and 2, in this case, refers to the HP and to the LP stages respectively. Classical models which describe convection processes of upstream structures through a successive blade/vane row are usually based on the assumption that vane and blade have opposite turning coefficients. Therefore, such models can not be used to fully describe the convention mechanism at the interface of the two stages where:

$$(\iota_{blade} < 0)_1 \quad (\iota_{vane} < 0)_2 \tag{6.6}$$

where $(\iota_{blade})_1$ and $(\iota_{vane})_2$ refers, in the present case, to the HP blades and to the TMTF respectively. In fact, the sign of the blade turning coefficient is representative of the way the upcoming structures are stretched and reoriented by the velocity gradients generated between the suction and the pressure sides of the blade row. Based on literature models, Figures 6.6(a) try to schematically explain the rotor wakes convection through the downstream vane in a co-rotating setup ($\iota_{blade} < 0$, $\iota_{vane} > 0$). Such process is well described in Hodson and Howell [33] who refers to an experimental study of a test cascade. In this case, the process is characterized by the rotor wakes bowing, reorientation, elongation, and stretching. Bowing of the wake fluid is most evident and originates near the leading edge plane where the mid-passage velocities are higher than the velocities near the blade surfaces. Stretching occurs as the first part of the wake reaches the leading edge. It is accelerated over the suction surface of the strut and moves

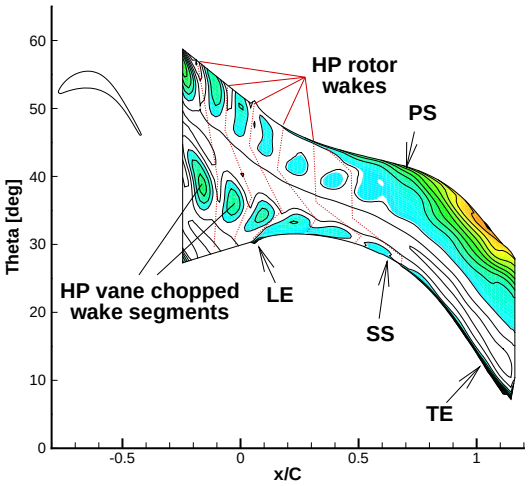

FIGURE 6.7: Rotor wakes convection process within the TMTF passage (30%*span*)

away from the upstream edge of the wake, thus increasing the wake width on the suction side of the passage. The velocity gradients along the leading half of the pressure surface are not as strong as on the suction surface, so this stretching effect is less pronounced on the pressure surface. Reorientation and elongation occur due to the crosspassage differences in the velocity. Figure 6.6(b) shows what happens to the rotor structures in the case of a counter–rotating turbine ($\iota_{blade} < 0, \iota_{vane} < 0$). In such setup, the turning induced by the struts acts favorably to the rotor structures convection. Figure 6.7 shows results from a unsteady calculation in blade-to-blade surface at 30% span. The isolines indicates entropy distribution by means of which it is possible to identify the wakes convection through the passage. The colored contours identify the HP vanes chopped segments ("wake avenues") being convected within the TMTF passage.

In counter-rotating turbine configuration, bowing and stretching of the rotor wake fluid near the strut leading edge is equally observed. Moreover, since the upstream flow is pre-swirled, the turning required to the strut is reduced and therefore also the internal velocity gradients. Reorientation and elongation are then sensibly reduced in this configuration resulting in a decrement of the mixing process through the strut.

Looking at Figure 6.7, similar conclusion can be drawn for the convection of the "wake avenues". Observing the transport of the chopped upstream vane segments, it is possible to see them not mixed out after $x/C = 0.5$.

Further considerations can be done about the decay of secondary vortices. Referring to the analytical model proposed in Chaluvadi et al. [8], the increasing in the vortex secondary kinetic energy through a blade row varies with the vortex-stretching ratio which is only a function of the blade turning. Therefore, in a counter-rotating configuration, where the strut turning is reduced, the mixing losses associated to the convected vortices has to be expected being lowered.

Figure 6.8 shows contour plots of streamwise vorticity evolution on a blade-to-blade

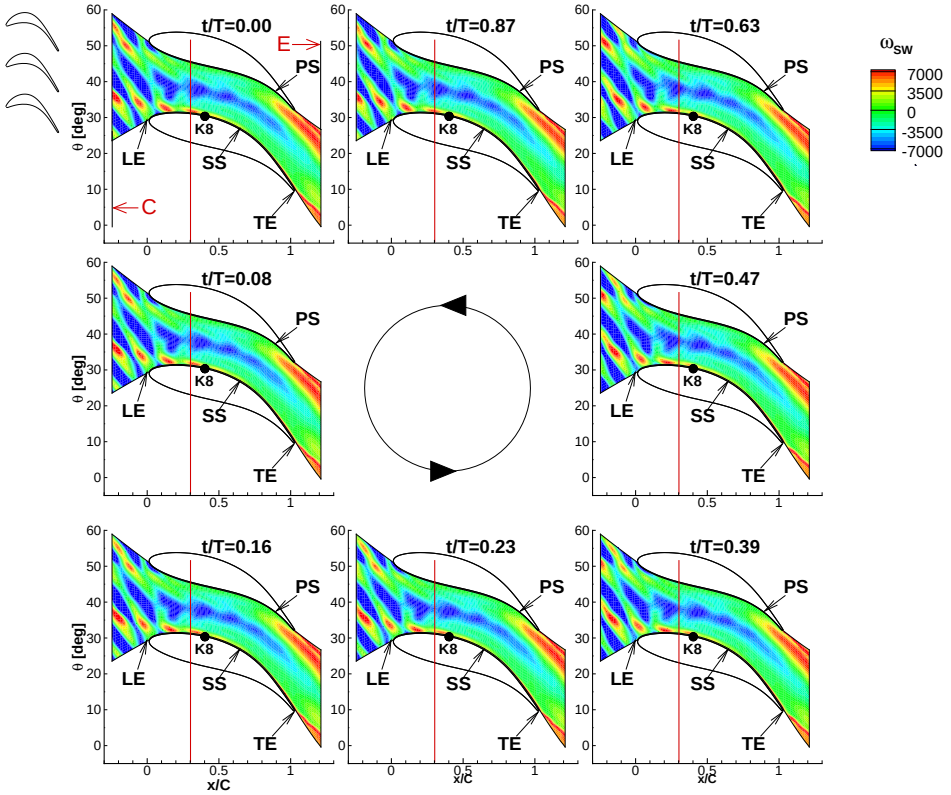

(a) Blade-to-blade plane (50%*span*)

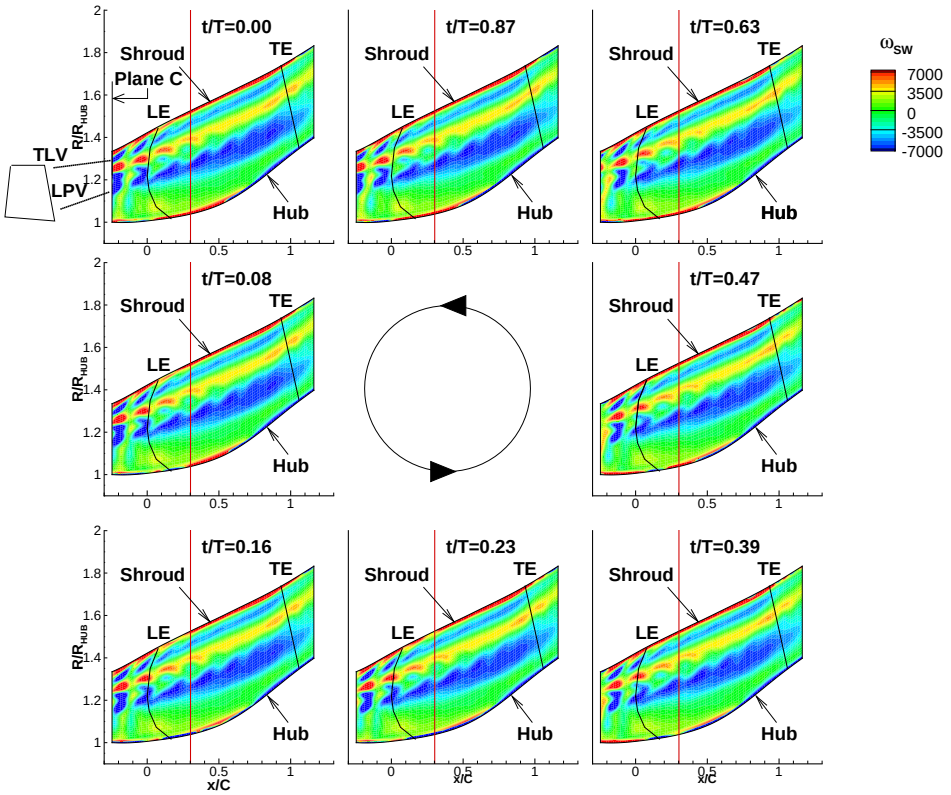

(b) Meridian plane (50%*pitch*)

FIGURE 6.8: Unsteady CFD: Streamwise vorticity evolution through the strut passage. K8 indicates the position of the piezoreristive sensor number 8 (Table 6.1)

surface (50% span) and on a meridional surface (50% pitch). From these maps it easy to identify the propagation of the high–pressure rotor structures already seen in Figure 6.5. Particularly interesting is the meridional view in Figure 6.8(b) where the vorticities generated by the upstream stage are seen traveling all through the TMTF passage and they can still be seen at the LP rotor inlet flow. The vertical red line at $x/C = 0.3$ in Figure 6.8 indicates the strut start *turning point* which was identified in Spataro et al. [80]. Moving downstream of this point the swirl induced by the turning struts generates a strong radial gradient so that the low–energy cores are seen pushed towards the lower half–channel.

Figure 6.9 presents different planes extracted from a steady state CFD simulation of

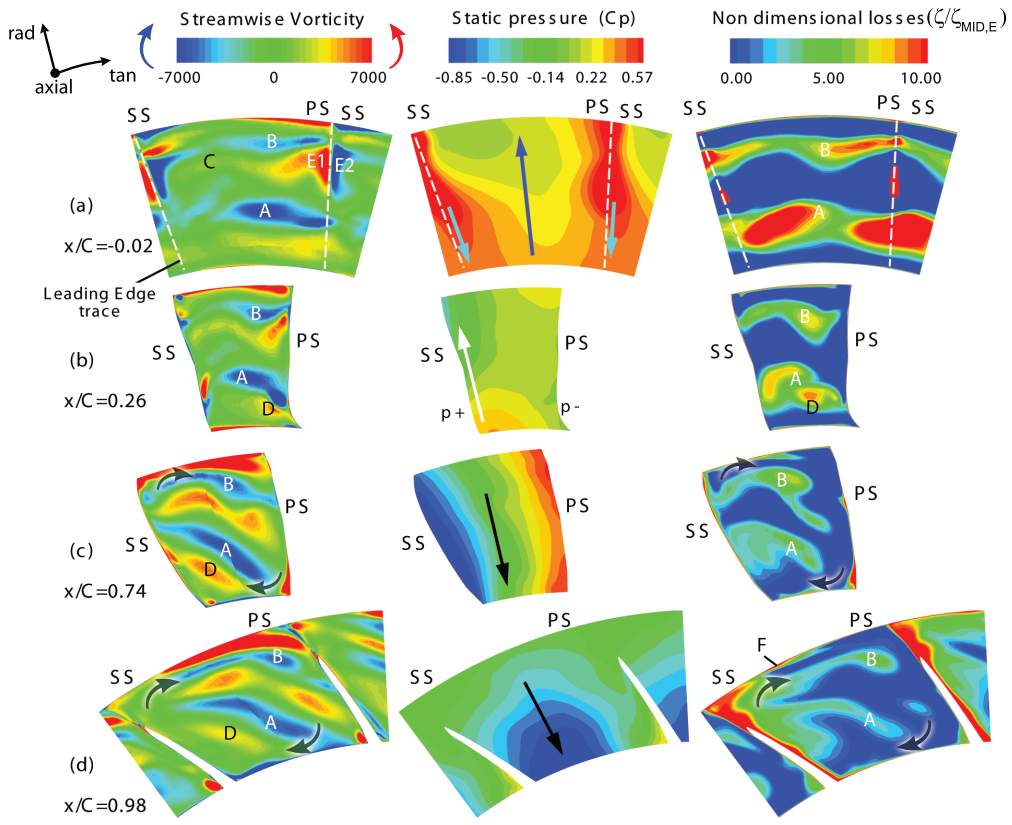

FIGURE 6.9: Flow evolution within the strut passage (view from downstream) (Spataro et al. [80])

the LP stage (Spataro et al [80]) at four different axial positions (to see the positions of these planes in the meridional plane, please refer to Figure 4.1). This time, the CFD calculation was set with the five-hole probe measurements reported in Figure 6.1 as inlet boundary condition [80].

Focusing on the vorticity map of Fig. 6.9 (a), the zones A, B, and C respectively can be related to the traces of the high pressure rotor LPV, TLV and the rotor upper passage vortex (UPV). They are transported and convected downstream into the vane passage. Looking at the pressure distribution, the flow in Fig. 6.9 (a) appears mainly subjected

to a hub-to-shroud force. This is induced by the first bend of the S-shaped channel which is also responsible for accelerating the flow at the casing. Moreover, the sweep design of the leading edge induces spanwise gradients which push the flow towards the endwalls. In the lower channel the direction of this gradient is opposite to the gradient induced by the bend and, although its entity is lower, it can be still identified with the blue arrows in Fig. 6.9 (a).

On the other hand, the sweep design plays a major role in the generation of the structures E1 and E2 on the upper part of the leading edge. Whenever the flow approaches the blade wall, a boundary layer is generated. A leading edge orthogonally-oriented vorticity is then induced; this component is then multiplied with the spanwise velocity created by the blade sweep design [80].

The lower and the upper halves of the strut were found facing negative and positive incidence respectively. A hub-to-shroud pressure gradient is then visible in Fig. 6.9 at $x/C = 0.26$. Such a pressure gradient is responsible for inducing a vorticity in the secondary plane which is transformed in a full span extended vortex as soon as the flow subdues the struts swirl effect $x/C > 0.3$ (red line in Figure 6.8, this point is referred as *turning point*). The development of the radial equilibrium gradient (black arrow in Fig. 6.9 (c) and (d)) is then encouraged.

Consequently, a large passage vortex indicated by means of the black arrows at $x/C = 0.74$ and $x/C = 0.98$ is observed. This vortex propagates downstream and will be seen playing a major role in LP rotor inlet flow. Further, its effects on the flow field will be discussed even downstream of the LP rotor.

The strut loading distribution map reported in [80] showed that, in the upper part of the vane passage, the flow has positive incidence which leads to a circumferential pressure gradient at the casing endwall and that will favorite a cross-flow from pressure to suction side typical for a upper passage vortex. Despite this, it is now important to remark that the vane was designed with the target to minimize the generation of secondary flows by means of a complex 3D design. The structure indicated as F in the loss map of Figure 6.9 (d) shows a quite confined vane upper passage vortex which is driven by the casing cross-flow and does not reach the suction side because of the aft-loaded design of the strut.

Experimentally, the unsteady flow field through the TMTF was investigated by means of 12 piezoresistive sensors type KULITE XCE-0.62 (sensors 1–10) and KULITE LE-062-25A (sensors 11–12) (linear frequency range $\Delta f = 0 - 20kHz$) aligned along a streamline visible in Figure 6.10(a). Sensors 1–3 were placed at the strut leading edge, in order to measure the unsteady spanwise variation of the flow incidence. The sensors from 3 to 12 were placed parallel to streamlines where the CFD prediction showed a possible transition occurrence.

The sensors position coordinates can be read in Table 6.1.

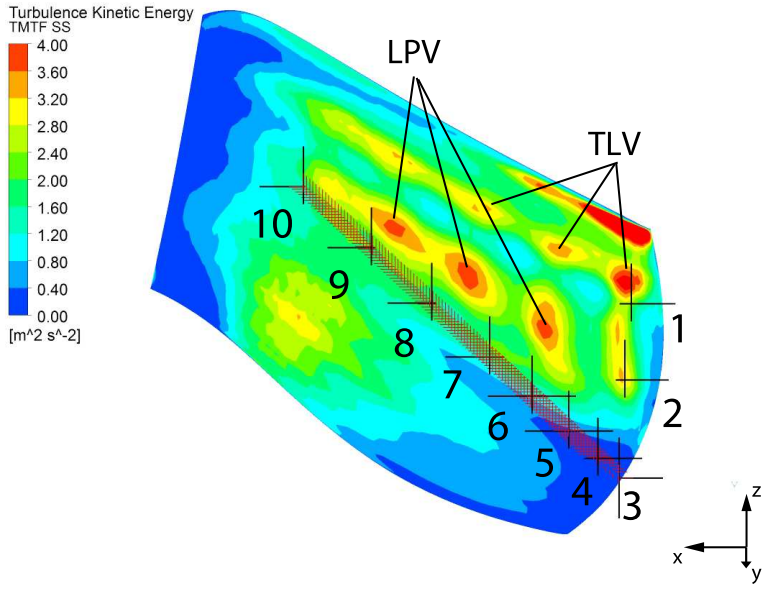

(a) Unsteady CFD: instantaneous Turbulence kinetic energy distribution on the strut suction side and piezoresistive sensors position

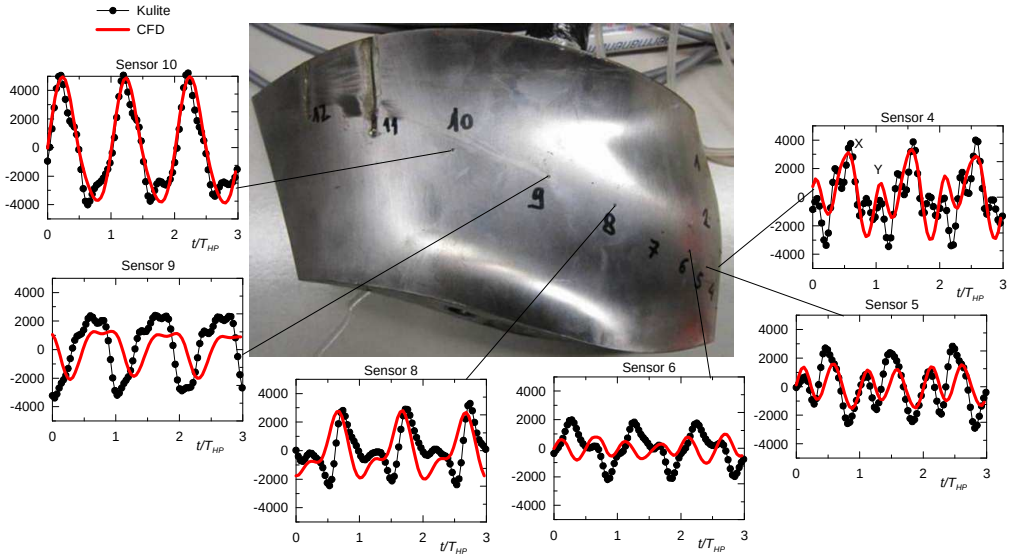

(b) Unsteady CFD Vs fast response pressure sensors: comparison of the time signal at CP-A clocking position

FIGURE 6.10: Time signal on the strut suction side

Figure 6.10(a) shows an instantaneous turbulent kinetic energy distribution on the strut suction side and the position of the first 10 sensors. Sensors 11 and 12 were flush mounted on the rear side of the suction side.

On the upper part of the strut suction side, two streamwise red patterns are visible. These are indicative of the periodic impingement of the rotor lower passage and tip leakage vortices (LPV and TLV in Figure 6.10(a)). Figure 6.10(b) shows the comparison between the unsteady CFD and the pressure sensors time signal at one fixed clocking position. By means of such fast response sensors it was possible to investi-

TABLE 6.1: Fast response sensors meridional position

Sensors position on the strut suction surface					
Sensor n.	span (H)	ax. pos. (x/C)	Sensor n.	span (H)	ax. pos. (x/C)
1	–	0.05	7	0.43	0.35
2	0.50	0.07	8	0.50	0.47
3	0.19	0.08	9	0.55	0.60
4	0.24	0.12	10	0.59	0.74
5	0.30	0.18	11	–	–
6	0.37	0.26	12	–	–

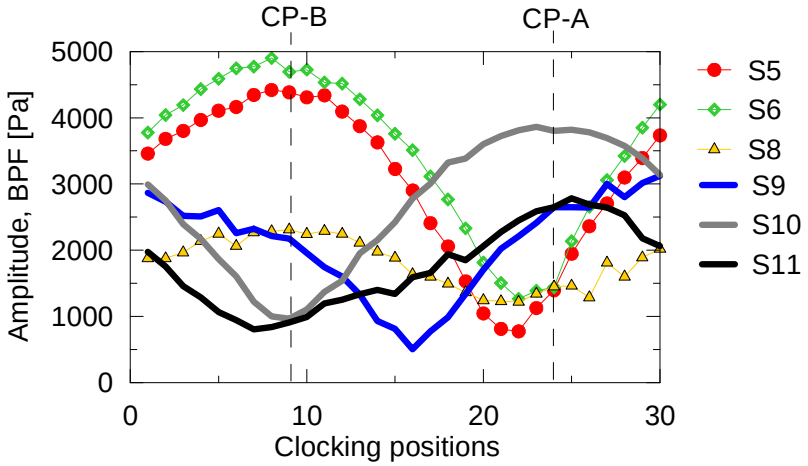

(a) Experimental clocking analysis of the pressure fluctuations amplitude on the strut suction side while moving the HP vanes along one stator pitch

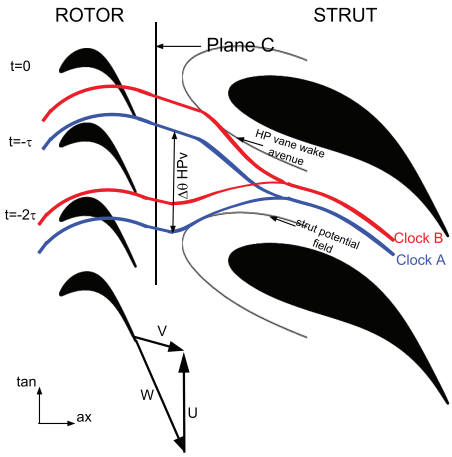

(b) Two–dimensional vane–vane clocking effect on the flow pattern within the strut passage

FIGURE 6.11: HP vane - TMTF clocking analysis

gate the propagation of pressure waves through the duct. Further, a clocking analysis (see Figure 6.11(a)) was performed by rotating the first stator over one HP vane pitch ($\Delta\theta_{HPv} = 15deg$) with a spacial resolution of $\Delta\theta_{res} = 0.5deg$. The study highlights a strong dependency of the pressure field within the strut passage from the vane–vane relative position.

These results on the stator-stator interaction remark the effect of the HP vane chopped wake segments on the modulation of the HP rotor shocks observed in Figure 6.4. Moreover, it confirms what observed in Figure 6.7 about the upstream vane structures playing a major role in the flow convection mechanism.
Generalizing what already described in Figure 6.7 for different vane-vane positions, in Figure 6.11(b) a sketch about the influence of the clocking effect on the convection process is proposed. Here, two clocking positions, namely Clock A and B, are drawn. For simplicity reasons, the effects of the vane–vane interaction are represented just for the two–dimensional propagation of the HP stator chopped wakes. Such "wake avenues" are showed being distorted by the strut potential field and their reorganization within the strut passage leads to an acceleration of the mixing process. Therefore, the clocking position triggers the flow patterns which determine the level of the stage mixing losses. Actually, in this kind of stages, as already observed by Schennach et al. [74], it has to be expected three-dimensional clocking effects (i.e. vortices interaction) playing a major role in the stage efficiency than two-dimensional effects (i.e. wakes: even if these are generally 3D structures they can be assimilated to two dimensional structures for clocking studies which looks at blade-to-blade planes). Considering a one-and-half stage transonic turbine, the intensity of the rotor structures (in particular the low passage vortex and the rotor shocks) varies along the HP vane pitch due to the change in the rotor incidence. This means that the downstream vane will face three-dimensional structures discharged by the rotor which intensity in pitchwise direction is modulated by the upstream vanes.
In order to correctly interpret the unsteady CFD data presented in this thesis, it was thought to indicate the two clocking positions simulated with CP-A and CP-B in Figure 6.11(a). In the followings of this chapter, the unsteady CFD results presented will refer to the CP-A position.
In this section the convection and propagation of the upstream flow structures through the strut passage was described. Moreover, the generation of new structures within the duct due to the TMTF design was detailed.
Finally, the analysis on the unsteady flow field showed that the flow structures transport mechanism and the pressure waves propagation through the strut duct are highly dependent from the HP vane-strut clocking position.
In the next section, the flow field downstream of the TMTF (which represents also the inlet condition for the LP rotor) will be described.

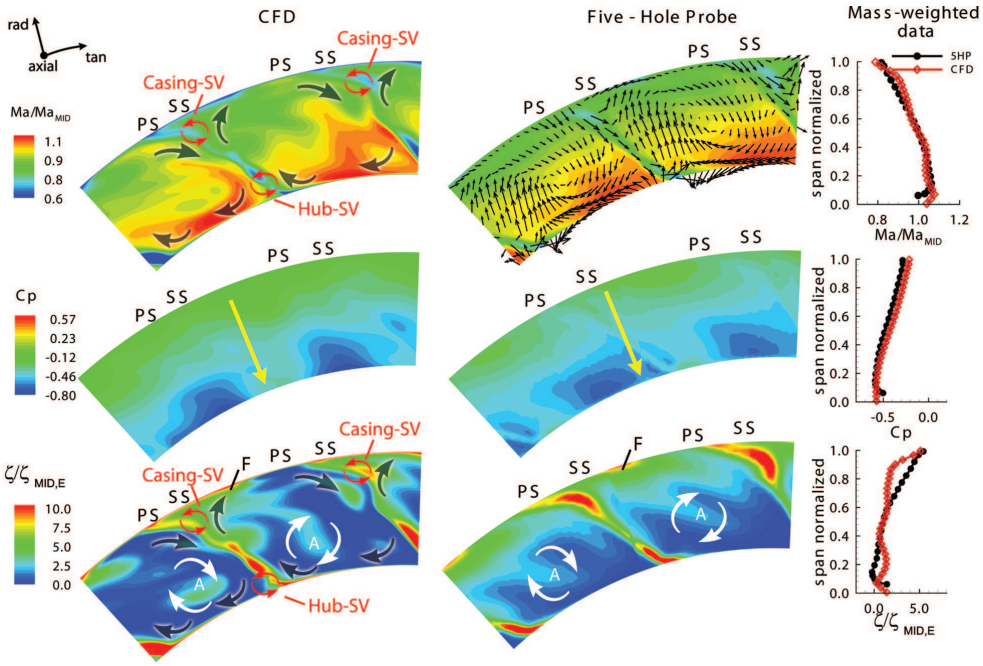

FIGURE 6.12: Steady CFD and Five hole probe data - LP rotor inlet flow: contour plots of Mach number, static pressure and total pressure losses (view from downstream) (Spataro et al. [80])

6.1.3 Flow field at the LP rotor inlet

Figure 6.12 ([80]) shows a comparison between five-hole probe measurements and steady state numerical data in Plane E which is located at $x/C = 1.28$. On the left side, contour plots of Mach number, static pressure and total pressure losses are shown, while (on the right side) their spanwise mass-weighted distributions are reported. The Mach number is normalized on its mass-weighted value at midspan.

The contour plots as well as the mass-weighted distributions show a good agreement between the two approaches on catching the main flow features. Measurements were performed along two complete vane pitches (45 degrees) in order to get the full HP vane - LP vane periodicity. For the same reason two strut pitches have been simulated (the time-mean flow at the HP stage exit plane has 15 degrees periodicity, while one strut pitch is 22.5 degrees).

The flow leaving the TMTF is subjected to a radial hub-to-shroud pressure gradient that pushes the field towards the hub (yellow arrow in Fig. 6.12). The pressure distribution induced on the channel by the second bend will enhance this force, while the component related to the swirl effect (which is still the predominant contribution) will decrease proceeding downstream of the vane passage. In fact, in this section of the machine the flow is unguided and is moving towards larger radii: the swirl effect will become weaker following the momentum conservation law ($v_t \cdot r = const$).

The main visible structures in this plane are the large wakes generated by the struts:

these regions of low momentum induce, on one side, high losses and, on the other side, a periodic discontinuity in the circumferential flow angle and pressure distribution which will influence the aeroelastic response of the downstream rotor.

Looking at the Mach number distribution of Fig. 6.12, the mean flow in both radial and tangential direction is characterized by high velocity gradients: the radial gradients of velocity are due to the diffusing channel swirl and to the endwall boundary layers, while the gradients in the circumferential direction are due to the turning of the flow induced by the struts. The velocity vectors superimposed to the experimental Mach number distribution are defined as the difference between the local velocity vector and a reference flow direction (see for example Chaluvadi et al. [7] and Persico et al. [60]). Decomposing the flow vectors in their circumferential and radial components, an averaging process for each of the two directions is performed in order to obtain the reference vectors. Considering i and j the radial and circumferential indexes respectively, the reference flow vector components are calculated as:

$$\overline{V}_{i,j} = \left\{ \begin{array}{l} \overline{V_r} = \frac{1}{M} \sum_j^M V_{ri,j}|_i \\ \overline{V_\theta} = \frac{1}{N} \sum_i^N V_{\theta i,j}|_j \end{array} \right\} \tag{6.7}$$

where V_r and V_θ represent the circumferential and radial velocity components respectively, whilst M and N are the number of circumferential and radial points respectively. Therefore, the secondary flow vectors V_{sec} can be calculated as $(V_{sec})_{i,j} = V_{i,j} - \overline{V}_{i,j}$. This procedure is necessary because of the very high velocity gradients that characterize the mean flow in both directions. They reveal the presence of the vane passage vortex [46, 71] extending over the full channel height. The same vortex is indicated in the CFD map by means of black arrows.

The effect of the HP rotor can be still visualized in structure A in Fig. 6.12 which is a representative trace of the lower passage vortex. This vortex is co-rotating with the vane passage vortex. The reader should be aware that the CFD was set in this study (Spataro et al. [80]) as steady-state simulation and should not think to this feature in terms of net influence on the flow field. In reality, in fact, the structure propagation will be triggered by the unsteady field of the upstream rotor.

A weak vane upper passage vortex (structure F) can be observed, also in this view, still confined at the casing endwall.

Further remarkable structures on this plane consist of two vortices indicated as SV in Fig. 6.12. These are shed vortices resulting from the interaction between two passage vortices generated within the vane channel and convected downstream of the strut trailing edge. Figure 6.13 tries to clarify this mechanism which leads to a non conventional casing shed vortex counter-rotating with respect to a "traditional" upper shed vortex. These low momentum structures induce two loss cores visible on the losses map in the upper and

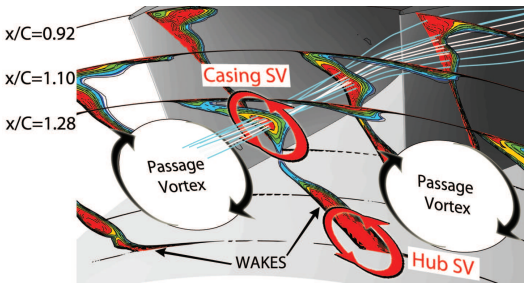

FIGURE 6.13: Evolution of total pressure losses at the vane trailing edge and schematic representation of the generated vortices (Spataro et al. [80])

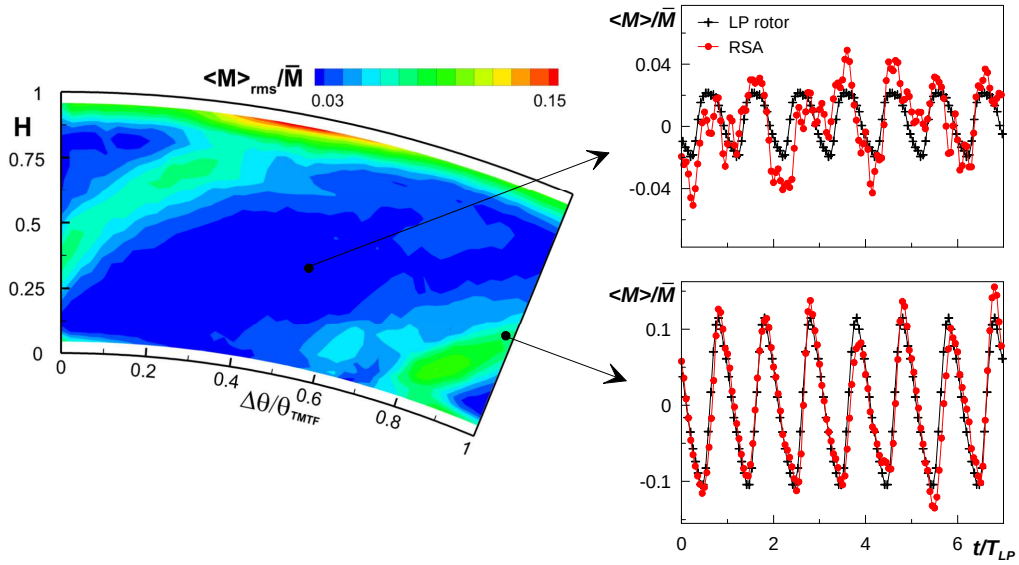

FIGURE 6.14: Fast response probe measurements - LP rotor exit flow: contour plots of the RMS of the deterministic fluctuations of velocity (Lengani et al. [45])

lower wakes ends. Moreover, looking at the spanwise mass-weighted distribution, it is interesting to see that with this steady CFD setup the losses in the region concerning the casing shed vortex are underestimated, while they are overestimated where the hub shed vortex is expected to occur.

6.1.4 Flow field at the LP rotor outlet

An experimental analysis on the time-resolved field in this region was presented in Lengani et al [45]. In particular, since this region is located downstream of two turbines, it was particularly interesting to study the effects of two different phase averaging (LP rotor and RSA) during the data reduction.

Figure 6.14 shows the temporal evolution of the purely periodic Mach number due to two different decompositions, the LP rotor phase in black and the RSA in red. It shows that the oscillations induced by the LP rotor are lower than the one due to the overall unsteadiness (RSA). However, in the region with the highest level of RMS (TMTF wake

and tip passage vortex) the situation is different, there the TMTF-LP rotor interaction generates the highest contribution to the overall unsteadiness. As an example, the temporal fluctuations are shown for the TMTF wake region in the bottom right plot of Figure 6.14. In this case, the oscillations are due to the LP rotor and its interaction with the TMTF. The temporal evolution of the $< M >$ due to the overall unsteadiness ($< M >_{RSA}$) is, in fact, very similar to the unsteadiness of the LP rotor alone. Hence, the unsteady rotor-rotor interaction plays a minor role in determining large RMS of coherent fluctuations of velocity. Similar considerations may be done for the coherent fluctuations of the flow yaw angle which are reported in [45].
Therefore, the study showed that the velocity and angle coherent fluctuations are determined, mainly, by the interactions of the LP blade with the structures emanated by the TMTF, namely its passage vortex and wake. In fact, in the region where the rotor–rotor interactions are measured, the overall unsteadiness presents very low fluctuations. Hence, in such positions, the unsteadiness will not represent a problem for the following stages [45].
The highest fluctuation in the total and static pressure field were found being induced by the TMTF-LP blades interaction (Figure 6.25). However, the extension of the area where the rotor-rotor interaction lead to high fluctuations was seen to be larger. Indeed, fluctuations of pressure may lead to acoustic and vibrational problems. A careful design of the following stages has then to be done in order to reduce these excitations.
In order to simplify the study of such complex interaction patterns, it was thought to apply, in the baseline stage, the modal decomposition analysis which results are presented in the next section.
The reader is then invited to refer to Section 6.2.4.1 for further details on the aerodynamic field in this region. There, the flow features of the Baseline and multisplitter setup are commented by means of contour plots and the differences between both stages are highlighted.

6.1.4.1 Modal decomposition analysis

The modal decomposition procedure requires to have a full space–time periodicity of the acquired signal. The constructive complexity of the rig did not allow a continuous traversing of the pressure probe for the full periodicity of the rig (90 deg). Therefore, such procedure was applied to unsteady CFD data. The computational domain for this simulation can be seen in Figure 4.2 and further details on the simulation setup can be found in Spataro et al. [79]. Such analysis is well detailed in Lengani et al. [46].
Disregarding the time mean term, the modal decomposition is focused on the unsteady fluctuations ($< p_t >$, of eq. 5.1). To verify the validity of the CFD simulation in

comparison with the experimental results, average power spectra are provided in Figure 6.15. The amplitude spectra are obtained as average values over different circumferential positions at mid-span, more details on how the experimental data are obtained may be found in Section 5.2 or in Lengani et al. [44].

The results of the modal decomposition are shown in Fig. 6.16 considering the five different frequencies of interest identified from the CFD in Fig. 6.15. The resolution of the decomposition was set to resolve correctly the modes of interest multiples of 4, in this case. The domain for the decomposition was set to compute a maximum mode equal to ± 180.

Figure 6.16 shows the amplitude of the modal decomposition of the total pressure at mid-span. The amplitude is plotted as relative amplitude with respect to the maximum amplitude computed in this radial position. The circumferential mode is plotted on the abscissa dividing it by 4 (again, the machine has 90 deg periodicity), according to the resolution of the decomposition. However, the actual mode number will be referred to in the discussion (e.g. the mode -72 may be read on the graph in correspondence of -18). Remembering that 24 and 16 are the vane counts for the HP vanes and the TMTF respectively, whilst 36 and 72 are the blade counts for the HP and LP rotors respectively, it is possible to observe no direct trace of the HP rotor blades (mode 36). It has to be noted that, in this particular case with counter-rotating rotors, the convention that the rotation of the first (HP) rotor is positive has been adopted.

On the top of the figure the modal decomposition is plotted for the blade passing frequency of the LP rotor and its harmonic. The trace of the LP rotor blades, mode -72, was found being the predominant fluctuation. However, it is possible to identify a direct interaction of the LP rotor with the TMTF. The amplitude of the mode $-72+16 = -56$ is in fact around half of the fluctuations induced by the rotor itself. On the other hand, the fluctuations at the $2BPF_{LP}$ are negligible and no relevant modes may be observed. The spatial lobes induced by the HP rotor are plotted in the mid of the figure. The

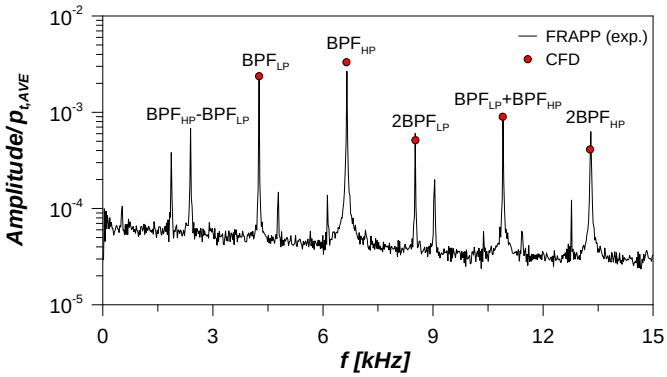

FIGURE 6.15: Average non-dimensional amplitude spectra at mid-span, downstream of CRT LP rotor (Lengani et al. [46])

unsteady flow induced by the HP rotor may be considered as a complex pattern of interactions. From eq. 5.11 the following modes may be computed:
a) HP stator-HP rotor interaction consists of the modes $36 + k24 = 36; 12; -12; -36$
b) HP rotor-TMTF interaction consists of the modes $36 + k16 = 20; 4; -12; -28$
c) HP stator-HP rotor-TMTF interaction consists of the modes $36 + k_1 24 + k_2 16 = 28; 20; 12; 4; -4; -12; 20; 28$
where k represents an integer number which assumes positive and negative values ($k = \ldots -2, -1, 0, 1, 2, \ldots$) All these different interactions may be observed in the plot. The largest amplitude is observed for the mode 12 which suggests that the HP rotor-TMTF interaction is not the predominant one. In fact, the mode 12 appears just in the HP stator-HP rotor interactions or in the ones of the three rows together. Similar considerations may be done for the $2BPF_{HP}$, however, their amplitude is less relevant.
On the bottom of Fig. 6.16, the modal decomposition for the sum of the blade passing frequencies of the two rotors is shown. The amplitude of the modes of total pressure, as it may be observed also in Fig. 6.15, is smaller than the amplitude at the blade passing frequencies of the rotor alone. However, some predominant modes may be observed. According to the theory of Holste and Neise [34], a mode -36 induced by the rotor-rotor interaction should be seen. This mode is computed directly from the number of blades and sense of rotation of the two rotors, $-36 = -72 + 36$. A mode -60 is instead observed as predominant in the picture. Considering the possible linear combinations between the blade counts, this mode is obtained if the HP vane number (24 vanes) is subtracted to the mode -36. Hence, this term is mainly due to the interactions between the HP stage and the LP rotor. As observed by other authors (e.g. Göttlich [24]), the pressure fluctuations of the HP stage, which are caused by the strong shock waves, do not decay within the duct.
The amplitude of the mode correlated to the total pressure is very similar to the one of the static pressure. Whereas, as shown in Lengani et al. [46], the velocity and flow angles fluctuations depend mostly on the TMTF-LP rotor interaction. However, considering a multi-disciplinary design, the present results may be taken into account for noise and vibration analysis, for which the fluctuations of pressure influence considerably these two aspects of turbomachinery design.
This analysis confirms again that a TMTF placed between two counter-rotating turbines convect and enforce the vorticities coming from the upstream turbine within the vane passage. This leads to a higher level of complexity of the LP turbine design due to an increased non-uniformity of the rotor inlet flow field as well as the consequent rotor-rotor interaction [80].

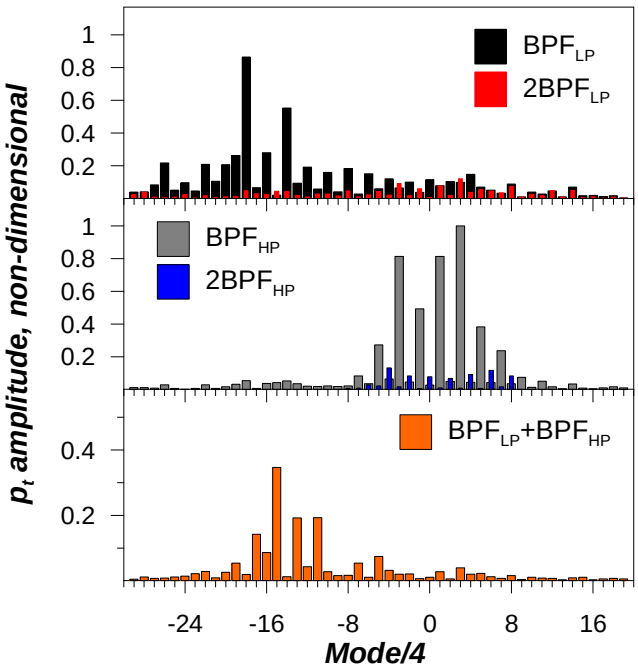

FIGURE 6.16: Unsteady CFD data: circumferential mode amplitude of total pressure for different frequencies, CRT (Lengani et al. [46])

6.2 Flow evolution through the Turning Mid Turbine Frame with Embedded Design

The analysis on the baseline configuration showed that, in order to improve LP turbine performance, a more suitable inlet condition for the low pressure rotor has to be provided (Section 6.1). Therefore, a setup which embeds two splitter vanes into the strut passage of the baseline configuration was developed and tested. The splitters have been designed targeting to a zero-incidence condition. For the splitter design process please refer to Section 3.4.

In the remainder of this section, the results presented refer to the data published in Spataro et al. [77], Spataro et al. [78] and Faustmann et al [18]. The meridional flow path with the position of the splitters can be seen in Figure 6.17.

6.2.1 Flow field upstream of the Mid Turbine Frame

Due to the increased blockage, a new operating point for the new setup had to be chosen. For the operating condition parameters of this new stage, please refer to Table 3.1. Figure 6.18 presents five-hole probe measurements performed at the LP stage inlet (Plane C in Figure 6.17). The comparison between the two setups is shown by means of spanwise distribution of circumferentially averaged measurements. In particular, it is possible to evince from these yaw angle curves that a difference less than 5 deg at

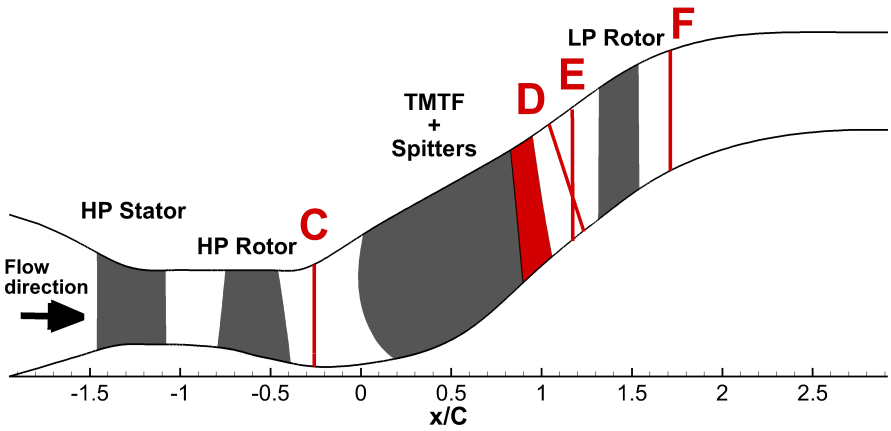

FIGURE 6.17: Two stage - two spool facility at the ITTM and measurement section (Spataro et al. [77])

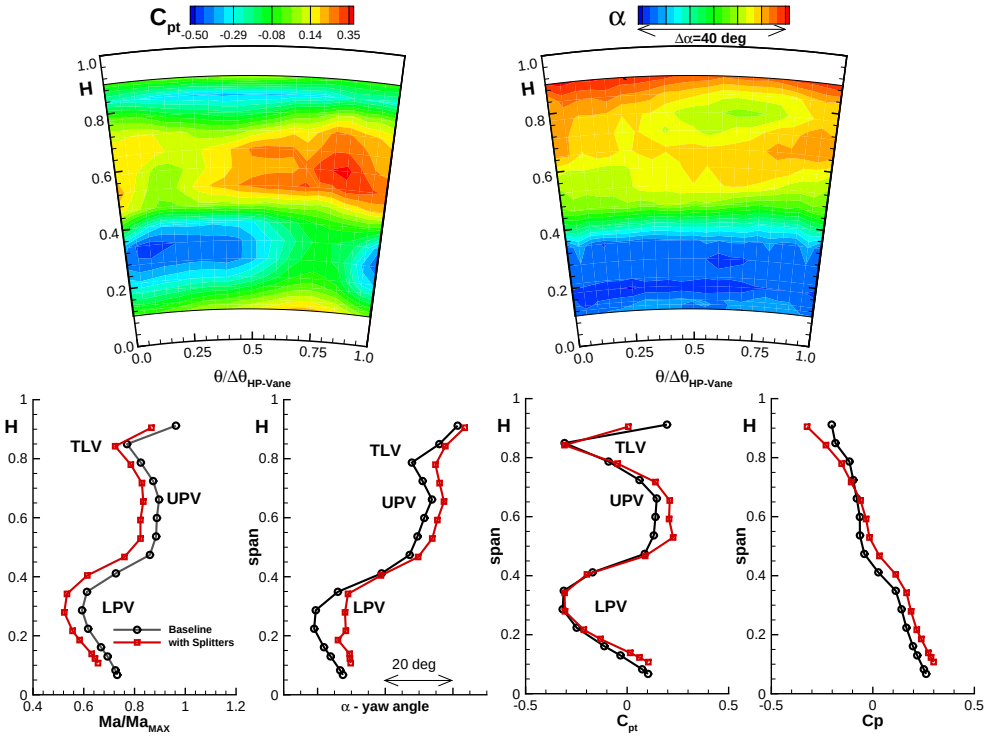

FIGURE 6.18: Five hole probe measurements - TMTF inlet flow (view from downstream) (Spataro et al. [77])

midspan was obtained. In fact, similar inflow angle distribution values represented the target in order to operate the new stage under comparable aerodynamic conditions. For a detailed discussion on the time-mean as well as on the time-resolved flow in this region, please refer to Section 6.1.1.

6.2.2 Flow field through Turbine Center Frame

Keeping the same inflow angle at the transition duct inlet, the convection mechanism of the rotor structures in the strut passage can be assumed, in this new stage, similar to what already described in Section 6.1.2.
The duct endwalls and the strut were instrumented with pressure taps which positions are visible in Figure 5.1 and in Figure 5.2 respectively. Comparing this setup with the baseline case, the static pressure measurements within the channel show a similar trend between the two setups, though in the embedded design, a strong flow acceleration is seen as soon as the flow is guided into the splitter passages [77]. This effect could be avoided in the design phase reshaping the meridian flow path or applying 3D endwall contouring techniques. Moreover, oil flow visualization techniques were applied in both

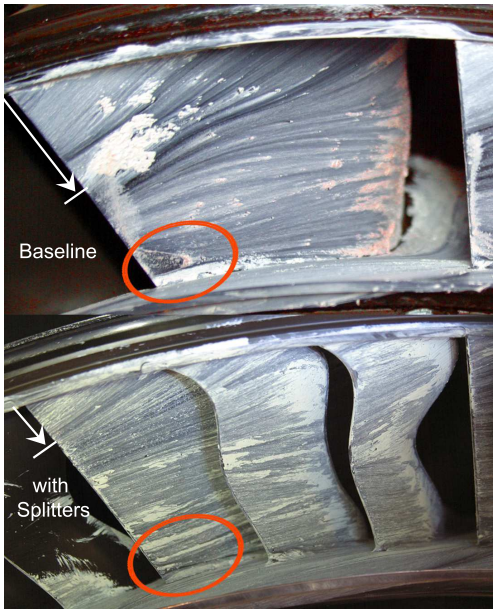

FIGURE 6.19: Oil flow visualization: comparison on the strut suction side for baseline and embedded design setups (view from downstream) (Spataro et al. [77])

setups. The baseline design showed a prominent downwash on the strut suction side. Such a crossflow (see Figure 6.19 "Baseline") is due to the hub-to-tip pressure gradient measured on the strut surface which acts on a large portion of low momentum flow related to the development of the boundary layers on the strut suction surface. In comparison with the Baseline case, the new stage (see Figure 6.19 "with Splitters") shows a reduction of the crossflow since the flow is re-energized as soon as it is led into the splitter passages. Therefore, as it will discussed in the next section, the reduction of the downwash on the strut suction side is already indicative of a better flow guidance towards the successive blade row.

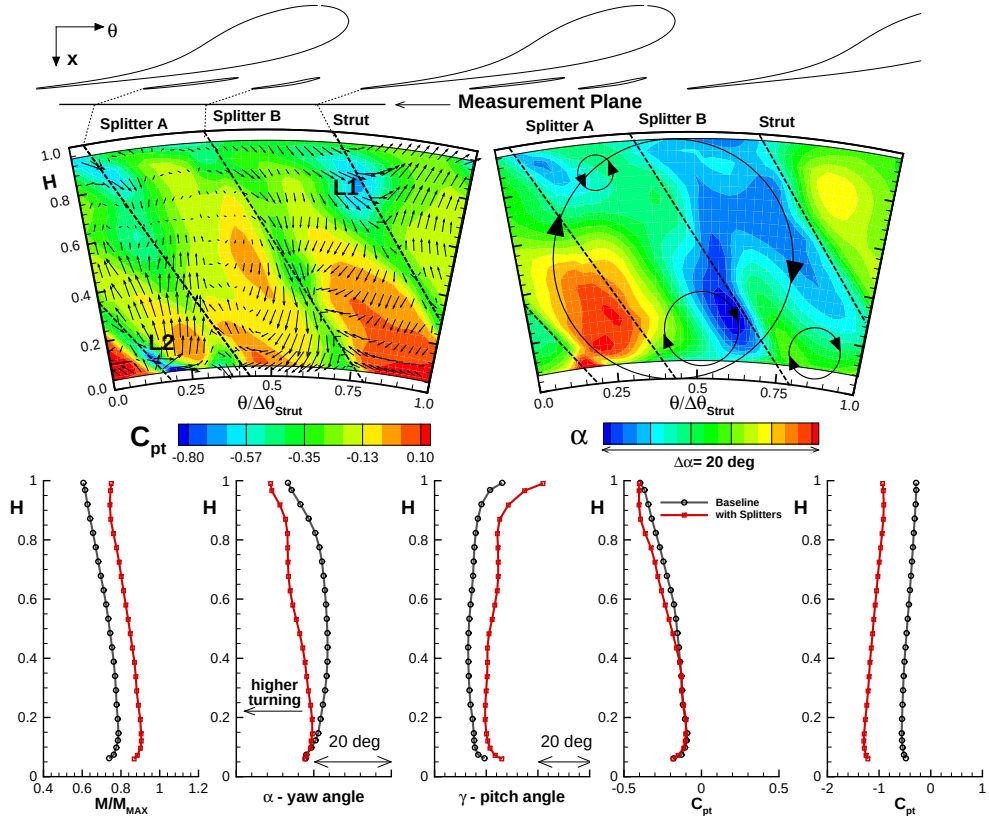

FIGURE 6.20: Five hole probe measurements - LP rotor inlet flow (view from downstream) (Spataro et al. [77])

6.2.3 Flow field at the LP rotor inlet

The better turning due to the new multisplitter setup is also confirmed by the five hole probe measurements performed in plane E which represents the LP rotor inlet flow (Figure 6.20).

The contour plots show total pressure (on the left side) and yaw angle (on the right side) distributions. The yaw angle was defined positive in the direction of the HP rotor angular speed, which means that the blue color identifies area of higher turning, while the red color the ones of lower turning. The comparison between baseline and multisplitter setups in terms of spanwise distributions of averaged Mach number, yaw angle, pitch angle, total pressure and static pressure is plotted at the bottom of the figure. The Mach number is normalized on its local maximum, while for the total and static pressure coefficient the definitions in Equation 6.1 and 6.2 were used, respectively. The contour plot of total pressure allows the identification of the position of the main structures such as strut and splitter wakes (dashed lines: Strut, Splitter A and Splitter B in Figure 6.20) as well as the main loss cores (L1, L2). L1 is representative of the strut shed vortex, while L2 is due to the strut corner separation observed in the baseline case.

The secondary velocity vectors superimposed on the C_{pT} distribution are defined as the difference between the local velocity vector and a reference flow direction in the same way as it was already explained in Section 6.1.3. In particular, for the reference flow vectors definition, Equation 6.7 was used.

Focusing now on the flow angles (yaw angle defined as $\alpha = tan^{-1}(V_\theta/V_m)$ and pitch angle as $\gamma = tan^{-1}(V_m/V_x)$), the effect of the splitter vanes in this plane is quite relevant since the mean turning and the pitch angles are enhanced by $5deg$ and $8deg$, respectively. Such a trend in the pitch angle is confirmed by the oil flow visualization in Fig. 6.19.

Moreover, looking at the yaw angle distribution in Figure 6.20 a notable effect of the splitters can be seen on the shape of the yaw angle distribution. This is driven by the modified pattern of the secondary flow structures of the struts.

In order to better understand this effect, a simplified scheme is proposed in Fig. 6.21. The sketch shows the tangential velocities, where the contribution of a flow led through the vane without generating any vortices ("*vortex-free*" field) and the effect of secondary vorticities were separated. Finally, their combination is shown.

Regarding the *vortex-free* field, it has to be noticed that the strut was designed to have, in first approximation, a linear spanwise variation of blade angle at the trailing edge (more turning at the shroud and lower turning at the hub). The result of this is the $vt(r)$ distribution in Figure 6.21 (a).

For the baseline case in Fig. 6.21 it was found out that, due to a negative incidence at the lower half channel of the strut, no classical lower passage vortex is generated at the strut leading edge. Instead, a large passage vortex extending over the full span starts to develop at $x/C \approx 0.3$ (see Section 6.1.2). On the other hand, the upper passage vortex was seen confined in the shroud endwall region. The yaw angle distribution in this plane was observed to be constant for $0.2 < H < 0.8$ (Fig. 6.20). Figure 6.21 (b) clarifies how such a distribution can be explained by the major role played by the strut passage vortex. This vortex induces an overturning in the lower half channel and an underturning in the upper one, therefore leading to a roughly constant distribution in this region (Fig. 6.21 (c)). For $H < 0.2$ and $H > 0.8$ the spanwise variation in the mean angle distribution is driven by the strut shed vortices (not sketched in Fig. 6.21).

The velocity vectors and the vortices sketches in Fig. 6.20 reveal the presence of the vane passage vortex [46, 71, 80] extending over the full channel height and of small vortices (two at the hub and one at the shroud) that can be seen at the endwalls.

Referring to the multisplitter configuration in Fig. 6.21 (b) the extended passage vortex is cut and reduced by the splitters. On the other hand, whenever the splitters are designed as turning vanes, within each channel new upper and lower passage vortices are generated (UPVs and LPVs). The existence and the strength of such vortices is related to the splitter deflection rate.

As a major conclusion, it can be stated that the splitters strongly may help to homogenize

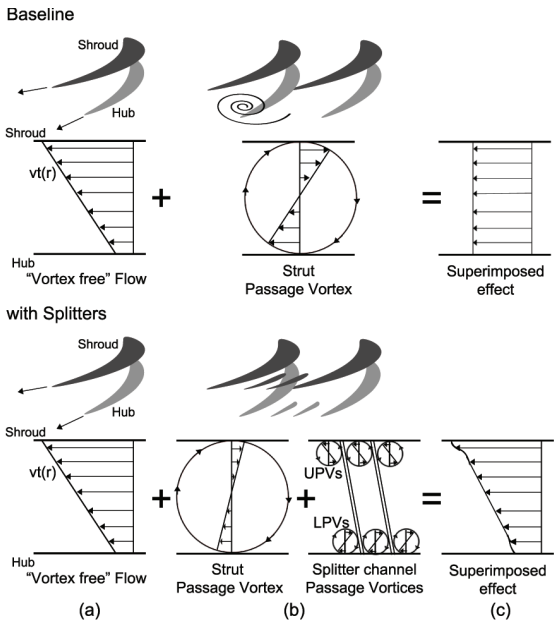

FIGURE 6.21: Embedded design concept: schematization of the strut secondary vortex suppression and splitter vortex generation mechanisms (Spataro et al. [77])

a complex field as the one which can be observed downstream of a TMTF.

Moreover, fast response probe measurements were also performed in this region (Plane D marked in Figure 6.17). Such measurements confirm the trend already shown shown in time-averaged flow analysis. Further information on the measurement grid can be found in Spataro et al. [78].

Figure 6.22 reports about the stochastic fluctuations where the term $p'_{t,RMS}/\rho v^2_{ax,AVE}$ is plotted. The highest stochastic fluctuations are identified in correspondence of the three

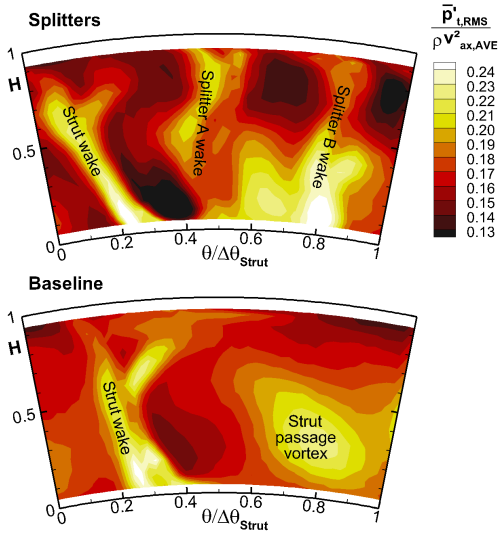

FIGURE 6.22: Fast response probe measurements - LP rotor inlet flow: time-averaged distributions of the RMS of the stochastic fluctuations of total pressure for the two configurations (Spataro et al. [78])

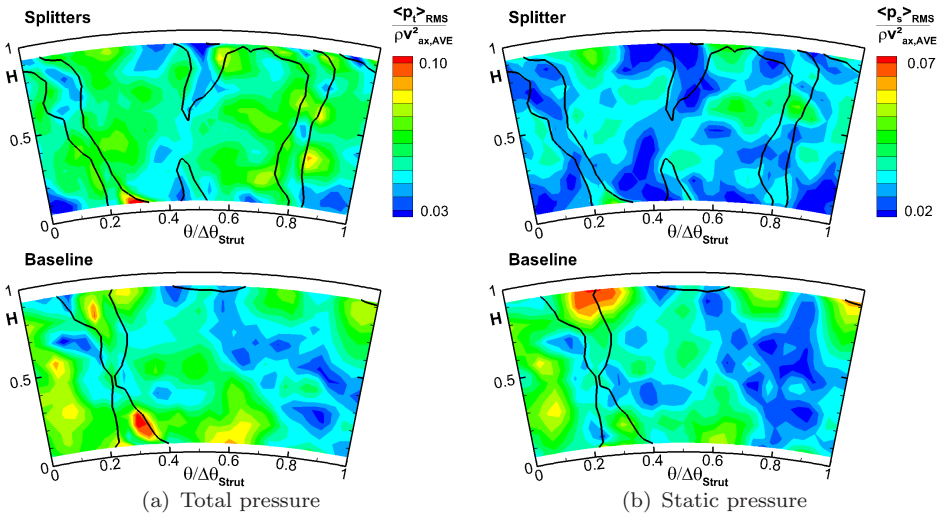

(a) Total pressure (b) Static pressure

FIGURE 6.23: Fast response probe measurements - LP rotor inlet flow: contour plots of the RMS of the deterministic fluctuations of pressure for the two configurations (Spataro et al. [78])

vane wakes. In particular, the strut wake and the pressure side splitter B present the largest value. Whereas, the wake of the suction side splitter A shows lower values with a local maximum in the tip region. The difference in the behavior of the two splitters is due to the large vortical structures that characterize the strut passage which cause a region of high turbulence. This effect is clearly shown in the stochastic fluctuations plot of the baseline setup (Fig. 6.22). The strut passage without splitters presents, in fact, a large region at high turbulence which is associated to the passage vortex. In the case of the splitter setup, the strength of this vortical structure, and its associated turbulence, is reduced by the presence of the splitter vanes. However, the presence of the splitters leads to higher local turbulence in their wake. This is more noticeable for the splitter close to the strut pressure side. On the other hand, the level of turbulence intensity of the wake of the strut itself is reduced in the splitter configuration. This is probably because the growth of the boundary layers on the aft-portion of the strut is reduced by the presence of the splitters.

These regions of high stochastic fluctuations are correlated to the mean flow structures of the exit flow of the vanes. In fact, there is a very low impact of the HP rotor unsteadiness on the generation of losses. A phase averaged map of the term $p'_{t,RMS}/\rho v^2_{ax,AVE}$ looks completely similar to the time averaged map shown in Fig. 6.22, and for this reason it is not shown.

A different behavior is shown by the deterministic fluctuations of pressure which are depicted in Fig. 6.23. This picture reports the contour plots of the RMS of the total and static pressure periodic components computed from the HP rotor phase (in this plane there are no significant contributions from the LP related structures or rotor-rotor interactions). The iso-countour lines of the RMS of the flow angle deterministic

fluctuation are superimposed on the plot to help identifying the vane wakes.

6.2.3.1 Optimizing a turning mid turbine frame with embedded design

In Spataro et al. [77], the author provided a discussion which should help the engineers in the design phase of such turning mid turbine frame whenever splitters should be embedded in a wide vane passage. In his opinion, the distribution of the strut blade loading along the chord is a critical design parameter for the aerodynamic optimisation of the component.
Two limit conditions which define a trade-off for the performance optimisation have been identified:

Aft loaded strut The development of secondary vortices associated with the wide chord vane is delayed in the passage. The level of losses connected to the rolling up of these structures through the duct is lowered. With such a design the streamwise point of maximum suction-to-pressure side gradient is moved in the rear in the passage. This means that the splitters would face a less uniform flow and therefore they have to be optimized by a highly 3D design in order to reach the zero-incidence condition for the whole span (profile losses minimization). Likely, this will lead to turning splitters, which implies on the one hand the need to optimise uneven flow passages, on the other hand the generation of new secondary structures that will be found at the inlet of the following rotor.

Front loaded strut Secondary vortices develop earlier in the passage but a more uniform pitchwise pressure gradient can be eventually reached at the splitter inlet. The splitters design could be more easily optimised due to the reduced transverse pressure gradient in front of the vanes. The target would be to design the splitter vanes under zero-incidence zero-lift condition. Such a design would minimize the profile losses as well as avoid the generation of splitter secondary structures. It is necessary to point out that due to the three-dimensional nature of a flow field confined in such a strut passage, a complex design of the splitters is anyway unavoidable.

In this setup, the strut was designed to perform as a aft-loaded vane. This solution made very difficult to get an optimal design for the splitters, therefore is understandable their highly 3D shape.
A control of the suction-to-pressure side gradient would, therefore, ease the splitter shaping in order to reach a zero-incidence (profile losses minimized) minimum-lift (splitter secondary losses minimized) operating condition.

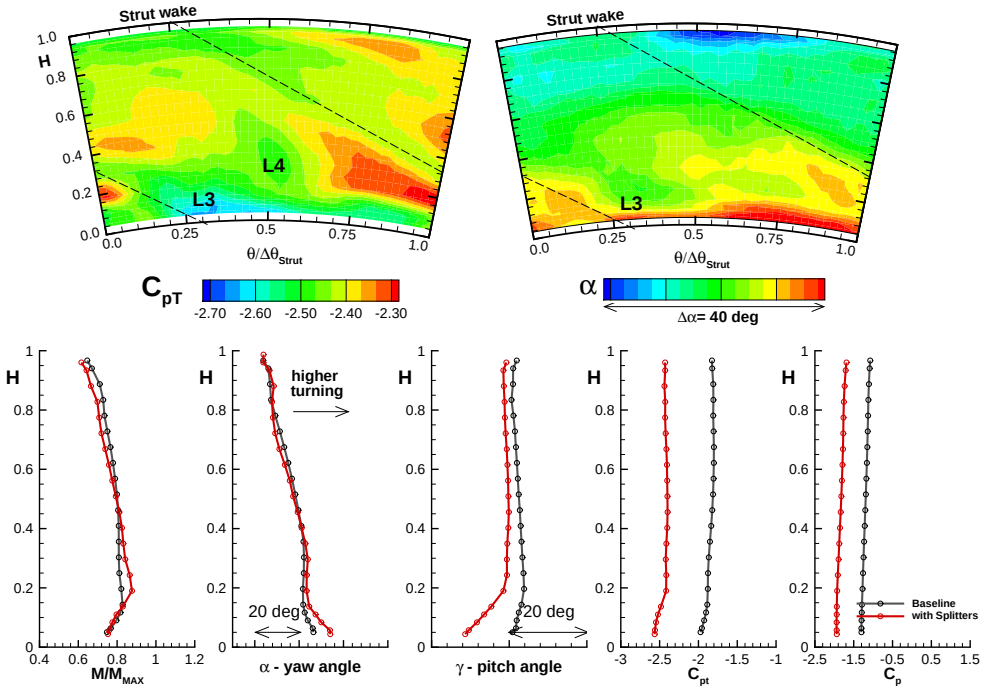

FIGURE 6.24: Five hole probe measurements - LP rotor exit flow: contour plots of total pressure and yaw angle. L3 loss core due to the strut passage vortex. L4 trace of the splitter B wake (view from downstream, Spataro et al. [77])

6.2.4 Flow field at the LP rotor outlet

6.2.4.1 Aerodynamic field

Figure 6.24 shows five-hole probe measurements in Plane F which, according to Figure 6.17, is located at $x/C = 1.71$ downstream of the LP rotor. Similar to Figure 6.20, the contour plots show total pressure (left side) and yaw angle (right side) distributions. The yaw angle was defined positive in the direction of the HP rotor angular speed, which means that, referring to the LP rotor geometry, the blue color identifies the area of lower turning, while the red color the ones of higher turning.

The comparison between baseline and multisplitter setups in terms of spanwise distributions of averaged Mach number, yaw angle, pitch angle, total pressure and static pressure is plotted in the lower charts. The Mach number is normalized on its local maximum, while for the total and static pressure coefficient the definition in Equation 6.1 and 6.2, respectively, is used. The total pressure contours allow the identification of the trace of the strut wake convected through the rotor (dashed line in Figure 6.24). L3 represents the loss core due to the strut passage vortex. This structure was already seen in the baseline design, but here, in the multisplitter setup, it is strongly reduced. L4 is a loss core due to the convection of the splitter B wake (see Figure 6.20) through

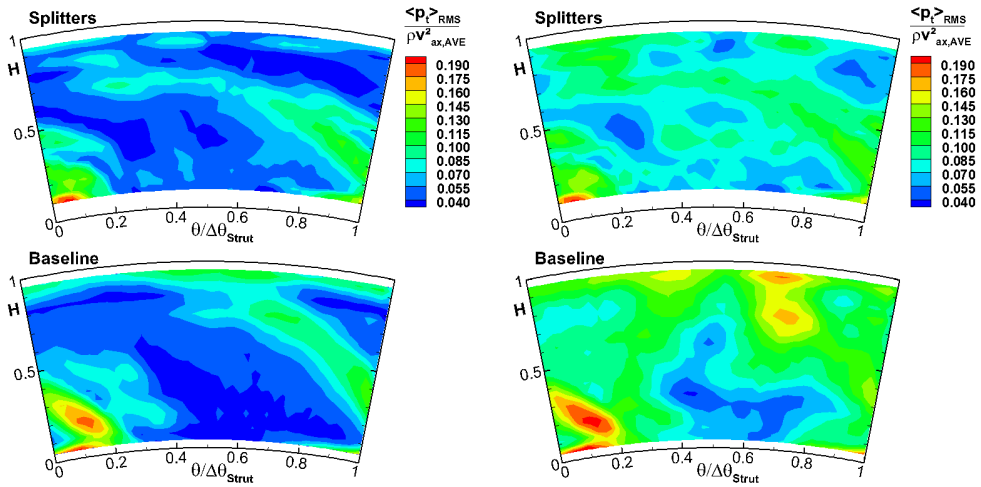

(a) LP phase (b) RSA

FIGURE 6.25: Fast response probe measurements - LP rotor exit flow: contour plots of RMS of the coherent fluctuations of the total pressure (view from downstream, Spataro et al. [78])

the rotor, which can be better visualized in the time resolved flow field (Spataro et al. [78]).

Looking at the flow angle contour plot in Figure 6.24, it is possible to see that the greatest non uniformities are located in the lower half channel. The comparison between the time-mean field measured in both setups (for the baseline distribution refer to [45, 72]) shows that the multisplitter setup is more homogeneous in both the circumferential and the radial directions.

The time-resolved flow in this region (see Plane F in Figure 6.17) was investigated by means of a fast response probe. Further information on the measurement grid can be found in Spataro et al. [78]. Figure 6.25 shows the RMS of total pressure (made non-dimensional by the the term $\rho v^2_{ax,AVE}$) for the two configurations and for the two different decompositions. Figures 6.25(a) and 6.25(b) show the RMS of $< p_t >$ computed from the LP rotor phase and from the RSA, respectively. The splitter configuration is depicted on the top of the picture, and on the bottom there is the baseline one.

The plot computed with the LP rotor phase clearly resembles the contours of $< \alpha >_{rms}$ [78]. The same areas at high fluctuations may be identified and they are mostly due to the strut and splitter wakes for the splitter case and to the strut wake and the passage vortex for the baseline case. Rather low fluctuations of pressure are measured at the tip for both setups. The contour plot computed from the RSA shows a different distribution with larger values of the RMS of $< p_t >$. The different regions with higher fluctuations are due to phenomena that are related to the HP rotor passing frequency and to the rotor-rotor interaction. In fact, the strong shock waves generated by the HP stator and rotor and by their unsteady interaction (e.g., [12]), do not decay within the duct as

shown in Figure 6.23 upstream of the LP rotor. These pressure waves propagate further downstream and cause a significant contribution in the pressure fluctuations at the exit of the test section. It is then important to observe that the pressure fluctuations are reduced by the presence of the splitters up-and downstream of the LP rotor. A different behavior has been shown for the deterministic fluctuations of pressure. The total and static pressure fluctuations are also caused by the HP rotor unsteadiness which has not decayed and by the rotor-rotor interaction. The presence of the splitters reduces the extent of the pressure fluctuations propagating from upstream and, hence, decreases the overall unsteadiness. These reduction mechanism is particularly done on the HP rotor unsteadiness, which is among the largest contribution of pressure fluctuation. The damping out of this contribution leads then to a significant reduction of the aero-acoustic and vibrational problems and, therefore, it was decided to investigate and compare also the acoustic fields of both stages. The results of such experimental campaign are discussed in the following section.

6.2.4.2 Acoustic field

A further analysis of the acoustic field for both the baseline and the multisplitter setup was experimentally performed and published in Faustmann et al. [18].
The measurement setup consisted of a microphone array fully traversable in circumferential direction (360 deg) downstream of the two–stage facility. The measurement setup is reported in Section 5.1.4. The analysis of the frequency spectra and of the azimuthal modes were performed by phase averaging the signal of the HP and LP triggers as well as by applying the Rotor Synchronic Averaging procedure (RSA) (Section 5.2).
In the frequency spectra, the peak of the HP rotor principal harmonic BPF_{HP} is found to be 3 dB lower in the multisplitter setup. In the azimuthal mode analysis the difference is even higher. An overall reduction of 5 dB was observed at the BPF_{HP} in the setup with the splitters.
This is also coherent with the result obtained from the unsteady aerodynamic measurements. The most important effect of the splitters has been observed in the coherent fluctuations of pressure. They were found to stem from the HP rotor unsteadiness, namely the HP rotor shock system which propagates within the duct. The presence of the splitters reduces the maximum of the fluctuations at the blade passing frequency of the upstream rotor when compared with the baseline case. The addition of the splitters into the strut passage increases the number of the second stator vanes which leads to a cut-off configuration.
The frequency spectra and the azimuthal mode analysis showed that the noise generated by the LP rotor is slightly higher in the setup with the splitters. The analysis shows

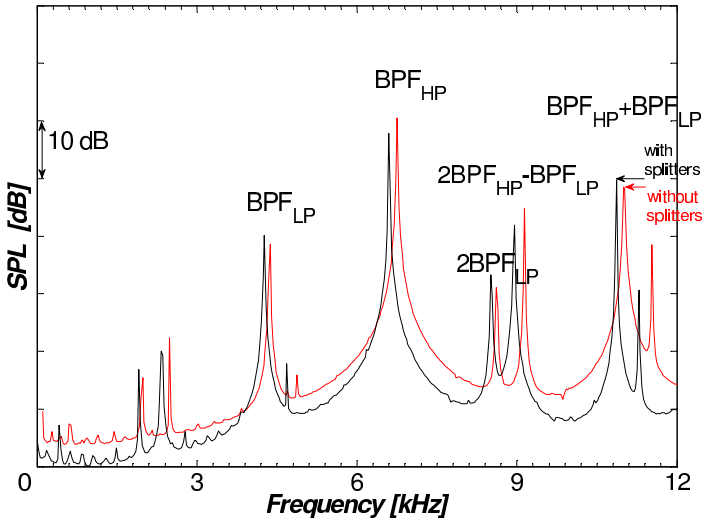

(a) Frequency spectra of the microphone array for the sum of the BPF of the two rotors after rotor synchronic averaging; without splitters (red) and with splitters (black)

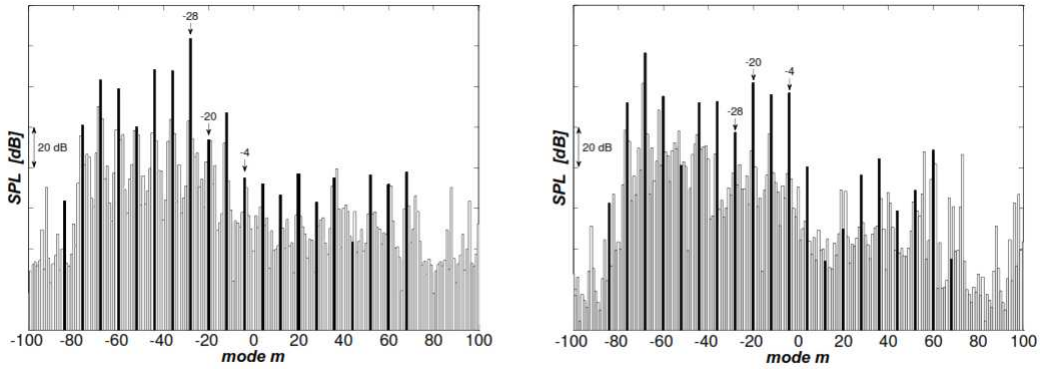

(b) Azimuthal mode analysis of the flow with the two triggers ($BPF_{HP} + BPF_{LP}$); without splitters (left) and with splitters (right). The black bars corresponds to the propagating modes associated to the deterministic fluctuations due to the blades/vanes interaction

FIGURE 6.26: Acoustic measurements downstream of the two–stage facility (Faustmann et al. [18])

that for the splitter design some modes are suppressed, while others are scattered or even more intensive than in the baseline configuration.

The frequency spectra after performing the FFT are very similar. Moreover, a similar behavior is seen in the sound pressure level of the propagating modes allocated to the different interaction phenomena. But there are differences in single modes of over 20 dB between both setups.

As a main result, this study shows that the unsteadiness content measured in the acoustic field downstream of the two-spool rig is highly affected by the HP rotor, whose fluctuations are found not to decay through the low pressure turbine. The overall noise propagation is damped by embedding the splitter vanes in the turning mid turbine frame which, in fact, act as a cut-off filter for the HP stage rotor.

6.3 Stage performance comparison

In the previous sections, the flow dynamics of both investigated setups was in detailed analyzed. In particular, it was showed the the embedded design concept is able to reduce the circumferential gradient providing a more uniform inlet flow condition for the downstream rotor. In the same way, improvements on the flow homogeneity and reduction on the overall unsteadiness level have been observed also downstream of the stage.

Concluding the work, it might be interesting to show how such an improvement in the flow analysis impacts on the stage efficiency. Therefore, for both setups the efficiency of the transition duct and of the whole stage were calculated and then compared.

Before proceeding with the performance analysis, it is important to notice that total and static pressure coefficients as defined in Equation 6.1 and 6.2 respectively cannot be considered as direct indicators of the stage performance, since the flow area through the duct is heavily affected, in this special case, by the splitter blockage.

Therefore, the following loss coefficient is used:

$$\zeta_{duct} = \frac{\hat{p}_{T,C} - \hat{p}_{T,E}}{\hat{p}_{T,C} - \hat{p}_{E}} \tag{6.8}$$

where $\hat{}$ indicates the average values and from which the definition of the duct efficiency follows:

$$\eta_{duct} = 1 - \zeta_{duct} \tag{6.9}$$

In Figure 6.27 the spanwise ζ_{duct} distribution is plotted for Plane E. The comparison shows in general a lower level of losses generated through the duct for the splitter setup. In particular a strong reduction is visible in the shroud region, where the intense loss core due to the strut shed vortex plays a major role on the losses generation.

The stage efficiency was computed between Plane C (Stage inlet) and Plane F (Stage outlet), using the following definition:

$$\eta_{LPstage} = \frac{\frac{\hat{T}_{T,C}}{\hat{T}_{T,F}} - 1}{\left(\frac{\hat{p}_{T,C}}{\hat{p}_{T,F}}\right)^{\frac{\kappa-1}{\kappa}} - 1} \tag{6.10}$$

The efficiency difference for duct and stage was computed as:

$$\Delta\eta_i = \frac{\eta_{i,Splitter} - \eta_{i,Baseline}}{\eta_{i,Baseline}} \tag{6.11}$$

with $i = duct, LPstage$. The results of such a comparison are reported below:

$\Delta\eta_{duct}$	+3.71%
$\Delta\eta_{LPstage}$	+6.08%

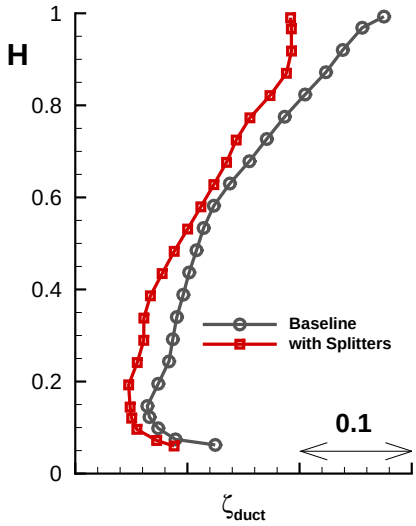

FIGURE 6.27: Spanwire total pressure losses distribution at the LP Rotor inlet for baseline and embedded design setups

More details about this analysis can be found in [77].

In this chapter, a detailed analysis of the flow field in two different turbine transition duct architectures was presented and discussed. It was shown that both the stages are operated under similar aerodynamic as well as acoustic conditions.

As a critical point for the design of such ducts, it was seen that the unsteady pressure fluctuations are propagating from the HP rotor further downstream of the LP stage.

The LP rotor inlet flow in the baseline design was characterized by the presence of large structures which are expected to be critical not only for his aerodynamic behavior, but also for his vibrational response.

The new tested architecture showed an improvement in the performance as well as in the tonal noise emission. This is mainly due to the LP rotor facing a more uniform flow which implies a better operating condition as well as a more uniform flow for the following stages. The embedded design was seen acting as a cut-off filter being the acoustic emission damped in the new design.

Finally, the performance analysis returned results consistent with what already observed in the detailed flow analysis.

Chapter 7

Conclusions

This thesis presents a detailed investigation on the fluid dynamics of two advanced turbine transition duct configurations. The study is based on experimental as well as on numerical analysis of the aerodynamics in a transonic two-stage two-spool counter-rotating turbine. The test turbine is located at the Institute for Thermal Turbomachinery and Machine Dynamics of Graz University of Technology.

In next generation engines architectures, the bulky struts within the turbine transition duct will be aimed to carry also the loading of the LP shaft bearing. Removing the bearings from the shaft rear part and placing them in the turbine front part allows a more general optimisation of the engine architecture.

In the first investigated setup, also called Baseline case through this work, such non-lifting struts and the first LP vane row were integrated into one turning strut row. This configuration of the turbine transition duct is commonly referred as Turning Mid Turbine Frame (TMTF).

The counter-rotating setup (CRT) typical of modern engines allows recovering the HP turbine residual swirl at the duct inlet. By means of such pre-swirl, it is possible to reduce the turning imposed to the strut for leading the flow towards the LP turbine properly.

On the other side, this special setup is responsible for a non conventional convection process of the HP flow structures within the strut passage. Such a transport mechanism was investigated and described in this work. In particular, it was remarked that, in a turbine counter-rotating setup, the strut cross passage velocity gradient is opposite and decreased than in a co-rotating setup. Therefore, in a CRT configuration, the re-orientation mechanism that drives the structure convection through the strut passage is reduced. Such a reduction acts also in the mixing of incoming structures due to the vane-vane interaction as “wake avenues” where the favorable pre-swirl eases the transport of such structures in the strut passage.

The analysis at the TMTF exit flow was found being very critical for the performance of the low pressure stage. In fact, it was observed the rotor facing strong circumferential gradients due to the upcoming strut structures. The TMTF large wakes and extended secondary flows constitute a potential source of vibration and tonal noise emission for the LP blades. Moreover, a detailed analysis on the time-resolved flow field showed that the propagation of pressure fluctuations due to the HP shock system constitutes, also downstream of the LP stage, a dominant contribution which can be observed also in the rotor-rotor interaction harmonics.

The second setup was then designed in order to go beyond the main criticality of a TMTF architecture. Therefore, in order to improve the LP rotor inlet condition, two splitter vanes were embedded in the TMTF passage. The complex design of the new vanes came from the need to minimize the profile losses on the splitters which face a highly three-dimensional flow in the strut passage. The author tried also to address some suggestions for designers who have to face similar problems in the optimisation of turning struts with embedded splitters.

The experimental investigations were performed at the same reduced mass-flow and reduced rotational speeds for each turbine with each setup. In particular, the operation of the LP stage under similar inlet and outlet flow angles allowed the aerodynamic comparability of the setups. Moreover, the same Mach number at the stage exit flow guaranteed also a proper comparison on the tonal noise generation.

The measurements in the new setups confirmed remarkable improvements of the flow at the LP rotor inlet. Circumferential gradients were shown being sensibly reduced and secondary vortices being suppressed. A more uniform flow field was observed also downstream of the LP stage, where the unsteady analysis showed also the role of the splitters as low-pass filter for the pressure fluctuation propagating from the HP stage.

The experimental study on the acoustic field confirmed what was already observed in the aerodynamic analysis. In fact, the measurements performed downstream of the two-stage turbine showed that the tonal noise associated to the HP rotor is reduced in the embedded design, while no remarkable differences between both setups were found for the LP rotor.

Finally, the comparison on the efficiency of the duct as well as of the whole LP stage showed promising results which suggest that the application of embedded concepts in the design of future components could lead to remarkable engine performance improvement.

Bibliography

[1] Global market forecast 2011-2030. Technical report, Airbus, Blagnac Cedex, France, 2011.

[2] J Adamczyk. Model equation for simulating flows in multi stage turbomachinery. In *Proceedings of the ASME Turbo Expo 1985, ASME Paper No 85-GT-226*, 1985.

[3] ANSYS, editor. *ANSYS CFX-Solver Modeling Guide*. ANSYS, 2010.

[4] GE Aviation. The history of aircraft engines. On the WWW, Sep 2012. URL `http://wwwgeaviationcom/aboutgeae/historyhtml`.

[5] P Bas and A Mooren. Optimization of the mixing chamber and intake of the test turbine at the institute of thermal turbomachinery and machine dynamics. *Katholieke Universiteit Leuven, Belgium*, 1998.

[6] E Canepa, D Lengani, F Satta, E Spano, M Ubaldi, and P Zunino. Boundary layer separation on a flat plate with adverse pressure gradients using vortex generators. In *Proceedings of ASME Turbo Expo 2006, ASME Paper No GT-2006-90809*, 2006.

[7] V S P Chaluvadi, A I Kalfas, M R Banieghbal, H P Hodson, and J Denton. An experimental study of the unsteady characteristics of the turbulent wake of a turbine blade. *AIAA Journal of Propulsion and Power*, 17.

[8] V S P Chaluvadi, A I Kalfas, H P Hodson, H Ohyama, and E Watanabe. Blade row interaction in a high a pressure steam turbine. *ASME Journal of Turbomachinery*, 125(1):14–24, 2003.

[9] N Courtiade, X Ottavy, and N Gourdain. Modal decomposition for the analysis of the rotor–stator interactions in a high-speed multistage compressor. In *In 10th International Symposium on Experimental and Computational Aerothermodynamics of Internal Flows, Paper No ISAIF-146*, 2011.

[10] A Marn D Lengani, B Paradiso. Turbulence measurements and analysis in a multistage axial turbine. *J Therm Sci*, 21:21–31, 2012.

[11] R Dénos, T Arts, G Paniagua, V Michelassi, and F Martelli. Investigation of the unsteady rotor aerodynamics in a transonic turbine stage. *ASME Journal of Turbomachinery*, 123:81–89, 2001.

[12] R Dénos and G Paniagua, editors. *Effects of Aerodynamic Unsteadiness in Axial Turbomachines*. VKI Lecture Series, LS 2005-03, 2005.

[13] R G Dominy and D A Kirkham. The influence of blade wakes on the performance of inter-turbine diffusers. *ASME Journal of Turbomachinery*, 118:347–352, January 1996.

[14] R G Dominy, D A Kirkham, and A D Smith. Flow development through inter-turbine diffusers. *ASME Journal of Turbomachinery*, 120:298–304, January 1998.

[15] R P Dring, H D Joslyn, L W Hardin, and J H Wagner. Turbine rotor-stator interaction. In *Proceedings of ASME Turbo Expo 1982, ASME Paper No 82-GT-3*, 1982.

[16] L Enghardt, U Tapken, W Neise, F Kennepohl, and K Heinig. Turbine blade/-vane interaction noise: Acoustic mode analysis using in-duct sensor rakes. In *Proceedings of the Seventh AIAA/CEAS-Aeroacoustics Conference, Maastricht, The Netherlands, 28-30 May, Paper No 2001-2153*, 2001.

[17] J Erhard. *Design, Construction and Commissioning of a Transonic Test Turbine Facility*. Phd thesis, Institute for Thermal Turbomachinery and Machine Dynamics of Graz University of Technology, 2000.

[18] C Faustmann, D Lengani, R Spataro, A Marn, E Göttlich, and F Heitmeir. Experimental investigation on the noise generation and propagation for different turning mid turbine frame setups in a two-stage two-spool test turbine. In *Proceedings of ASME Turbo Expo 2013, June 3-7, San Antonio, Texas, USA, ASME Paper No GT-2013-95698*, 2013.

[19] R Florea, L Bertuccioli, and T G Tillman. Flow-control-enabled aggressive turbine transition ducts and engine systems analysis. *AIAA J Propul Power*.

[20] P Gaetani, G Persico, V Dossena, and C Osnaghi. Investigation of the flow field in a high-pressure turbine stage for two stator-rotor axial gaps-part i: Three dimensional time-averaged flow field. *ASME Journal of Turbomachinery*, 129:572–579, July 2007.

[21] P Gaetani, G Persico, V Dossena, and C Osnaghi. Investigation of the flow field in a high-pressure turbine stage for two stator-rotor axial gaps-part ii: Unsteady flow field. *ASME Journal of Turbomachinery*, 129:580–590, July 2007.

[22] T Garside, R W Moss, R W Ainsworth, S N Dancer, and M G Rose. Heat transfer to rotating turbine blades in a flow undisturbed by wakes. In *Proceedings of ASME Turbo Expo 1994, ASME Paper No 94-GT-94*, 1994.

[23] E Göttlich. *Research on Intermediate Turbine Structure Aerodynamics*. Habilitation memorandum, Institute for Thermal Turbomachinery and Machine Dynamics, 2011.

[24] E Göttlich. Research on the aerodynamics of intermediate turbine diffusers. *Progress in Aerospace Sciences*, 47:249–279, 2011.

[25] E Göttlich, A Marn, R Pecnik, F J Malzacher, O Schennach, and H P Pirker. The influence of blade tip gap variation on the flow trough an aggressive s-shaped intermediate turbine duct downstream a transonic turbine stage - part ii: Time-resolved results and surface flow. In *Proceedings of ASME Turbo Expo 2007, ASME Paper No GT2007-28069*, 2007.

[26] E Göttlich, J Woisetschlger, P Pieringer, B Hampel, and F Heitmeir. Investigation of vortex shedding and wake-wake interaction in a transonic turbine stage using laser-doppler-velocimetry and particle-image-velocimetry. *ASME Journal of Turbomachinery*, 128:178–187, 2006.

[27] C W Haldeman, M G Dunn, R S Abhari, P D Johnson, and X A Montesdeoca. Aerodynamic test results of controlled pressure ratio engine (cope) dual spool air turbine rotating rig. In *Proceedings of ASME Turbo Expo 2000 (IGTI), May 811, Munich, Germany, ASME Paper 2000-GT-445*, 2000.

[28] K C Hall, J P Thomas, and W S Clark. Computation of unsteady nonlinear flows in cascades using a harmonic balance technique. *AIAA Journal*, 40.

[29] D E Halstead, D C Wisler, T H Okiishi G J Walker, H P Hodson, and H W Shin. Boundary layer development in axial compressors and turbines part 3 of 4: Lp turbines. *ASME Journal of Turbomachinery*, 119:225–237, 1997.

[30] Robert Hardman. A genius betrayed: The man who invented the jet engine ignored by his country. On the WWW, May 2007. URL `http://wwwdailymailcouk/news/article-500459/A-genius-betrayed-The-man-invented-je`

[31] N W Harvey, J C Cox, V Schulte, R Howell, and H P Hodson. The role of research in the aerodynamic design of advanced low-pressure turbine. *Trans 3rd European Conference on Turbomachinery*, 123:123132, 1999.

[32] F Haselbach, HP Schiffer, M Horsman, S Dressen, N Harvey, and S Read. The application of ultra high lift blading in the br715 lp turbine. *ASME Journal of Turbomachinery*, 124.

[33] H P Hodson and R J Howell. Bladerow interactions ,transition, and high-lift aerofoils in low-pressure turbines. *Annu Rev Fluid Mech*, 37:71–98.

[34] F Holste and W Neise. Noise source identification in a propfan model by means of acoustical near field measurements. *Journal of Sound and Vibration*, 203(4):641–665, 1997.

[35] J Hubinka. *Konstruktion, Aufbau und Betriebsführung eineszweiwelligen Turbinenprüfstandes*. Phd thesis, Institute for Thermal Turbomachinery and Machine Dynamics of Graz University of Technology, 2012.

[36] J Hubinka, B Paradiso, C Santner, H P Pirker, and E Göttlich. Design and operation of a two spool high pressure test turbine facility. In *Proceeding of the 9th ETC conference, Instambul, Turkey, pp 1531-1540*, 2011.

[37] J Hubinka, C Santner, B Paradiso, F Malzacher, and E Göttlich. Design and construction of a two shaft test turbine for investigation of mid turbine frame flows. In *Proceedings of ISABE 2009, Montreal, Quebec, Canada, AIAA Paper No ISABE-2009-1293*, 2009.

[38] A Hussain and W Reynolds. The mechanics of an organized wave in turbulent shear flow. *Journal of Fluid Mechanics*, 41:241258, 1970.

[39] B D Keith, D K Basu, and C Stevens. Aerodynamic test results of controlled pressure ratio engine (cope) dual spool air turbine rotating rig. In *Proceedings of ASME Turbo Expo 2000 (IGTI), May 811, Munich, Germany, ASME Paper 2000-GT-632*, 2000.

[40] T Korakianitis. Blade-loading effects on the propagation of unsteady flow and on forcing functions in axial-turbine cascades. *Journal de Physique III*, 2(2):507–525, April 1992.

[41] P Kupferschmied, O Köppel, W P Gizzi, and G Gyarmathy. Time resolved flow measurements with fast aerodynamic probes in turbomachinery. *Measurement Science and Technology*, 11(7):1036–1054, 2000.

[42] S Lavagnoli, T Yasa, G Paniagua, S Duni, and L Castillon. Aerodynamic analysis of an innovative low pressure vane placed in a s-shape duct. *ASME Journal of Turbomachinery*, 134(2):011013 (13 pages), 2012.

[43] D Lengani, B Paradiso, A Marn, and E Göttlich. Identification of spinning mode in the unsteady flow field of a lp turbine. *ASME Journal of Turbomachinery*, 134(5):051032 doi: 10.1115/1.4004875, 2012.

[44] D Lengani, C Santner, R Spataro, and E Göttlich. Analysis tools for the unsteady interactions in a counter-rotating two-spool turbine rig. *Experimental Thermal Fluid Science*, 42:248–257, October 2012.

[45] D Lengani, C Santner, R Spataro, B Paradiso, and E Göttlich. Experimental investigation of the unsteady flow field downstream of a counter-rotating two-spool turbine rig. In *Proceedings of ASME Turbo Expo 2012, June 11-15, Copenhagen, Denmark, ASME Paper No GT-GT2012-68583*, 2012.

[46] D Lengani, T Selic, R Spataro, A Marn, and E Göttlich. Analysis of the unsteady flow field in the turbines by means of modal decomposition. In *Proceedings of ASME Turbo Expo 2012, June 11-15, Copenhagen, Denmark, ASME Paper No GT-GT2012-68582*, 2012.

[47] W K Lord, D G MacMartin, and G Tillman. Flow control opportunities in gas turbine engines. In *AIAA paper AIAA-2000-2234, 2000*, 2000.

[48] A Mahallati, B R McAuliffe, S A Sjolander, and T J Praisner. Aerodynamics of a low-pressure turbine airfoil at low reynolds numbers part i: Steady measurements. *ASME Journal of Turbomachinery*, 135(1):011010–1 (9 pages), 2012.

[49] A Mahallati and S A Sjolander. Aerodynamics of a low-pressure turbine airfoil at low reynolds numbers part ii: Blade-wake interaction. *ASME Journal of Turbomachinery*, 135(1):011011–1 (10 pages), 2012.

[50] A Marn, E Göttlich, D Cadrecha, and H P Pirker. Shorten the intermediate turbine duct length by applying an integrated concept. *ASME Journal of Turbomachinery*, 131:041014 (10 pages), 2009.

[51] A Marn, E Göttlich, F J Malzacher, and H P Pirker. The effect of rotor tip clearance size onto the separated flow through a super-aggressive s-shaped intermediate turbine duct downstream of a transonic turbine stage. In *Proceedings of ASME Turbo Expo 2009, ASME Paper No GT2009-59934*, 2009.

[52] F R Menter. Two-equation eddy-viscosity turbulence models for engineering applications. *AIAA Journal*, 32(8):1598–1605, 1994.

[53] R J Miller, R W Moss, R W Ainsworth, and N W Harvey. The effect of an upstream turbine on a low-aspect ratio vane. In *Proceedings of ASME Turbo Expo 2004, June 14-17, Vienna, Austria, ASME Paper No GT-2004-54017*, 2004.

[54] R J Miller, R W Moss, R W Ainsworth, and C K Horwood. Time-resolved vane-rotor interaction in a high-pressure turbine stage. *ASME Journal of Turbomachinery*, 125:1–13, January 2003.

[55] R J Miller, R W Moss, R W Ainsworth, and C K Horwood. Wake, shock, and potential field interactions in a 15 stage turbinepart i: Vane-rotor and rotor-vane interaction. *ASME Journal of Turbomachinery*, 125:33–39, January 2003.

[56] R J Miller, R W Moss, R W Ainsworth, and C K Horwood. Wake, shock, and potential field interactions in a 15 stage turbinepart ii: Vane-rotor and rotor-vane interaction. *ASME Journal of Turbomachinery*, 125:40–47, January 2003.

[57] M Moser, U Tapken, L Enghardt, and L Neuhaus. An investigation of low pressure turbine blade/vane interaction noise: Measurements in a 1.5-stage rig. *Proceedings of the Institution of Mechanical Engineers, Part A: Journal of Power and Energy*, 223(6):687–695, 2009.

[58] U Orth. Unsteady boundary-layer transition in flow periodically disturbed by wakes. *ASME Journal of Turbomachinery*, 115.

[59] B Paradiso, C Santner, J Hubinka, and E Göttlich. Turning mid turbine frame behaviour for different hp turbine outflow conditions. In *Proceedings of ASME Turbo Expo 2011, June 6-10, Vancouver, British Columbia, Canada, ASME Paper No GT-2011-46502*, 2011.

[60] G Persico, P Gaetani, V Dossena, G D'Ippolito, and C Osnaghi. On the definition of the secondary flow in three-dimensional cascades. *I MECH E Journal of Power and Energy*, 223:667–676, 2009.

[61] G Persico, P Gaetani, and A Guardone. Design and analysis of new concept fast-response pressure probes. *Meas Sci Technol*, 16:1741–1750, 2005.

[62] H Pfeil, R Herbst, and T Schroder. Boundary layer and loss measurements on the rotor of an axial–flow turbine. *ASME Journal Eng Power*, 106.

[63] H Pfeil, R Herbst, and T Schröder. Investigation of the laminar–turbulent transition of boundary layers disturbed by wakes. *ASME Journal Eng Power*, 105.

[64] H P Pirker, H Jericha, and G Zhuber-Okrog. Auslegung und betriebsverhalten einer verdichteranlage für die luftversorgung wissenschaftlicher versuchseinrichtungen. *VDI Berichte*.

[65] L Porreca, M Hollenstein, A I Kalfas, and R S Abhari. Turbulence measurements and analysis in a multistage axial turbine. *AIAA J Propul Power*, 23.

[66] Z Qingjun, D Jianyi, W Huishe, Z Xiaolu, and X Jianzhong. Tip clearance effects on inlet hot streak migration characteristics in high pressure stage of a vaneless counter-rotating turbine. *ASME Journal of Turbomachinery*, 132:011005 (8 pages), 2010.

[67] So W Rienstra and A Hirschberg. *An Introduction to Acoustics*. Eindhoven University of Technology, 2004.

[68] Rolls Royce. *The Jet Engine*. Rolls Royce plc, 1996.

[69] C Santner. *Experimental Investigation of Turning Mid Turbine Frame Designs*. Phd thesis, Institute for Thermal Turbomachinery and Machine Dynamics of Graz University of Technology, 2013.

[70] C Santner, E Göttlich, A Marn A, J Hubinka, and B Paradiso. The application of low profile vortex generators in an intermediate turbine diffuser.

[71] C Santner, E Göttlich, F Wallin, and M Hoeger. Experimental investigation of turning mid turbine frame designs. In *Proceedings of ISABE 2011, September 12-16, Gothenburg, Sweden, ISABE Paper No ISABE-2011-1710*, 2011.

[72] C Santner, B Paradiso, F Malzacher, M Hoeger, J Hubinka, and E Göttlich. Evolution of the flow through a turning mid turbine frame applied between a transonic hp turbine stage and a counter-rotating lp turbine. In *Proceedings of* 9^{th} *European Turbomachinery Conference, March 21-25, Istanbul, Turkey, Paper No 110*, 2011.

[73] W Sanz, M Kelterer, R Pecnik, A Marn, and E Göttlich. Numerical investigation of the effect of tip leakage flow on an aggressive s-shaped intermediate turbine duct. In *Proceedings of ASME Turbo Expo 2009, ASME Paper No GT2009-59535*, 2009.

[74] O Schennach, J Woisetschläger, B Paradiso, G Persico, and P Gaetani. Three dimensional clocking effects in a one and a half stage transonic turbine. *ASME Journal of Turbomachinery*, 132:011019–1 (9 pages), 2010.

[75] O P Sharma, T L Butler, H D Joslyn, and R P Dring. Three-dimensional unsteady flow in an axial flow turbine. *AIAA Journal of Propulsion and Power*, 1:2938, 1985.

[76] G Sovran and E D Klomp. Experimentally determined optimum geometries for rectilinear diffusers with rectangular conical or annular cross section. *Fluid mechanics of internal flow, Elsevier*.

[77] R Spataro, E Göttlich, D Lengani, C Faustmann, and F Heitmeir. Development of a turning mid turbine frame with embedded design - part i: Design and steady measurements. In *Proceedings of ASME Turbo Expo 2013, June 3-7, San Antonio, Texas, USA, ASME Paper No GT-2013-95279*, 2013.

[78] R Spataro, E Göttlich, D Lengani, C Faustmann, and F Heitmeir. Development of a turning mid turbine frame with embedded design - part ii: Unsteady measurements. In *Proceedings of ASME Turbo Expo 2013, June 3-7, San Antonio, Texas, USA, ASME Paper No GT-2013-95280*, 2013.

[79] R Spataro, E Göttlich, C Santner, and F Heitmeir. A numerical comparison on the aerodynamic performances of a two-stage two-spool turbine facility predicted by steady and unsteady simulations. In *Proceedings of* 10^{th} *European Turbomachinery Conference, April 21-25, Lappenranta, Finland, Paper No 39*, 2013.

[80] R Spataro, C Santner, Davide Lengani, and E Göttlich. On the flow evolution through a lp turbine with wide-chord vanes in an s-shaped channel. In *Proceedings of ASME Turbo Expo 2012, June 11-15, Bella Center, Copenhagen, Denmark, ASME Paper No GT-2012-68178*, 2012.

[81] P Spittle. Gas turbine technology. *Physics Education*, 38:504–511.

[82] R Starr and J Anderson. 2012 aerospace & defense industry perspective. On the Booz & Co website, at `http://wwwboozcom/media/uploads/BoozCo-Aerospace-Defense-Letter-2012pdf`, May 2012. PDF file.

[83] K L Suder, M D Hathaway, T H Okiishi, A J Strazisar, and J J Adamczyk. Measurements of the unsteady flow field within the stator row of a transonic axial-flow fan: part 1-measurement and analysis technique. Technical Memorandum 88945, NASA, 1997.

[84] R Mocanu R Jurek R Gacek T J Praisner, E Grover. Predictions of unsteady interactions between closely coupled hp and lp turbines with co-and counterrotation. In *Proceedings of ASME Turbo Expo 2010, June 1418, Glasgow, UK, ASME Paper No GT2010-23681*, 2010.

[85] F Taddei, M De Lucia, C Cinelli, and C Schipani. Experimental investigation of low pressure turbine noise: Radial mode analysis for swirling flows. In *ISABE conference Beijing, AIAA Paper I12-S4-4*, 2009.

[86] Jo M Tyler and To G Sofrin. Axial flow compressor noise. *SAE Transaction*, 70:309–332, 1962.

[87] F Wallin and L E Eriksson. Response surface-based transition duct shape optimization. In *Proceedings of ASME Turbo Expo 2006, GT2006-90978*, 2006.

[88] F Wallin and L E Eriksson. Non-axisymmetric endwall shape optimization of an intermediate turbine duct. In *AIAA paper ISABE-2007-1300*, 2007.

[89] F Wallin and L E Eriksson. Design of an aggressive flow–controlled turbine duct. In *Proceedings of ASME Turbo Expo 2008, GT2008-51202*, 2008.

[90] Lutz Warsitz. *The First Jet Pilot - The Story of German Test Pilot Erich Warsitz Lutz Warsitz*. Aviation Memoirs, 2008.

[91] M H Waters and E T Schaire. Analysis of turbofan propulsion system weight and dimension. Technical Memorandum 1, NASA, Ames Research Center, May 1977. See also URL `http://ntrsnasagov/archive/nasa/casintrsnasagov/19770012125_1977012125pdf`.

[92] M M Weaver, S R Manwaring, R S Abhari, M G Dunn, M J Salay, K K Frey, and N Heidegger. Forcing function measurements and predictions of a transonic vaneless counter rotating turbine. In *Proceedings of ASME Turbo Expo 2000, May 811, Munich, Germany, ASME Paper 2000-GT-375*, 2000.

[93] Wikipedia. Jet engine. On the WWW. URL `http://enwikipediaorg/wiki/Jet_engine`.

[94] T Yasa, S Lavagnoli, and G Paniagua. Impact of a multi-splitter vane configuration on the losses in a 1.5 turbine stage. *Proceedings of IMechE Vol 225*, 225:964–974, 2011.

Appendix: Related Publications

This thesis is related to several publications which are reported in the following of this appendix. A list of such works is reported below:

1. R.Spataro et al., 2012, On the flow evolution through a LP turbine with wide-chord vanes in an S-shaped channel, Presented at the ASME Turbo Expo 2012 in Copenhagen, Denmark, Paper number GT2012-68178

2. R.Spataro et al., 2013, A numerical comparison on the aerodynamic performances of a two-stage two-spool turbine facility predicted by steady and unsteady simulations, Presented at the 10th ETC Conference in Lapperranta, Finland

3. D.Lengani et al., 2012, Analysis tools for the unsteady interactions in a counter-rotating two-spool turbine rig, Published in *Experimental Thermal and Fluid Science*

4. D.Lengani et al., 2012, Experimental investigation of the unsteady flow field downstream of a counter-rotating two-spool turbine rig, Presented at the ASME Turbo Expo 2012 in Copenhagen, Denmark, Paper number GT2012-68583

5. D.Lengani et al., 2012, Analysis of the unsteady flow field in the turbines by means of modal decomposition, Presented at the ASME Turbo Expo 2012 in Copenhagen, Denmark, Paper number GT2012-68582

6. R.Spataro et al., 2013, Development of a turning mid turbine frame with embedded design - part I: Design and steady measurements, Presented at the ASME Turbo Expo 2013 in San Antonio, Texas, USA, Paper number GT2013-95279 (already accepted for the publication on the *Journal of Turbomachinery*)

7. R.Spataro et al., 2013, Development of a turning mid turbine frame with embedded design - part II: Unsteady measurements, Presented at the ASME Turbo Expo 2013 in San Antonio, Texas, USA, Paper number GT2013-95280 (already accepted for the publication on the *Journal of Turbomachinery*)

Proceedings of ASME 2012 TURBO EXPO
GT2012
June 11-15, 2012, Bella Center, Copenhagen, Denmark

GT2012-68178

ON THE FLOW EVOLUTION THROUGH A LP TURBINE WITH WIDE-CHORD VANES IN AN S-SHAPED CHANNEL

Rosario Spataro, Cornelia Santner, Davide Lengani, Emil Göttlich
Institute for Thermal Turbomachinery and Machine Dynamics
Graz University of Technology
Graz, A-8010, Austria
Email: rosario.spataro@tugraz.at

ABSTRACT

The paper discusses the time averaged flow field in a test facility located at the Institute for Thermal Turbomachinery and Machine Dynamics (ITTM) of Graz University of Technology. The rig was designed in order to reproduce the flow leaving a transonic turbine through a following counter rotating low pressure stage. This configuration is common in modern multi-shaft jet engines and will become a standard in the future.

The discussion on the flow field is based on numerical results obtained by a commercial CFD code and validated by aerodynamic measurements and oil flow visualization performed on the facility itself. The meridional flow path of the machine is characterized by a diffusing S-shaped duct between the two rotors. Within the duct turning struts lead the flow to the following rotor. The LP stage inlet condition is given by the outlet flow of the high pressure turbine whose spanwise distribution is strongly affected by the shape of the downstream S-channel. A special focus is concentrated on the generation and propagation of secondary flows in such a turning mid turbine frame (TMTF). The aim of the present work is to isolate the flow structures moving from the outlet of the transonic stage through the low pressure stage and identify their effect on the time-averaged flow.

The main outcome of this paper is that, whenever a TMTF is placed between counter-rotating high pressure and low pressure turbines, the structures coming from the upstream rotor will not decay (like in a co-rotating setup), but they will be convected and transported towards the downstream rotor. Moreover, the turning of the struts will enhance the vorticities generated by the upstream turbine. The application of technical solutions such as embedded TMTF designs or endwall contouring should be aimed to reach LP rotor uniform inlet conditions, minimize the TMTF secondary flows and thus to damp the rotor-rotor interaction.

NOMENCLATURE

C	low pressure vane axial chord
$const$	constant
Cp_T	total pressure coefficient
Cp	static pressure coefficient
H	channel height
HP	High Pressure
LP	Low Pressure
$m_{r,in}$	Reduced mass flow, stage inlet
Ma	Mach number
MID	midspan
$n_{r,in}$	Reduced rotational speed, stage inlet
p_T	total pressure
p	static pressure
r	radial coordinate
SW	streamwise
$TMTF$	Turning Mid Turbine Frame
v	velocity
v_t	tangential velocity
x	axial coordinate
α	Yaw angle (from meridional dir.)
ζ	total pressure loss
ω	vorticity

INTRODUCTION

The challenge in the design of commercial jet-engines is nowadays subjected to more and more rigorous constrains in terms of size and weight. Saving fuel and reducing polluted emissions are ambitious tasks for the engines manufacturing companies. Different architectures are being studied in addition to the *turbofan* configuration which represents a standard for modern jet-engines.

Therefore in the last years a lot of research programs (i.e. the EU-project DREAM) tried to explore alternative configura-

tions such as the *open-rotor technology* or the *geared turbofan* with the intention to combine the advantages of a propeller in terms of efficiency with the high thrust-to-power ratio of the turbojet propulsion. The studies are currently facing problems like for example the aeroelastic interaction between the propeller and structures (wings, pylon, fuselage, etc.). These other lead to vibrational mechanical fatigue as well as induced acoustic emission.

In this context, the trend to set up high power engines in multi-shaft architecture (up to 3 shafts in Rolls Royce TRENT engines family) is necessary in order to maximize the pressure ratio at a fixed number of stages and to assign adequate rotational directions of the spools. In particular, counter-rotating shaft setups can be used to compensate the gyroscopic effect of the rotating masses as well as to minimize the aerodynamic losses in the intermediate stage (i.e. General Electric GEnx, Rolls Royce TRENT 1000, Pratt & Whitney PW1500).

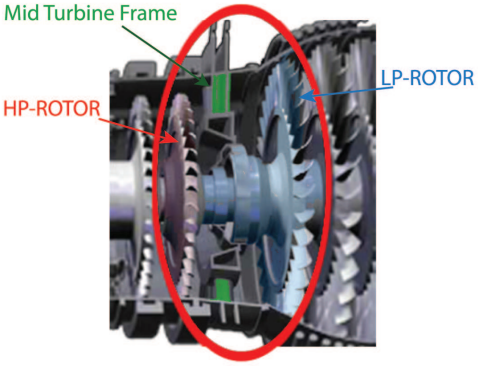

FIGURE 1: Example of multi-shaft engine with mid turbine frame (Pratt & Whitney PW1500)

The fan tip velocity is a design constrain proportional to the maximum stress in the component and which imposes the engine noise emission limit. Since the turbofan front section and hence the fan radii have to be enlarged in order to maximize the engine bypass-ratio and therefore the propulsion efficiency, lower LP-shaft angular speed is required. On the other hand, the rotational speed of the high pressure stage has to be increased in order to reach higher maximum cycle pressure.

Furthermore, the design engineer has to deal with the decreasing rotational speed level of the low pressure shaft aimed to avoid or minimize the use of a mechanical gear to couple the fan with the low pressure shaft (which would enhance the overall weight and vibrational level of the engine). The increased difference in the shafts rotational speeds will lead to an increasing difference of the components diameters (compressors and turbines). Therefore the design of the component between the HP and LP turbines is very important for the aerodynamic performances of the engine. Such component is also called turbine center frame.

This work is focused on the aerodynamics of a mid turbine frame (MTF) with turning struts between two counter-rotating rotors. The above cited considerations on the diameter differences lead to a S-shaped design for the meridional section. Here, an ideal flow path will guarantee a diffusing flow without separation at the endwalls as well as proper LP turbine inlet conditions. An additional function for these components can be found in the possibility to locate the shafts rear bearings within the hub in order to optimize the engine axial length. This results in thick struts within the MTF channels of state-of-the art and next generation engines. These struts have to be thick enough to provide fairings with starlike structure and to be able to place oil supply lines for the bearings. Next generation engines will be characterized by turning struts such as in the Turning Mid Turbine Frame (TMTF) studied and presented in this paper.

In the last decade experimental rigs as the ones at the University of Durham [1], University of Cambridge [2], Oxford University [3], Ohio State University [4], Von Karman Institute [5], Chalmers University [6] and Graz University of Technology [7] have been extensively studied in order to understand the aerodynamics of inter-turbine diffusers. Recently Göttlich [8] published a review on the present state of the research of these components.

The fundamental work by Dominy et al. [9] on swan-necked diffusers identified the influence of the cross-passage pressure gradients in S-shaped ducts. In particular, experimental and numerical data revealed clearly the effects of the two bends on the generation of secondary flows as the flow develops through the diffuser. Swirl was found to influence the character of the flow [1] particularly through the skewing of the wakes. Later works [3] show how the flow approaching the inlet of the stage downstream of an unshrouded high pressure turbine is dominated by two co-rotating streamwise vortexes, the tip leakage flow being out of phase (phase relative to the upstream rotor) with the lower passage vortex. Similar configurations were later investigated with wide chord vanes within the S-shaped channel. In those cases the aim was to lead the flow to an ideal co-rotating [5, 10] or counter-rotating low pressure rotor [11] downstream of the struts. Miller et al. [10] showed that the bound circulation caused by the geometry of the duct and vane is relatively independent of vane inlet conditions. Anyway in none of the cited cases the MTF flow field was studied between upstream and downstream rotors within the same setup.

The possibility to investigate the flow in a turning mid turbine frame placed between two counter-rotating rotors makes the facility located at the Institute for Thermal Turbomachinery of Graz University of Technology unique. The aerodynamic design of the machine was conducted by MTU Aero Engines. Details on the test turbine can be found in [12–14].

Santner et al. [15] presented the influence of the HP turbine secondary flows and wakes on the TMTF. Paradiso et al. [16] discussed the flow field and the performances of the facility whenever the machine is operated at off-design conditions. Lengani et al. [17] showed by means of a modal decomposition analysis of the unsteady flow field that in such machines rotor-rotor interaction can be observed downstream of the LP stage.

The aim of this paper is to present the problematics which the designer of low pressure turbines should be aware of whenever high pressure and low pressure stages are connected via a TMTF. Therefore, the influence of the structures generated by the high pressure turbine will be discussed in the paper and it

will be pointed out how they are convected in the vane passage instead of decaying like in co-rotating shaft setups. These vortexes interact with the vorticities generated within the TMTF, and can be found at the inlet of the downstream rotor.

EXPERIMENTAL APPARATUS AND METHODOLOGY

Facility

The transonic test turbine facility is a continuously operating two-stage cold-flow open-circuit plant, which consists of a transonic HP stage and a counter-rotating LP stage (a schematic drawing is shown in Fig. 2). This unique configuration allows the testing of rig inserts under engine representative conditions. Both turbines are designed with overhung-type turbine shafts and additionally the LP turbine is mounted on an axially movable frame. This allows easy disk assembly without dismantling the bearings and the simple application of transition ducts and TMTF designs with different axial lengths. The facility is driven by pressurized air delivered by a separate 3 MW compressor station. The shaft power of the HP stage drives a three-stage radial brake compressor. The power of the LP turbine is absorbed by a water brake with a maximum power of 700 kW. Detailed information on the design and construction of the original single stage facility can be found in Erhard and Gehrer [12]. For the design of the LP-stage together with the TMTF see Hubinka et al. [14] and for the operation Hubinka et al. [13].

Table 1 summarizes the main parameters for the HP stage and the LP stage (TMTF+LP rotor), and the operating condition.

Measurement techniques

The experimental investigation was conducted by means of 5 hole probes traversed in a plane just downstream of the HP stage (Plane C in Fig. 2), and in a plane downstream of the struts (Plane E in Fig. 2). Moreover one of the struts was instrumented with pressure taps along three lines located at 25%, 50% and 75% span. In Plane C the probe was traversed radially over 95% of the blade height and over one HP-vane pitch which corresponds to one third of two struts pitches. In each measurement point the probes were turned into the flow to reach the highest accuracy and to ensure to be always within the calibration range of the probe. Due to the uncommon flow direction relative to the measurement location, in some planes special developed five-hole-probes (IST, RWTH Aachen) with an inclined probe head of 2.5mm diameter were applied. The probes were calibrated for Mach numbers between 0.1 and 0.8, yaw angles between -20 deg and +20 deg, pitch angles between -16 deg and +20 deg. Negative values of the yaw angle indicate a counter-rotating flow (with respect to the HP rotor circumferential speed) and negative values of the pitch angle indicate the flow direction towards the machine axis.

The correlation between the calibration characteristic and the value to be measured is given by a multi-parameter approximation.

The measurement system consists of eleven multi channel pressure transducers PSI 9016 with a total amount of 176 channels and an accuracy of 0.05% full scale and four National Instruments Field Point FP-TC-120 eight-channel thermocouple input modules and one FP-RTD-122 resistance thermometer input module. The measurement uncertainties of the static pressure taps on the vane surface are $\pm 100Pa$.

A mixture of synthetic motor oil and titanium oxide is used to visualize the trajectory of the shear stress at the walls. The mixture has been uniformly painted in the whole passage surfaces of different exit guide vanes in order to verify the periodicity of the flow and the reliability of the results. The applied oil film was exposed to the flow for approximately one hour after reaching the stable operating condition.

TABLE 1: Blading parameters and operating conditions.

Blading parameters				
	HP vane	HP blade	TMTF	LP blade
Vane/ blade no.	24	36	16	72
h/c_{ax}	1.15	1.37	0.53	2.94
Re(10^{-6})	2.38	1.1	1.86	0.46
Tip gap	-	unshrouded	-	shrouded
Operating conditions				
		HP stage		LP stage
$n_{r,in}$ $[rpm/\sqrt{K}]$		524.4		195.3
$m_{r,in}$ $[kg/s \cdot \sqrt{K}/(bar)]$		81.2		214.6
Stage p_t ratio		3		1.3
Power [kW]		1710		340

Numerical setup

A steady-state numerical investigation was performed on the LP stage. The computational domain is shown in Figure 2. A mixing plane was placed between the LP vanes (stationary domain) and the LP rotor (rotating domain).

The measured field in Plane C (one HP vane pitch, 15 deg) was used as inlet boundary condition for the numerical simulation. Further, in order to gain the full HP vane - LP vane periodicity (45 deg), the plane was replicated and translated three times. The outlet boundary for the numerical investigation was placed at an axial distance of $(x_{out} - x_{LProtor_{TE}})/C_{LProtor} = 6$ downstream of the LP rotor trailing edge. At this coordinate static pressure taps within the facility measure the static pressure of the outflow.

The mesh generated for the numerical investigation consists of 2.5 million nodes with a y^+ which was kept lower than 1 next to the blade surface and lower than 2 next to the endwalls. A grid independence study was done as assumption for the numerical investigation. A commercial CFD code (Ansys CFX©v12.1) was used as solver. The code solves the Navier Stokes equation system with first order accuracy in areas where the gradients change sharply to prevent overshoots and undershoots and maintain robustness, and second order

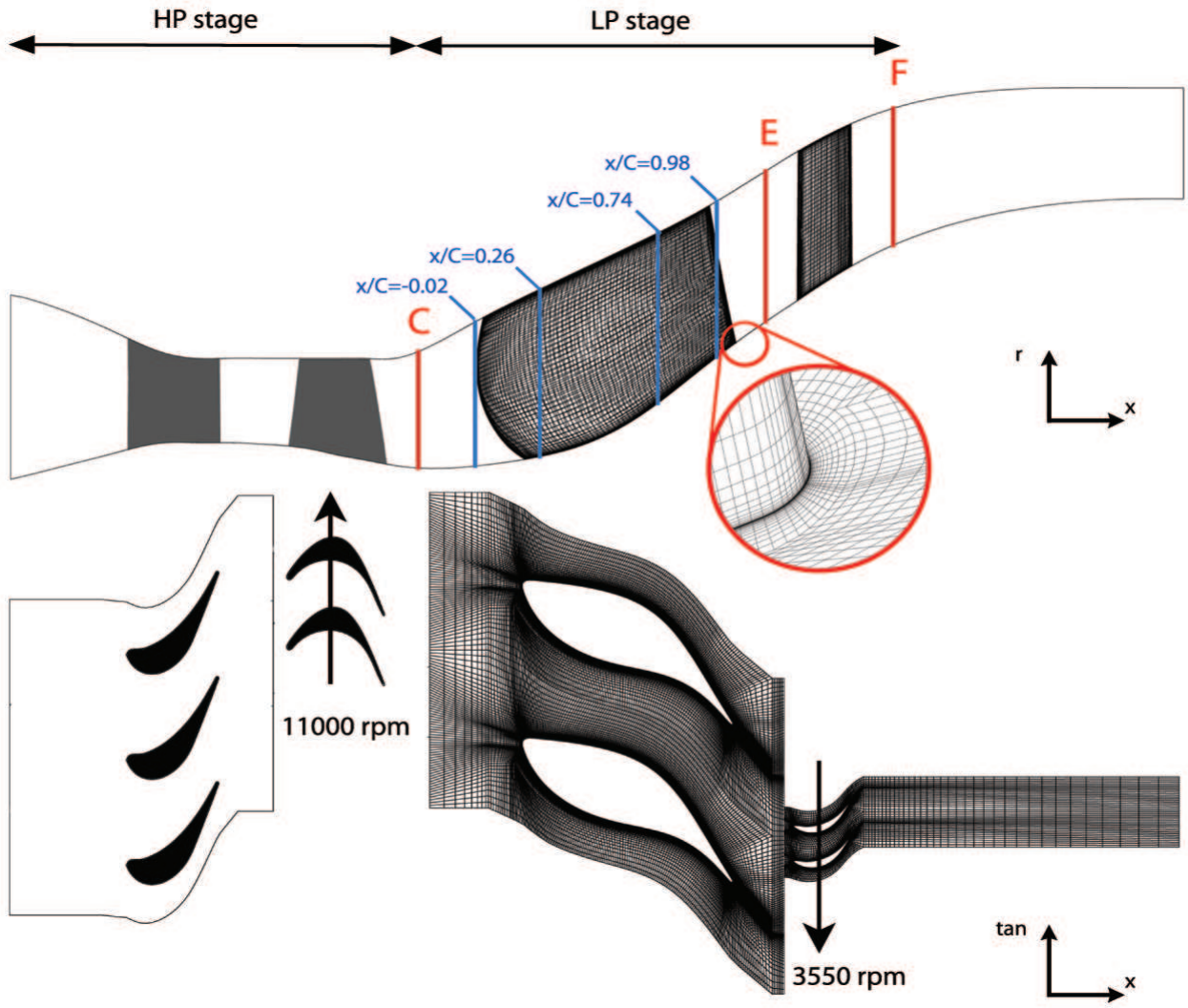

FIGURE 2: Two stage - two spool facility at the ITTM and computational domain

in flow regions with low variable gradients to enhance accuracy [18]. The turbulence was modeled using a k-ω SST turbulence model (Menter [19]).

RESULTS AND DISCUSSION

For a clear understanding of the flow evolution within the LP vane channel, it is necessary to provide the reader a description of the features of the incoming flow. Therefore, in the first part of this section, the results from five hole probe measurements in Plane C will be presented and discussed. The explanation of the flow evolution through the TMTF will is carried out by means of planes extracted at fixed axial coordinates, pressure distributions on the strut surface (measured data will be used to validate the CFD results) and flow visualization performed by oil techniques. A description of the measured and computed flow field downstream of the TMTF (plane E) will conclude this section.

LP stage inlet flow

The upstream turbine is a low aspect ratio stage with an unshrouded rotor, therefore secondary flows are predominant in the stator-rotor interaction [20, 21].

Figure 3 shows the time-averaged measurements of the non-dimensional total pressure (Cp_T) and the yaw angle (α) downstream of the HP stage. On the left side contour plots of the total pressure and of the yaw angle are shown, while, on the right side, their mass-average distribution is depicted. The spanwise location is plotted in terms of radial coordinate normalized with the channel height (r/H). The total pressure is shown in terms of Cp_T which was defined as follows:

$$Cp_T = \frac{p_T - \bar{p}_{T,C}}{\bar{p}_{T,C} - \bar{p}_C} \tag{1}$$

Due to the tip clearance of the shroudless HP turbine less energy is extracted close to the casing. This leads to a tip-leakage flow located at $r/H > 0.9$, which induces higher total pressure (higher Cp_T) and a less turned flow at the casing. The maximum variation of the yaw angle distribution over the channel height is of about 42 deg, therefore the downstream TMTF will require a 3D vane design to optimize the incidence over the full span.

In such turbines, the main flow features which dominate

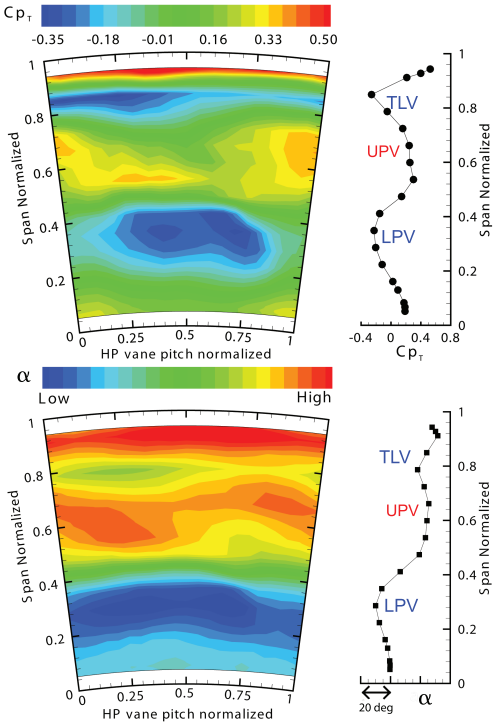

FIGURE 3: Plane C - Total pressure and yaw angle distribution at TMTF inlet plane (view from downstream)

the downstream time-resolved flow field are secondary flows. Since these structures generate total pressure losses and induce changes in the mean flow angle, looking at the charts in Fig. 3, they can be identified with a spanwise trend variation of yaw angle and total pressure. Therefore, it is possible to locate the consequences of the rotor tip leakage vortex at $r/H = 0.8$ (TLV), of the rotor upper passage vortex at $r/H = 0.65$ (UPV) and of the rotor lower passage vortex at $r/H = 0.3$ (LPV) (co-rotating with the TLV [22, 23]). Any visible circumferential variation of these features in the contour plots derives then from the stator-rotor interaction between the HP vanes and the HP rotor.

In a conventional axial turbine, the spanwise distribution of the discharged flow is characterized by the influence of a radial equilibrium gradient induced by the swirl effect, which pushes the flow field towards the hub. In the investigated case the presence of the downstream bend of the channel plays a major role: a pressure gradient is generated from the hub to the shroud (counter acting the swirl effect). In this plane the flow is pushed towards the casing where higher flow velocities, higher Mach number and higher total pressure levels can be observed.

Flow within the channel

The blade loading distribution at three different span positions ($r/H = 0.25$, $r/H = 0.50$, $r/H = 0.75$) is shown in Fig. 4. The static pressure is plotted in terms of a non-dimensional coefficient:

$$Cp = \frac{p - \bar{p}_C}{\bar{p}_{T,C} - \bar{p}_C} \tag{2}$$

The agreement between measured and computed data appears generally good enough to correctly predict the trend in the spanwise distribution. The experimental distribution was already presented and discussed by Santner et al. [15,24] and Paradiso et al. [16]. The vane was found facing negative incidence in the lower half of the channel, zero-incidence at midspan and positive incidence in the upper part of the channel.

For a better understanding of the flow evolution it is important to identify the main sources of the pressure gradients acting on the fluid, which can be listed as follows:

1. the first bend of the meridional path (upstream of the LP vane) generates a pressure distribution which pushes the flow towards the casing;
2. the deflection imposed to a flow in annular configuration generates a suction-to-pressure side gradient and a radial pressure gradient. The latter pushes the fluid towards the hub endwall and its entity will increase with the increasing turning induced by the strut (swirl effect);
3. the second bend of the meridional flow path located downstream of the TMTF path induces a pressure gradient that pushes the flow towards the hub;
4. the 3D design of the vane also influences the spanwise pressure gradients as extensively studied in literature [25–27].

In the previous section the main structures downstream of the high pressure rotor have been identified. Figure 5 shows the time-mean streamwise vorticity, pressure distributions and total pressure losses at four planes at fixed axial positions. The non dimensional coordinate x/C refers to the vane axial chord at midspan section. The positions of these planes in the machine are visualized in Fig. 2.

In this paper an approach similar to the one applied by Miller et al. [10] and Hu et al. [28] was chosen, where the streamwise vorticity is used to explain the evolution of the secondary flows. This is defined as follows:

$$\omega_{SW} = \frac{v_x \cdot \omega_x + v_y \cdot \omega_y + v_z \cdot \omega_z}{v} \tag{3}$$

Total pressure losses are computed as:

$$\zeta = \frac{\bar{p}_{T,C} - p_T}{\bar{p}_{T,C} - \bar{p}_C} \tag{4}$$

where $\bar{p}_{T,C}$ represents the mass-weighted total pressure on Plane C upstream of the strut. In the paper the losses will be plotted normalized on the mass-weighted value at midspan of the TMTF exit plane (Plane E).

The production of streamwise vorticity is controlled by both the local unsteady radial gradient of total pressure and stretching or compression of existing vortices. This paper will not focus on the investigation of the production or destruction mechanisms, but the aim here is only to examine their net effect on secondary flow development [10].

Focusing on the vorticity map of Fig. 5 (a), the zones A, B, and C respectively can be related to the traces of the high pressure rotor LPV, TLV and UPV. They are transported and convected downstream into the vane passage. Looking at the

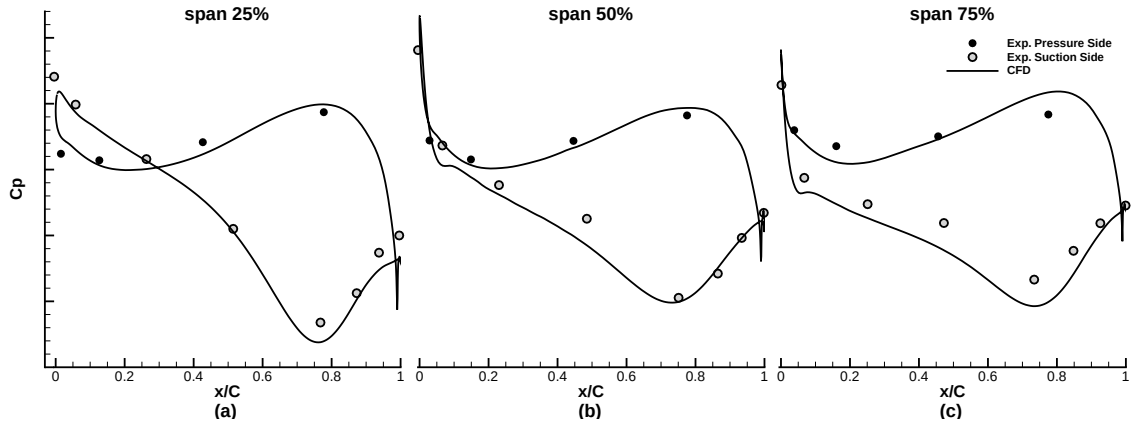

FIGURE 4: Spanwise TMTF vane loading distribution

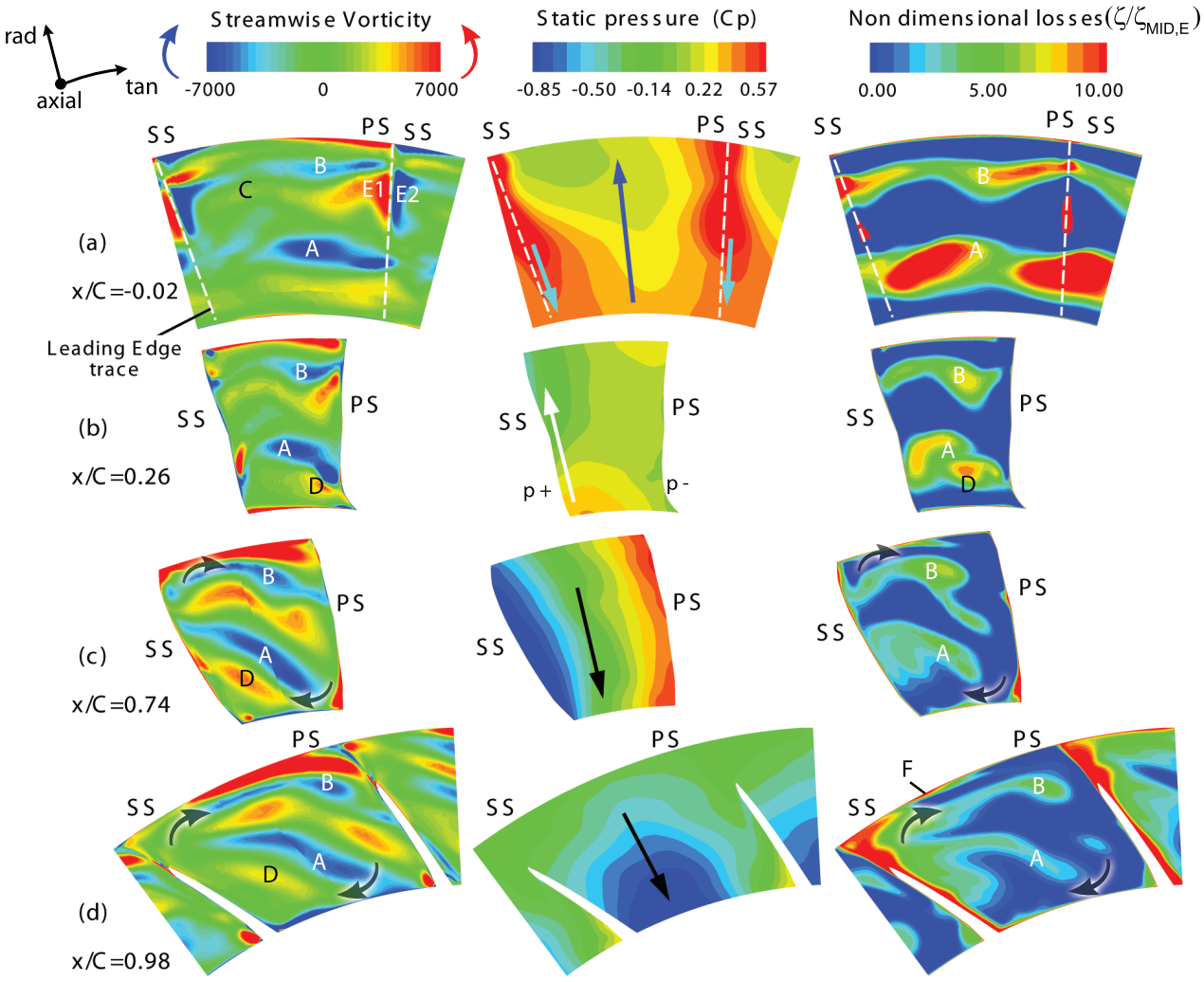

FIGURE 5: Flow evolution within the strut passage

pressure distribution, the flow in Fig. 5 (a) appears mainly subjected to a hub-to-shroud force. This is induced by the first bend of the S-shaped channel which is also responsible for accelerating the flow at the casing. Moreover, the sweep design of the leading edge induces spanwise gradients which push the flow towards the endwalls. In the lower channel the direction of this gradient is opposite to the gradient induced by the bend and, although its entity is lower, it can be still identified with

the blue arrows in Fig. 5 (a). On the other hand, the sweep

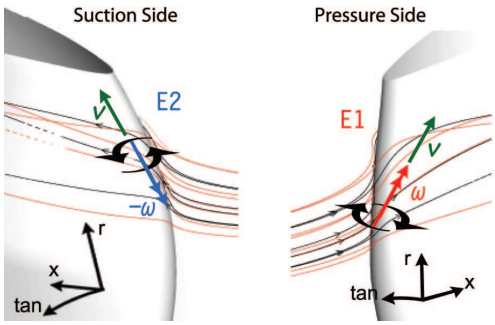

FIGURE 6: Vorticities generated by the swept strut leading edge

design plays a major role in the generation of the structures E1 and E2 on the upper part of the leading edge. Whenever the flow approaches the blade wall, a boundary layer is generated. A leading edge orthogonally-oriented vorticity is then induced; this component is then multiplied with the spanwise velocity created by the blade sweep design (see [26]). The effect is that the streamwise vorticity results increased at the leading edge of the vane as Fig. 6 helps to visualize.

The effect of the negative incidence at the hub revealed in Fig. 4 (a) is then reflected in the pressure distribution of Fig. 5 (b). On the suction side the white arrow indicates a gradient which pushes the low momentum structures towards the shroud. At the endwall the pressure-to-suction side gradient avoids any favorable condition for the development of a "traditional" lower passage vortex. Indeed, this condition favorites the generation of another structure indicated as D and counter-rotating with respect to the expected lower passage vortex. The interaction between the structures A and D produces a pressure loss core which can be visualized in the loss map. Moving towards the rear part of the vane channel, the turning struts will induce swirl in the flow. This results in two main consequences: the first is to favourite the development of the radial equilibrium gradient (black arrow in Fig. 5 (c) and (d)); the second is to enhance the vorticity of the rotating structures convected in the front part of the channel (A and B).

Figure 5 (d) shows a plane at a fixed axial position which intersects the vane because of the sweep design of the trailing edge. In this plane the highest peak of losses is generated by the boundary layers on the vane surface which are subjected to an adverse velocity gradient moving towards the trailing edge where they mix within the wake.

In particular, it is interesting to notice how the whole field in the planes at $x/C = 0.74$ and $x/C = 0.98$ is subjected to a twisting motion which evolves with the same rotational direction of the structures A and B. This vortex will be called *vane passage vortex* in order to distinguish it from a conventional hub passage vortex.

Figure 4 (c) shows that, in the upper part of the vane passage, the flow has positive incidence which leads to a circumferential pressure gradient at the casing endwall and that will favorite a cross-flow from pressure to suction side typical for a upper passage vortex. Despite this, it is now important to remark that the vane was designed with the target to minimize the generation of secondary flows by means of a complex 3D design. The structure indicated as F in the loss map of Fig. 5 (d) shows a quite confined vane upper passage vortex which is driven by the casing cross-flow and does not reach the suction side because of the aft-loaded design of the strut. Figure

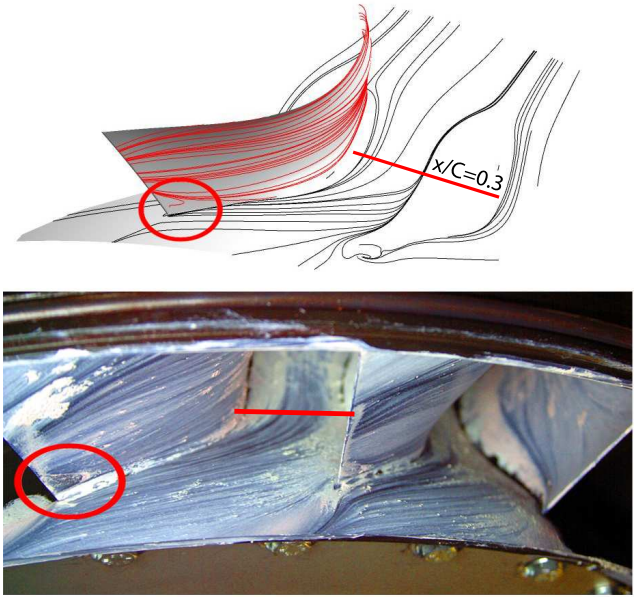

FIGURE 7: Surface streamline (top) and oil flow visualization (bottom) at suction side and hub regions

7 shows the surface streamlines plotted from the CFD and the shear stress lines from the oil flow visualizations at the suction side and at the hub. The cross flow at the endwall starts to develop after about $x/C = 0.3$. This picture clarifies that there is no "traditional" passage vortex (which would be generated immediatly downstream of the leading edge). Indeed, the structures coming from upstream are convected and subjected to the swirl by the turning of the vane.

The same figure shows also a corner separation at the trailing edge (red circle), which derives from the design intent to test the capability of the CFD to predict it in a turning strut without fillet which operates at its loading limits (Santner et al. [15]).

TMTF exit flow

Figure 8 shows a comparison between five-hole probe measurements and numerical data on Plane E which is located at $x/C = 1.28$. On the left side, contour plots of Mach number, static pressure and total pressure losses are shown, while (on the right side) their spanwise mass-weighted distribution is reported. The Mach number is normalized on its mass-weighted value at midspan.

The contour plots as well as the mass-weighted distributions show a good agreement between the two approaches on catching the main flow features. Measurements were performed along two complete vane pitches (45 degrees) in order

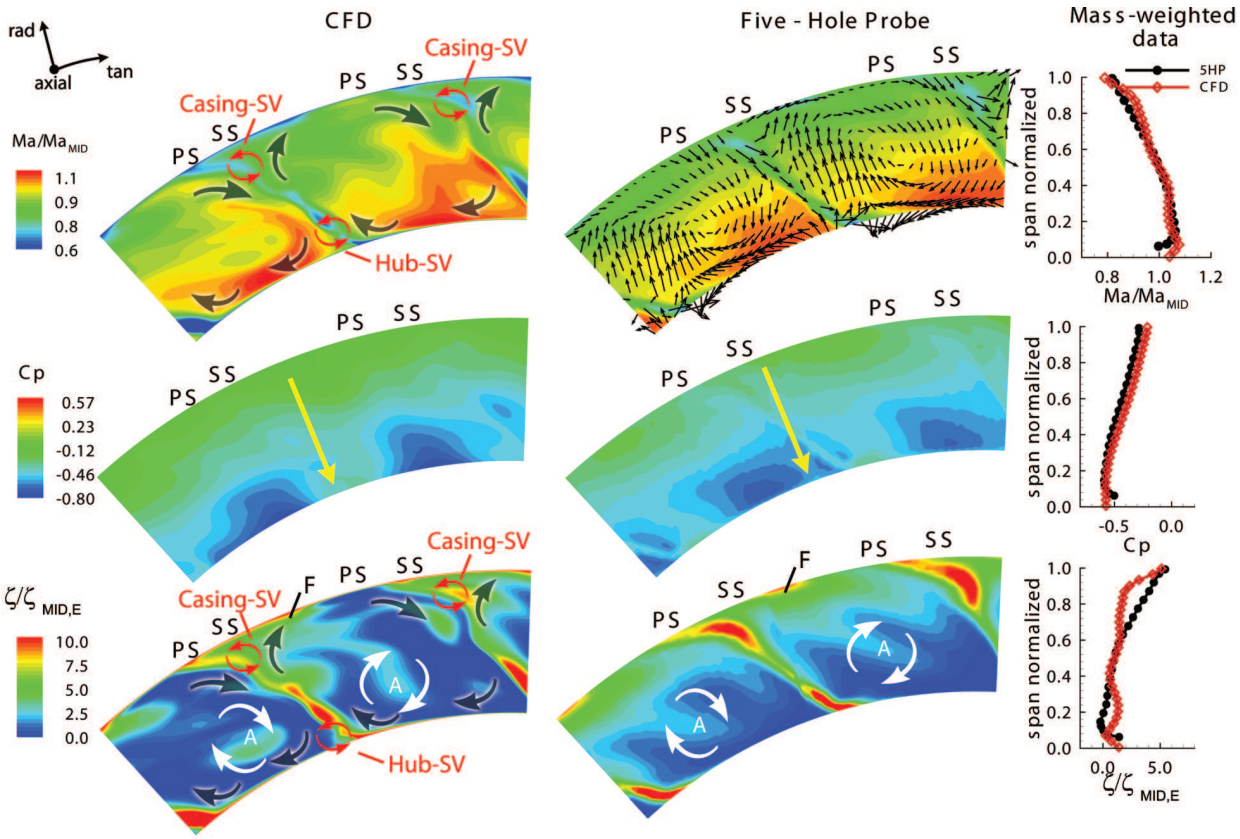

FIGURE 8: Plane E - TMTF exit flow at $x/C = 1.28$: contour plots of Mach number, static pressure and total pressure losses

to get the full HP vane - LP vane periodicity. For the same reason two strut pitches have been simulated (the time-mean flow at the HP stage exit plane has 15 degrees periodicity, while one LP vane pitch is 22.5 degrees).

The flow leaving the TMTF is subjected to a radial hub-to-shroud force that pushes the field towards the hub (yellow arrow in Fig. 8). The pressure distribution induced on the channel by the second bend will enhance this force, while the component related to the swirl effect (which is still the predominant contribution) will decrease proceeding downstream of the vane passage. In fact, in this section of the machine the flow is unguided and is moving towards larger radii: the swirl effect will become weaker following the momentum conservation law ($v_t \cdot r = const$).

The main visible structures in this plane are the large wakes generated by the struts: these regions of low momentum induce on one side high losses and on the other side a periodic discontinuity in the circumferential flow angle and pressure distribution which will influence the aeroelastic response of the downstream rotor.

Looking at the Mach number distribution of Fig. 8, the mean flow in both radial and tangential direction is characterized by high velocity gradients: the radial gradients of velocity are due to the diffusing channel and the endwall boundary layers, while the gradients in the circumferential direction are due to the turning of the flow induced by the struts. The velocity vectors superimposed to the experimental Mach number distribution are defined as the difference between the local velocity vector and a reference flow direction (see for example Chaluvadi et al. [29] and Persico et al. [30]). In the present case the reference flow vector has been determined subtracting from the local values the averages of the circumferential and radial velocity components in radial and circumferential directions respectively. This procedure is necessary because of the very high velocity gradients that characterize the mean flow in both directions. They reveal the presence of the vane passage vortex [17, 24] extending over the full channel height. The same vortex is indicated in the CFD map by means of black arrows.

The effect of the HP rotor can be still visualized in structure A in Fig. 8 which is a representative trace of the lower passage vortex. This vortex is co-rotating with the vane passage vortex. The reader should be aware that the CFD was set as steady-state simulation and should not think to this feature in terms of net influence on the flow field since, in reality, the structure propagation will be triggered by the unsteady field of the upstream rotor.

The vane upper passage vortex (structure F) can be observed, also in this view, still confined at the casing endwall.

Further remarkable structures on this plane consist of two vortices indicated as SV in Fig. 8. These are shed vortices resulting from the interaction between two passage vortices generated within the vane channel and convected downstream of the strut trailing edge. Figure 9 tries to clarify this mechanism which leads to a non conventional casing shed vortex counter-rotating with respect to a “traditional” upper shed vortex. These low momentum structures induce two loss cores visible on the losses map in the wakes upper and lower ends. Moreover, looking at the spanwise mass-weighted distribution,

it is interesting to see that the CFD underestimates the losses in the region concerning the casing shed vortex and overestimates them where the hub shed vortex is expected to occur.

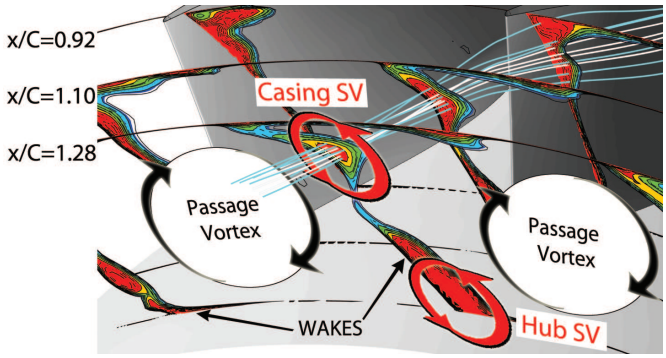

FIGURE 9: Evolution of total pressure losses at the vane trailing edge and schematic representation of the generated vortices

CONCLUSIONS

The paper described the time-mean flow evolution through a turning mid turbine frame by means of five-hole probe measurements, oil flow visualization and steady-state CFD results. Numerical and experimental data showed a good agreement on catching the main flow features. The typical flow field at the exit of the HP stage mainly appears altered by the effect of the first bend of the meridional channel.

The results show that the main flow structures coming from the upstream stage are convected and transported to the inlet of the downstream turbine instead of decaying like in a co-rotating-rotors setup. Moreover, while the upper part of the TMTF channel shows a confined vane upper passage vortex, no "traditional" passage vortex is created in the lower part of the channel. Indeed, the swirl induced by the turning struts leads to a large vortex which, taking into consideration the aft-loaded design of the vane, develops later on in the passage and extends over the full channel height.

The radial distribution of the time-mean flow at the LP rotor inlet plane (TMTF exit plane) is subjected to the pressure gradient induced by the swirled flow as well as by the presence of the second bend of the meridional flow path. Higher velocities and lower pressures are located in the lower region of the channel generating a force which pushes the flow towards the hub endwall. The main structures observed in the LP rotor inlet plane are the wakes of the strut, the passage vortex generated by the TMTF and two intense shed vortices resulting from the interaction between two adjacent vane passage vortices. Moreover, a clear trace of the HP rotor lower passage vortex was found in this plane.

The outcome is that a TMTF placed between two counter-rotating turbines will convect and enforce the vorticities coming from the upstream turbine within the vane passage. This leads to a higher level of complexity of the LP turbine design due to an increased non-uniformity of the rotor inlet flow field as well as the consequent rotor-rotor interaction.

The aerodynamic designer who faces a similar situation should be aware of these problematics and work on solutions which would limit the development of secondary flows generated within the TMTF (i.e. 3D blade design, endwall contouring, etc.) or on the application of embedded design (i.e. splitter vanes within the channel).

ACKNOWLEDGMENT

The authors would like to thank Hermann P. Pirker, Josef Hubinka and Berardo Paradiso (currently affiliated at Politecnico di Milano) for the important support during the experimental campaign. This work was financed by the European Union within the EU-project DREAM (contract No. ACP7-GA-2008-211861) in which the LP stage was designed, manufactured and operated.

REFERENCES

[1] Dominy, R. G., and Kirkham, D. A., 1996. "The influence of blade wakes on the performance of inter-turbine diffusers". *ASME Journal of Turbomachinery,* ***118***, January, pp. 347–352.

[2] Pullan, G., Denton, J., and Dunkley, M., 2003. "An experimental and computational study of the formation of a streamwise shed vortex in a turbine stage". *ASME Journal of Turbomachinery,* ***125***, April, pp. 291–297.

[3] Miller, R. J., Moss, R. W., Ainsworth, R. W., and Harvey, N. W., 2003. "The development of turbine exit flow in a swan-necked inter-stage diffuser". In Proceedings of ASME Turbo Expo 2003, June 16-19, Atlanta, Georgia, USA, ASME Paper No. GT-2003-38174.

[4] Davis, R. L., Yao, J., Clark, J. P., Stetson, G., Alonso, J. J., Jameson, A., Haldeman, C. W., and Dunn, M. G., 2002. "Unsteady interaction between a transonic turbine stage and downstream components". In Proceedings of ASME Turbo Expo 2012, June 3–6, Amsterdam ,The Netherlands, ASME Paper No. GT-2002-30364.

[5] Lavagnoli, S., Yasa, T., Paniagua, G., Duni, S., and Castillon, L. "Aerodynamic analysis of an innovative low pressure vane placed in a s-shape duct". *ASME Journal of Turbomachinery,* ***134***.

[6] Axelsson, L. U., 2009. "Experimental investigation of the flow field in an aggressive intermediate turbine duct". Phd thesis, Department of Applied Mechanics of Chalmers University of Technology. ISBN0:978-91-7385-264-7.

[7] Marn, A., 2008. "On the aerodynamics of aggressive intermediate turbine ducts for competitive and environmentally friendly jet engines". Phd thesis, Institute for Thermal Turbomachinery and Machine Dynamics of Graz University of Technology. ISBN0:978-91-7385-264-7.

[8] Göttlich, E., 2011. "Research on the aerodynamics of intermediate turbine diffusers". *Progress in Aerospace Sciences,* ***47***, pp. 249–279.

[9] Dominy, R. G., Kirkham, D. A., and Smith, A. D., 1998. "Flow development through inter-turbine diffusers". *ASME Journal of Turbomachinery,* ***120***, January, pp. 298–304.

[10] Miller, R. J., Moss, R. W., Ainsworth, R. W., and Harvey,

N. W., 2004. “The effect of an upstream turbine on a low-aspect ratio vane”. In Proceedings of ASME Turbo Expo 2004, June 14-17, Vienna, Austria, ASME Paper No. GT-2004-54017.

[11] Marn, A., Göttlich, E., Cadrecha, D., and Pirker, H. P., 2009. “Shorten the intermediate turbine duct length by applying an integrated concept”. *ASME Journal of Turbomachinery,* ***131***, p. 041014 (10 pages).

[12] Erhard, J., and Gehrer, A., 2000. “Design and construction of a transonic test turbine facility”. In Proceedings of ASME Turbo Expo 2000, May 8–11, Munich, Germany, GT-48.

[13] Hubinka, J., Paradiso, B., Santner, C., Pirker, H. P., and Göttlich, E., 2011. “Design and operation of a two spool high pressure test turbine facility”. In Proceeding of the 9th ETC conference, Instambul, Turkey, pp 1531-1540.

[14] Hubinka, J., Santner, C., Paradiso, B., Malzacher, F., and Göttlich, E., 2009. “Design and construction of a two shaft test turbine for investigation of mid turbine frame flows”. In Proceedings of ISABE 2009, Montreal, Quebec, Canada, ASME Paper No. ISABE-2009-1293.

[15] Santner, C., Paradiso, B., Malzacher, F., Hoeger, M., Hubinka, J., and Göttlich, E., 2011. “Evolution of the flow through a turning mid turbine frame applied between a transonic hp turbine stage and a counter-rotating lp turbine”. In Proceedings of 9^{th} European Turbomachinery Conference, March 21-25, Istanbul, Turkey, Paper No. 110.

[16] Paradiso, B., Santner, C., Hubinka, J., and Göttlich, E., 2011. “Turning mid turbine frame behaviour for different hp turbine outflow conditions”. In Proceedings of ASME Turbo Expo 2011, June 6-10, Vancouver, British Columbia, Canada, ASME Paper No. GT-2011-46502.

[17] Lengani, D., Selic, T., Spataro, R., Marn, A., and Göttlich, E., 2012. “Analysis of the unsteady flow field in the turbines by means of modal decomposition”. In Proceedings of ASME Turbo Expo 2012, June 11–15, Copenhagen, Denmark, ASME Paper No. GT-GT2012-68582.

[18] ANSYS, ed., 2010. *ANSYS CFX-Solver Modeling Guide*. ANSYS.

[19] Menter, F. R., 1994. “Two-equation eddy-viscosity turbulence models for engineering applications”. *AIAA Journal,* ***32***(8), pp. 1598–1605.

[20] Dénos, R., and Paniagua, G., eds., 2005. *Effects of Aerodynamic Unsteadiness in Axial Turbomachines*. VKI Lecture Series, LS 2005-03.

[21] Persico, G., Mora, A., Gaetani, P., and Savini, M., 2010. “Unsteady aerodynamics of a low aspect ratio turbine stage: modelling issues and flow physics”. In Proceedings of ASME Turbo Expo 2010, June 14–18, Glasgow, UK, ASME Paper No. GT2010-22927.

[22] Miller, R. J., Moss, R. W., Ainsworth, R. W., and Horwood, C. K., 2003. “Time-resolved vane-rotor interaction in a high-pressure turbine stage”. *ASME Journal of Turbomachinery,* ***125***, January, pp. 1–13.

[23] Gaetani, P., Persico, G., Dossena, V., and Osnaghi, C., 2007. “Investigation of the flow field in a high-pressure turbine stage for two stator-rotor axial gaps-part 2: Unsteady flow field”. *ASME Journal of Turbomachinery,* ***129***, July, pp. 580–590.

[24] Santner, C., Göttlich, E., Wallin, F., and Hoeger, M., 2011. “Experimental investigation of turning mid turbine frame designs”. In Proceedings of ISABE 2011, September 12-16, Gothenburg, Sweden, ISABE Paper No. ISABE-2011-1710.

[25] Pullan, G., and Harvey, N. W., 2008. “The influence of sweep on axial flow turbine aerodynamics in the endwall region”. *ASME Journal of Turbomachinery,* ***130***, pp. 041011–1 (10 Pages).

[26] Spataro, R., D’Ippolito, G., and Dossena, V., 2011. “The influence of blade sweep tecnique in linear cascade configuration”. In Proceedings of ASME Turbo Expo 2011, June 6-10, Vancouver, British Columbia, Canada, ASME Paper No. GT-2011-45728.

[27] D’Ippolito, G., Dossena, V., and Mora, A., 2011. “The influence of blade lean on straight and annular turbine cascade flow field”. *ASME Journal of Turbomachinery,* ***133***, pp. 011013–1 (9 pages).

[28] Hu, S., Zhang, Y., Zhang, X. F., and Vlasic, E., 2011. “Influences of inlet swirl distribution on an inter-turbine duct part 1: casing swirl variation”. In Proceedings of ASME Turbo Expo 2011, June 6-10, Vancouver, British Columbia, Canada, ASME Paper No. GT-2011-45554.

[29] Chaluvadi, V. S. P., I.Kalfas, A., Banieghbal, M. R., Hodson, H. P., and Denton, J. D. “An experimental study of the unsteady characteristics of the turbulent wake of a turbine blade”. *AIAA Journal of Propulsion and Power,* ***17***.

[30] Persico, G., Gaetani, P., Dossena, V., D’Ippolito, G., and Osnaghi, C., 2009. “Design and analysis of new concept fast-response pressure probes”. *I MECH E Journal of Power and Energy,* ***223***, pp. 667–676.

A NUMERICAL COMPARISON ON THE AERODYNAMIC PERFORMANCE OF A TWO-STAGE TWO-SPOOL TURBINE FACILITY PREDICTED BY STEADY AND UNSTEADY SIMULATIONS

Rosario Spataro, Emil Göttlich, Cornelia Santner, Franz Heitmeir

Institute for Thermal Turbomachinery and Machine Dynamics
Graz University of Technology, Graz, Austria, A-8010
Email: rosario.spataro@tugraz.at

ABSTRACT

The paper discusses the time-averaged and the time-resolved flow in a two-stage two-spool test rig located at the Institute for Thermal Turbomachinery and Machine Dynamics (ITTM) of Graz University of Technology. The facility consists of a transonic turbine stage followed by a counter-rotating subsonic low pressure turbine. The rig was designed and operated within the EU-project DREAM, where the target was to built up a machine able to investigate the aerodynamics of interturbine S-shaped channels. An optimized design of this component represents a critical goal for the performances of modern and future jet engines.

The turbine design techniques are nowadays still carried out by optimizations based on steady-state simulations: nevertheless since a long time it is well known how the engine performances are strongly dependent by the unsteady effects. The use of interfaces such as mixing plane or frozen rotor cuts off the real interactions between successive blade rows so that pressure losses and aeroacoustic effects are consequently estimated incorrectly. Such considerations are important for the designer who has to face a highly three dimensional unsteady flow like in a transonic turbine stage.

Therefore, the aim of the present paper is to provide a quantitative comparison in terms of performance estimation error whenever a numerical simulation is undertaken in order to catch the time-mean or the time-resolved flow.

This paper used data part of the EU-project DREAM (ValiDation of Radical Engine Architecture SysteMs, contract No. ACP7-GA-2008-211861).

NOMENCLATURE

C	low pressure vane axial chord	$n_{r,in}$	Reduced rotational speed, stage inlet
Cp_T	total pressure coefficient	p_T	total pressure
Cp	static pressure coefficient	p	static pressure
H	channel height	r	radial coordinate
HP	High Pressure	$TMTF$	Turning Mid Turbine Frame
LP	Low Pressure	v	velocity
$m_{r,in}$	Reduced mass flow, stage inlet	v_t	tangential velocity
Ma	Mach number	x	axial coordinate
α	Yaw angle (from meridional dir.)	η	efficiency

INTRODUCTION

Modern civil jet-engine companies have to face ambitious targets in terms of size and weight reduction. Therefore, over the last years, a lot of research work was put in getting beyond the standards of state-of-the-art propulsion systems.

In large engines, whenever it is required to maximize the pressure ratio at a fixed number of stages keeping adequate rotational speeds, a conventional solution is to set up the system in multi-shaft configuration (up to 3 shafts in Rolls Royce TRENT engines family). In particular, counter-rotating spools can be used to compensate the gyroscopic effect of the rotating masses as well as to minimize the aerodynamic losses in the intermediate stage (i.e. General Electric GEnx, Rolls Royce TRENT 1000, Pratt & Whitney PW1500).

In order to increase the engine bypass-ratio and, therefore, the propulsion efficiency, the fan front section has to be enlarged. This is limited by structural and acoustic limits on the fan tip velocity. At the same time, the HP-shaft rotational speed should be increased whenever a higher cycle maximum pressure is required.

The resulting larger difference in the shafts rotational speeds leads to an increasing difference in the components diameters (compressors and turbines). Therefore, focusing on the turbine, the resulting S-shaped design of the diffuser between the HP and LP turbines is quite important for the optimisation of the overall engine aerodynamic performance. Such a component is also called mid turbine frame (MTF).

Since the flow in these diffusers is highly 3D and characterized by a high content of unsteadiness, it is important for the design engineer responsible for the performance estimation to be aware of how the different CFD settings influence the solution.

Conventionally, the first step in performing blade row calculation (Tucker (2011)) is represented by the use of mixing planes interfaces.

The fidelity in modeling the steady flow within the machine could be improved using a frozen rotor interface (Tucker (2011)): here, the wakes are passed to the downstream domains, but no relative wake movement is transferred. Anyway, for a good prediction of the aerodynamic efficiency or of the acoustic tonal noise, the unsteady flow should be modeled. In fact, as noted by Meneveau and Katz (2002) and Rhie et al (1995) the unsteady stresses resulting from the movement of the wakes will be typically of a similar or higher magnitude than the turbulent stresses. Starting with Adamczyk (1985), a lot of effort was put in trying to model unsteady effects.

The use of sliding planes is necessary for prediction distortion transfer, getting the acoustics tonal noise and generally having high fidelity calculations (Tucker (2011)). Here, every timestep the rotor mesh(s) slide/rotate in the tangential direction relative to the stator(s). Modeling a real machine a problem of computational effort occurs whenever $360deg$ annulus calculation is required (including all blades). On the other hand, in order to reduce the blade count per domain passage, different hypothesis (i.e. scaling the pitch keeping the same pitch-to-chord ratio) could be stated to resize the circumferential extent.

In the last years, a lot of papers were presented on the prediction of the unsteady flow field of high pressure turbines Arnone and Pacciani (1996); Dénos et al (2001); Miller et al (2003b); Gaetani et al (2007). Lavagnoli et al (2012); Yasa et al (2011) presented an aerodynamic analysis of a low pressure vane placed in an S-shape duct downstream of a transonic turbine stage. Miller et al (2003a) used the unsteady CFD to explain the flow evolution through an inter-turbine diffuser placed downstream of a HP turbine. In none of these cases an inter-turbine diffuser was modeled between two rotors.

The machine which is object of the present paper is located at the Institute for Thermal Turbomachinery (ITTM) of Graz University of Technology. The aerodynamic design was conducted by MTU Aero Engines. Details on the test turbine can be found in Erhard and Gehrer (2000); Hubinka et al (2009, 2011). In this setup turning struts are located within the inter-turbine diffuser (turning mid turbine frame, TMTF).

Santner et al (2011) presented the influence of the HP turbine secondary flows and wakes on the TMTF. Lengani et al (2012b) showed by means of a modal decomposition analysis of the unsteady flow field that in such machines rotor-rotor interaction can be observed downstream of the LP stage.

Spataro et al (2012) discussed the flow evolution through the S-shaped channel by means of a steady simulation and showed how the structures coming from the HP stage propagates through the TMTF and their influence at the LP rotor inflow.

The aim of this work is to provide a comparison between different numerical setups, whenever the highly unsteady 3D flow field of a two-Stage two-Spool transonic turbine has to be predicted by means of simulating both stages.

EXPERIMENTAL APPARATUS AND METHODOLOGY

Facility

The transonic test turbine facility is a continuously operating two-stage cold-flow open-circuit plant, which consists of a transonic HP stage and a counter-rotating LP stage (a schematic drawing is shown in Fig. 1). Detailed information on the design and construction of the original single stage facility can be found in Erhard and Gehrer (2000). For the design of the LP-stage together with the TMTF see Hubinka et al (2009) and for the operation Hubinka et al (2011).

Table 1 summarizes the main parameters for the HP stage and the LP stage (TMTF+LP rotor) and the operating condition.

Measurement techniques

The experimental investigations were conducted by means of 5 hole probes traversed in three planes: the first one located just downstream of the HP stage (Plane C in Figure 1), the second one is located downstream of the turning LP vane (Plane E in Fig. 1), while the third plane can be found downstream of the LP rotor (Plane F in Fig. 1). Moreover one of the struts was instrumented with pressure taps along three spanwise location at 25%, 50% and 75% span. In the measurements planes the probe was traversed radially over 95% of the blade height and over one HP-vane pitch (Plane C) and over one LP-vane pitch (Planes E and F). Further details about the measurements uncertainities can be found in Santner et al (2011).

Table 1: Blading parameters and operating conditions.

Blading parameters				
	HP vane	HP blade	TMTF	LP blade
Vane/ blade no.	24	36	16	72
h/c_{ax}	1.15	1.37	0.53	2.94
Re(10^{-6})	2.38	1.1	1.86	0.46
Tip gap	-	unshrouded	-	shrouded
Operating conditions				
		HP stage	LP stage	
$n_{r,in}$ $[rpm/\sqrt{K}]$		524.4	195.3	
$m_{r,in}$ $[kg/s \cdot \sqrt{K}/(bar)]$		81.2	214.6	
Stage p_t ratio		3	1.3	
Power [kW]		1710	340	

Numerical setup

In this paper several numerical simulations with different setups are compared. The domain boundaries and the interface locations are shown in Figure 1. Four steady CFD simulations (Case A, B, C and D in Table 2) are compared with an unsteady solution (Unsteady CFD in Table 3)).

The measured field at the machine inlet was used as inlet boundary condition for the numerical simulation, while the outlet boundary was placed at an axial distance of $(x_{out} - x_{LProtor_{TE}})/C_{LProtor} =$

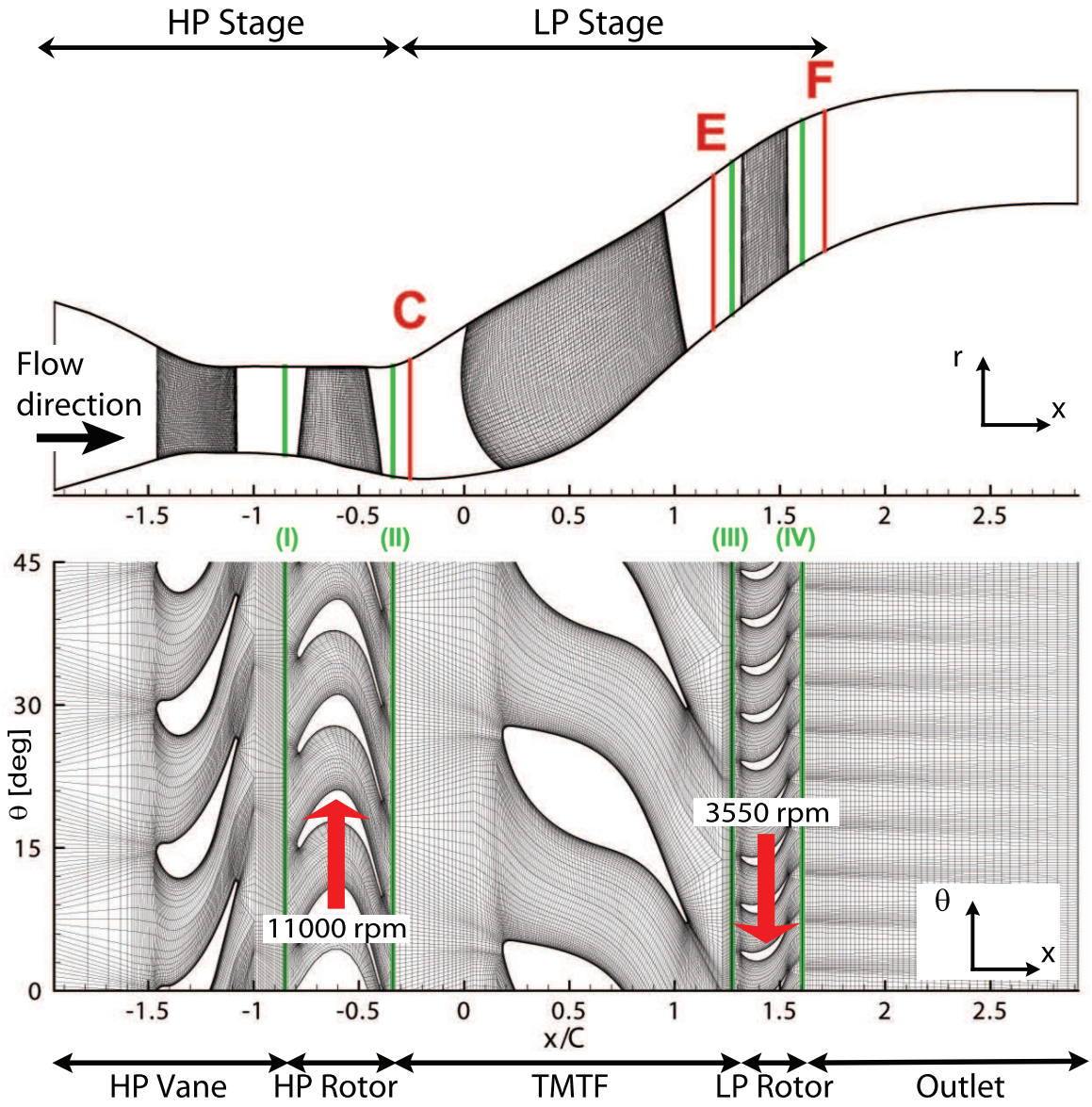

Figure 1: Two-Stage two-Spool facility at the ITTM and computational domain

6 downstream of the LP rotor trailing edge. At this coordinate static pressure taps within the facility measure the static pressure of the outflow.

The mesh was generated keeping the y^+ lower than 1 next to the blade surface and lower than 2 next to the endwalls. Details on the mesh sizes can be found in Table 2. A grid independence study was done as assumption for the numerical investigation. A commercial CFD code (Ansys CFX©v12.1) was used as solver. The code solves the Navier Stokes equation system with first order accuracy in areas where the gradients change sharply to prevent overshoots and undershoots and maintain robustness, and second order in flow regions with low variable gradients to enhance accuracy (ANSYS (2010)). The turbulence was modeled using a k-ω SST turbulence model (Menter (1994)). Before proceeding with the discussion of the results, it is important to present the differences between the setups (Table 3):

Case A In this simulation each domain consists of one blade passage mesh. The outlet domain has a pitchwise extension of 5 degrees of pitch extension (the same as the LP rotor's mesh). All interfaces (I, II, III, IV) are mixing planes.

Table 2: CFD Setups.

Mesh passage per domain and Mesh size (in million of nodes)						
	HP Vane	HP Rotor	TMTF	LP Rotor	Outlet	Tot Mesh size
Mesh size	0.67	0.39	1.03	0.23	0.06	
no. Radial points	60	60	60	60	60	
no. Blade to blade points	80	60	110	50	50	
Case A	1	1	1	1	1	2.38
Case B	1	9	4	1	1	8.59
Case C	1	1	1	1	1	2.38
Case D	1	1	1	1	1	2.38
Unsteady	6	9	4	18	18	16.87

Domain Interfaces for different numerical setups				
	(I)	(II)	(III)	(IV)
Case A	Mix pl	Mix pl	Mix pl	Mix pl
Case B	Mix pl	Frz rot	Mix pl	Frz rot
Case C	Mix pl	Mix pl	Mix pl	Frz rot
Case D	Mix pl	Mix pl	Mix pl	– (*)
Unsteady	Slide	Slide	Slide	Slide

(*) counter rotating endwalls for the downstream domain

Case B Interfaces II and IV were changed to frozen rotors. Therefore, the same periodicity is required for the HP rotor and the TMTF (90 degrees), and for the LP rotor and the outlet domain (5 degrees). Interfaces I and III were kept as mixing planes.

Case C The mesh setup for this case is the same as for Case A: interfaces I, II and III are mixing planes, while interface IV was turned to frozen rotor.

Case D For this case the mesh of the outlet domain and the one of the LP rotor were merged together removing interface IV. This leads to one rotational domain (LP rotor + Outlet) where counter rotating wall velocity was assigned to the hub and shroud endwalls in order to fix them in the absolute frame. Interfaces I, II and III are mixing planes.

Unsteady In order to simulate the time-resolved flow, an unsteady CFD was performed using sliding interfaces. Therefore it was required to satisfy the machine full periodicity computing 90 degrees for each domain. This leads to a quite heavy calculation where the mesh refinement was constrained by the server maximal memory (32 GB). The timestep was set to 1/100 of the HP rotor blade passing period ($t_s = 1.5e-6s$). The numerical scheme is time marching where the code solves second order backward equations.

RESULTS AND DISCUSSION

In this section the results from the CFD calculations are presented and compared with the experimental data. The CFD calculations were set in order to provide a guide line for engineers who face similar problems.

A first baseline configuration (Case A) is set by putting mixing planes between each domain of the setup. This is often the first choice for a steady simulation setup because of the low computational cost, and because it is thought to provide anyway a reasonable prediction even if the flow physics are not well known.

A second setup (Case B) was chosen as an alternative solution for calculating the machine performances by a steady run. Here the aim was to improve the prediction by considering the losses generated by the development of the rotors structures through the channel. Therefore two frozen rotors were placed downstream of the HP stage and of the LP rotor respectively. Such solution implies an increased computational cost due to a more extended mesh.

The third and the forth cases (Case C and D) have to be seen as two possible attempts to improve performance estimation keeping the same computational cost as Case A.

Finally, the time averaged transient data were analyzed.

A discussion is presented aimed to point out the differences between the CFD data and measurements on the machine performance evaluation. It is shown how in such a setup the prediction firstly has a significant dependency from the choice of the interface settings, and secondly evidence the importance of modeling the structures released by the rotors whenever the maximum agreement with the experiments is required.

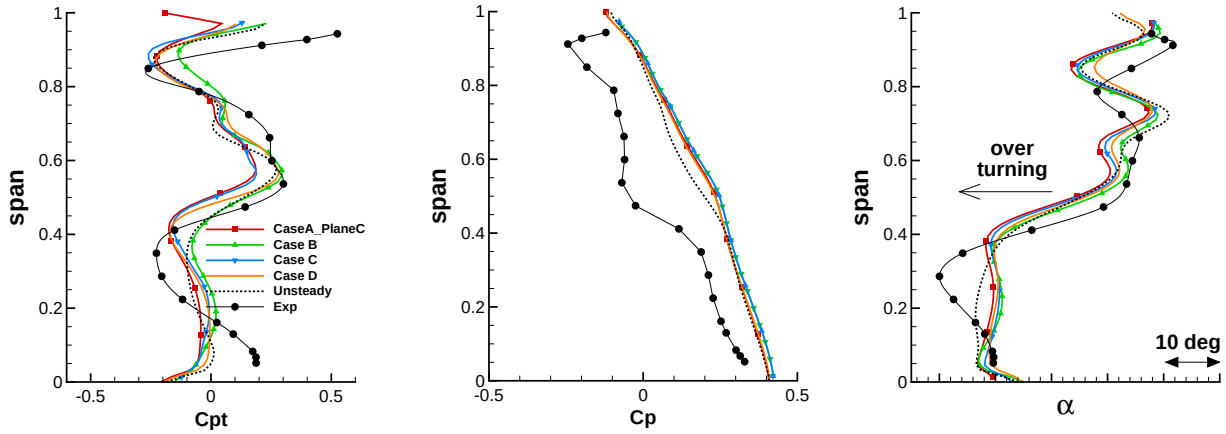

(a) Total pressure (b) Static pressure (c) Yaw angle

Figure 2: Plane C - Spanwise mass-averaged distributions at the TMTF inlet

TMTF Inflow

The upstream HP turbine is a low aspect ratio stage with an unshrouded rotor where secondary flows are predominant in the stator-rotor interaction Dénos and Paniagua (2005); Persico et al (2010).

Figure 2(a) shows a comparison of spanwise circumferentially averaged total pressure distribution between measurements (dots) and CFD cases (A, B, C, D and Unsteady).

The total pressure is plotted as total pressure coefficient Cp_T and defined as:

$$Cp_T = \frac{p_T - \bar{p}_{T,C}}{\bar{p}_{T,C} - \bar{p}_C} \tag{1}$$

where $\bar{p}_{T,C}$ and $\bar{p}_C$ are the experimental mass-weighted total pressure and static pressure in Plane C, respectively.

Figure 2(b) shows the same comparison in terms of static pressure coefficient Cp is defined as follows:

$$Cp = \frac{p - \bar{p}_C}{\bar{p}_{T,C} - \bar{p}_C} \tag{2}$$

Figure 2(c) represent the experiments-numerics comparison in terms of yaw angle (α). Experimental data show a maximum variation of the yaw angle over the channel height of about 42 deg.

The first bend of the duct induces a tip-to-hub pressure gradient (Figure 2(b)) which pushes the

low energy structures towards the shroud (wakes and passage vortices) (Figure 2(a)). For a more detailed description of the flow field of the machine in this region refer to Spataro et al (2012).

Looking at the spanwise distribution in this plane, the CFD shows a vertical shift of $r/H \approx 0.1$ in predicting the location of secondary losses. Figure 2(a) shows how problems with the simulations can be found in the lower half of the channel, where the HP stator-rotor interaction induces a loss distribution which is difficult to predict with steady solutions. Case B as well as the unsteady CFD show anyway a better agreement of the two curves in this region.

When comparing the steady solutions (Case A, B, C, D) in Figure , Case B shows an under prediction of the HP rotor tip leakage losses. Even in this case the unsteady solution shows a better agreement with the measurements. Between $r/H = 0.6$ and $r/H = 0.8$, in correspondence of the HP rotor higher passage vortex, the CFD seems over predicting the losses.

Looking at the yaw angle distribution in Figure 2(c), it is still possible to identify the vertical displacement between numerical data and measurements. Moreover, the computed HP rotor upper passage vortex is also overestimating the flow underturning between $r/H = 0.6$ and $r/H = 0.8$, while at the lower channel half the CFD underestimates the spanwise changes in flow angle. At midspan Case B (Figure 2(c)) seems to provide the best match with the experiments between the steady simulations. Looking at the shape of the curve in the lower half of the channel (where secondary vortices and stator-rotor interaction mechanism influence the distribution) the unsteady run seems to best predict the trend. This prediction problem was already observed by Wallin et al (2011) which performed numerical simulation on this machine using another setup for the TMTF.

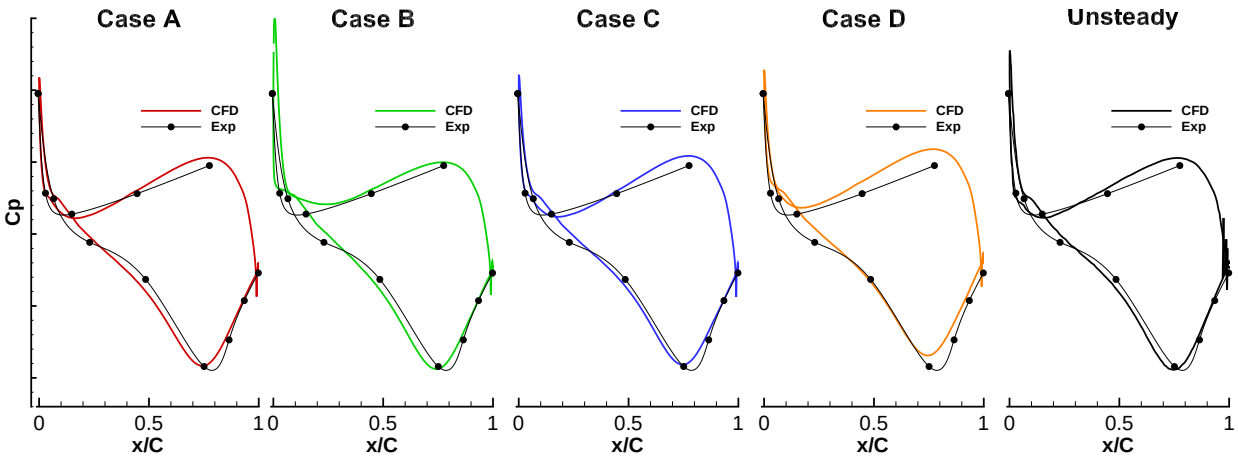

Figure 3: TMTF Blade loading at midspan

Within the TMTF passage

Moving downstream of Plane C, the flow is led towards the LP rotor by turning struts. The aerodynamics of these wide-chord vanes is quite important for the flow control within the S-shaped channel. Therefore one of these struts was instrumented with pressure taps.

Figure 3 shows the TMTF blade loading at midspan. Numerical data for each setup (A, B, C, D and Unsteady) are superimposed to the static pressure measurements. It was already observed by Santner et al (2011) that the strut at this span position faces negative flow incidence.

Case D in Figure 3 shows the worst agreement with the experimental data. The flow incidence in Case B is influenced by the frozen rotor placed between the HP rotor and the TMTF, but the dependency from the rotor-strut relative position is anyway negligible. Case B and the unsteady CFD provide the best overall prediction in terms of blade loading distribution on the vane.

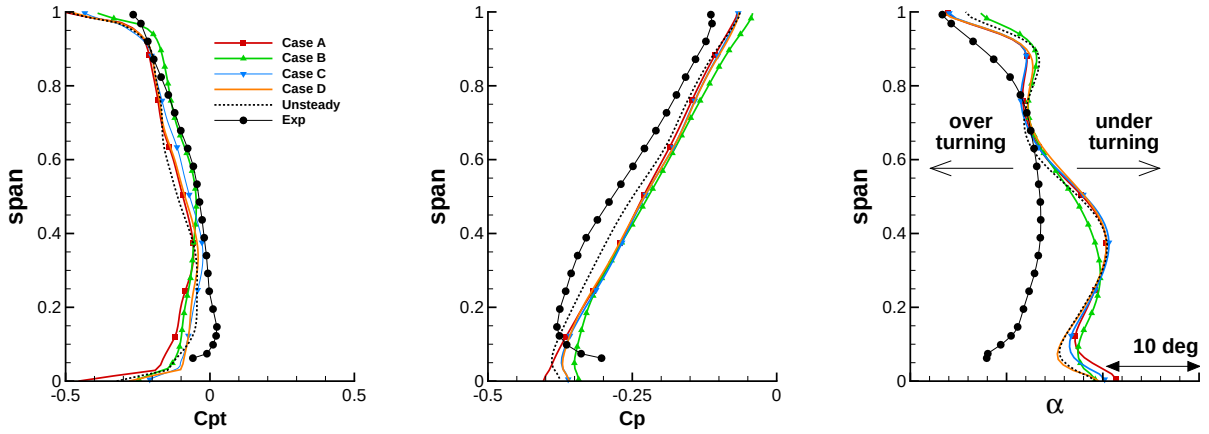

(a) Total pressure (b) Static pressure (c) Yaw angle

Figure 4: Plane E - Spanwise mass-averaged distributions at the TMTF outflow

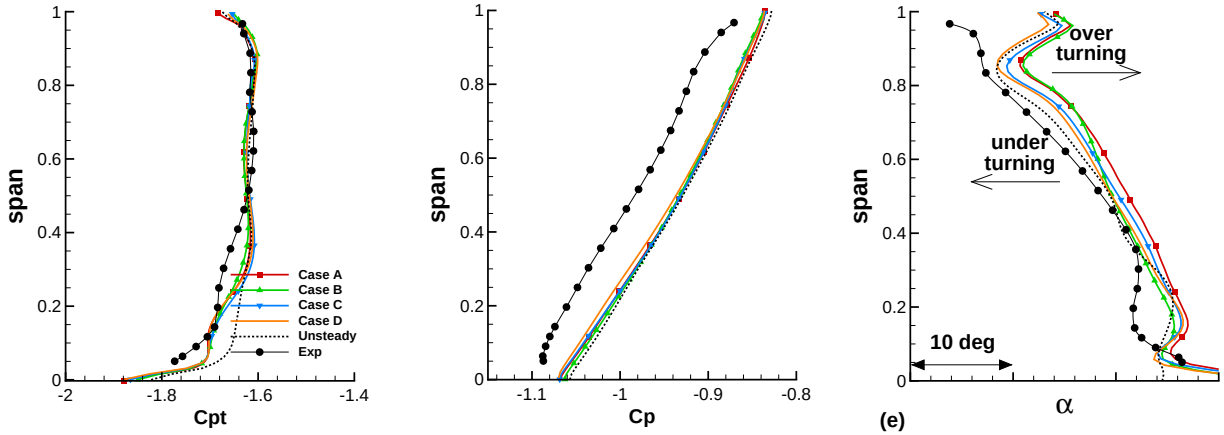

(a) Total pressure (b) Static pressure (c) Yaw angle

Figure 5: Plane F - Spanwise mass-averaged distributions downstream of the LP rotor

TMTF exit flow

In Figure 4 the mass-weighted spanwise distribution of total pressure (a), static pressure (b) and yaw angle (c) at the TMTF outlet (Plane E in Figure 1) are plotted.
The flow leaving the TMTF is subjected to a radial hub-to-shroud pressure gradient that pushes the field towards the hub (Figure 4). This gradient is generated by the swirl effect imposed by the turning strut and by the second bend of the S-shaped diffuser (Spataro et al (2012)).
Unsteady measurements (Lengani et al (2012a)) as well as a steady simulation of the second stage (Spataro et al (2012)), showed that the structures of the HP rotor are convected through the channel and can be visualized at the TMTF exit plane.

All the cases provide a good prediction in this plane in terms of total pressure (Table 3 shows an error below 1%). The static pressure in Figure 4(b) is slightly overestimated for Case B and C, while Case D shows the maximum displacement with the experimental data. The unsteady CFD provides the best overall agreement with the measurements in this plane.

The yaw angle distribution in Figure 4(c) shows no remarkable differences between the different CFD cases. Generally, the CFD appears underestimating the flow turning imposed by the struts. On the other hand, the simulations show more pronounced effects of secondary structures on the flow under and over turnings. Such differences in the yaw angle where already highlighted by Wallin et al

(2011) who presented pre- and post-test prediction results about the flow in this machine together with another TMTF setup.

LP Rotor exit flow

Moving downstream of the LP rotor, measurements were conducted in Plane F (Figure 1). Figure 5 shows the mass-weighted spanwise distribution of total pressure 5(a), static pressure 5(b) and yaw angle 5(c) in Plane F.

Figure 5(b) reveals the effect of the second bend of the S-shaped channel as well as of the LP rotor swirl on the hub-to-shroud pressure gradient responsible for pushing the low energy structures towards the hub.

Moreover, the flow in this region is characterized by a high level of unsteadiness. The perturbations due to the HP rotor in terms of velocity and flow angle are negligible in this downstream plane. Indeed, the largest fluctuations of velocity are due to the TMTF-LP rotor interaction, they occur in the wake and secondary flows of the TMTF. Large fluctuations of static and total pressure are instead due to both rotors to the same extent. Details on the flow field in this region can be found in Lengani et al (2012a,b).

Case B, C and the Unsteady solution appear to provide a very good agreement on the distributions.

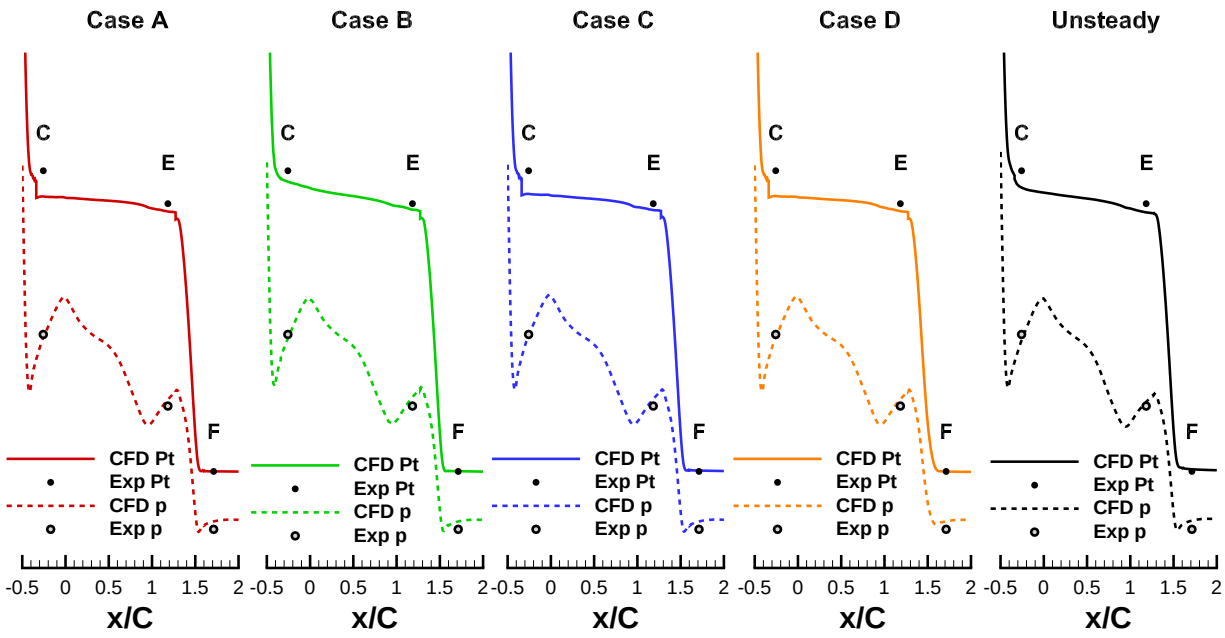

Figure 6: Streamwise total and static pressure evolution along the duct

Flow quantities distribution along the streamwise direction

In order to make a summary of this analysis and to have an idea of the streamwise loss development, Figure 6 reports the comparison between measured and the circumferentially averaged calculated data of total pressure and static pressure along the duct. It is important to notice here that the experimental data are obtained averaging over 95% of the full span, that means that the wall boundary layers are excluded from the averaging process, resulting in a slighty overestimated total pressure.

The axial coordinate x is normalized using the TMTF midspan axial chord C. Generally, the total pressure curves show two vertical drops for $x/C < -0.4$ and $x/C > 1.6$, induced by the work extracted by the rotors, while the horizontal segment $-0.4 < x/C < 1.6$ indicates the inter-turbine

diffuser. In an ideal case (inviscid flow) the total pressure would not change through the TMTF. In reality, viscous effects (i.e. wake mixing or structures propagation) take place and they will induce a slope in this curve. Therefore, the stronger is the slope, the stronger is the local loss.

Comparing the numerical predictions with the experimental data, Figure 6 shows how the trend in evolution of the total pressure is well captured by Case B and the Unsteady CFD. This is due to the use of frozen rotor (Case B) or sliding plane (Unsteady case) located at $x/C = -0.4$ (Interface II Figure 1), where the idea was to model the evolution of the HP rotor structures (tip leakage vortex, lower passage vortex,...) entering the duct. All other cases (A,C and D) show a jump at interface II (Figure 1) caused by the mixing plane. Therefore, performance prediction appears to be overestimated in those cases where the assumption of mixed out flow at the duct inlet is assumed.

The dashed lines in Figure 6 show the propagation of averaged static pressure. Looking at the axial coordinates it is possible to see how the flow recovers pressure within the clean diffusing duct, while the drop which appears between $0 < x/C < 1$ is due to the acceleration induced by the turning TMTF struts.

Table 3: Numerical performance prediction comparison

	Total pressure ($\Delta p_T\%$)			**Static pressure** ($\Delta p\%$)			**TMTF efficiency ($\Delta\eta\%$)**
	Plane C	Plane E	Plane F	Plane C	Plane E	Plane F	Plane C - Plane E
Case A	-2.05%	0.61%	0.01%	0.01%	0.50%	0.82%	8.01%
Case B	-0.93%	-0.45%	0.03%	-0.09%	0.73%	0.81%	1.91%
Case C	-1.85%	-0.49%	0.10%	0.23%	0.54%	0.81%	7.51%
Case D	-2.02%	-0.58%	-0.02%	0.05%	0.52%	0.78%	8.00%
Unsteady	-1.33%	-0.71%	0.23%	-0.54%	0.39%	0.96%	2.79%

In order to complete the comparison with a quantitative estimation of the errors, Table 3 reports the percentage difference of total pressure and static pressure for each measurement plane defined as:

$$\Delta p_T\% = \frac{\bar{p}_{T,cfd} - \bar{p}_{T,exp}}{\bar{p}_{T,exp}} \cdot 100 \tag{3}$$

$$\Delta p\% = \frac{\bar{p}_{cfd} - \bar{p}_{exp}}{\bar{p}_{exp}} \cdot 100 \tag{4}$$

Moreover, in the same table, assuming incompressible flow in the duct (since $Ma_{TMTF} < 0.6$), the error in estimating the efficiency is reported. This is defined as follows:

$$\eta = \frac{\bar{p}_{T,C} - \bar{p}_{T,E}}{\bar{p}_{T,C} - \bar{p}_{E}} \rightarrow \Delta\eta\% = \frac{\eta_{cfd} - \eta_{exp}}{\eta_{exp}} \cdot 100 \tag{5}$$

Table 3 shows how the use of mixing planes in steady simulation (Case A, C and D) leads to the bigger errors in terms of absolute total and pressure level prediction (difference between experiments and numerical prediction of the duct efficiency between 7.5% and 8.01%). The setups where the rotor structures is not assumed to be mixed out at the duct inlet show a consistent improvement for the performance evalutation: the difference in estimating the pressure level is generally below 1% and for the duct efficiency the error is limited to 1.91% and 2.79% for Case B and Unsteady CFD respectively.

CONCLUSIONS

Several numerical simulations of a two-stage two-spool transonic turbine with turning struts between the rotors were undertaken. A special focus was put on the loss development through the LP

stage. The results were compared with measurements performed in three different planes (downstream of the HP stage, at the LP rotor inflow and at the LP rotor outflow respectively) in terms of spanwise total pressure, static pressure and yaw angle distribution as well as with the strut blade loading at midspan.

A baseline case where all the interfaces were set as mixing plane (Case A) was compared with other three steady simulations set with different domain interface options (Case B, C, D). Moreover the time-averaged flow of an unsteady simulation was analysed.

The comparison of the first measuring plane (Plane C - downstream of the transonic stage) shows problems for the CFD in predicting the quantities distribution at the lower half of the channel (where the stator-rotor interaction is more critical) and at the tip leakage region. The best agreement in terms of quantities distributions in this plane is anyway reached by the unsteady computation.

The comparison at the TMTF exit flow (Plane E) shows no remarkable differences between the CFD cases in terms of yaw angle, but a still appreciable offset can be seen in the pressure distributions.

The strut blade loading at midspan is found best predicted by Case B and Unsteady CFD.

The results from this numerical comparison show that before starting a simulation aimed to predict the aerodynamic performance of a similar setup, a careful choice of the CFD settings should be conducted. In particular, a calculation set in order to minimize the computational cost (i.e. computing one passage per domain and placing mixing planes) could induce large errors in modeling the real flow field.

A comparison about the streamwise evolution of mass averaged total pressure and static pressure show that the use of interfaces which do not mix out the flow field downstream of the rotors (i.e. frozen rotor, or sliding plane) has a remarkable positive effect on the performance prediction.

A promising research for a correct prediction of unsteady effects as well as a reduction of computational costs consists in the development of numerical methods which apply chorochronic (time-space) periodicity in order to reduce the domain extensions (i.e. phase-lagged and time-inclined approaches).

ACKNOWLEDGEMENTS

The authors would like to thank H. Peter Pirker, Josef Hubinka and Berardo Paradiso (currently affiliated at Politecnico di Milano) for the important support during the experimental campaign. This work was financed by the European Union within the EU-project DREAM (contract No. ACP7-GA-2008-211861) in which the LP stage was designed, manufactured and operated.

References

Adamczyk J (1985) Model equation for simulating flows in multi stage turbomachinery. In: Proceedings of the ASME Turbo Expo 1985, ASME Paper No. 85-GT-226

ANSYS (ed) (2010) ANSYS CFX-Solver Modeling Guide. ANSYS

Arnone A, Pacciani R (1996) Rotor-stator interaction analysis using the navier-stokes equation and a multigrid method. ASME Journal of Turbomachinery 118:679–689

Dénos R, Paniagua G (eds) (2005) Effects of Aerodynamic Unsteadiness in Axial Turbomachines. VKI Lecture Series, LS 2005-03

Dénos R, Arts T, Paniagua G, Michelassi V, Martelli F (2001) Investigation of the unsteady rotor aerodynamics in a transonic turbine stage. ASME Journal of Turbomachinery 123:81–89

Erhard J, Gehrer A (2000) Design and construction of a transonic test turbine facility. In: Proceedings of ASME Turbo Expo 2000, May 8-11, Munich, Germany, GT-48

Gaetani P, Persico G, Dossena V, Osnaghi C (2007) Investigation of the flow field in a high-pressure turbine stage for two stator-rotor axial gaps-part 2: Unsteady flow field. ASME Journal of Turbomachinery 129:580–590

Hubinka J, Santner C, Paradiso B, Malzacher F, Göttlich E (2009) Design and construction of a two shaft test turbine for investigation of mid turbine frame flows. In: Proceedings of ISABE 2009, Montreal, Quebec, Canada, ASME Paper No. ISABE-2009-1293

Hubinka J, Paradiso B, Santner C, Pirker HP, Göttlich E (2011) Design and operation of a two spool high pressure test turbine facility. In: Proceeding of the 9th ETC conference, Instambul, Turkey, pp 1531-1540

Lavagnoli S, Yasa T, Paniagua G, Duni S, Castillon L (2012) Aerodynamic analysis of an innovative low pressure vane placed in a s-shape duct. ASME Journal of Turbomachinery 134(2):011,013 (13 pages)

Lengani D, Santner T, Spataro R, Paradiso B, Göttlich E (2012a) Experimental investigation of the unsteady flow field downstream of a counter-rotating two-spool turbine rig. In: Proceedings of ASME Turbo Expo 2012, June 11-15, Copenhagen, Denmark, ASME Paper No. GT-GT2012-68583

Lengani D, Selic T, Spataro R, Marn A, Göttlich E (2012b) Analysis of the unsteady flow field in the turbines by means of modal decomposition. In: Proceedings of ASME Turbo Expo 2012, June 11-15, Copenhagen, Denmark, ASME Paper No. GT-GT2012-68582

Meneveau C, Katz J (2002) A deterministic stress model for rotor-stator interactions in simulations of average-passage flow. ASME Journal of Fluids Engineering 124:550–554

Menter FR (1994) Two-equation eddy-viscosity turbulence models for engineering applications. AIAA Journal 32(8):1598–1605

Miller RJ, Moss RW, Ainsworth RW, Harvey NW (2003a) The development of turbine exit flow in a swan-necked inter-stage diffuser. In: Proceedings of ASME Turbo Expo 2003, June 16–19, Atlanta, Georgia, USA, ASME Paper No. GT-2003-38174

Miller RJ, Moss RW, Ainsworth RW, Horwood CK (2003b) Time-resolved vane-rotor interaction in a high-pressure turbine stage. ASME Journal of Turbomachinery 125:1–13

Persico G, Mora A, Gaetani P, Savini M (2010) Unsteady aerodynamics of a low aspect ratio turbine stage: modelling issues and flow physics. In: Proceedings of ASME Turbo Expo 2010, June 14-18, Glasgow, UK, ASME Paper No. GT2010-22927

Rhie C, Gleixner A, Spear D, Fischberg C, Zacharias R (1995) Development and application of a multistage navier-stokes solver:part1-multistage modeling using body forces and determinsitic stresses. ASME Journal of Turbomachinery 120:205–229

Santner C, Paradiso B, Malzacher F, Hoeger M, Hubinka J, Göttlich E (2011) Evolution of the flow through a turning mid turbine frame applied between a transonic hp turbine stage and a counter-rotating lp turbine. In: Proceedings of 9^{th} European Turbomachinery Conference, March 21-25, Istanbul, Turkey, Paper No. 110

Spataro R, Santner C, Lengani D, Göttlich E (2012) On the flow evolution through a lp turbine with wide-chord vanes in an s-shaped channel. In: Proceedings of ASME Turbo Expo 2012, June 11-15, Bella Center, Copenhagen, Denmark, ASME Paper No. GT-2012-68178

Tucker P (2011) Computation of unsteady turbomachinery flows:part 1 - progress and challenges. Progress in Aerospace Sciences 47:522–545

Wallin F, Ore S, Göttlich E, Santner C (2011) Aero-design and validation of a turning mid turbine frame. In: Proceedings of ISABE 2011, September 12-16, Gothenburg, Sweden, ISABE Paper No. ISABE-2011-1713

Yasa T, Lavagnoli S, Paniagua G (2011) Impact of a multi-splitter vane configuration on the losses in a 1.5 turbine stage. Proceedings of IMechE Vol 225 225:964–974

Experimental Thermal and Fluid Science xxx (2012) xxx–xxx

Contents lists available at SciVerse ScienceDirect

Experimental Thermal and Fluid Science

journal homepage: www.elsevier.com/locate/etfs

Analysis tools for the unsteady interactions in a counter-rotating two-spool turbine rig

Davide Lengani *, Cornelia Santner, Rosario Spataro, Emil Göttlich

Inst. f. Thermal Turbomachinery and Machine Dynamics, Graz University of Technology, Inffeldgasse 25/A, A-8010 Graz, Austria

ARTICLE INFO

Article history:
Received 14 July 2011
Received in revised form 24 January 2012
Accepted 12 May 2012
Available online xxxx

Keywords:
Counter-rotating turbine
Rotor–rotor interaction
Phase locked averaging
Intermediate turbine duct

ABSTRACT

Counter-rotating turbines represent the state of the art of actual and future aero-engines, built for a considerable reduction of weight and fuel consumption. However, in the open literature there is a limited number of experimental and computational research about the unsteady interactions in such complex configurations. The paper presents an experimental investigation on the two-spool counter-rotating transonic turbine at Graz University of Technology. The rig was designed in cooperation with MTU Aero Engines and Volvo Aero and considerable efforts were put on the adjustment of all relevant model parameters. The test setup consists of a high pressure (HP) stage, a diffusing mid turbine frame with turning struts and a shrouded low pressure (LP) rotor.

A two-sensor fast response aerodynamic pressure probe (2S-FRAPP) has been employed to provide time-resolved aerodynamic area traverses downstream of the LP turbine. Structures at the blade passing frequency of each rotor are resolved by the use of the shaft encoders. Furthermore, a newly developed phase averaging procedure is introduced to take into account the combined rotor–rotor interactions. Different reconstructions of the time resolved flow field are then presented in the paper, where a detailed description of the post-processing tools and their interpretation is provided.

1. Introduction

Modern turbo-fan engines are designed with a very high bypass ratio in order to fulfill different requirements such as small specific fuel consumption and low emissions. With this geometry the flow has to be guided from the high pressure (HP) system to the low pressure (LP) system, and viceversa, by annular ducts with a respectable radial offset. Intermediate turbine diffusers provided with turning vanes should guide the flow from the HP turbine to the LP turbine safely and without disturbances or boundary layer separations.

As recently reviewed by Göttlich [1], many efforts have been done in the last years on this field by different research groups on sophisticated test turbines (Oxford [2], Ohio State University [3], Von Karman Institute [4], Chalmers University of Technology [5] and Graz University of Technology [6]). It has been shown that the unsteady flow features caused by the HP stage, secondary flows, tip leakage vortex, wakes and trailing edge shocks, influence considerably the aerodynamics of the turning mid turbine frame (TMTF). In particular, the vortices produced by the HP rotor close to the endwalls energize the duct boundary layer there enabling it to better withstand the adverse pressure gradient. However, the unsteadiness does not decay within the duct and it influences the secondary flows of the turning vanes embedded in the diffuser and hence its outlet flow.

Therefore, the next step of these researches is to focus on the effect of the diffusing duct together with up-and downstream components [1]. Just recently, Hubinka et al. [7] developed an engine relevant test setup for turning mid turbine frames with up-and downstream turbine stages. A further characteristic of this test turbine is that the two shafts are counter-rotating. Even though such feature represents the state of the art of current aero-engines, the literature on the unsteady interactions in counter-rotating test turbines is still limited. In the last 10 years, different research groups, in particular GE Aircraft Engines [8,9] and Pratt and Whitney [10,11], have performed unsteady measurements in two-spool test rigs. Similarly, different numerical studies have been recently performed, see for example Qingjun et al. [12]. Most of these works, in particular Keith et al. [9] and Praisner et al. [11], concluded that the level of unsteadiness and frequency contents in a counter-rotating turbine is very high and may not be predicted from classical considerations. There is still a lack of systematic analyses which account for the different sources of unsteadiness in configurations relevant for the current and the new engine architectures.

The work presented in this paper includes time-resolved aerodynamic area traverses performed on the research facility developed by Hubinka et al. [7]. A two sensor fast response aerodynamic pressure probe (2S-FRAPP) in a four-sensor virtual mode is used to provide the unsteady flow field in different planes

* Corresponding author. Tel.: +43 316 873 7739.
E-mail address: davide.lengani@tugraz.at (D. Lengani).

0894-1777/$ - see front matter © 2012 Elsevier Inc. All rights reserved.
http://dx.doi.org/10.1016/j.expthermflusci.2012.05.010

Nomenclature

2S-FRAPP	2 sensor fast response aerodynamic pressure probe
BPF	blade passing frequency
c_{ax}	axial chord
C_{pt}	total pressure coefficient
FHP	five hole probe
h	channel height
H	relative channel height
HP	high pressure
LP	low pressure
$\dot{m}$	mass flow
M	Mach number
m_r	reduced mass flow $= \frac{\dot{m}\sqrt{T_{t,in}}}{p_{t,in}}$
n_r	reduced rotational speed $= \frac{Rotational\ Speed}{\sqrt{T_{t,in}}}$
p	static pressure
p_t	total pressure
PLA	phase locked average
Re	reynolds number
REV	revolution period
t	time
T	blade passing period
T_t	total temperature
TMTF	turning mid turbine frame
v	velocity
ρ	flow density
θ	circumferential coordinate
$\langle\,\rangle$	purely periodic component

Subscripts

AVE	circumferentially averaged properties
in	stage inlet
MEAN	area averaged value
MAX	maximum value, in the local plane

Superscripts

$\bar{}$	time averaged properties
$\tilde{}$	phase locked properties
$'$	stochastic fluctuating component

of the turbine. The paper focuses on the post processing procedures downstream of the LP turbine, where the unsteadiness of both rotors influences the flow. In the present case, a classical post processing decomposition, developed for unsteady flows in the 1970s (see for example Hussain and Reynolds [13]), which normally takes into account the presence of one main unsteady perturbation, does not provide a global view of the phenomena. It is possible to isolate just the fluctuations induced by the rotor itself by means of a phase averaging procedure based on the shaft encoder of one of the two rotors (e.g. [14,15]). Hence, a procedure for the decomposition of the original time-signal, which preserves the phases between the two rotors, has been developed.

The first part of the paper presents the experimental facility and a detailed description of the data processing tools. In the second part, after a brief introduction of the mean flow, which is documented in the works of Santner et al. [16] and Paradiso et al. [17], the paper focuses on the systematic description and analysis of the sources of unsteadiness. Different reconstructions of the unsteady signal are then shown in terms of time snapshots of Mach number and total pressure in order to identify the relative effects of the two rotors on the flow field and to verify the validity of the post-processing procedures that have been proposed.

2. Experimental apparatus and methodology

2.1. Facility

The transonic test turbine facility is a continuously operating two-stage cold-flow open-circuit plant, which consists of a transonic HP stage and a counter-rotating LP stage (a schematic drawing is shown in Fig. 1). This unique configuration allows the testing of rig inserts under aerodynamic conditions relevant for modern aero-engine. Both turbines are designed with overhung-type turbine shafts and additionally the LP turbine is mounted on an axially movable frame. This allows easy disk assembly without dismantling the bearings and the simple application of transition duct and TMTF designs with different axial lengths. The facility is driven by pressurized air delivered by a separate 3 MW compressor station. The shaft power of the HP stage drives a three-stage radial

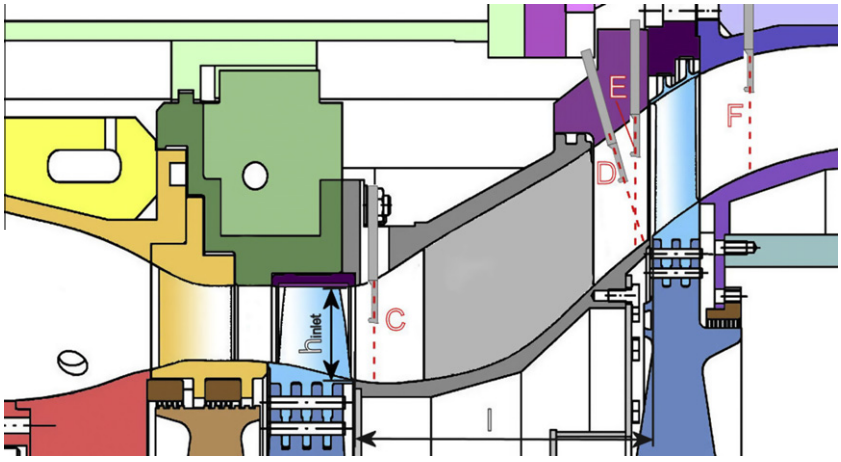

Fig. 1. Schematic meridional section of the test setup with probe measurement planes (C, D, E, F), the results in the paper concern plane F.

Please cite this article in press as: D. Lengani et al., Analysis tools for the unsteady interactions in a counter-rotating two-spool turbine rig, Exp. Therm. Fluid Sci. (2012), http://dx.doi.org/10.1016/j.expthermflusci.2012.05.010

Table 1
Blading parameters and operating conditions.

	HP vane	HP blade	TMTF	LP blade
Blading parameters				
Vane/blade No.	24	36	16	72
Aspect ratio h/c_{ax}	1.15	1.37	0.53	2.94
Reynolds number (10^{-6})	2.38	1.1	1.86	0.46
Tip gap	–	Unshrouded	–	Shrouded
		HP stage		LP stage
Operating conditions				
n_r $(rpm/\sqrt{K})$		524.4		195.3
$m_{r,in}$ $(kg/s \cdot \sqrt{K}/(bar))$		81.2		214.6
Blade passing frequency (Hz)		6640		4260
Stage total pressure ratio		3		1.3
Power (kW)		1710		340

brake compressor. The power of the LP turbine is absorbed by a water brake with a maximum power of 700 kW. Detailed information on the design and construction of the original single stage facility can be found in Erhard and Gehrer [18]. For the design of the LP-stage together with the TMTF see Hubinka et al. [7] and for the operation Hubinka et al. [19].

2.1.1. Test setup

As already mentioned, the investigated test setup consists of a single stage unshrouded transonic HP turbine, and an S-shaped turning mid turbine frame (TMTF) followed by a shrouded counter-rotating LP turbine. Fig. 1 represents a meridional section of the test facility. The incoming air is accelerated by the HP vanes in circumferential direction and impinges on the HP rotor designed with a cylindrical outer contour. Then it is turned by the struts of the TMTF in negative direction relative to the rotation of the HP rotor and the air enters the counter-rotating LP rotor assembled at a larger diameter.

Table 1 displays the main design parameters for the HP stage and the LP stage (TMTF + LP rotor), the design of which was provided by MTU Aero Engines. The HP turbine consists of 24 choked vanes and 36 blades. For the LP stage a blade count of 16 struts and 72 blades was chosen in order to minimize the risk of excitation of the LP turbine.

The HP vanes as well as the outer casing downstream of the TMTF struts are fully rotatable in circumferential direction. This enables area traverses for probe and rake measurements in the four planes identified in Fig. 1. To gain a detailed understanding of the rotor–rotor interaction downstream of the LP turbine, fast response aerodynamic pressure probe measurements were performed.

2.1.2. Operating conditions

Table 1 displays also the main parameters of the operating point. The investigated aero design has an overall pressure ratio of 4. The total pressure ratio is 3 for the HP turbine and 1.3 for the LP turbine. The HP vanes are operating under choked conditions. The absolute Mach number at TMTF inlet with a value of about 0.5 is representative for realistic duct inlet conditions of modern jet engines with a single stage HP turbine at cruise operating point.

2.2. Measuring techniques

Unsteady flow measurements were performed by means of a 2-sensor fast response aerodynamic probe (2S-FRAPP) [20], operated as a virtual four sensor probe for 3D aerodynamic measurements. Flow parameters including total and static pressure, flow angles and velocity components are derived from three rotations of the probe and a set of calibration coefficients (see for example [21]). The dimensions of each piezoresistive sensor are 0.4×0.8 mm, the distance between the two sensors is approximately 2.2 mm and the tip diameter of the probe is 1.8 mm. This concludes that the sensing area of the probe is in the order of 3.9 mm^2. The absolute uncertainties of the used probe techniques are equal to ±0.3 deg for the flow angles, ±100 Pa for the total pressure and ±0.4% for the Mach number.

The present paper describes the results obtained by the 2S-FRAPP in an annular sector in plane F (marked in Fig. 1). Plane F is a plane perpendicular to the horizontal direction and is located at 77% of the rotor chord downstream of the blade trailing edge. Full area traverses were performed over one strut pitch (22.5 deg) downstream of the TMTF. The measurement grid consists of 21 positions along the blade span and of 46 positions over one TMTF pitch.

An analog low pass filter (80 kHz) has been applied to the 2S-FRAPP signals to prevent aliasing. Then, the signal of the probe and the two shaft encoders were acquired simultaneously. Such measurement allows the decomposition of the flow with respect to the phases of one of the two rotors, and hence the effects of the two rotors on the flow may be observed separately. Furthermore, as it will be shown in the following section, it allows also the reconstruction of a phase that takes into account the relative rotor–rotor positions.

2.3. Data reduction method

Data is acquired at 200 kHz for 2 s, it corresponds to more than 100 revolutions of the LP turbine and more than 350 of the HP turbine. The determination of the flow properties is made possible after phase averaging: the periodic fluctuations of velocity, pressures and flow angles are determined at each phase from the phase averaged values of the three rotations of the probe [21].

Phase averaging is commonly performed in rotating machinery by means of one pulse per revolution obtained from a shaft encoder (see for example the early papers from Sharma et al. [14] and Suder et al. [15]). This pulse is used to determine the beginning of each revolution, which represents also the end of the previous one. In the present paper each revolution is resampled to a fixed number of samples in order to correct the small speed variations of the turbine shafts [22]. The phase averaged values are then computed as the average of the samples at the same phase. Such procedure is very well established and allows the identification of the structures correlated to the rotor rotational speed. However, for the present experiments it is not sufficient, because it does not provide any informations about rotor–rotor interactions. Since the two rotors are counter-rotating and their rotational speeds are uncorrelated, a phase locked average based on the phase of one of

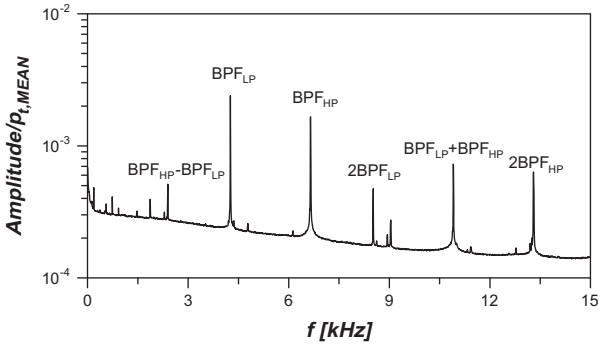

Fig. 2. Average non-dimensional amplitude spectrum.

the two rotors removes completely the fluctuations of the flow quantities induced by the other rotor.

As a preliminary analysis of the relative influence of the two rotors in plane F, an average power spectrum is shown in Fig. 2. The spectrum is obtained averaging 21 × 46 spectra, namely the whole measurement area. The spectra were determined from the raw signal of the probe when aligned with the mean flow. For clarity, the frequencies of interest, associated with sharp frequency peaks, are marked over the picture. Such operation allows the identification of the frequencies and hence the phenomena that characterize this plane.

The highest amplitude may be identified at the blade passing frequency of the LP rotor (BPF_{LP}). Significant contributions may be observed also for the far upstream HP rotor, in particular its blade passing frequency (BPF_{HP}). Further peaks with lower amplitude corresponds to the higher order harmonics of the two rotors. Not only the multiple of the blade passing frequencies characterize the flow field, peaks of lower amplitude appear at any linear combination $i \cdot BPF_{LP} + k \cdot BPF_{HP}$, with i,k integer numbers. Just $BPF_{LP} + BPF_{HP}$ and $BPF_{HP} - BPF_{LP}$ are marked over the graph to avoid superposition of an excessive number of symbols and keep the picture readable. For the same reason the frequency spectrum has been cut at 15 kHz, a multitude of peaks with decreasing amplitude is traceable up to 40 kHz according to the linear combination proposed.

2.3.1. Rotor-synchronic averaging, ideal case

To take into account for the full unsteadiness, hence the interactions at the frequencies $i \cdot BPF_{LP} + k \cdot BPF_{HP}$ (with i and k integer), a special phase averaging procedure has been studied and it is proposed here.

Fig. 3 shows a schematic representation of the shaft triggers. The time made non-dimensional by the revolution period of the LP turbine (REV_{LP}) is plotted on the abscissa, and the trigger level is plotted on the ordinate. The trigger level is a symbolic number associated to different origins of the trigger. A trigger level equal to 2 corresponds to the shaft encoder signals and identifies the beginning and end of the revolutions of each rotor, gray filled diamonds for the LP turbine and black filled dots for the HP turbine (the label REV_{HP} superimposed to the plot helps the identification of a revolution of the HP rotor, while the revolution period of the LP turbine may be read on the x-axis). The trigger level equal to 1 corresponds to the identification of the blades within the revolution, namely every revolution is divided into equi-distant intervals

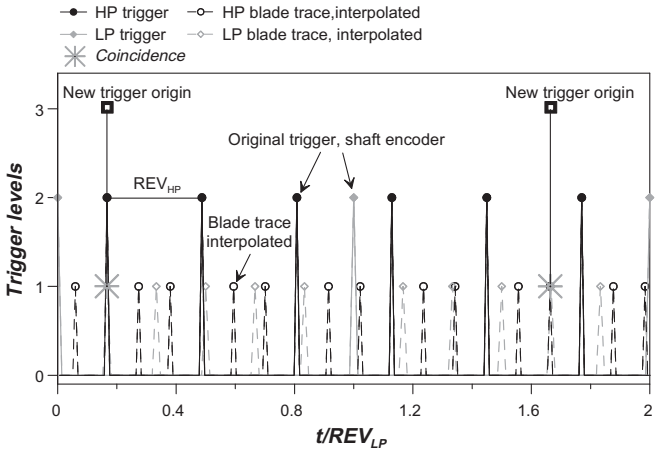

Fig. 3. Schematic representation of trigger post-processing; the trigger level is a symbolic number associated to the different origins of the triggers: a value of 2 corresponds to the original shaft encoder triggers, a value of 1 to the interpolated blade periods within a revolution, and a value of 3 to the new trigger origin as coincidence positions of the previous levels. The blades of the two rotors are always in the same absolute position at the trigger "level 3".

corresponding to the trace of the blade passing period. For readability of the graph the HP rotor has been simplified to 3 blades (hollow black circles), 3 constant blade period within one revolution, and 6 blades for the LP turbine (hollow gray diamond) maintaining the original HP blade to LP blade count ratio (36–72). As marked over the picture such blade triggers are interpolated. The identification of equidistant period has the only assumption that within one revolution the rotational speed of the rotor remains constant. Considering the very high rotational speed this hypothesis may be considered always verified. A simple algorithm is then written with the purpose of identifying positions of coincidence between the triggers of the two rotors at levels 1 and/or 2. The coincidence is considered as the origin of a new trigger, indicated as "level 3" in the picture.

From this idealized scheme, it may be shown that the periods identified with the coincidence positions may be directly correlated to the different sources of unsteadiness. The time interval Δt between two successive "level 3" triggers is a multiple of the blade passing periods of the HP and LP rotor. It may be written that:

$$\Delta t = mT_{HP} = nT_{LP} \tag{1}$$

with m, n non-zero and positive integer numbers. Hence, the unsteadiness due to the single rotor (BPF_{LP} and BPF_{HP} and their multiples) is correctly resolved. Furthermore, as previously observed, the rotor–rotor interactions may be identified for the frequencies $f_{HP,LP} = i \cdot BPF_{LP} + k \cdot BPF_{HP}$ with i and k non-zero integer numbers. This frequency may be rewritten considering the blade passing periods of the HP and LP rotor and their link ($T_{LP} = m/n\ T_{HP}$) observed from Eq. (1):

$$f_{HP,LP} = \frac{i}{T_{LP}} + \frac{k}{T_{HP}} = \frac{i}{(m/n)T_{HP}} + \frac{k}{T_{HP}} \tag{2}$$

Rearranging and considering Eq. (1), the frequency $f_{HP,LP}$ of the rotor–rotor interactions results:

$$f_{HP,LP} = \frac{in + km}{mT_{HP}} = \frac{in + km}{\Delta t} \tag{3}$$

with $(in + km)$ a positive integer number. Eq. (3) proves that the interaction frequency $f_{HP,LP}$ is always a multiple of the new trigger frequency $1/\Delta t$.

2.3.2. Rotor-synchronic averaging, real case

In the exemplification of Fig. 3 the ratio of the revolution period of the two rotors is kept constant and equal to the real one and two coincidence positions may be identified ($t/REV_{LP} = 0.165, 1.66$ in Fig. 3). In the real case there are 12 times more blades and then more coincidence positions. However, in the real case the rotational speed of the rotors may be kept constant within a certain accuracy, ±1.5/1000 for both rotors in this facility. Even if such variations are really small, they are taken into account, since the signals of the two shafts are acquired at a very high frequency. At the same time, an accuracy for the coincidence of the triggers has to be chosen. In the present paper the triggers have been considered to have a coincidence when their time difference was below 1/1000 of the blade passing period of the HP rotor (the lowest among the two rotors). Under such conditions, for the 2 s of acquisition time, there are around 600 coincidences, and the variation of such number is within ±2% for all the measurement positions.

Nevertheless, the small variations of the rotational speed of the two rotors, unlike the example of Fig. 3, lead to intervals between each coincidence position that are not constant. To perform a phase averaging procedure like explained in the beginning of this section a start and an end of the periodic phenomena has to be

chosen (it is commonly the shaft encoder signal when phase averaging on the revolution period of a rotor). In the present case, where the phase averaging is meant to be performed out of synchronic positions of the rotor, the beginning of the phase is obtained as previously explained while the end is chosen following these two criteria:

(1) a fixed number of LP blades is counted after the coincidence position, this is automatically done as the "level 1" trigger is interpolated;
(2) within this time interval the ratio of HP blade periods to LP blade periods is computed, if the ratio is different from the theoretically predicted (see Eq. (1)) for more than a fixed uncertainty the period is discarded.

The very stable operating conditions of the facility allowed the evaluation of 7 LP blade passing periods without discarding any interval, since the computed blade ratio has variations below 0.5%.

With this procedure the relative position of the HP rotor blades and the LP rotor blades, in the absolute frame of reference, is coherently preserved at any phase of the newly derived averaging period. Basically, the positions of the rotors are re-synchronized within the period of this new phase averaging that will be referred to as rotor synchronic averaging (RSA) in the followings.

Further, it has to be noted that the parameters discussed up to now, in particular the accuracy of the coincidence and the accuracy of the ratio of T_{HP} and T_{LP} within one averaging period, are the only ones to affect the RSA procedure. For example, there is no need to assume that the blades of the rotors are identical. In fact, when the RSA is performed over a very large number of periods (600 periods in the present case) derived from random combinations of HP and LP blades, the averaging removes the unsteadiness at low frequencies due to the rotor geometrical asymmetries. From the spectral analysis of the classically phase averaged signal (shown in the last section of the paper) it emerged that almost the whole signal energy is included at the blade-passing frequency and its harmonics for the LP rotor. For the HP rotor, since the blades are transonic, the generation of shock waves increases the sensitivity to small geometrical asymmetries (see for example [23]) and hence energy peaks at low frequencies may be also observed in Fig. 2. However, this does not affect the quality of the results from the RSA.

3. Results and discussion

This section provides time-snapshots of the time resolved evolution of the flow and further power spectra in order to validate the RSA procedure. Before discussing the time resolved flow structures, the time averaged flow downstream of the LP rotor is briefly introduced. The understanding of the mean flow features is, in fact, necessary to discuss the more complex time resolved flow evolution.

Results are presented in Figs. 4–6 as contour plots of the absolute Mach number and the total pressure in the absolute (stationary) reference frame. These quantities are plotted as non-dimensional coefficients: the Mach number is shown in terms of M/M_{MAX}, where M_{MAX} is the maximum value of the time averaged Mach number in the local measurement plane; whereas, the total pressure is plotted as non-dimensional coefficient C_{pt} defined as:

$$C_{pt} = \frac{p_t - p_{MAX}}{0.5\rho v_{MAX}^2} \tag{4}$$

where p_{MAX} is the maximum value of the time averaged static pressure measured in the local measurement plane. According to these definitions and to the radial pressure gradient induced by the diffusing duct, negative values of the pressure coefficients may be observed. The definitions are applied to both time averaged quantities (Fig. 4) and time-resolved, phase locked averaged, quantities (Figs. 5 and 6) and are adopted to preserve the original distributions of the Mach number and total pressure, as they will be referred in the discussion.

These aerodynamic area traverse plots are views in the downstream direction on a sector covering one pitch of the TMTF. Consequently, the pictures cover 4 and 1/2 LP rotor blades and 2 and 1/4 blades of the HP rotor. In the plots the LP rotor has a clockwise sense of rotation while it is the opposite for the HP rotor.

3.1. Time averaged flow field

Detailed discussions of the flow through the duct were provided by Santner et al. [16] and Paradiso et al. [17]. Briefly, they found that the TMTF exit flow is characterized by large pressure gradients in the radial and circumferential directions induced by the duct curvature and by the swirl evoked by the turning struts. Aerodynamic losses were identified, mainly, in two regions at low momentum corresponding to the wake of the TMTF and to a large passage vortex developing in the bottom part of the vane channel. Similarly, the mean flow at the outlet of the LP rotor is still largely influenced by these flow structures.

The distribution of the Mach number in plane F (Fig. 4a) shows large velocity defects in the endwall regions, at the tip the Mach number is lower than at the hub. The adverse pressure gradient imposed on the flow by the area expansion leads to such a velocity distribution. In the circumferential direction, at the tip and at midspan, the Mach number distribution is almost uniform. In fact, the presence of the LP rotor reduces the circumferential velocity gradients of the upstream plane. However, at the hub there is a local

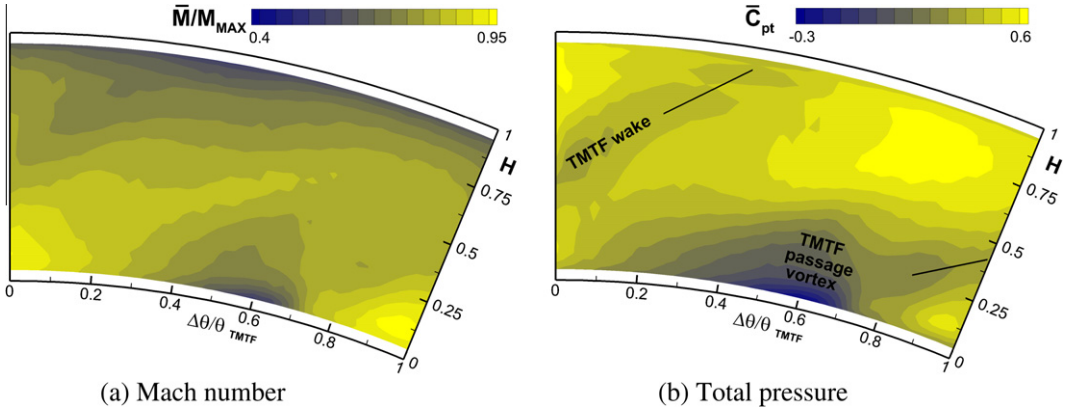

(a) Mach number (b) Total pressure

Fig. 4. Time-averaged distributions of the Mach number and total pressure. The main flow structures evoked by the TMTF are marked over the experimental results.

Please cite this article in press as: D. Lengani et al., Analysis tools for the unsteady interactions in a counter-rotating two-spool turbine rig, Exp. Therm. Fluid Sci. (2012), http://dx.doi.org/10.1016/j.expthermflusci.2012.05.010

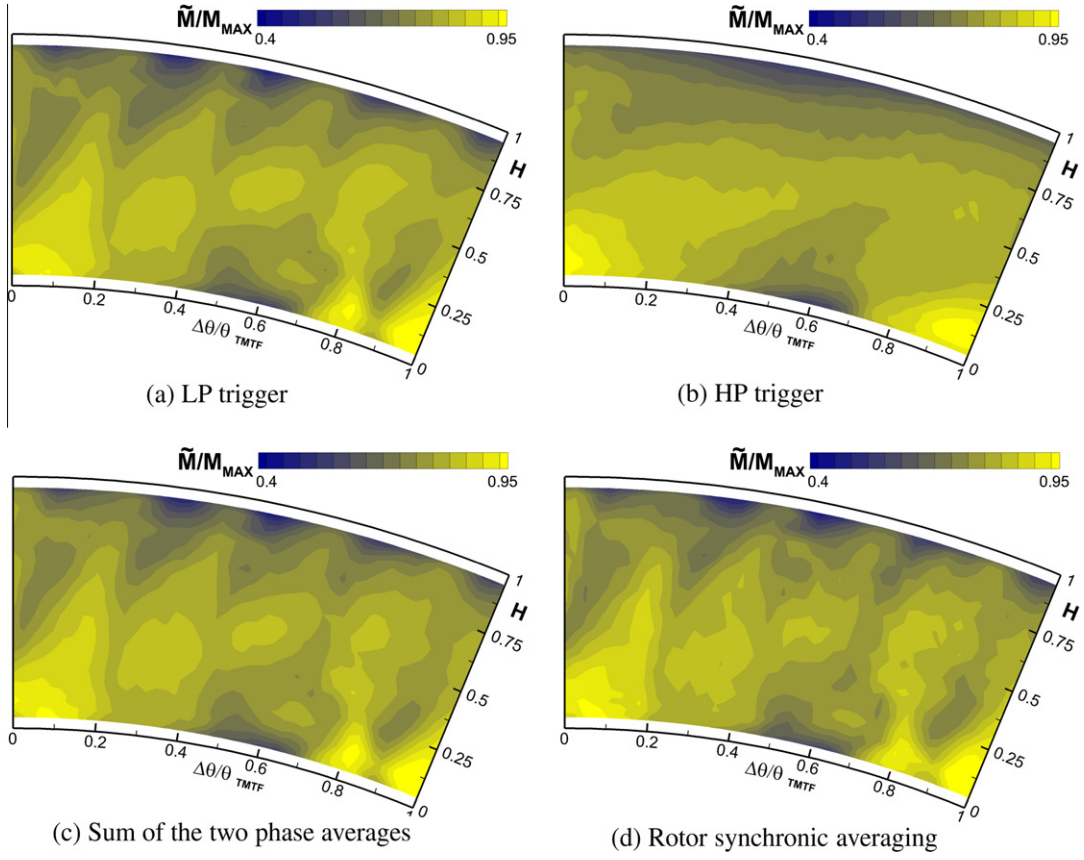

Fig. 5. Time-snapshots of the phase resolved Mach number.

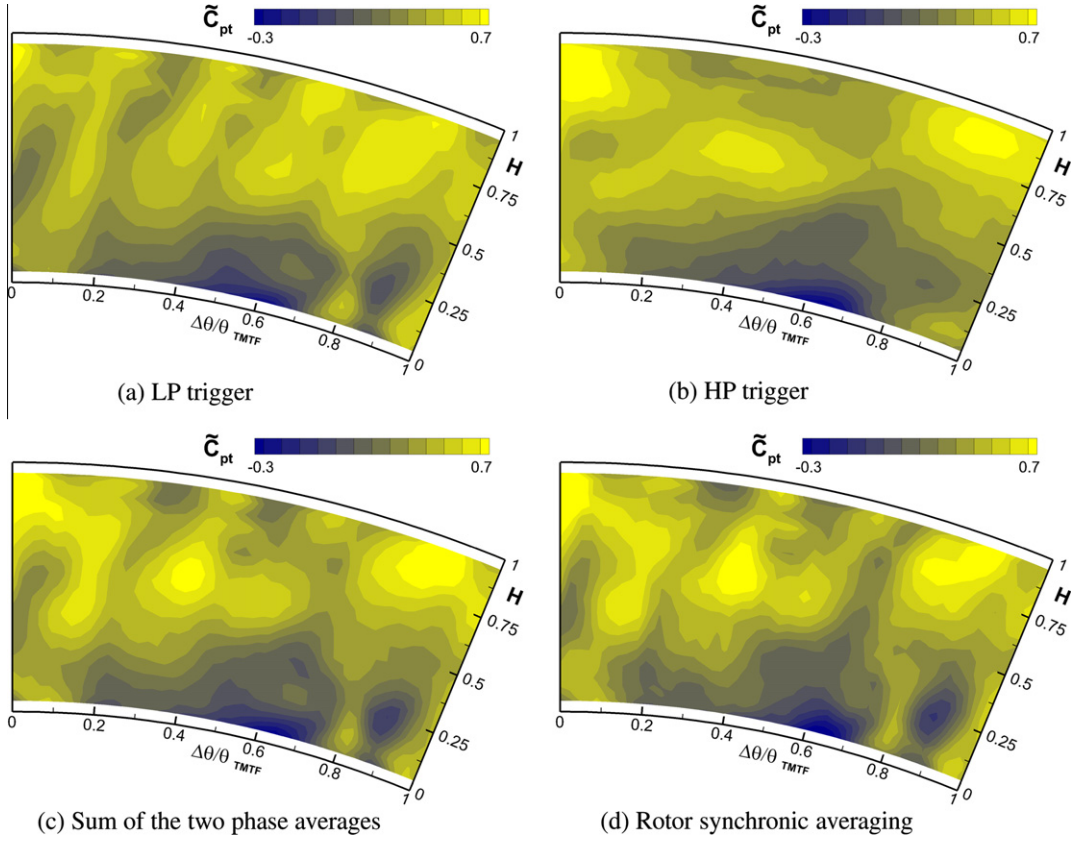

Fig. 6. Time-snapshots of the phase resolved total pressure.

Please cite this article in press as: D. Lengani et al., Analysis tools for the unsteady interactions in a counter-rotating two-spool turbine rig, Exp. Therm. Fluid Sci. (2012), http://dx.doi.org/10.1016/j.expthermflusci.2012.05.010

reduction of the Mach number between 0.5 and 0.65 of the TMTF pitch ($\Delta\theta/\theta_{TMTF}$).

This structure is the trace of the TMTF passage vortex identified by Santner et al. [16] which is pushed towards the hub by the radial pressure gradient. Furthermore, this area, marked over Fig. 4b as "TMTF passage vortex", is characterized by the lowest values of total pressure.

The mean flow is characterized by another region at low total pressure, which starts at $\Delta\theta/\theta_{TMTF} \cong 0.8$ at the hub, and that, for periodicity, ends at $\Delta\theta/\theta_{TMTF} \cong 0.4$ at the tip. This inclined/skewed region at low total pressure identifies the trace of the TMTF wake, as marked over Fig. 4b. The wake of the TMTF is in fact skewed by the swirling motion induced by the TMTF and also by the LP rotor.

3.2. Time resolved flow field

Time-averaging the flow quantities, as provided in Fig. 4, removes completely the effects of the 2 rotors. However, since the following discussion will be based on the effect of the 2 rotors it was necessary to briefly present such distributions for comparison. In this section, to analyze the sources of unsteadiness, the time resolved flow field is discussed by means of four different decompositions of the flow quantities. Phase averaging was performed triggering the flow with the 2 triggers in order to isolate the effects of the two rotors. Whereas the RSA procedure, as introduced in Section 2.3.1, was developed to provide the phase resolved flow field considering the combined effects of both rotors.

A classical decomposition of the variable p is the so-called triple decomposition procedure [13]:

$$p(t) = \bar{p} + \langle p(t)\rangle + p'(t) \tag{5}$$

where $\langle p(t)\rangle$ is the purely periodic component associated with a coherent periodic structure and $p'(t)$ is the random fluctuation associated mainly with turbulence. This decomposition is valid when a single source of periodic unsteadiness is characterizing the flow. However, considering the presence of two rotors at uncorrelated frequencies (2 uncorrelated coherent periodic structures) the decomposition may be rewritten:

$$p(t) = \bar{p} + \langle p(t)\rangle_1 + \langle p(t)\rangle_2 + \langle p(t)\rangle_{1,2} + p'(t) \tag{6}$$

where the 2 distinct purely periodic components $\langle p(t)\rangle_1$, $\langle p(t)\rangle_2$ have their own period and frequency, and $\langle p\rangle_{1,2}(t)$ indicates the cross-interactions which generate the frequency peaks at $i \cdot BPF_{LP} + k \cdot BPF_{HP}$ (with i and k not zero). The rotor synchronic average provides the following time resolved distribution:

$$\tilde{p}(t)_{RSA} = \bar{p} + \langle p(t)\rangle_1 + \langle p(t)\rangle_2 + \langle p(t)\rangle_{1,2} \tag{7}$$

As observed from Eqs. (1) and (3), the energy content at the blade passing frequencies of the two rotors and their combined interactions is directly linked to this phase averaging procedure. Hence, the RSA preserves the frequency content of all coherent structures of the original signal.

A further reconstruction of the signal is also proposed. Even in such complex flow, the contributions of the time-mean and of one purely periodic part (e.g. $\langle p(t)\rangle_1$) give the phase locked average quantity $\tilde{p}$ within the phase of the period of the phenomenon "1":

$$\tilde{p}(t)_1 = \bar{p} + \langle p(t)\rangle_1 \tag{8}$$

When such average is performed over a sufficiently high number of periods of the phenomenon "1" the effects of the fluctuations $\langle p(t)\rangle_2$, the random unsteadiness $p'(t)$ as well as the combined interactions $\langle p\rangle_{1,2}(t)$ are removed. In the present case such operation is the classical phase average performed considering the shaft encoder of one of the two rotors. To resolve the unsteadiness of the flow it may be thought to sum the results of the classical phase averaging procedures. In detail, the purely periodic fluctuations $\langle p(t)\rangle_1$ and $\langle p(t)\rangle_2$ may be obtained from Eq. (8) as difference of the phase average and the time mean value. Then, $\langle p(t)\rangle_1$ and $\langle p(t)\rangle_2$ may be added to the time mean value $\bar{p}$ in order to obtain the following time resolved distribution:

$$\tilde{p}(t)_{sum} = \bar{p} + \langle p(t)\rangle_1 + \langle p(t)\rangle_2 \tag{9}$$

However, this distribution resolves partially the unsteadiness of the flow, it does not account for the rotor–rotor interactions ($\langle p\rangle_{1,2}(t)$) when compared to Eq. (7). It has to be noted that $\tilde{p}(t)_{sum}$ is periodic for the least common multiple of the two periods in analogy with Eq. (1) which is resolved by the RSA, but it does not capture the terms observed in Eq. (3). The reconstruction of the original signal $\tilde{p}(t)_{sum}$ will be referred to as sum of the phase averages.

The classical phase averages (LP and HP shaft encoder) and consequently their sum have been further post-processed. The results obtained from these averages are shown in terms of an average-blade passing period, which is computed as the average among the 72 (LP rotor) or (36 HP rotor) blade passages. Due to the high number of blade passing periods it is possible to compute the average-representative blade passing period increasing the temporal resolution. The sum of the phase averages was then reconstructed as the sum of the averages on the blade passing periods of the 2 rotors.

Time-snapshots of the Mach number and total pressure distribution downstream of the LP rotor are depicted in Figs. 5 and 6, respectively, considering the four different decompositions. On top of the figures the phase locked averages on the LP and HP rotor triggers are shown on the left and the right side, respectively, while on the bottom the sum of the phase averages and the RSA are shown.

3.2.1. Mach number distributions

Clear traces of the LP rotor blades are shown triggering with the LP rotor shaft encoder (Fig. 5a). The 4 and 1/2 blades of the LP rotor may be observed as disturbances to the mean flow depicted in Fig. 4a. There are, in fact, regions at alternately higher and lower velocities than the mean flow. For example, at the hub the region of higher Mach are also circumferentially shifted with respect to the mean flow. Locally, the acceleration inside the blade passage leads to higher velocities than the mean flow, while the trace of the blade wake leads to lower velocities.

The effect of this rotor on the flow is way different from what is classically observed in the open literature of LP turbines (e.g. [24,25]). The rotor wake seems not to be the main contribution to loss generation. Instead, the secondary flows at the tip lead to a particular "triangle shaped" region. Whereas at the hub, the area at low velocity ($0.5 < \Delta\theta/\theta_{TMTF} < 0.7$), identified discussing the mean flow (Fig. 4), is almost undisturbed by the LP rotor blades. This vortical structure forces the accelerated flow of the blade passages to lift up.

The Mach number distribution of the mean flow is posed again in Fig. 5b where the 2S-FRAPP is triggered with the HP rotor. The picture shows that the effect of the HP rotor on the velocity distribution is less relevant than the one of the LP rotor. Small differences with the mean flow may be observed just at midspan in the range of $0.4 < \Delta\theta/\theta_{TMTF} < 0.8$. The TMTF passage vortex that generates the region of low velocity at the hub is influenced by the unsteadiness of the HP rotor and then small fluctuations, due to such far upstream bladings, are visible in this area.

These two time snapshots (Fig. 5a and b) are two distinct, uncorrelated, phases with respect to the LP and HP trigger, respectively. Once summed up the result is provided in Fig. 5c, where the structures of the LP blades are the main flow features. However, a local reduction of the velocity may be observed at midspan in the range of $0.6 < \Delta\theta/\theta_{TMTF} < 0.8$ (compare Fig. 5c to Fig. 5a).

Please cite this article in press as: D. Lengani et al., Analysis tools for the unsteady interactions in a counter-rotating two-spool turbine rig, Exp. Therm. Fluid Sci. (2012), http://dx.doi.org/10.1016/j.expthermflusci.2012.05.010

Fig. 5d, where the RSA is displayed, presents a result similar to Fig. 5a and c. This confirms that the influence of the HP rotor on the velocity distribution is lower than the one of the LP rotor. Furthermore, it provides a first validation for the RSA procedure. In fact, Fig. 5c and d have small differences that are due to the effects of the combined rotor–rotor tones. Such interaction is just taken into account by the RSA, as it will be shown in the last section of the paper, and modifies weakly the velocity distribution.

3.2.2. Total pressure distributions

A different behavior is shown in Fig. 6, where total pressure distributions are depicted for the four decompositions. The influence of the LP rotor blades may be observed triggering with the LP rotor shaft encoder (Fig. 6a). As previously observed for the mean flow (Fig. 4b), the largest values of the total pressure are measured from midspan to the tip. The 4 and 1/2 blades of the LP rotor may be identified as the regions with alternately high and low total pressure, where the high values correspond to the regions at high Mach number (Fig. 5a).

The effects of the HP rotor are visible in Fig. 6b, where the total pressure distribution due to this rotor differs from the distribution of the mean flow (Fig. 4b). In the present view there are 2 and 1/4 blades of the HP rotor, but this number is not clearly correspondent to what is depicted in the figure. Furthermore, the nuclei at high total pressure appear at different channel heights. Such structures are not immediately linked to the number of HP blades but may be correlated to the interaction between rotors and stators with different blade/vane number, which generates spinning modes [25,26].

Summing up the two periods (Fig. 6c) or performing the RSA (Fig. 6d) provides similar and very particular total pressure patterns. Hence, the combined tones ($i \cdot BPF_{LP} + k \cdot BPF_{HP}$) have a small influence on the total pressure distribution. In fact, the regions at low and high total pressure are mostly dependent on the relative position of both rotors, particularly, on the combination of the effects of each rotor.

3.2.3. Frequency analysis

Considering Eq. (7), the comparisons between Fig. 6c and d, and between Fig. 5c and d, reveal that the periodic term $\langle p(t)\rangle_{1,2}$ has a lower amplitude than $\langle p(t)\rangle_1$ and $\langle p(t)\rangle_2$. In order to demonstrate that just the RSA procedure preserves the complete energy content of the original signal, according to Eq. (7), the Fourier analysis of the phase locked quantities is provided. As previously discussed (see Section 2.3), this analysis identifies sharp frequency peaks at the frequency of interest. Hence, peaks at all the interaction frequencies $i \cdot BPF_{LP} + k \cdot BPF_{HP}$, which are directly associated to the purely periodic terms of Eq. (7), may be observed just by the RSA.

For this purpose, average non-dimensional amplitude spectra are shown in Fig. 7. These spectra are obtained from the phase locked averages based on the LP rotor shaft, on the HP rotor shaft and from the RSA, from top to bottom, respectively. In order to provide accurate Fourier transformation, the criteria to perform the phase average on the LP and HP rotors and by the RSA has been changed. In the case of the LP rotor, the phase average is extended to 3 revolutions of the LP rotor (instead of 1). In the case of the HP rotor, the phase average is extended to 9 revolutions. In the case of the RSA 3 revolutions of the LP rotor are counted after the coincidence of the trigger (instead of the 7 LP blade passing periods considered in Section 2.3.1). Within this interval, since the rotational speeds of the two rotors have very small fluctuations, the ratio between HP and LP blade passing periods has variations below 1.5%. After this further post-processing the frequency resolution is equal to 21 Hz for the three different spectra.

The FFT performed over the phase average based on the LP rotor trigger mainly preserves the energy content at the harmonics of the LP blade passing frequency (Fig. 7a). Similarly, the phase average based on the HP shaft encoder preserves the harmonics of the HP rotor blade passing frequency (Fig. 7b). On the contrary, the RSA (Fig. 7c) maintains the harmonics of the blade passing frequencies of both rotors and clearly shows peaks at $BPF_{LP} + BPF_{HP}$,$BPF_{HP} - BPF_{LP}$,$2BPF_{LP} - BPF_{HP}$ and other linear combinations. Furthermore, at low frequencies (below 1.5 kHz), just one peak is shown and it corresponds to $2BPF_{HP} - 3BPF_{LP}$. This confirms that the RSA averages out the small asymmetries of the HP rotor blades. In fact, the amplitude peaks at frequencies lower than 1.5 kHz in Fig. 7b (for the HP rotor) indicate the presence of small geometrical differences for the HP blades, as stated in Section 2.3.2, but these peaks do not appear for the RSA (Fig. 7c).

The relative low influence of the rotor–rotor interactions may be better understood from Fig. 7c. In fact, the amplitude of $BPF_{LP} + BPF_{HP}$, which is the largest contribution to the term $\langle p(t)\rangle_{1,2}$, is three times lower than the amplitudes at the BPF_{LP} and BPF_{HP}. However, $BPF_{LP} + BPF_{HP}$,$BPF_{HP} - BPF_{LP}$,$2BPF_{LP} - BPF_{HP}$ and other lin-

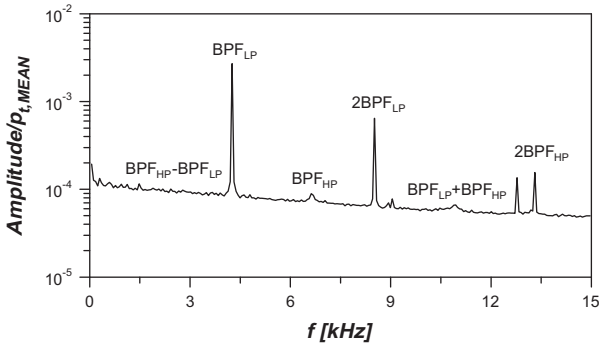

(a) LP trigger

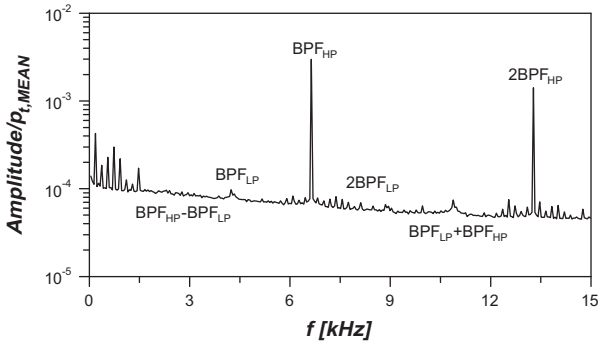

(b) HP trigger

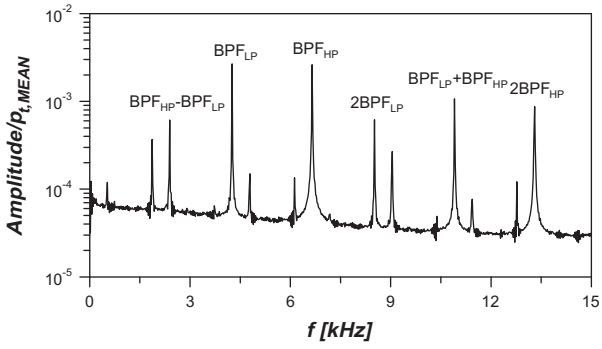

(c) Rotor synchronic averaging

Fig. 7. Average non-dimensional amplitude spectrum obtained from phase locked averages.

ear combinations are shown as sharp peaks, improving the noise to signal ratio observed in the FFT of the raw signal (Fig. 2).

It has to be noted that the sum of the phase average, represented in Figs. 5c and 6c, maintains the peaks at the blade passing frequencies of the two rotors but not the other interactions ($i \cdot BPF_{LP} + k \cdot BPF_{HP}$). In fact, since the reconstructed signal $\tilde{p}(t)_{sum}$ is obtained adding the purely periodic component of the two classical phase averages (see Eq. (9)), it may just contain the same energy contents of Fig. 7a and b.

Therefore, the small differences that may be observed between Figs. 5c and 6c (sum of the phase averages) and Figs. 5d and 6d (RSA) are due to the different energy contents. It is only the RSA that provides a true representation of the periodic flow within the counter-rotating turbine. The data obtained by means of this procedure must then be used to compute the correct values of time-resolved loss evolution. However, the classical phase locked average provides the relative influence of each rotor on the flow field and simplifies the identification of the flow structures.

4. Conclusion

Different procedures for the decomposition and analysis of the unsteady flow field downstream of a two-spool counter-rotating turbine have been proposed and discussed in the paper. Since the two rotors of the facility rotate on different spools with uncorrelated rotational speeds, a special phase averaging procedure has been developed. At each phase of this new procedure the HP and LP rotor blades maintain a coherent relative position. Hence, such averaging preserves all the possible rotor–rotor interactions. Classical phase averaging by means of the shaft encoders has been also performed in order to understand the relative effect of each rotor on the flow field. Furthermore, the proper sum of these two last phase averaging procedures has been introduced and compared to the rotor synchronic average.

Such tools have been used for the analysis of 2S-FRAPP measurements downstream of the LP turbine rotor. In particular, velocity and total pressure fields have been discussed for the four different reconstructions of the signal. The LP rotor blades have the largest influence on the Mach number distribution: locally there are higher velocities than the mean flow, which are due to the flow acceleration within the blade passage. In this case the rotor synchronic average is very similar to the phase average performed by means of the LP rotor.

On the contrary the total pressure distribution is affected by both rotors to the same extent. The fluctuations of total pressure induced by the LP rotor are still correlated to the local acceleration induced within the blade passage. Whereas the fluctuations induced by the HP rotor are due to the complex modal interaction originating from the unequal number of blades and vanes.

The superposition of the fluctuations induced by the two rotors, represented by the "sum" of the two phase averages, shows distributions very similar to the rotor synchronic average. Briefly, the influence of the two rotors on the flow may be interpreted by means of a superposition of effects. However, the energy content of the original signal is preserved just by the RSA. Even though the mutual interactions between the two rotors is reduced by the presence of low aspect ratio turning struts and of a diffusing duct, the correct reconstruction of the periodic flow is provided just by the RSA.

To the knowledge of the authors, this is among the first attempts of interpretation of unsteady data in a counter-rotating turbine test rig. The rotor synchronic average was developed to observe the global evolution of the flow under such complex conditions. Such technique may be used together with the classical phase locked averaging procedure to isolate the effects of the rotors, determine the influence of their mutual interactions, and account for the overall deterministic unsteadiness.

Acknowledgements

The research leading to these results has received funding from the European Union Framework Programme (FP7/2007–2013) under Grant agreement No. 211861 as well as from the Austrian Ministry for Science and Research. MTU Aero Engines and Volvo Aero are acknowledged for allowing us to publish the data.

References

[1] E. Göttlich, Research on the aerodynamics of intermediate turbine diffusers, Prog. Aerospace Sci. 47 (4) (2011) 249–279.
[2] R.J. Miller, R.W. Moss, R.W. Ainsworth, N.W. Harvey, The effect of an upstream turbine on a low-aspect ratio vane, in: Proceedings of ASME Turbo Expo 2004, June 14–17, Vienna, Austria, ASME Paper No. GT-2004-54017, 2004.
[3] R.L. Davis, J. Yao, J.P. Clark, G. Stetson, J.J. Alonso, A. Jameson, C.W. Haldeman, M.G. Dunn, Unsteady interaction between a transonic turbine stage and downstream components, in: Proceedings of ASME Turbo Expo, June 3–6, Amsterdam,The Netherlands, ASME Paper No. GT-2002-30364, 2002.
[4] S. Lavagnoli, T. Yasa, G. Paniagua, L. Castillon, S. Duni, Aerodynamic analysis of an innovative low pressure vane placed in an S-shape duct, J. Turbomach. 134 (2012) 011013 (13 pages).
[5] L.-U. Axelsson, Experimental Investigation of the Flow Field in an Aggressive Intermediate Turbine Duct, PhD. Thesis, Department of Applied Mechanics of Chalmers University of Technology, ISBN0:978-91-7385-264-7, 2009.
[6] A. Marn, On the Aerodynamics of Aggressive Intermediate Turbine Ducts for Competitive and Environmentally Friendly Jet Engines, PhD. Thesis, Institute for Thermal Turbomachinery and Machine Dynamics of Graz University of Technology, 2008.
[7] J. Hubinka, C. Santner, B. Paradiso, F. Malzacher, E. Göttlich, F. Heitmeir, Design and construction of a two shaft test turbine for investigation of mid turbine frame flows, in: 19th International Symposium on Airbreathing Engines, September 7–11, Montreal, Canada, ISABE Paper ISABE-2009-1293, 2009.
[8] M.M. Weaver, S.R. Manwaring, R.S. Abhari, M.G. Dunn, M.J. Salay, K.K. Frey, N. Heidegger, Forcing function measurements and predictions of a transonic vaneless counter rotating turbine, in: Proceedings of ASME Turbo Expo 2000 (IGTI), May 8–11, Munich, Germany, ASME Paper 2000-GT-375, 2000.
[9] B.D. Keith, D.K. Basu, C. Stevens, Aerodynamic test results of controlled pressure ratio engine (cope) dual spool air turbine rotating rig, in: Proceedings of ASME Turbo Expo 2000 (IGTI), May 8–11, Munich, Germany, ASME Paper 2000-GT-632, 2000.
[10] C.W. Haldeman, M.G. dunn, R.S. Abhari, P.D. Johnson, X.A. Montesdeoca, Experimental and computational investigation of the time-averaged and time resolved pressure loading on a vaneless counter-rotating turbine, in: Proceedings of ASME Turbo Expo 2000 (IGTI), May 8–11, Munich, Germany, ASME Paper 2000-GT-445, 2000.
[11] T.J. Praisner, E. Grover, R. Mocanu, R. Jurek, R. Gacek, Predictions of unsteady interactions between closely coupled HP and LP turbines with co-and counter-rotation, in: Proceedings of ASME Turbo Expo 2010, June 14–18, Glasgow, UK, ASME Paper No. GT2010-23681, 2010.
[12] Z. Qingjun, D. Jianyi, W. Huishe, Z. Xiaolu, X. Jianzhong, Tip clearance effects on inlet hot streak migration characteristics in high pressure stage of a vaneless counter-rotating turbine, J. Turbomach. 132 (2010) 011005 (8 pages).
[13] A. Hussain, W. Reynolds, The mechanics of an organized wave in turbulent shear flow, J. Fluid Mech. 41 (1970) 241–258.
[14] O.P. Sharma, T.L. Butler, H.D. Joslyn, R.P. Dring, Three-dimensional unsteady flow in an axial flow turbine, AIAA J. Propul. Power 1 (1) (1985) 29–38.
[15] K.L. Suder, M.D. Hathaway, T.H. Okiishi, A.J. Strazisar, J.J. Adamczyk, Measurements of the unsteady flow field within the stator row of a transonic axial-flow fan: part 1-measurement and analysis technique, NASA Tech. Memorand. 88945 (1987).
[16] C. Santner, B. Paradiso, F. Malzacher, M. Hoeger, J. Hubinka, E. Göttlich, Evolution of the flow through a turning mid turbine frame applied between a transonic hp turbine stage and a counter-rotating lp turbine, in: Proceedings of 9th European Turbomachinery Conference, March 21–25, Istanbul, Turkey, Paper No. 110, 2011.
[17] B. Paradiso, C. Santner, J. Hubinka, E. Göttlich, M. Hoeger, Turning mid turbine frame behavior for different hp turbine outflow conditions, in: Proceedings of ASME Turbo Expo 2011, June 6–10, Vancouver, Canada, ASME Paper No. GT2011-46506, 2011.
[18] J. Erhard, A. Gehrer, Design and construction of a transonic test turbine facility, in: Proceedings of ASME Turbo Expo 2000 (IGTI), May 8–11, Munich, Germany, ASME Paper 2000-GT-480, 2000.
[19] J. Hubinka, B. Paradiso, C. Santner, E. Göttlich, F. Heitmeir, Design and operation of a two spool high pressure test turbine facility, in: Proceedings of 9th European Turbomachinery Conference, March 21–25, Istanbul, Turkey, Paper No. 112, 2011.

Please cite this article in press as: D. Lengani et al., Analysis tools for the unsteady interactions in a counter-rotating two-spool turbine rig, Exp. Therm. Fluid Sci. (2012), http://dx.doi.org/10.1016/j.expthermflusci.2012.05.010

[20] P. Kupferschmied, O. Köppel, W.P. Gizzi, G. Gyarmathy, Time resolved flow measurements with fast response aerodynamic probes in turbomachinery, Measur. Sci. Technol. 11 (7) (2000) 1036–1054.
[21] L. Porreca, M. Hollenstein, A.I. Kalfas, R.S. Abhari, Turbulence measurements and analysis in a multistage axial turbine, J. Propul. Power 23 (1) (2007) 227–234.
[22] D. Lengani, B. Paradiso, A. Marn, A method for the determination of turbulence intensity by means of a fast response pressure probe and its application in a LP turbine, J. Therm. Sci. 21 (2012) 21–31.
[23] A. McAlpine, M.J. Fisher, On the prediction of "buzz-saw" noise in aero-engine inlet ducts, J. Sound Vibrat. 248 (1) (2001) 123–149.
[24] N. Arndt, Blade row interaction in a multistage low-pressure turbine, ASME J. Turbomach. 115 (1993) 137–146.
[25] D. Lengani, B. Paradiso, A. Marn, E. Göttlich, Identification of spinning mode in the unsteady flow field of a low pressure turbine, J. Turbomach. 134 (2012) 1715–1724.
[26] J.M. Tyler, T.G. Sofrin, Axial flow compressor noise, SAE Trans. 70 (1962) 309–332.

Please cite this article in press as: D. Lengani et al., Analysis tools for the unsteady interactions in a counter-rotating two-spool turbine rig, Exp. Therm. Fluid Sci. (2012), http://dx.doi.org/10.1016/j.expthermflusci.2012.05.010

Proceedings of ASME Turbo Expo 2012
GT2012
June 11-15, 2012, Copenhagen, Denmark

GT2012-68583

EXPERIMENTAL INVESTIGATION OF THE UNSTEADY FLOW FIELD DOWNSTREAM OF A COUNTER-ROTATING TWO-SPOOL TURBINE RIG

Davide Lengani, Cornelia Santner, Rosario Spataro, Berardo Paradiso*, Emil Göttlich
Inst. f. Thermal Turbomachinery and Machine Dynamics
Graz University of Technology, Austria
Email: davide.lengani@tugraz.at

ABSTRACT

The paper presents an experimental investigation of the unsteady flow field in the two-spool counter-rotating transonic turbine at Graz University of Technology. The test setup consists of a high pressure (HP) stage, a diffusing mid turbine frame with turning struts (TMTF) and a shrouded low pressure (LP) rotor. The two rotors are mounted on mechanically independent shafts in order to provide engine-representative operating conditions. The rig was designed in cooperation with MTU Aero Engines and Volvo Aero within the EU project DREAM (ValiDation of Radical Engine Architecture SysteMs).

A two-sensor fast response aerodynamic pressure probe (2S-FRAP) has been employed to provide time-resolved aerodynamic area traverses downstream of the LP turbine. Such measurement allows estimating the total deterministic unsteadiness transported through the duct. In particular, it has been possible to isolate the structures induced by each rotor by means of the encoders mounted on the two shafts. A global ensemble averaged field, which takes into account the rotor-rotor interactions, is also provided. The time resolved distributions of the flow quantities are then discussed in details. The perturbations due to the HP rotor in terms of velocity and flow angle are negligible in this downstream plane. Indeed, the largest fluctuations of velocity are due to the TMTF-LP rotor interaction, they occur in the wake and secondary flows of the TMTF. Large fluctuations of static and total pressure are instead due to both rotors to the same extent.

Nomenclature

2S-FRAP	2 sensor fast response aerodynamic pressure probe
BPF	Blade passing frequency
c_{ax}	Axial chord
C_{pt}	Total pressure coefficient
FHP	Five hole probe
h	Channel height
H	Relative channel height
HP	High pressure
LP	Low pressure
M	Mach number
$m_{r,in}$	Reduced mass flow, stage inlet
$n_{r,in}$	Reduced rotational speed, stage inlet
p_t	Total pressure
PLA	Phase locked average
Re	Reynolds number
REV	Revolution period
RSA	Rotor-synchronic average
T	Blade passing period
TMTF	Turning mid turbine frame
v	velocity
ρ	Flow density
θ	Circumferential coordinate
$<>$	purely periodic component

Subscripts

AVE	Circumferentially averaged properties
MAX	Maximum value, in the local plane

Superscripts

$\bar{}$	Time averaged properties
$\sim$	Phase locked properties
$'$	Stochastic fluctuating component

INTRODUCTION

The trend for further increasing the by-pass ratio of modern aero-engines leads to a very large radial off-set between the high (HP) and low pressure (LP) turbines. The intermediate turbine diffuser must be able to guide the flow to the low pressure turbine with low disturbances and avoiding flow separation. Furthermore, a new concept of integrated design [1],

*Currently affiliated with Dipartimento di Energia, Politecnico di Milano.

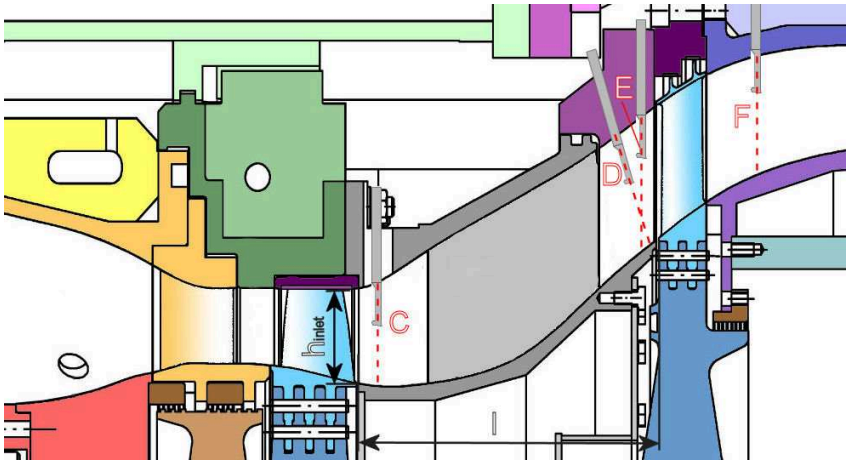

FIGURE 1. Schematic meridional section of the test setup with probe measurement planes (C, D, E, F).

which combines the function of a strut with that of a LP-vane, has been recently developed. The first LP stage is, then, constituted by the intermediate turbine diffuser provided with turning vanes (TMTF) and an LP rotor embedded at the outlet of the duct.

The aerodynamic performances of the diffusing duct and hence of the first LP stage are influenced by many effects, as recently reviewed by Göttlich [2]. Wakes, secondary flows, swirl, tip leakage flow and trailing edge shocks occurring in the exit flow of the HP stage and their unsteady interactions with the struts embedded in the duct generate a very complex flow field. For these reasons, many efforts have been done in the last years on this field by different research groups on sophisticated test turbines (Oxford [3], Ohio State University [4], Von Karman Institute [5], Chalmers University of Technology [6] and Graz University of Technology [7]). It has been shown that the vortices produced by the HP rotor close to the endwalls energize the duct boundary layer there enabling it to better withstand the adverse pressure gradient. However, the unsteadiness does not decay within the duct and it influences the secondary flows of the turning vanes embedded in the diffuser and hence its outlet flow. Particularly, the extent of the unsteadiness at the outlet of the duct, downstream of the first LP rotor, is critical for the aerodynamic performances, vibrations and acoustic emissions of the successive LP stages, and, then, need a careful analysis.

Therefore, the next step of these research is to focus on the effect of the diffusing duct together with up-and downstream components [2]. Just recently, Hubinka et al. [8] developed an engine relevant test setup for turning mid turbine frames with up-and downstream turbine stages. The work presented in this paper includes time-resolved aerodynamic area measurements performed on this research facility. A two sensor fast response aerodynamic pressure probe (2S-FRAP) in a four-sensor virtual mode has been used to provide the unsteady flow field in different planes of the research turbine. The paper focuses on the analysis of the unsteady flow at the exit of the test section downstream of the LP rotor. The sources of unsteadiness are identified considering the HP stage-TMTF-LP rotor interaction by means of the proper analysis of the time signal of the probe. Thus, the deterministic fluctuations of the flow quantities, velocity, flow angles and total pressure, are quantified in order to provide the inlet conditions for the design of the successive stages.

EXPERIMENTAL APPARATUS AND METHODOLOGY

Facility

The transonic test turbine facility is a continuously operating two-stage cold-flow open-circuit plant, which consists of a transonic HP stage and a counter-rotating LP stage (a schematic drawing is shown in Fig. 1). This unique configuration allows the testing of rig inserts under aerodynamic conditions relevant for modern aero-engine. Both turbines are designed with overhung-type turbine shafts and additionally the LP turbine is mounted on an axially movable frame. This allows easy disk assembly without dismantling the bearings and the simple application of transition duct and TMTF designs with different axial lengths. The facility is driven by pressurized air delivered by a separate 3 MW compressor station. The shaft power of the HP stage drives a three-stage radial brake compressor. The power of the LP turbine is absorbed by a water brake with a maximum power of 700 kW. Detailed information on the design and construction of the original single stage facility can be found in Erhard and Gehrer [9]. For the design of the LP-stage together with the TMTF see Hubinka et al. [8] and for the operation Hubinka et al. [10].

Test setup As already mentioned, the investigated test setup consists of a single-stage unshrouded transonic HP turbine, and an S-shaped turning mid turbine frame (TMTF) followed by a shrouded counter-rotating LP turbine. Figure 1 represents a meridional view of the test section. The incoming air is accelerated by the HP vanes in circumferential direction and impinges on the HP rotor designed with a cylindrical outer contour. Then it is turned by the struts of the TMTF in negative direction relative to the rotation of the HP rotor and the air enters the counter-rotating LP rotor assembled at a larger diameter.

Table 1 displays the main design parameters for the HP stage and the LP stage (TMTF+LP rotor), the design of which was provided by MTU Aero Engines. The HP turbine consists of 24 choked vanes and 36 blades. For the LP stage a blade

count of 16 struts and 72 blades was chosen.

The HP vanes as well as the outer casing downstream of the TMTF struts are fully rotatable in circumferential direction. This enables area traverses for probe and rake measurements in the four planes identified in Fig. 1.

Operating conditions Table 1 displays also the main parameters of the operating point. The investigated aero design has an overall pressure ratio of 4. The total pressure ratio is 3 for the HP turbine and 1.3 for the LP turbine. The HP vanes are operating under choked conditions. The absolute Mach number at TMTF inlet with a value of about 0.5 is representative for realistic duct inlet conditions of modern jet engines with a single stage HP turbine at cruise operating point.

TABLE 1. Blading parameters and operating conditions.

Blading parameters				
	HP vane	HP blade	TMTF	LP blade
Vane/ blade no.	24	36	16	72
h/c_{ax}	1.15	1.37	0.53	2.94
Re(10^{-6})	2.38	1.1	1.86	0.46
Tip gap	-	unshrouded	-	shrouded
Operating conditions				
	HP stage		LP stage	
$n_{r,in}$ $[rpm/\sqrt{K}]$	524.4		195.3	
$m_{r,in}$ $[kg/s \cdot \sqrt{K}/(bar)]$	81.2		214.6	
Stage p_t ratio	3		1.3	
Power [kW]	1710		340	

Measuring techniques

Full area traverses with a five-hole-probe (FHP) were performed to obtain the steady flow field. The measurement uncertainty for the Mach number is within +0.005 and -0.004, for the total pressure is within $\pm$300 Pa, and for the flow angles is $\pm$0.3 deg. These values contain the error due to the approximation and the systematic error of the multi channel pressure transducers used to operate the facility.

Unsteady flow measurements were performed by means of a 2-sensor fast response aerodynamic probe (2S-FRAP) [11], operated as a virtual four sensor probe for 3D aerodynamic measurements. Flow parameters including total and static pressure, flow angles and velocity components are derived from three rotations of the probe and a set of calibration coefficients (see for example Porreca et al. [12]). This probe is a modified version of the conventional cylindrical single sensor probe: the sensor sensible to the yaw angle is classically mounted on the cylindrical part and the second sensor, sensitive to pitch angle variation, is mounted on the shaped probe head. The dimensions of each piezoresistive sensor are 0.4 $\times$ 0.8 mm, the distance between the two sensors is approximately 2.2 mm and the tip diameter of the probe is 1.8 mm. This concludes that the sensing area of the probe is in the order of 3.9 mm^2. The absolute uncertainties of the used probe techniques are equal to $\pm$0.3 deg for the flow angles, and $\pm$0.4% for the Mach number. The uncertainty on the absolute value of the total pressure is $\pm$300 Pa when the uncertainty of the multi channel pressure transducers, employed to operate the facility, is also considered.

The present paper describes the results obtained by the two probes in annular sectors in planes D and F (marked in Fig. 1). Plane D is a plane inclined by 110 deg to the horizontal direction and, at midspan, its distance from the vane trailing edge is 14% of the TMTF axial chord; whereas, plane F is perpendicular to the horizontal direction and is located at 77% of the LP rotor chord downstream of the LP blade trailing edge. Full area traverses were performed over one strut pitch (22.5 deg) downstream of the TMTF. The measurement grid consists, for both planes (D and F), of 21 positions along the blade span and of 46 positions over one TMTF pitch.

Data reduction method

Data is acquired at 200 kHz for 2 seconds, it corresponds to more than 100 revolutions of the LP turbine and more than 350 of the HP turbine. The determination of the flow properties is made possible after phase averaging: the periodic fluctuations of velocity, pressures and flow angles are determined at each phase from the phase averaged values of the three rotations of the probe [12].

Phase averaging was performed triggering the flow with the 2 shaft encoders according to the triple decomposition procedure [13], for a generic variable p:

$$p(t) = \overline{p} + < p > + p'(t) \tag{1}$$

where $< p >$ is the purely periodic component associated with a coherent periodic structure and $p'(t)$ is the random fluctuation associated mainly with turbulence. This decomposition is used to characterize a single source of periodic unsteadiness and, in the present case, allows isolating the effects of each rotor. However, considering the presence of two rotors (HP and LP rotor) at uncorrelated frequencies (2 uncorrelated coherent periodic structures) the decomposition may be rewritten as:

$$p(t) = \overline{p} + < p >_{HP} + < p >_{LP} + < p >_{HP,LP} + p'(t) \tag{2}$$

where the 2 distinct purely periodic components $< p >_{HP}$, $< p >_{LP}$ have their own period and frequency, and $< p >_{HP,LP}$ indicates the cross-interactions which generate energy content at the frequencies of the linear combination $i \cdot BPF_{LP} + k \cdot BPF_{HP}$ (with i and k integer and not zero). A particular phase averaging, rotor synchronic average (RSA), has been developed in order to provide the following time resolved distribution:

$$\tilde{p}_{RSA} = \overline{p} + < p >_{HP} + < p >_{LP} + < p >_{HP,LP} \tag{3}$$

The RSA, as described in the following section, preserves the frequency content of the coherent structures of the original signal.

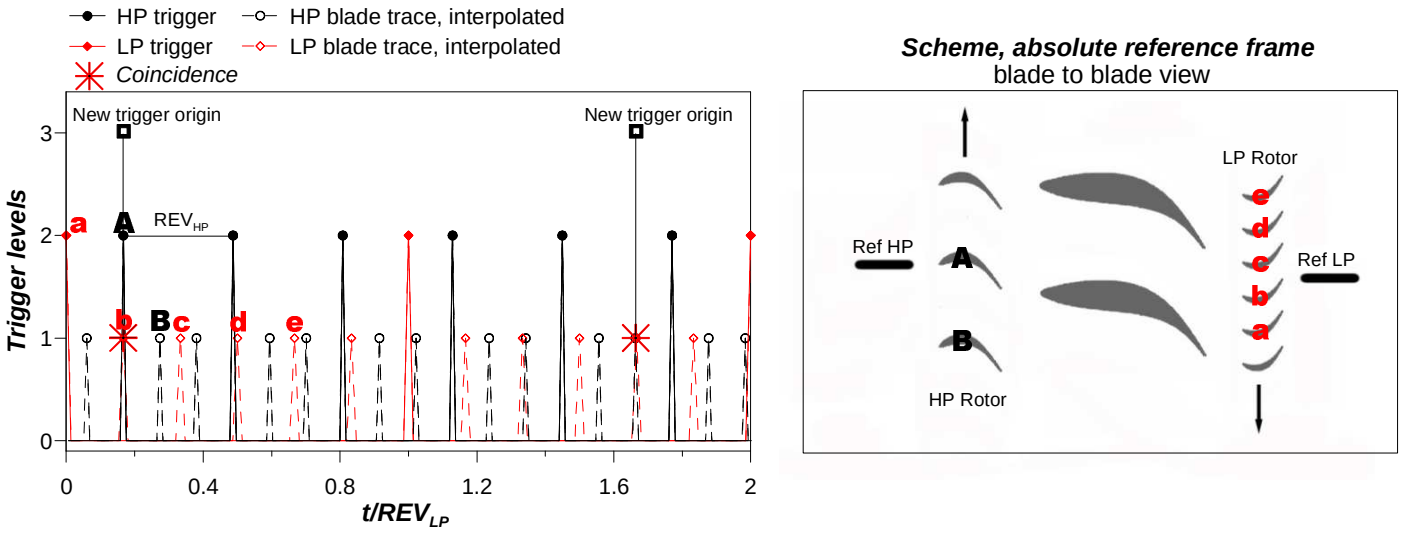

FIGURE 2. On the left, schematic representation of trigger post-processing; the trigger level is a symbolic number: a value of 2 corresponds to the shaft encoder triggers, a value of 1 to the interpolated blade periods within a revolution, and a value of 3 to the new trigger origin as coincidence positions of the previous levels. On the right, a scheme of the blade to blade view, the absolute reference for the two rotors (Ref. HP, Ref. LP) schematically represents the shaft encoder position.

Rotor-synchronic averaging Figure 2 shows a schematic representation of the shaft triggers. The non-dimensional time, which is the time divided through the revolution period of the LP turbine (REV_{LP}), is plotted on the abscissa, and the trigger level is plotted on the ordinate. The trigger level is a symbolic number associated to different origins of the trigger. A trigger level equal to 2 corresponds to the shaft encoder signals and identifies the beginning and end of the revolutions of each rotor, red filled diamonds for the LP turbine and black filled dots for the HP turbine (the label REV_{HP} superimposed to the plot helps the identification of a revolution of the HP rotor, while the revolution period of the LP turbine may be read on the x-axis). The trigger level equal to 1 corresponds to the identification of the blades within the revolution, namely every revolution is divided in equi-distant intervals corresponding to the trace of the blade passing period. For readability of the graph, the HP rotor has been simplified to 3 blades (hollow black circles), 3 constant blade periods within one revolution, and 6 blades for the LP turbine (hollow red diamonds) maintaining the original HP blade to LP blade count ratio (36 to 72), such blade triggers are interpolated. A simple algorithm is then written with the purpose of identifying positions of coincidence between the triggers of the two rotors at levels 1 and/or 2. When this condition is satisfied the blades of the two rotors are always in the same absolute position, as it is shown in the blade to blade view of Fig. 2, on the right. The coincidence is, then, considered as the origin of the phase averaging procedure indicated as "level 3" trigger in the picture. The end of the averaging period is instead chosen following these two criteria:
1) a fixed number of LP blades is counted after the coincidence position;
2) within this time interval the ratio of HP blade periods to LP blade periods is computed, if the ratio is different from the theoretically predicted for more than a fixed uncertainty the period is discarded.

The very stable operating conditions of the facility allowed the evaluation of 7 LP blade passing periods without discarding any interval since the computed blade ratio has variations below 0.5%. Furthermore, considering an uncertainty of $1/1000$ of the blade passing period of the HP rotor for the determination of the trigger "level 3", 600 coincidence positions are found within the 2 seconds of acquisition time. Finally, the 600 periods identified following these criteria are phase averaged.

RESULTS AND DISCUSSION

Results are presented in this section as contour plots in the absolute (stationary) reference frame. Mach number and total pressure are plotted as non-dimensional coefficients: the Mach number is shown in terms of M/M_{MAX}, where M_{MAX} is the maximum value of the time average Mach number in the local measurement plane; whereas, the total pressure is plotted as non dimensional coefficient C_{pt} defined as:

$$C_{pt} = \frac{p_t - p_{MAX}}{0.5\rho v_{MAX}^2} \tag{4}$$

where p_{MAX} is the maximum value of the time averaged static pressure measured in the local measurement plane. According to these definitions and to the radial pressure gradient induced by the diffusing duct, negative values of the pressure coefficients may be observed. The definitions are applied to both time averaged and time-resolved quantities, and are adopted to preserve the original distributions of the Mach number and total pressure, as they will be referred to in the discussion.

The aerodynamic area traverse plots (Fig. 3 to 6) are views in the downstream direction on a sector covering one pitch of the TMTF. Consequently, the pictures cover 4 and 1/2 LP rotor blades and 2 and 1/4 blades of the HP rotor. In the plots the LP rotor has a clockwise sense of rotation while it is the opposite for the HP rotor.

Results from the two probes (FHP and 2S-FRAP) agree very well in the plane downstream of the LP rotor, and hence the discussion of this plane is based just on the 2S-FRAP. Similarly, a good agreement between the two probes was found for plane D. However, in this upstream plane, the 2S-FRAP was out of calibration range in a small region; the results shown for plane D (Fig. 3) are obtained from the FHP measurements.

Time averaged flow field

Before discussing the time resolved flow structures, the time averaged flow upstream and downstream of the LP rotor is introduced (Fig. 3 and 4, respectively). The understanding of the mean flow features is, in fact, necessary to discuss the more complex time resolved flow evolution.

In these plots secondary velocity vectors, which help identifying the secondary flows, are superimposed to the total pressure distribution. Such vectors are defined as the difference between the local velocity vector and a reference flow direction (see for example Chaluvadi et al. [14], Persico et al. [15], and Bagshaw et al. [16]). In the present case the reference flow vector has been determined subtracting from the local values the averages of the circumferential and radial velocity components in the radial and the circumferential directions respectively. This procedure is made necessary by the velocity gradients that characterize the mean flow in both directions.

Detailed discussions of the flow in plane D, upstream of the LP rotor, were provided by Santner et al. [17], Paradiso et al. [18], and Spataro et al. [19]. They found that high velocity gradients characterize the mean flow in both radial and circumferential directions: the radial gradients of velocity are due to the diffusing channel and to the endwall boundary layers while the gradients in the circumferential direction are due to the turning of the flow evoked by the struts. The regions with lower momentum were identified in the TMTF wake.

Figure 3 shows the time mean total pressure, and confirms that the wake region (marked as "TMTF wake" over the plot) presents the lowest momentum. Particularly, the lowest values of total pressure may be observed at the tip on the vane wake

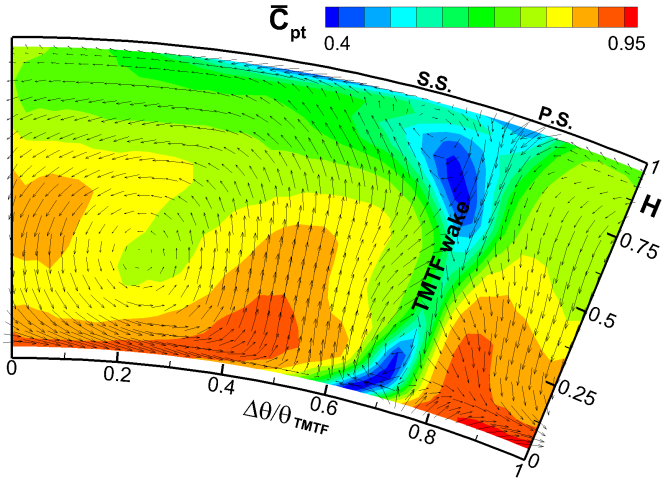

FIGURE 3. Time-averaged distributions of the total pressure coefficient and secondary velocity vectors in plane D.

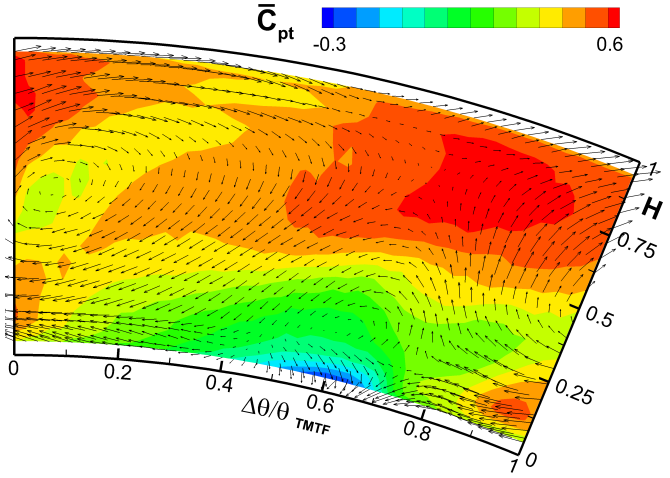

FIGURE 4. Time-averaged distributions of the total pressure coefficient and secondary velocity vectors in plane F.

suction side (on the left of the wake, marked as "S.S." on the plot), and, similarly, low values of total pressure are measured in the wake suction side close to the hub. Two vortices are superimposed to these two areas at low total pressure in the wake tip and hub. A third relevant vortical structure that covers the lower side of the span may be instead identified as the passage vortex [19], the core of which ($\Delta\theta/\theta_{TMTF} \cong 0.2$) presents a local reduction of the total pressure.

This large vortical structure may be observed also downstream of the LP rotor (Fig. 4). This vortex is pushed towards the hub by the radial pressure gradient and together with the TMTF wake hub vortex generates the region at lowest total pressure. The mean flow is characterized by another large vortical structure, which leads to another region at low total pressure. This vortex may be observed at around midspan for $\Delta\theta/\theta_{TMTF} \cong 0.1$ and it has the same sense of rotation of the vortex observed at the tip in the suction side branch of the wake in plane D. The wake of the TMTF is in fact skewed by the swirling motion induced by the TMTF and also by the rotor, therefore, the intensity of such vortex is enhanced. The inclined/skewed region at low total pressure that is surrounded by this vortex may be then thought as the trace of the remaining of the TMTF wake.

Time resolved flow field

LP rotor phase As previously discussed, the flow downstream of the LP rotor is characterized by multiple sources of unsteadiness (see eq. 2). In order to simplify the analysis of such complex flow the time resolved results are discussed at first considering the phase average based on the LP rotor. As previously mentioned (eq. 1), such phase averaging preserves just the coherent fluctuations due to the LP rotor. Three time snapshots are extracted from one blade passing period in order to show the time evolution of the Mach number, and total pressure (Fig. 5 and 6, respectively). To allow the identification of the blade wake positions, the isocontour lines of the periodic fluctuations of the Mach number ($< M >= \tilde{M} - \overline{M}$) are superimposed on the plot of Fig. 5. The

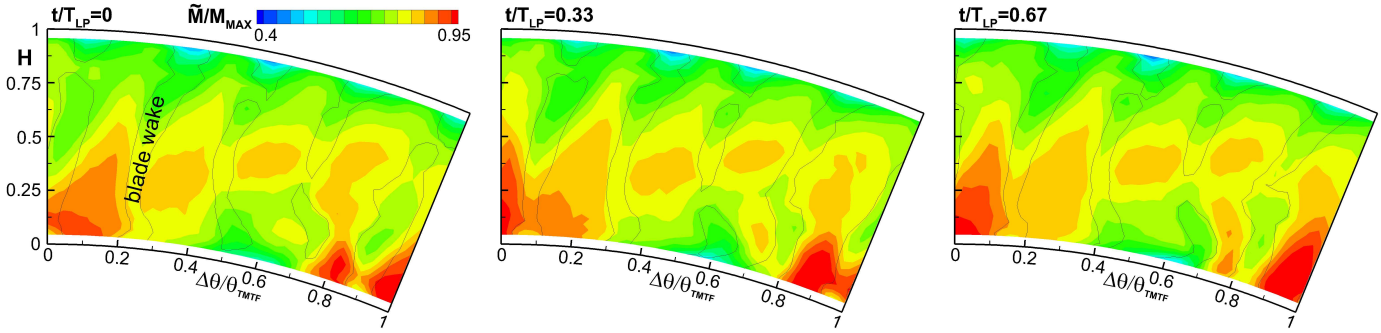

FIGURE 5. Time-resolved distribution of the absolute Mach number, and iso-contour lines of $< M > /M_{MAX} = -2\%$, plane F.

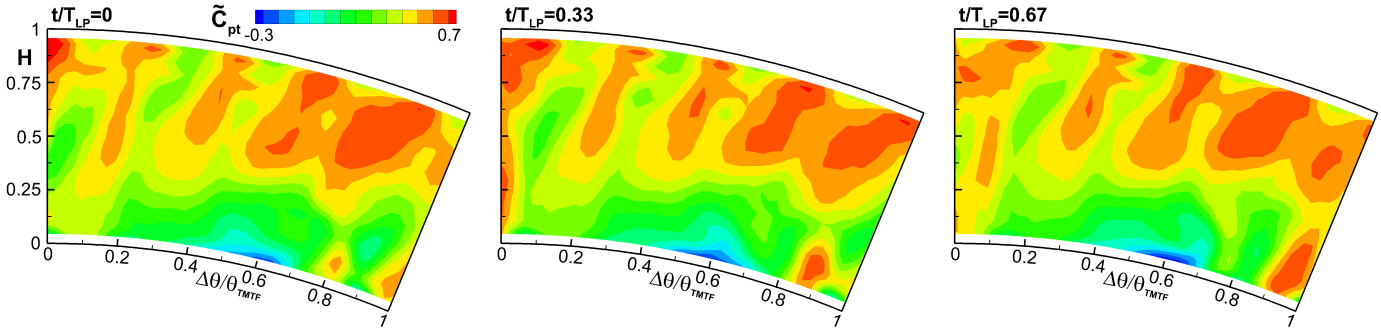

FIGURE 6. Time-resolved distribution of the total pressure, plane F.

position of one of the rotor wake is marked over the experimental results and it is enclosed by the iso-contour lines of $< M > /M_{MAX} = -2\%$, and, similarly, the other blade wakes may be identified enclosed within the iso-contour lines. Hence, a clear trace of the 4 and 1/2 blades of the LP rotor, which is moving in the clockwise direction, may be observed. The flow features caused by the rotor blade are strongly influenced by the TMTF flow field and the duct geometry. In fact, the largest velocity defects occur in the tip region and in correspondence of the TMTF passage vortex.

At the tip, the duct curvature (see Fig. 1) makes the flow turning, the radial pressure gradient pushes the flow towards the hub, and, hence, the velocity at the outer casing is reduced. At the same time, each blade generates a tip passage vortex which characterizes the velocity distribution in the region closer to the tip. Furthermore, a particular "triangular shape" may be observed in the half top midspan, it arises from the radial gradients induced by the duct and the circumferential pressure gradient within each blade passage. These structures slightly change with the relative circumferential position of blade and struts (compare the different time steps of Fig. 5). The highest gradients of velocity may be identified in the region of the TMTF wake, as shown in Fig. 4.

At the hub, the large vortical structure observed in the mean flow (Fig. 4) characterizes strongly the time resolved flow field. It generates a strong circumferential gradient of velocity. For example, in the last time snapshot, the Mach number passes from its minimum value to its maximum between $\Delta\theta/\theta_{TMTF} \cong 0.6$ and $\Delta\theta/\theta_{TMTF} \cong 0.95$. Due to this structure it is hard to identify the trace of the blade passage vortex which is, also, pushed towards the inner casing by the radial pressure gradient. Furthermore, the blade sweep (see for example [20]) should reduce the effect of secondary flows. However, the trace of the blade velocity defect may be still observed from the iso-contour line of $< M >$. This trace is bowed and becomes thicker while the blade is passing through the TMTF vortical structure: in the last time step, at $\Delta\theta/\theta_{TMTF} \cong 0.75$ the blade passage seems then thinner, leading to the large gradients of velocity in circumferential direction and in time.

Similar considerations may be obtained from the total pressure time resolved evolution (Fig. 6). Its largest fluctuations may be observed in this particular position ($0.7 < \Delta\theta/\theta_{TMTF} < 1.0$), where the shape of the total pressure varies considerably between the different time steps. On the other hand, the core of low total pressure identified in the time mean result (Fig. 4) seems just slightly influenced by the unsteady blade motion. At the tip, as observed for the velocity distribution, the highest fluctuations of the total pressure may be identified for $\Delta\theta/\theta_{TMTF} \cong 0.35$, where the LP rotor is interacting with the TMTF wake.

To summarize, it has to be noted that this behaviour is different from what is classically observed in the open literature of LP turbines (e.g., [21, 22]). In fact, in conventional LP turbines, the flow at the outlet of adjacent blade passages is rather similar, the circumferential gradients are due to the blade loading, and the thickness and velocity defect of the blade wake depends on the vane wake-blade interactions (e.g., [23]). Furthermore, such 2D interaction phenomenon is the predominant in the generation of losses. Instead, in the present case, the rotor is interacting with a strut of completely different solidity and aspect ratio (see Table 1). In particular, adjacent blade passages present different velocity and total pressure distributions. The regions with lower momentum may be then found within the blade wake, and mostly in large portion of plane where the rotor interacts with the large vortical structures evoked by the TMTF.

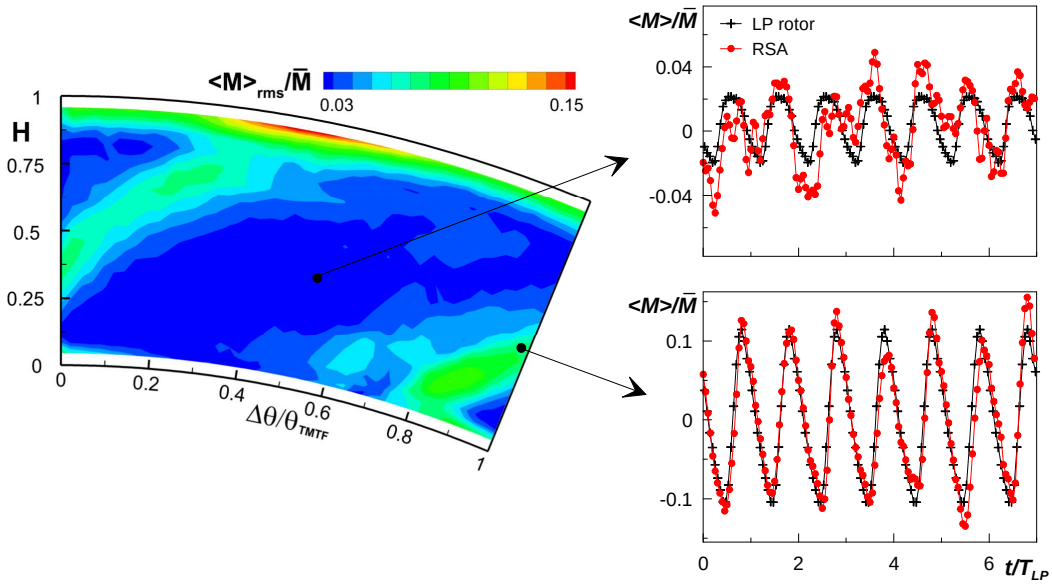

FIGURE 7. Temporal evolution of the coherent fluctuations of the Mach number, at selected locations (right); and their root mean square computed from the RSA (left), plane F.

Overall unsteadiness The flow field presented in the previous plots (Fig. 5 and 6) is related just to the structures, coherent fluctuations, induced by the LP rotor. However, the unsteadiness in the second stage of a counter rotating turbine is related also to the HP rotor and the rotor-rotor interactions (see eq. 3). The overall periodic unsteadiness is captured just by the RSA, which preserves the energy content of the original signal and separates it from the stochastic unsteadiness (turbulence). As described before, the phase average field computed by the RSA is constituted of 7 LP blade passing periods. The flow over the blade passing periods identified with this procedure is not exactly periodic. In fact, it is influenced by the HP rotor which has a periodicity different from the LP rotor. In order to provide informations about the overall periodic unsteadiness, the root mean square (RMS) of the coherent periodic fluctuations of different flow quantities is then provided in the following figures (Fig. 7 to 9). This quantity, computed as described by Tiedemann and Kost [24], represents an integral measure for the purely periodic component of the signal. Considering eq. 3, the periodic part obtained by the RSA ($< p >_{RSA}$), for a generic variable p, may be computed as $\tilde{p}_{RSA} - \overline{p}$:

$$< p >_{RSA} = < p >_{LP} + < p >_{HP} + < p >_{LP,HP} \qquad (5)$$

The RMS of this quantity is represented by one value for each measurement position. It estimates the amplitude of the temporal fluctuations induced by the unsteady interactions with the upstream rows, namely the HP stage and the TMTF (similar considerations may be found in [24, 25]). Furthermore, it may provide informations for the design of the successive stage as it will be discussed in the followings.

Figure 7 shows the contour plot of the RMS of the Mach number periodic component ($< M >_{rms}$) computed from the RSA. The largest fluctuations may be observed in correspondence of the trace of the TMTF wake and at the tip. The first region is the inclined line, which starts at $\Delta\theta/\theta_{TMTF} \cong 0.8$ at the hub, and that, for periodicity, ends at $\Delta\theta/\theta_{TMTF} \cong 0.4$ at the tip. The contour of this area matches quite well with the region at low mean total pressure identified in Fig. 4. The second region extends over the whole TMTF pitch for 15% of the blade height at the tip, and its maximum may be observed when it intersects the TMTF wake. This effect is due to the blade tip passage vortex which extends its fluctuations when it interacts with the TMTF structure from upstream. Another core of high fluctuations may be also identified at $\Delta\theta/\theta_{TMTF} \cong 0.6$, close to the hub, where the remainings of the TMTF vortices are located (see Fig. 4), however, the magnitude of its fluctuations is lower than in the previous two regions.

However, for the largest portion of the measurement plane the fluctuations of Mach number are rather small, below 3% of the local time mean value $\overline{M}$. It is now important to note that in this large region the $< M >_{rms}$ is not only due to the periodic fluctuations induced by the LP rotor but also to the fluctuations of the HP rotor and their interaction. The top right plot

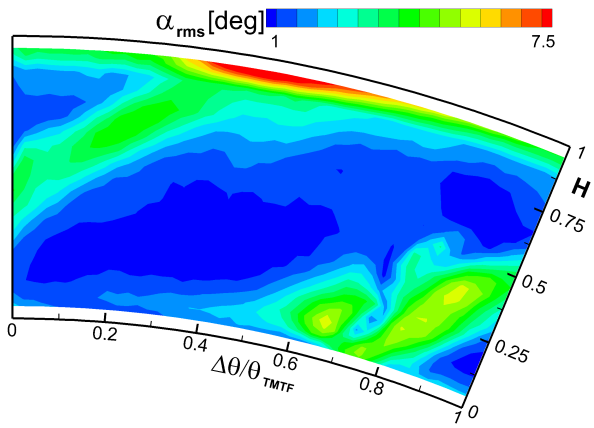

FIGURE 8. Root mean square of the coherent fluctuations of the flow yaw angle computed from the RSA, plane F.

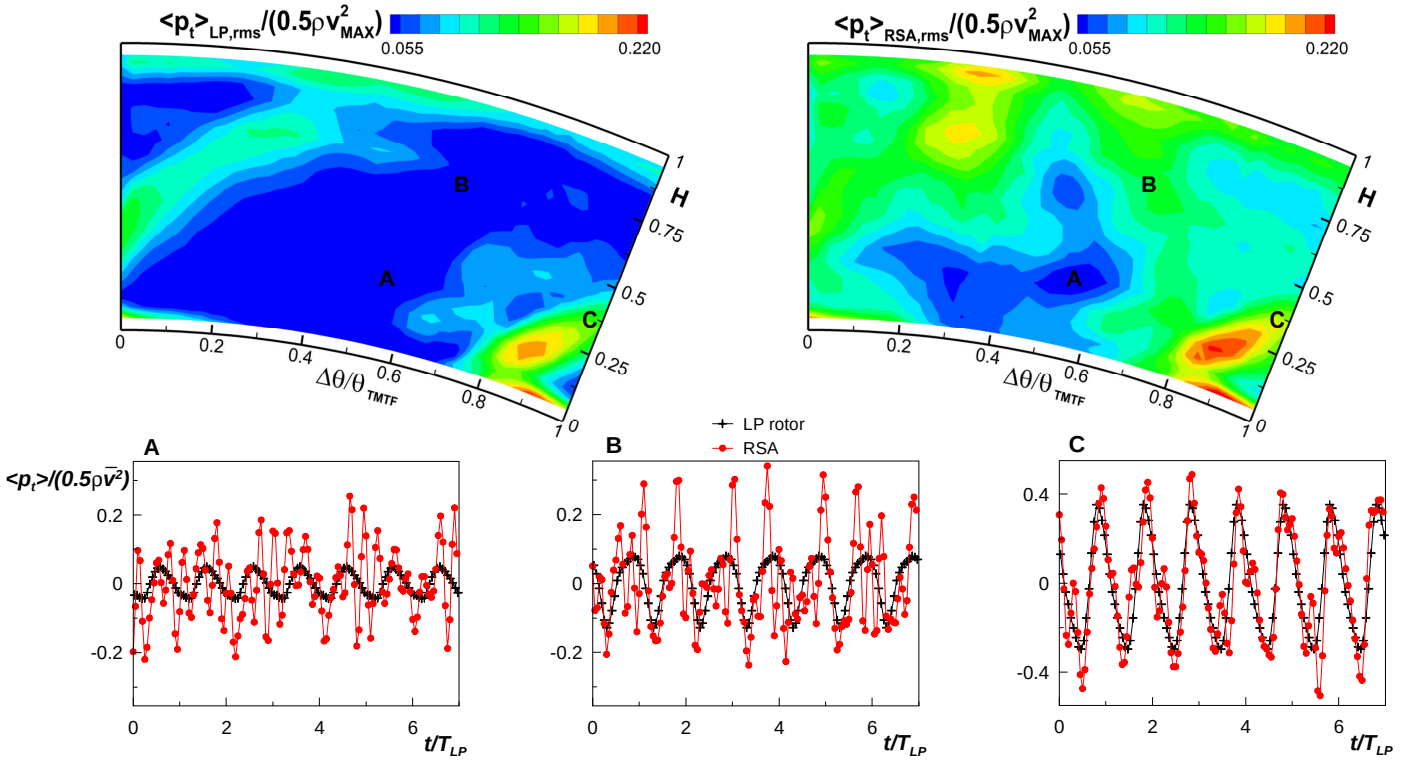

FIGURE 9. Temporal evolution of the coherent fluctuations of total pressure, at selected locations (bottom), and their root mean square (top), plane F.

of Fig. 7 shows the temporal evolution of the purely periodic Mach number due to two different decompositions, the LP rotor phase in black and the RSA in red. It shows that the oscillations induced by the LP rotor are lower than the one due to the overall unsteadiness (RSA). However, in the region with the highest level of RMS (TMTF wake and tip passage vortex) the situation is different, there the TMTF-LP rotor interaction generates the highest contribution to the overall unsteadiness. As an example, the temporal fluctuations are shown for the TMTF wake region in the bottom right plot of Fig. 7. In this case, the oscillations are due to the LP rotor and its interaction with the TMTF. The temporal evolution of the $< M >$ due to the overall unsteadiness ($< M >_{RSA}$) is, in fact, very similar to the unsteadiness of the LP rotor alone. Hence, the unsteady rotor-rotor interaction plays a minor role in determining large RMS of coherent fluctuations of velocity.

Similar considerations may be done for the coherent fluctuations of the flow yaw angle on the cross-section plane shown in Fig. 8. In this figure, the temporal evolution of the coherent fluctuations is not represented, since its behaviour is similar to the one discussed above. However, some differences may be identified in the distribution of the RMS. The yaw angle fluctuations close to the center of the remaining of the TMTF passage vortex are now of the same order of magnitude of the fluctuations in the trace of the TMTF wake. Whereas, the largest fluctuations may still be identified in the tip region, where the tip passage vortex of the LP blades interact with the TMTF. Similarly, in this same region, the pitch angle (not shown) presents its highest fluctuations.

This plot provides also a very important information. The successive vane row will experience, in the particular positions previously identified, very large, unsteady, variations of the incidence. Considering that for a sinus the maximum amplitude is equal to the $\sqrt{2}$ of its RMS, a measured RMS of 5 deg corresponds to a minimum to maximum oscillation of circa 14 deg. Such incidence deviation is considerably high and may lead not only to reduced performance but also to very high unsteady loading and hence excessive vibrations.

A further and non negligible contribution to the unsteady loading comes from the total and static pressure fluctuations. In the present configuration the oscillations of total and static pressure, and their radial time mean distributions have been found similar and, hence, in the next figure (Fig. 9) just the total pressure is shown. The considerations that will be done discussing the total pressure may be considered valid also for the static pressure, which, of course presents lower values and oscillations.

The behaviour of the RMS of total pressure is different from what previously observed. For this reason, Fig. 9 shows the RMS of total pressure (made non-dimensional by the maximum dynamic pressure) for two different decompositions and not just for the RSA. On the top left part of the picture, the RMS of $< p_t >$ is computed from the LP rotor phase and, indeed, it shows the same characteristics of the RMS of $< M >$ computed from the RSA (Fig. 7 on the left). On the top right part of Fig. 9, the RMS of $< p_t >$ is instead computed from the RSA, and it shows larger values than the RMS of $< p_t >$ just due to the LP rotor. The pressure fluctuations propagating from the HP stage, which are caused by the strong shock waves generated by the stator and rotor rows and by their unsteady interaction (e.g., [26]), do not decay within the duct. As described by Göttlich [2], the trailing edge shocks emanating from the

upstream HP vanes and blades cause pressure waves entering the duct periodically. These pressure waves cause, then, a significant contribution in the pressure fluctuations at the exit of the duct.

Furthermore, the area at high fluctuations may not be immediately linked to the TMTF structures. However, as it is shown in Lengani et al. [27], they may be correlated to the interaction between rotors and stators with different blade/vane number, which generates spinning modes [22, 28].

As performed for Fig. 7, the temporal evolution of the purely periodic total pressure, at selected locations, is shown in the bottom of Fig. 9 for the two different decompositions (LP rotor phase in black, and RSA in red). Even in the point marked as "A", where the RMS is low for both decompositions, it is possible to observe a strong influence of the structures emanated by the HP stage. The RSA temporal evolution in this point is, in fact, characterized by fluctuations at high frequency, not correlated to the LP rotor, which corresponds to two times the BPF of the HP rotor. In point "B" the influence of the rotor-rotor interaction is clear. Large peaks of $< p_t >_{RSA}$ appear at a particular periodicity which depends also on the linear combination of the two blade passing frequencies. Indeed, in this position, the fluctuations are due to the HP stage-TMTF-LP rotor modal interactions [27]. However, the largest fluctuations, point "C", are still measured in correspondence of the TMTF structures, the trace of its wake in this case. In this position the rotor-rotor interaction, which may be observed as the energy content at high frequencies in the RSA (red line), plays a minor role in determining such large fluctuations. The LP blade-TMTF wake interaction, still, shows the highest contribution to the RMS of total pressure. However, for the pressure fluctuations, the rotor-rotor interaction may not be neglected.

CONCLUSIONS

The development of the unsteady flow downstream of a two-stage counter-rotating turbine has been reported in the paper. The two stages are representative of modern jet-engine intermediate turbine ducts in realistic two spool conditions. Thus, the data set provided may be applied for computational code validation. Furthermore, the time resolved measurements have been adopted to characterize the sources of unsteadiness and their relative influence at the exit of the two stages. In fact, in such a configuration the outlet flow field is characterized by energy contents which are associated to the blade passing frequencies of the two rotors and their linear combinations.

It has been shown that the velocity and angle coherent fluctuations are determined, mainly, by the interactions of the LP blade with the structures emanated by the TMTF, namely its vortical structures and wake. In fact, in the region where the rotor-rotor interactions are measured, the overall unsteadiness presents very low fluctuations. Hence, in such positions, the unsteadiness will not represent a problem for the following stages. On the other hand, in the regions of LP blade-TMTF interaction the fluctuations of the flow angle and, hence, of the incidence of the following vane row are quite large. Due to the low aspect ratio of the TMTF these regions are extended for more than 15 % of the pitch and may, then, lead to large unsteady forcing and vibrations. However, the present investigation identified these areas and the causes which provoke such high angle fluctuations. According to this, it may be thought to have special design for the vane row downstream of a diffusing duct, or eventually to control, by means of active or passive devices, the flow exiting the TMTF. Different methods for reducing the wakes of airfoils have been proposed in literature (e.g., [29,30]) and they may be eventually applied to the TMTF, the low aspect ratio of which may facilitate their application.

Furthermore, it has been shown that total and static pressure fluctuations are also caused by the rotor-rotor interactions. Their highest fluctuations still depend on the TMTF-LP blade interaction. However, the rotor-rotor interactions lead to a larger area at high fluctuations. Indeed, fluctuations of pressure may lead to acoustic and vibrational problems. A careful design of the following stages has then to be done in order to damp out these excitations. On the other hand, flow control, duct and vane shape optimization, and endwall contouring are promising actions to optimize the design of the LP stage embedded in the duct and eventually reduce the extent of unsteadiness at its outlet.

ACKNOWLEDGMENT

The research leading to these results has received funding from the European Union Framework Programme (FP7/2007-2013) under grant agreement n° 211861 as well as from the Austrian Ministry for Science and Research. MTU Aero Engines and Volvo Aero are acknowledged for allowing us to publish the data. The authors are grateful to Prof. A. Kalfas for the discussions about the 2S-FRAP probe.

REFERENCES

[1] Marn, A., Göttlich, E., Cadrecha, D., and Pirker, H. P., 2009. "Shorten the intermediate turbine duct length by applying an integrated concept". *J Turbomach*, ***131***, October, p. 041014(10 pages).

[2] Göttlich, E., 2011. "Research on the aerodynamics of intermediate turbine diffusers". *Prog Aerospace Sci*, ***47***(4), pp. 249–279.

[3] Miller, R. J., Moss, R. W., Ainsworth, R. W., and Harvey, N. W., 2004. "The effect of an upstream turbine on a low-aspect ratio vane". In Proceedings of ASME Turbo Expo 2004, June 14-17, Vienna, Austria, ASME Paper No. GT-2004-54017.

[4] Davis, R. L., Yao, J., Clark, J. P., Stetson, G., Alonso, J. J., Jameson, A., Haldeman, C. W., and Dunn, M. G., 2002. "Unsteady interaction between a transonic turbine stage and downstream components". In Proceedings of ASME Turbo Expo, June 3-6, Amsterdam,The Netherlands, ASME Paper No. GT-2002-30364.

[5] Lavagnoli, S., Yasa, T., Paniagua, G., Castillon, L., and Duni, S., 2012. "Aerodynamic analysis of an innovative low pressure vane placed in an s-shape duct". *J Turbomach*, ***134***, p. 011013 (13 pages).

[6] Axelsson, L.-U., 2009. "Experimental Investigation of the Flow Field in an Aggressive Intermediate Turbine Duct". PhD Thesis, Department of Applied Mechanics

of Chalmers University of Technology. ISBN0:978-91-7385-264-7.

[7] Marn, A., 2008. "On the Aerodynamics of Aggressive Intermediate Turbine Ducts for Competitive and Environmentally Friendly Jet Engines". PhD Thesis, Institute for Thermal Turbomachinery and Machine Dynamics of Graz University of Technology.

[8] Hubinka, J., Santner, C., Paradiso, B., Malzacher, F., Göttlich, E., and Heitmeir, F., 2009. "Design and construction of a two shaft test turbine for investigation of mid turbine frame flows". In 19^{th} International Symposium on Airbreathing Engines, September 7–11, Montreal, Canada, ISABE Paper ISABE-2009-1293.

[9] Erhard, J., and Gehrer, A., 2000. "Design and construction of a transonic test turbine facility". In Proceedings of ASME Turbo Expo 2000(IGTI), May 8–11, Munich, Germany, ASME Paper 2000-GT-480.

[10] Hubinka, J., Paradiso, B., Santner, C., Göttlich, E., and Heitmeir, F., 2011. "Design and operation of a two spool high pressure test turbine facility". In Proceedings of 9^{th} European Turbomachinery Conference, March 21-25, Istanbul, Turkey, Paper No. 112.

[11] Kupferschmied, P., Köppel, O., Gizzi, W. P., and Gyarmathy, G., 2000. "Time resolved flow measurements with fast aerodynamic probes in turbomachinery". *Measurement Science and Technology,* ***11***(7), pp. 1036–1054.

[12] Porreca, L., Hollenstein, M., Kalfas, A. I., and Abhari, R. S., 2007. "Turbulence measurements and analysis in a multistage axial turbine". *Journal of Propulsion and Power,* ***23***(1), pp. 227–234.

[13] Hussain, A., and Reynolds, W., 1970. "The mechanics of an organized wave in turbulent shear flow". *Journal of Fluid Mechanics,* ***41***, pp. 241–258.

[14] Chaluvadi, V. S. P., Kalfas, A. I., Banieghbal, M. R., Hodson, H. P., and Denton, J. D., 2001. "blade row interaction in a high pressure turbine". *AIAA Journal of Propulsion and Power,* ***17***(4), pp. 892–901.

[15] Persico, G., Gaetani, P., Dossena, V., D'Ippolito, G., and Osnaghi, C., 2009. "On the definition of the secondary flow in three-dimensional cascades". *I MECH E Journal of Power and Energy,* ***223***, pp. 667–676.

[16] Bagshaw, D. A., Ingram, G. L., Gregory-Smith, D. G., and Stokes, M. R., 2008. "An experimental study of three-dimensional turbine blades combined with profiled endwalls". *I MECH E Journal of Power and Energy,* ***222***, pp. 103–110.

[17] Santner, C., Paradiso, B., Malzacher, F., Hoeger, M., Hubinka, J., and Göttlich, E., 2011. "Evolution of the flow through a turning mid turbine frame applied between a transonic hp turbine stage and a counter-rotating lp turbine". In Proceedings of 9^{th} European Turbomachinery Conference, March 21-25, Istanbul, Turkey, Paper No. 110.

[18] Paradiso, B., Santner, C., Hubinka, J., Göttlich, E., and Hoeger, M., 2011. "Turning mid turbine frame behavior for different hp turbine outflow conditions". In Proceedings of ASME Turbo Expo 2011, June 6-10, Vancouver, Canada, ASME Paper No. GT2011-46506.

[19] Spataro, R., Santner, C., Lengani, D., and Göttlich, E., 2012. "On the flow evolution through a LP turbine with wide-chord vanes in an s-shaped channel". In Proceedings of ASME Turbo Expo 2012, June 11-15, Copenhagen, Denmark, ASME Paper No. GT2012-68178.

[20] Pullan, G., and Harvey, N. W., 2008. "The influence of sweep on axial flow turbine aerodynamics in the endwall region". *J Turbomach,* ***130***, October, p. 041011 (10 pages).

[21] Arndt, N., 1993. "Blade row interaction in a multistage low-pressure turbine". *J Turbomach,* ***115***, January, pp. 137–146.

[22] Lengani, D., Paradiso, B., Marn, A., and Göttlich, E., 2011. "Identification of spinning mode in the unsteady flow field of a LP turbine". In Proceedings of ASME Turbo Expo 2011, June 6-10, Vancouver, Canada, ASME Paper No. GT2011-46226.

[23] Hodson, H. P., and Howell, R. J., 2005. "The role of transition in high lift low pressure turbines for aero engines". *Progress in Aerospace Science,* ***41***(6), August, pp. 419–454.

[24] Tiedemann, M., and Kost, F., 2001. "Some aspects of wake-wake interactions regarding turbine stator clocking". *J Turbomach,* ***123***, pp. 526–533.

[25] Persico, G., Gaetani, P., and Osnaghi, C., 2009. "A parametric study of the blade row interaction in a high pressure turbine stage". *J Turbomach,* ***131***, July, p. 031006 (13 pages).

[26] Dénos, R., Arts, T., Paniagua, G., Michelassi, V., and Martelli, F., 2001. "Investigation of the unsteady rotor aerodynamics in a transonic turbine stage". *J Turbomach,* ***123***, January, pp. 81–89.

[27] Lengani, D., Selic, T., Spataro, R., Marn, A., and Göttlich, E., 2012. "Analysis of the unsteady flow field in turbines by means of modal decomposition". In Proceedings of ASME Turbo Expo 2012, June 11-15, Copenhagen, Denmark, ASME Paper No. GT2012-68582.

[28] Tyler, J. M., and Sofrin, T. G., 1962. "Axial flow compressor noise studies". *SAE Transaction,* ***70***, pp. 309–332.

[29] Cimbala, J. M., and Park, W. J., 1990. "An experimental investigation of the turbulent structure in a two-dimensional momentumless wake". *J Fluid Mech,* ***213***, pp. 479–509.

[30] Leitch, T. A., Saunders, C. A., and Ng, W. F., 2000. "Reduction of unsteady stator-rotor interaction using trailing edge blowing". *J Sound Vibrat,* ***235***(2), pp. 235–245.

Proceedings of ASME Turbo Expo 2012
GT2012
June 11-15, 2012, Copenhagen, Denmark

GT2012-68582

ANALYSIS OF THE UNSTEADY FLOW FIELD IN TURBINES BY MEANS OF MODAL DECOMPOSITION

Davide Lengani, Thorsten Selic, Rosario Spataro, Andreas Marn, Emil Göttlich
Inst. f. Thermal Turbomachinery and Machine Dynamics
Graz University of Technology, Austria
Email: davide.lengani@tugraz.at

ABSTRACT

This paper presents the results of a modal decomposition method applied to the time resolved data of two different test turbines. The analysis is carried out on the measurements performed by fast response aerodynamic pressure probes as well as on CFD simulations. As shown in the earlier aeroacoustic theory, a plurality of rotating patterns, also called spinning modes, are generated by the rotor-stator interactions. The modes may be computed from the flow quantities, such as total pressure, velocity and flow angles, through Fourier decompositions performed in time and space. The deterministic unsteadiness is then simplified to a limited number of Fourier coefficients. At a fixed radial position, circumferential lobes are identified for any multiple of the blade passing frequency. Therefore, the flow may be described as the superposition of rotating patterns, the spatial characteristics of which are correlated to the linear combinations of blade/vane number.

This analysis has been applied to a one and a half stage low pressure turbine and to a two-stage counter-rotating transonic turbine. In the former test case there is a limited number of modes that characterize the flow field. Hence, the decomposition in modes simplifies considerably the evaluation of the sources of unsteadiness and deterministic stresses. The second test case presents more complex interactions. In fact, the presence of two rotors induces oscillations at frequencies that corresponds to the linear combinations of the two blade passing frequencies. Circumferential modes are identified for the most characteristic frequencies and their physical meaning is discussed.

INTRODUCTION

The unsteady interactions between stator and rotor rows affect considerably the aerodynamic performances of turbomachinery. As recently reviewed by Adamczyk [1], He [2] and Tucker [3], the accuracy of computational models depends on their ability to account for deterministic and stochastic unsteadiness. Similarly, since the 80s, many studies have been performed in turbine research facilities (e.g. [4–7]) in order to increase the knowledge and understanding of the unsteady flow interactions. Furthermore, not only the aerodynamic performances, but also the blade fatigue life and the acoustic noise emissions depends strongly on this inherently unsteady flow.

In the pioneering work of Tyler and Sofrin [8] it has been shown that stator-rotor interaction represents a prime mechanism of noise generation. The application of their theory revealed that the sound propagation of tones at the blade passing frequency (BPF) of a rotor may be effectively cut-off, and then reduced, with a proper choice of the blade to vane count ratio (see for example [9, 10]). Similarly, the amplitude of the aeromechanical excitations of a rotor blade depend considerably upon the stator/rotor blade count (e.g. Li and He [11]).

A design that requires a different count of blades and vanes should be, then, properly interfaced with the aerodynamic design. Numerical investigations have shown that the unsteady flow is inaccurately predicted by blade count modification techniques (e.g. [12, 13]). Conventional unsteady solvers represent a quite time consuming and costly solution to simulate turbomachinery with unequal blade/vane count. Hence, in the last years many efforts have been done to provide reliable frequency domain or time-domain Fourier methods (e.g. [14–16] among many others). Furthermore, as reviewed by He [2], all such methods are based on a Fourier approach to model the unsteady interactions which are also suited to the analysis of vibration and acoustic. These works have been done to provide a multi-disciplinary design of a turbomachine.

Recently, the modal decomposition proposed by Tyler and Sofrin [8] have been applied to the unsteady aerodynamic data obtained in compressors by Arnaud et al. [17] and Courtiade et al. [18]. They computed spatial and temporal Fourier coef-

ficients that account for the deterministic unsteadiness of the flow. As also identified by the aerodynamic investigation of Lengani et al. [19], the flow, in the absolute (stationary) reference frame, may be considered as the superposition of rotating patterns. Coherently, circumferential modes were identified by Moser et al. [20] for an aeroacoustic investigation in the same test rig of Lengani et al. [19]. Furthermore, Dorney and Sharma [21] suggested to reduce the flow in Fourier coefficients to provide boundary condition for computational investigations. The analysis of experimental data in terms of temporal and spatial Fourier coefficients may then increase the physical understanding of the unsteady interactions and improve their applicability to CFD design tools.

The present paper extends the analysis proposed by Lengani et al. [19]. A double Fourier decomposition is described and applied to the data obtained in this previous work. Namely, area aerodynamic measurements from a fast response aerodynamic pressure probe (FRAPP) were performed in a 1 and 1/2 stage low pressure turbine. The paper describes the post-processing procedure adopted to compute the double Fourier decomposition and, then, its application to the experimental data. A further test case, the experimental results of which have been presented in [22–24], is also discussed. Time resolved aerodynamic measurements, obtained from a counter rotating turbine rig [25], are analyzed by means of experimentally validated CFD results. The modal decomposition is applied to the CFD results in order to explain the unsteady flow field downstream of the two-spool counter rotating turbine rig.

NOMENCLATURE

A	Fourier coefficient of the circumferential mode
B	Number of blades
BPF	Blade passing frequency
C_{pt}	Total pressure coefficient
CRT	Counter-rotating turbine
exp.	Experiment
EGV	Exit guide vane
f	Frequency
H	Relative channel height
HP	High pressure
LP	Low pressure
m	Circumferential mode
M	Mach number
n	Index of the harmonic of the BPF
n_c	Number of circumferential points
n_t	Number of points within the revolution period
p_s	Static pressure
p_t	Total pressure
q	Generic flow variable
r	Radius
STTF	Subsonic test-turbine facility
t	Time
T	Blade passing period
TMTF	Turning mid turbine frame
v	Absolute velocity
V	Number of vanes
w	Relative velocity
α	Flow angle in the blade to blade plane
ρ	Flow density
θ	Circumferential coordinate
Ω	Rotor angular velocity
$<>$	Deterministic periodic component

Subscripts

AVE	Circumferentially averaged properties
MAX	Maximum value, in the local plane
r	relative

Superscripts

$-$	Time averaged properties
$\sim$	Ensemble-averaged properties
$'$	Stochastic fluctuating component

THEORETICAL BACKGROUND

A classical method for the decomposition of unsteady flows is the triple decomposition procedure [26], for a generic variable q:

$$q(t) = \overline{q} + < q(t) > + q'(t) \tag{1}$$

where $\overline{q}$ is the time average value, $< q(t) >$ is the purely periodic component associated with a coherent periodic structure and $q'(t)$ is the random fluctuation associated mainly with turbulence. In rotating machinery, a shaft encoder is commonly used (see for example the early works of [6, 7]) to provide the fluctuations induced by the rotor by means of a phase averaging procedure. The phase averaged value $\tilde{q}$ is equal to:

$$\tilde{q} = \overline{q} + < q(t) > \tag{2}$$

Hence, the unsteadiness not linked with the rotor rotational speed is removed by this operation.

Inside a turbomachine, this expression has been further decomposed by Adamczyk [27], in particular, the time mean value $\overline{q}$ is evaluated as the sum of two contributions:
1) an axisymmetric term, which is computed as the circumferential average value over the machine circumference.
2) an average passage to passage flow field (stator-stator in the absolute reference frame) which arises from circumferential gradients induced by the stator rows.
The periodic fluctuating component $< q(t) >$ is associated to the relative motion between the blade rows. In the stationary reference frame, it is possible to decompose this quantity as the sum of an average rotor blade passage flow and the stator/rotor interactions. Similarly, in a simulation based on Fourier methods the rotor blade flow is solved in the relative frame of reference and phase lag periodic conditions are applied to account for stator/rotor interactions [2].

Modal theory

An apparently different decomposition of a variable in time and space was provided by Tyler and Sofrin [8]. In order to describe the sound generating mechanisms, they wrote the pressure fluctuations at any circumferential positions downstream of a compressor stage as a sum of harmonics. The theoretical model that they proposed has been verified by numerous aeroacoustic experimental investigations, and it is valid also for

turbines (e.g. [20]). In particular, for an ideal rotor with identical blades the pressure fluctuations at a circumferential position θ are represented as the following Fourier series [10]:

$$p(\theta,t) = \sum_{n=0}^{\infty} \sum_{m=-\infty}^{\infty} A(m,n) e^{inB\Omega t - im\theta} \tag{3}$$

where n is the harmonic index (1 for the BPF, 2 for the 2*BPF, etc.), Ω the rotor angular velocity, $A(m,n)$ the coefficient of the Fourier series for each harmonic n and for each circumferential mode m.

The pressure field is constituted by a superposition of an infinite number of rotating patterns, where the number of lobes is given by successive values of m. Each m-lobed pattern rotates at the speed $\frac{nB}{m}\Omega$ required to generate the n^{th} multiple of the BPF. According to this convention, positive modes correspond to pattern rotating with the rotor direction, while, negative modes are related to pattern rotating in the opposite direction. Furthermore, Tyler and Sofrin [8] showed that the mode m of the spatial Fourier decomposition is restricted just to some particular values:

$$m = nB + kV, \;\; with \;\; k = ..., -1, 0, 1, ... \tag{4}$$

where a simple stator-rotor interaction is considered, B is the number of rotor blades and V is the number of stator blades.

It is possible to consider the interactions of the rotor with a complete vane assembly by simply superimposing the effect of the single event. For example, in a turbine, a mode m^* generated by a stator-rotor interaction will be scattered in the modes $m = m^* + kV_2, \;\; with \;\; k = ..., -1, 0, 1, ...$ by the following stator rows. Hence, for a stator-rotor-stator assembly the following modes are predicted:

$$m = nB + k_1 V_1 + k_2 V_2, \;\; with \;\; k_1, k_2 \;\; integer \tag{5}$$

where V_1 and V_2 are the number of vanes of the first and second stator row, respectively. A further extension of the present theory was provided by Holste and Neise [28]. They described the possible modes which may propagate in case of rotor-rotor interaction with different rotational speed, counter or co-rotating.

Modal decomposition of the flow field

The modal theory has been developed for the pressure field. However, as experimentally observed by Lengani et al. [19], rotating patterns characterize all the aerodynamic quantities, the components of the velocity, the flow angles, and the pressure fluctuations. Hence, the decomposition of eq. 3 may be applied to the aerodynamic field. For example, Hall et al. [15], represented the flow variables as a Fourier series in time with spatially varying coefficients in order to satisfy the temporal periodicity of the flow in a time-harmonic balance computational method.

On the basis of the modal theory, a double Fourier decomposition method was developed by Courtiade et al. [18]. They perform a spatial Fourier decomposition of a generic flow quantity q in space in order to obtain a spatial mode for different time steps. Then, they apply a second Fourier transform in time of the spatial modes. The information obtained from the first decomposition is the structure of the spatial lobes. The second transformation is then necessary to understand the rotational speed of the lobes and the stator/rotor interactions which generate the mode.

In the present paper a similar double Fourier decomposition is proposed. However, the order of the decompositions is the opposite of the method of Courtiade et al. [18]. For every radial and circumferential position of the measurement mesh a discrete Fourier transform is applied to the phase averaged generic flow quantity q (normalization factor are voluntary omitted in the formulation):

$$q(f)_{\theta,r} = \sum_{n_t} q(t)_{\theta,r} e^{-in_t f} \tag{6}$$

where the limits of the integration are defined by the number of points n_t within the revolution period, obtained from the phase averaging procedure. This is the classic discrete Fourier transform in time which reveals the frequencies that characterize the flow field.

Thereafter, a discrete Fourier transformation in the circumferential direction is applied to the complex number $q(\theta, r, f)$:

$$A(m)_{r,f} = \sum_{n_c} q(\theta)_{r,f} e^{-in_c m} \tag{7}$$

where the limit of the integration are defined now by the number of points n_c in the circumferential direction. The operation is performed at any fixed frequency f and radius r and now the variable $q(\theta)_{r,f}$ is integrated over the circumferential position θ. The Fourier coefficients $A(m)_{r,f}$ are, then, a set of complex numbers which are functions of the frequency and of the radius at which the data are obtained. Further, a similar Fourier decomposition was performed along the radial direction. However, radial modes may not be easily correlated to the turbine geometry like the circumferential modes and for this reason the following discussion will focus just on circumferential modes.

In this last formulation the fluctuations of the generic variable $q(\theta)_{r,f}$ are written as complex numbers in the frequency domain. According to the Fourier transform theory a transformation of complex numbers leads to values of $A(m)_{r,f}$ which are not symmetric with respect to the spatial frequency (namely, the modes m). Modes, as predicted by the modal theory, are, then, positive or negative, spinning in the same direction or in the opposite direction of the rotor, respectively, following the convention previously adopted.

Equation 7 may be applied to different circumferential boundaries, where the spatial extension of the boundary defines the minimum mode computable. In fact, the minimum mode computable, except for the mode 0, is directly proportional to the circumferential arc adopted in the decomposition. For example, measurements across a sector of 15 deg will lead to a minimum computable mode equal to 24. Similarly, the number of circumferential points define the maximum mode computable. Therefore, it is easy to demonstrate that all the

modes of interest are computed when eq. 7 is applied to the blade/vane count periodicity condition of a test rig.

Analogy with conventional decomposition

At any frequency and radial position a set of coefficients $A(m)_{r,f}$ is defined. Comparing eq. 3 and eq. 7, it turns out that the contribution to the deterministic unsteadiness is constituted by the multiple of the blade passing frequency. Performing an analogy with the Adamczyk's decomposition [27], this set of coefficients is the sum of different contributions:
1) the frequency 0 (time mean value) and circumferential mode 0 corresponds to the axisymmetric term;
2) the frequency 0 (time mean value) and circumferential mode different from zero corresponds to the average stator to stator flow field;
3) the unsteadiness due to the rotor and its interactions with the stator rows correspond to the sum of the modes $A(m)_{r,f}$ at all the multiple of the blade passing frequency.
This last contribution may be further decomposed, considering eq. 5, in the following two terms:
3') for k_1, k_2 equal to zero: the modes $m = nB$ at the rotational speed $\frac{nB}{m}\Omega$ correspond to the average rotor blade passage flow. For example, at the BPF a mode corresponding to the blade number is observed, at 2 times the BPF a mode corresponding to 2 times the blade number is observed and so on. All these modes rotate at the rotational speed of the rotor (eq. 3), therefore, they are the trace of the rotor signal.
3") for k_1, k_2 not zero: all the lobed structures arising from the stator/rotor interactions are identified.

TEST CASES

Experimental test facilities

The Institute for Thermal Turbomachinery and Machine Dynamics (ITTM) at Graz University of Technology operates a 3 MW compressor station to supply a couple of test facilities with pressurized air. Experiments were carried out on two continuously operating cold-flow turbines, namely, a subsonic test turbine facility (STTF) and a transonic counter-rotating test turbine facility (CRT). In the next two subsections a brief description of the two test turbines is provided. A full description of the STTF-test facility is given in Moser et al. [29], whereas, a full description of the CRT-facility is provided by Hubinka et al. [25, 30].

Subsonic (LP) turbine The subsonic low pressure turbine is constituted by 1 and 1/2 stage, which is representative of the last stage of a commercial engine with turbine exit casing. The test section is provided with a LP stage (stator and rotor with 96 vanes and 72 blades, respectively) followed by low aspect ratio exit guide vanes (EGV), constituted by 15 vanes (Tab. 1).

The aerodynamic design of the low pressure turbine was performed by MTU Aero Engines. Considerable effort was put into the adjustment of all relevant model parameters to reproduce the full scale LPT situation. The operating points were defined according to a current LP turbine design practice using scaling along reduced speed, mass flow and pressure ratio. The present paper reports the result obtained for an operating condition representative of take-off (see Lengani et al. [19] for more details). At the rotor exit mid-span, the Reynolds number is equal to 240000 and the relative Mach number is equal to 0.53.

Counter-rotating transonic turbine The transonic test turbine facility consists of a transonic HP stage and a counter-rotating LP stage, where an S-shaped turning mid turbine frame (TMTF) guides the flow from the unshrouded HP rotor to the LP rotor. The HP turbine consists of 24 choked vanes and 36 blades (Tab. 1). For the LP stage, a blade count of 16 turning struts and 72 blades was chosen in order to minimize the risk of excitation of the LP rotor.

This unique configuration allows the testing of rig inserts under aerodynamic conditions relevant for modern aeroengine, the operating condition was provided by MTU Aero Engines. The investigated aero design has an overall pressure ratio of 4. The total pressure ratio is 3 for the HP turbine and 1.3 for the LP turbine. The HP vanes are operating under choked conditions. The absolute Mach number at the TMTF inlet is 0.5. This is representative for realistic duct inlet conditions of modern jet engines with a single stage HP turbine at cruise operating point.

Measurement technique

Unsteady flow measurements were performed by means of two different fast-response aerodynamic pressure probes. In the subsonic turbine a cylindrical one sensor probe has been used, see Persico et al. [31] for more details. In the transonic turbine a 2-sensor probe, operated as a virtual four sensor probe for 3D aerodynamic measurements [32], has been used. For both probes, the extended uncertainty is in the order of $\pm 0.5\%$ of the kinetic head for the pressure measurements and of ± 0.3 deg for the flow angles.

The present paper focuses its discussion on the measurement carried out in annular sectors downstream of the rotor of the STTF facility and downstream of the second rotor (LP rotor) of the counter-rotating turbine. Measurements are performed for 24 deg (EGV pitch) for the STTF facility, and 22.5 deg (TMTF pitch) for the CRT facility. Table 1 summarizes these data and provides further information such as the distance of the measurement plane from the rotor trailing edge, the circumferential resolution of the traversing, and the number of points per measurement mesh.

For the STTF, the area of investigation is larger than the stator/rotor periodicity of the LP turbine, which is 15 deg. In the case of the CRT, the area of investigation is smaller than the turbine periodicity, which is 90 deg. However, in the CRT, due to the complexity of the test rig, it is not possible to continually traverse, with a probe, more than one TMTF pitch.

Data is acquired for more than 100 revolutions of the rotor upstream of the measurement planes. The determination of the flow properties is made possible after phase averaging. The periodic fluctuations of velocity, pressures and flow angles are determined from the phase averaged values obtained from the three rotations of the probes and a set of calibration coefficients (see for example Porreca et al. [33]). The final resolution

TABLE 1: Configurations of the turbines and summary of measurement/CFD investigations.

	Subsonic LP turbine (STTF) [19]	**Counter-rotating turbine (CRT) [24]**
Blade rows:	Stator/Rotor/EGV	HP Stator/HP Rotor/TMTF/LP Rotor
Number of blades/vanes:	96/72/15	24/36/16/72
Rig periodicity:	120 deg	90 deg
Measurement/CFD plane:	downstream of rotor, exp.	downstream of the LP rotor, exp. and CFD
Distance of plane from rotor trailing edge:	60% of rotor axial chord	77% of rotor chord
Annular sector investigated (exp.):	24 deg	22.5 deg
Measurement circumferential resolution:	0.7 deg	0.5 deg
Measurement mesh (circumferential x radial):	35 x 28 points	46 x 21 points
Interactions analyzed:	stator/rotor, 15 deg, exp.	all rows, 90 deg, CFD

in time of the measurements is up to $t/T = 0.025$.

The interested reader may find more details on the measurement campaigns, the probes and the data post-processing method in Lengani et al. [19] for the subsonic turbine, and in Lengani et al. [24] for the transonic turbine.

Computations, CRT

The numerical investigation on the two shaft facility (CRT) was performed by a commercial CFD code (CFX©v12.1). The computational grid consists of 14 millions elements divided in five domanins (two rotating for the rotors and three stationary for the vanes and the outflow), all of them with 90 degrees periodicity. The mesh adopted for the unsteady computation is similar to the mesh provided in Spataro et al. [34] for a steady computation but extended to the 90 degrees periodicity and to the HP stage. A grid refinement study was performed for the steady CFD, as described by Spataro et al. [34].

The unsteady simulation required about 28 gigabyte of memory. The y^+ was kept below 1 next to the blade surface and below 2 next to the endwall. The code solves the Navier Stokes equation system with first order accuracy in areas where the gradients change sharply to prevent overshoots and undershoots and maintain robustness, and second order in flow regions with low variable gradients to enhance accuracy [35]. The turbulence model used was the SST$-k-\omega$ by Menter [36]. The unsteady flow was computed by second order backward equations: the timestep was chosen as $1/100$ of the high pressure rotor blade passing period. The conditions at the inlet and outlet boundaries were taken from the experimental measurements performed by Santner et al. [22] and Hubinka et al. [30].

RESULT AND DISCUSSION

The present section discusses the results of the modal decomposition applied to the two test turbines described above. Table 1 provides a small summary of the investigated cases and details of the measurements and CFD. In particular, the STTF results have been used to describe the method. Whereas, the modal decomposition of the CFD results of the CRT facility have been used to describe the flow features of the experimental results.

Low pressure turbine

The time-resolved evolution of the flow downstream of the STTF turbine rotor is discussed in this section. A brief summary of the flow features is provided in order to introduce the results of the modal analysis. A more detailed discussion of the flow is given in Lengani et al. [19], where the modal theory was introduced in order to explain the spinning modes which characterize the flow. Averages in different relative reference systems were used to quantify the influence of the unsteadiness due to the stator/rotor interaction. However, the present discussion will show that the modal decomposition simplifies and completes this analysis. Such decomposition reduces the problem of the unsteady flow features to circumferential modes of known amplitude and rotational speed.

Results are presented in Fig. 1 as contour plots of the relative Mach number in the absolute (stationary) reference frame. These plots are views in the downstream direction on a sector covering one pitch of the exit guide vane and consequently 6.4 pitches of the stator vane and 4.8 rotor blade passages.

The flow features that are caused by the rotor blades, hub secondary vortex, the tip leakage vortex and the rotor wake, are identified in Fig. 1. The largest velocity defects may be observed in the endwall regions. In particular, the tip leakage vortex shows a nucleus with considerably lower relative Mach numbers than the hub secondary vortex.

Due to the high aspect ratio of the rotor blade the region between 15% and 80% passage height is characterized by velocity defects related to the blade wakes. This is the result of two-dimensional interaction mechanisms such as vane wake-blade interaction [4, 5]. Furthermore, due to the unequal vane/blade count (see Tab. 1) the shape and the strength of the wake and consequently of the rotor core flow is not circumferentially constant. Similarly, circumferential variations in the vane/blade mutual potential interactions are due to the variations of incidence induced by the relative motion. In fact, the rotor blades during their motion are facing different viscous effects from the stator vanes. These complex interactions generate spinning modes [19].

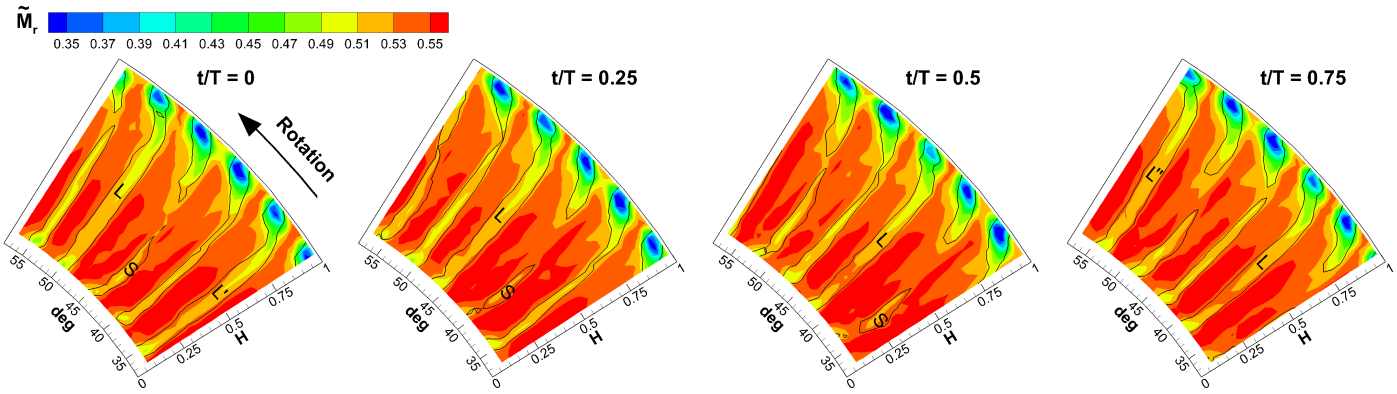

FIGURE 1: Time-resolved distribution of the relative Mach number, STTF.

To help the reader following the evolution of the blade velocity defects and underline the spinning mode the iso-contour line of the relative total pressure coefficient is superimposed on each plot of Fig 1. The relative total pressure coefficient is here defined as the difference between the ensemble averaged relative total pressure and its circumferential average and made non dimensional:

$$\tilde{C}_{ptr} = \frac{\tilde{p}_{tr} - p_{tr,AVE}}{0.5\rho w^2_{AVE}} \tag{8}$$

This definition allows the identification of the blade wake and secondary flows within one region, delimited by two iso-contour lines, along the whole span. A value of $\tilde{C}_{ptr} = -5\%$ has been chosen to represent the low momentum areas.

An area enclosed within the iso-contour lines, marked with the letter "S" superimposed on the plot identifies a blade wake with very low width at a circumferential position of around 44 deg in the first time step ($t/T = 0$). A similar flow configuration is visible at the circumferential position of around 40 deg in the time step $t/T = 0.25$ and successively at 35 deg in the time instant $t/T = 0.5$. From this last position it leaves the measurement plane. It is evident that this flow feature rotates clockwise in the area under investigation. This phenomenon characterizes the whole flow field. For example, the wake with the largest width identified here with the letter "L" rotates clockwise of around 4 degrees each quarter of the blade passing period. Furthermore, all these flow features are repeated every three blade passages at a fixed time snapshot, see for example the iso-contour lines marked as L and L$'$ for $t/T = 0$ and the lines marked as L and L$''$ for t/T =0.75.

Modal decomposition, analysis The rotating pattern here identified is rotating clockwise and it moves 15 deg while one blade moves counterclockwise by about 5 deg during the blade passing period. It means that this pattern "spins" three times faster than the rotor and in the opposite direction. This spinning mode corresponds to the mode $m = -24$, and the modal theory (see eq. 3) predicts its rotational speed $\frac{B}{m}\Omega = \frac{72}{-24}\Omega = -3\Omega$, and the sign confirms the sense of rotation (opposite to the rotor). To demonstrate the existence of such spinning mode a simple sketch, adapted from the original work of Tyler and Sofrin [8] (cf. Fig. 16A and 16B of their paper), was provided in Lengani et al. [19]. However, the decomposition by means of the mathematical formulations of eq. 6 and 7 provides a larger amount of detailed data.

The results of the modal decomposition are shown in Fig. 2 for three different flow quantities and two frequencies of interest, namely, the blade passing frequency (BPF) and its harmonic (2BPF). As reported in Tab. 1, the unsteady aerodynamic measurements were performed for 24 deg, while the stator/rotor periodicity is 15 deg. Hence, the measurement domain has been reduced to 15 deg. Under such condition, the resolution of the modal decomposition is 24 modes and, then, the decomposition is set to resolve correctly the modes of interest ($m = 72i + 96k$, multiples of 24). According to the measurement mesh and considering the Nyquist-Shannon sampling theorem the maximum mode computable is ± 264. However, it is well known that the circumferential fluctuations with a very large number of lobes (small circumferential wave length) have the fastest decay rate (see, for example, He et al. [37]), and, hence, they are negligible.

Figure 2a shows the amplitude of the modal decomposition of the Mach number for three different radial positions: tip ($H = 0.95$), mid-span ($H = 0.5$), hub ($H = 0.125$). These positions are selected to highlight the effect of the flow structures identified from Fig. 1: interaction of the stator tip secondary flows with the tip leakage vortex (tip), the stator wake and rotor (mid-span) and the stator hub secondary flow with rotor hub secondary flow (hub). The Fourier coefficients $A(m)_{r,f}$, computed from equations 6 and 7, are complex numbers. Their amplitude is sufficient to describe the stator/rotor interactions, and then their phase is not shown or commented in the following sections of the paper. The amplitude is plotted as relative amplitude with respect to the fluctuations induced at the tip by the rotor tip leakage vortex (mode 72 at the BPF). The circumferential mode is plotted on the abscissa dividing it by 24, hence a value of -1 corresponds to the mode -24, a value of 3 to the mode 72 and so on. To avoid confusion in the discussion, the actual mode number will be referred to $(-24, 72, \ldots)$.

In this picture, the dominant unsteady fluctuation is due to the rotor trace itself (mode 72 for the BPF and mode 144 for the 2BPF). Coherently with the results of Fig. 1, the fluctuations induced by the tip leakage vortex are much higher than the one due to the wake (mid-span) or to the hub passage vortex (hub).

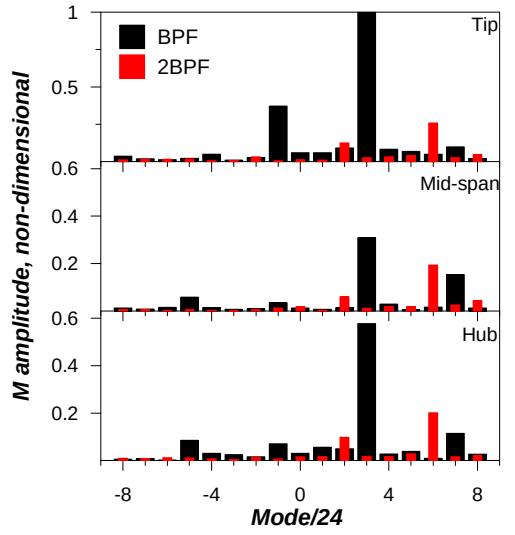

(a) Mach number

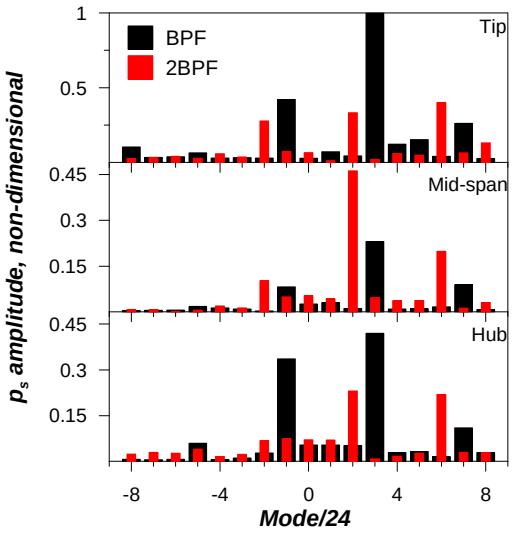

(b) Static pressure

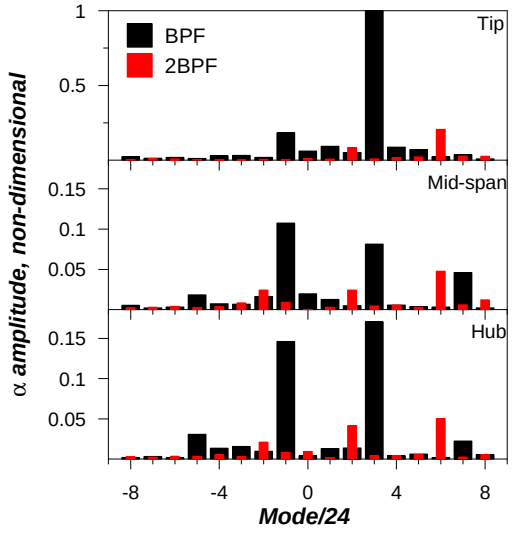

(c) Flow angle

FIGURE 2: Circumferential mode amplitudes, STTF; from top to bottom of each subfigure: tip, mid-span, hub.

Furthermore, stator/rotor interactions with a lower amplitude are observed for the modes $m = 72 + 96k = -120, -24, 168$ at the BPF, and for the mode $m = 2 * 72 - 96 = 48$ at the 2BPF. Therefore, the flow field may be interpreted as superposition of more modes than just the modes -24 and 72. In particular, at mid-span the mode 168 has an amplitude larger than the mode -24. Since its wave length is smaller than the one of the rotor, such mode will decay along the machine axis faster than the rotor structure. At mid-span and at the hub, the distribution of the Mach number could be approximated just considering the viscous effect of the rotor and not its interactions with the stator.

The modal decomposition of the static pressure is associated to the same modes (Fig. 2b). However, the stator/rotor interaction plays a different role: at mid-span the largest contribution to the fluctuations of the static pressure is due to this interaction (mode $m = 2 * 72 - 96 = 48$ at the 2BPF) and not to the structures of the rotor itself. Furthermore, at the hub, the amplitude of the mode -24 is now comparable to the amplitude of the rotor induced unsteadiness. Just at the tip, the rotor itself represents the largest contribution to the unsteadiness, but the contributions due to the stator/rotor interaction are still relevant (modes $-24, 168$ at the BPF and modes ± 48 at the 2BPF).

Similar considerations are obtained from Fig. 2c, where the amplitude of the flow angle modal decomposition is plotted. The unsteadiness at the tip is mainly determined by the rotor, namely, by the mode 72 due to the deterministic fluctuations induced by the tip leakage vortex. On the contrary, at mid-span and at the hub, the overall fluctuations caused by the stator/rotor interaction overcome the fluctuations of the rotor alone.

The results of the modal decomposition show that the amplitude of the circumferential modes associated to the flow variables depicted in Fig. 2 does not present a clear trend. Each variable is, in fact, the solution of different equations of the Navier-Stokes set of equations. Hence, as also observed by the computational method proposed by Hall et al. [15], different spatial and temporal Fourier coefficients are associated to the different flow variables.

However, the circumferential modes that characterize the deterministic unsteadiness are well defined by this analysis, in particular, only the modes predicted by eq. 4 have a large amplitude. The overall deterministic unsteadiness of any variable is constituted just by contributions at specific temporal frequencies (BPF and 2BPF in this case) and spatial frequencies (e.g. modes $-24, 72, 168$ at BPF and modes ± 48 and 144 at 2BPF)). Normally, CFD methods based on Fourier coefficients account for temporal or spatial periodicity [2], while the decomposition of experimental results proposed here shows spatial and temporal periodicity. Any flow quantity may be interpreted as a superposition of a limited number of spinning modes (e.g. 6 relevant modes in this case) the sense of rotation and spatial wave length of which are predictable (see eq. 3 and 4).

Counter-rotating turbine

The time-resolved evolution of the the flow downstream of the CRT low pressure rotor is described in this section. Before discussing the modal decomposition, a brief summary of the

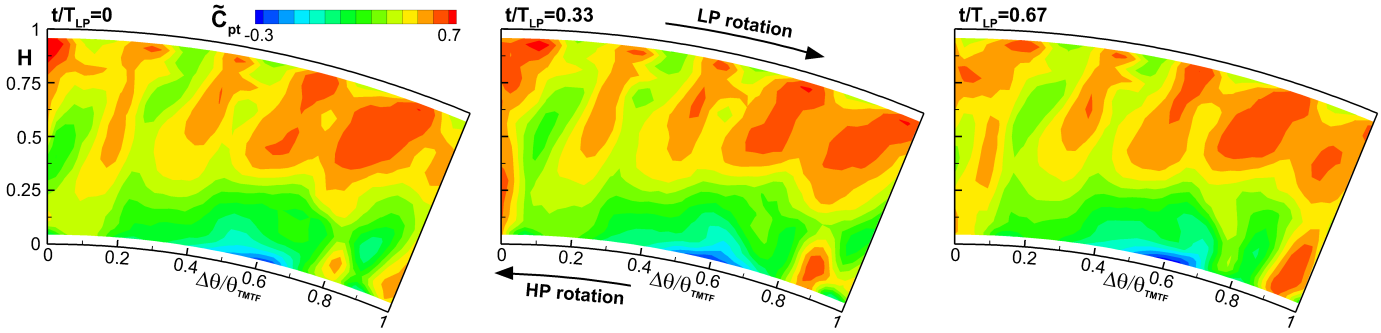

FIGURE 3: Time-resolved distribution of the total pressure, LP rotor induced fluctuations downstream of the LP rotor, CRT.

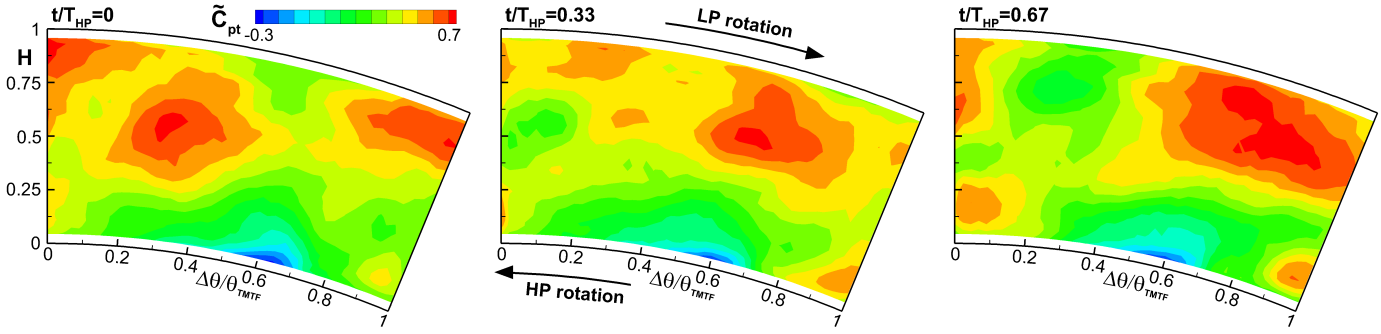

FIGURE 4: Time-resolved distribution of the total pressure, HP rotor induced fluctuations downstream of the LP rotor, CRT.

flow features is provided. Detailed results of the unsteady flow behaviour were provided in Lengani et al. [24].

Results are presented as contour plots of the total pressure in the absolute (stationary) reference frame (Fig. 3 and 4). These plots are views in the downstream direction on a sector covering one pitch of the TMTF and consequently 4.5 LP rotor blade passages and 2.25 HP rotor blade passages (see table 1). In the figures, the total pressure is plotted as a non dimensional coefficient C_{pt} defined as:

$$C_{pt} = \frac{p_t - p_{s,MAX}}{0.5\rho v_{MAX}^2} \tag{9}$$

where $p_{s,MAX}$ is the maximum value of the time averaged static pressure measured in the local measurement plane. According to this definition and to the radial pressure gradient induced by the diffusing duct, the pressure coefficients may present negative values. This definition has been adopted in order to preserve the original distribution of the total pressure, as it will be referred to in the discussion.

Downstream of a counter-rotating turbine the flow is characterized by multiple sources of unsteadiness, namely, the structures arising from the HP rotor, from the LP rotor, and from their interactions. The results are shown in Fig. 3 and 4 considering the phase average on the LP rotor and on the HP rotor, respectively, in order to simplify the analysis of such complex flow. Considering eq. 1, the phase average on one of the two rotor shaft removes the coherent fluctuations due to the other rotor.

Three time snapshots are extracted from one blade passing period of the LP rotor (Fig. 3) and of the HP rotor (Fig. 4) in order to show the time evolution of the total pressure. The influence of the LP rotor blades, which rotates clockwise, is shown in the first figure. The flow features caused by the 4 and 1/2 blades of the LP rotor may be identified as the regions with alternately high and low total pressure along the circumferential direction.

The effects of the HP rotor are visible in Fig. 4. In each time step there should be the trace of 2 and 1/4 blades of the HP rotor. However, this number is not clearly correspondent to what is depicted in the pictures. Furthermore, the nuclei at high total pressure appear at different radial positions and it is not possible to identify a clear sense of rotation (as marked over the picture the HP rotor rotates in the counterclockwise direction). The fluctuations of the flow induced by the HP rotor are a sum of rotating patterns due to the interactions with the stator rows. Hence, the modal decomposition may provide a better analysis of the interactions that are observed.

As previously mentioned, the constructive complexity of the rig did not allow a continuous traversing of the pressure probe for the full periodicity of the rig (90 deg). Therefore, a CFD unsteady simulation considering the rig periodicity was performed. Disregarding the time mean term, the modal decomposition is focused on the unsteady fluctuations ($< p_t >$, of eq. 1). Hence, to verify the validity of the CFD simulation in comparison with the experimental results, average amplitude spectra are provided in Fig. 5. The amplitude spectra are obtained as average values over different circumferential positions at mid-span. A similar method of validating CFD was used by Peters and Spakovszky [38] for a counter-rotating propfan.

The plot provides information on the frequencies and hence the phenomena that characterize the flow. In fact, as marked over the picture, sharp frequency peaks correspond to

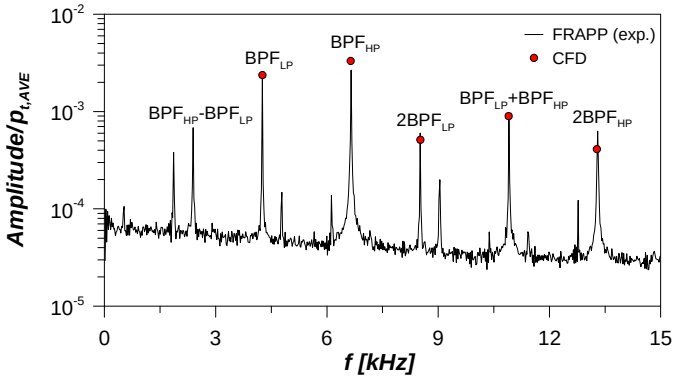

FIGURE 5: Average non-dimensional amplitude spectra at mid-span, downstream of CRT LP rotor. Comparison between experimental and CFD results.

the blade passing frequencies of the two rotors and their linear combinations. The two higher contributions correspond to the blade passing frequencies of the two rotors (BPF_{LP} and BPF_{HP}). Further peaks at lower amplitude appear at any linear combination $i \cdot BPF_{LP} + k \cdot BPF_{HP}$, with i,k integer numbers (just $BPF_{LP} + BPF_{HP}$ and $BPF_{HP} - BPF_{LP}$ are marked over the graph to keep the picture readable).

At selected, characteristic frequencies the CFD results are superimposed on the graph. The mean amplitude of the fluctuations, and their relative magnitude, computed from the CFD show a good agreement with the experimental results. Hence, the results from the CFD are further analyzed by means of the modal decomposition in the followings, in order to better understand the flow interactions inside the turbine.

Modal decomposition, analysis The results of the modal decomposition performed from the CFD are shown in Fig. 6 considering the frequencies of interest marked in Fig. 5. As reported in Tab. 1, the simulation was performed for 90 deg, that corresponds to the rig periodicity. As previously explained, the resolution of the decomposition is set to resolve correctly the modes of interest, multiples of 4, in this case. The domain for the decomposition was set to compute a maximum mode equal to ± 360.

Figure 6 shows the amplitude of the modal decomposition of the total pressure at mid-span. The amplitude is plotted as relative amplitude with respect to the maximum amplitude computed in this radial position. The circumferential mode is plotted on the abscissa dividing it by 4, according to the resolution of the decomposition. However, the actual mode number will be referred to in the discussion (e.g. the mode -72 corresponds to the value -18 read on the graph axis). To make the graph more readable the modes of interest are labeled over the picture. It has to be noted that, in this particular case with counter-rotating rotors, the convention that the sense of rotation of the first (HP) rotor is positive has been adopted.

On the top of the figure the modal decomposition is plotted for the blade passing frequency of the LP rotor and its harmonic. As also observed in Fig 3, the trace of the LP rotor blades, mode -72, is the predominant fluctuation. However, it is possible to identify a direct interaction of the LP rotor with

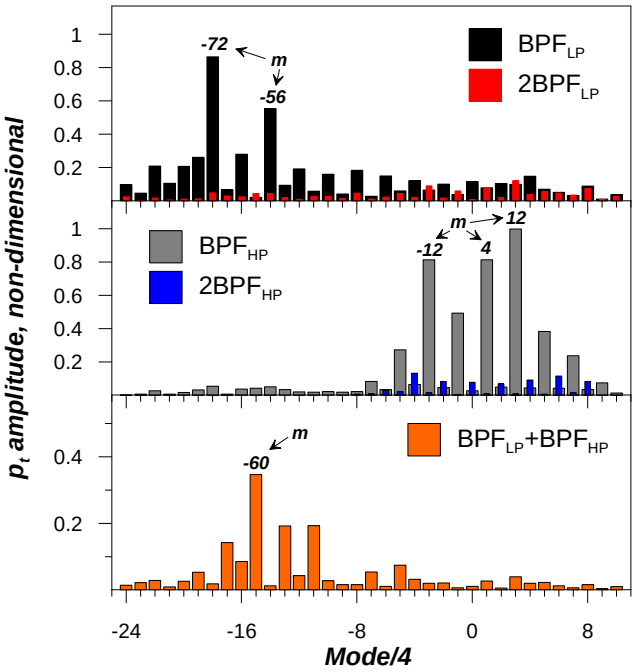

FIGURE 6: Circumferential mode amplitude of total pressure for different frequencies obtained from CFD data, CRT. The main modes are marked over the plot

the TMTF. The amplitude of the mode $-72+16=-56$ is in fact around half of the fluctuations induced by the rotor itself. On the other hand, the fluctuations at the $2BPF_{LP}$ are negligible and the modes at this frequency are not relevant.

The spatial lobes induced by the HP rotor are plotted in the mid of the figure. In agreement with the time resolved evolution of Fig. 4, there is no direct trace of the HP rotor blades (mode 36). The unsteady flow induced by the HP rotor is a complex pattern due to stator/rotor/stator interactions. Particularly, eq. 5 predicts, for the BPF_{HP}, the following modes:
a) HP stator-HP rotor interaction consists of the modes $36+k\cdot 24 = ...36;12;-12;-36...$
b) HP rotor-TMTF interaction consists of the modes $36+k\cdot 16 = ...36;20;4;-12;-28...$
c) HP stator-HP rotor-TMTF interaction consists of the modes $36+k_1\cdot 24+k_2\cdot 16 = ...28;20;12;4;-4;-12;20;28...$
All these different interactions are shown in the plot. The largest amplitude is observed in the middle plot of Fig. 6 for the mode 12 which suggests that the HP rotor-TMTF interaction is not the predominant one. In fact, the mode 12 appears just in the HP stator-HP rotor interactions or in the ones of the three rows together. Similar considerations may be done for the $2BPF_{HP}$, however, their amplitude, as computed from the CFD, is less relevant.

On the bottom of Fig. 6, the modal decomposition is shown for the sum of the blade passing frequencies of the two rotors ($BPF_{LP}+BPF_{HP}$). The amplitude of the modes at this frequency (see also Fig. 5) is smaller than the amplitude at the blade passing frequencies of the rotor alone. However, some predominant modes characterize the rotor-rotor interaction. According to the theory of Holste and Neise [28], a mode -36 should be observed. This mode is computed directly from

the number of blades and sense of rotation of the two rotors, $-36 = -72 + 36$. A mode -60 is instead observed as predominant in the picture. Considering the possible linear combinations between the blade counts, this mode is obtained if the HP vane number (24 vanes) is subtracted to the mode -36. Hence, this term is mainly due to the interactions between the HP stage and the LP rotor. As observed by other authors (e.g. Göttlich [39]), the pressure fluctuations of the HP stage, which are caused by the strong shock waves, do not decay within the duct.

These results confirm the finding of Lengani et al [24]. In that paper, with a more conventional analysis of the unsteady experimental data, a large overall unsteadiness at the outlet of the LP rotor due to both stages has been observed. However, the present analysis extend the results discussed there, identifying and quantifying the amplitude of any source of deterministic unsteadiness.

CONCLUSIONS

The modal decomposition introduced by Tyler and Sofrin [8] has been applied for the analysis of experimental and numerical results obtained in two different test turbines. The paper summarizes the theoretical background behind the decomposition and its capability to isolate the effects of the aerodynamic unsteady interactions between stator and rotor rows. The flow unsteadiness is decomposed in circumferential lobed patterns for the harmonics of the blade passing frequency. It has been shown that the number of lobed patterns or spinning modes is limited and they are associated to two different sources of unsteadiness: the unsteadiness due to the rotor alone is identified for patterns with a number of lobes multiple of the rotor blade number, while the unsteadiness due to the stator/rotor interaction is identified for different, but well defined, spatial modes.

In the simpler case presented, a 1 and 1/2 stage LP turbine, the modal decomposition shows that the amplitude of the fluctuations induced by the stator/rotor interaction is sometimes comparable to the unsteadiness induced by the rotor alone. A different trend has been shown for a multistage configuration (a two stage counter-rotating test turbine). The downstream plane is characterized by spinning patterns with a spatial periodicity different from that of the rotor. In fact the trace of the upstream rotor decays within the flow path and the largest deterministic stresses are due to the unsteady interactions of both stages of the turbine.

With the present analysis method, the overall deterministic unsteadiness of the flow is simplified, even for complex multistage configurations, to a limited number of Fourier coefficients in time and space. Similarly, many CFD methods have been recently developed on the basis of the Fourier analysis in order to consider the spatial or temporal periodicity of the rows in relative motion. Hence, the paper propose a link between experimental results and CFD simulations. The results from this analysis may be, in fact, used as boundary conditions, as Fourier coefficients, for a multi-disciplinary design. For this same purpose, flush mounted microphones are currently employed in both test turbines to complement the aerodynamic measurements with aeroacoustic data.

ACKNOWLEDGMENT

The research leading to these results has received funding from the European Union Framework Programme (FP7/2007-2013) under grant agreement n° 211861, from the Austrian Ministry for Science and Research as well as the EU project VITAL, contract no. AIP4-CT-2004-012271. The authors would like to thank H.P. Pirker for operating the compressor station.

REFERENCES

[1] Adamczyk, J. J., 2000. "Aerodynamic analysis of multistage turbomachinery flows in support of aerodynamic design". *J Turbomach,* ***122***, April, pp. 189–217.

[2] He, L., 2010. "Fourier methods for turbomachinery applications". *Prog Aerospace Sci,* ***46***, pp. 329–341.

[3] Tucker, P. G., 2011. "Computation of unsteady turbomachinery flows: Part 1 progress and challenges". *Prog Aerospace Sci,* ***47***, pp. 522–545.

[4] Binder, A., Förster, W., Kruse, H., and Rogge, H., 1985. "Experimental investigation into the effect of wakes on the unsteady turbine rotor flow". *ASME Journal of Engineering for Gas Turbines and Power,* ***107***(2), pp. 458–465.

[5] Hodson, H. P., 1985. "Measurements of wake-generated unsteadiness in the rotor passages of axial flow turbines". *ASME Journal of Engineering for Gas Turbines and Power,* ***107***(2), pp. 467–476.

[6] Sharma, O. P., Butler, T. L., Joslyn, H. D., and Dring, R. P., 1985. "Three-dimensional unsteady flow in an axial flow turbine". *AIAA Journal of Propulsion and Power,* ***1***(1), pp. 29–38.

[7] Suder, K. L., Hathaway, M. D., Okiishi, T. K., Strazisar, A. J., and Adamczyk, J. J., 1987. Measurements of the unsteady flow field within the stator row of a transonic axial-flow fan. NASA technical memorandum 88945.

[8] Tyler, J. M., and Sofrin, T. G., 1962. "Axial flow compressor noise studies". *SAE Transaction,* ***70***, pp. 309–332.

[9] Groeneweg, J. F., Sofrin, T. G., Rice, E. J., and Gliebe, P. R., 1991. "Turbomachinery noise". In *Aeroacoustics of Flight Vehicles: Theory and Practice, Vol. 1: Noise Sources*, H. Hubbard, ed., NASA RP-1258. ch. 3, pp. 151–209.

[10] Rienstra, S. W., and Hirschberg, A., 2004. *An Introduction to Acoustics*. Eindhoven University of Technology.

[11] Li, H. D., and He, L., 2003. "Blade count and clocking effects on three-bladerow interaction in a transonic turbine". *J Turbomach,* ***125***, October, pp. 632–640.

[12] Arnone, A., and Pacciani, R., 1996. "Rotor-stator interaction analysis using the navier-stokes equation and a multigrid method". *J Turbomach,* ***118***, October, pp. 679–689.

[13] Dorney, D. J., Flitan, H. C., Ashpis, D. E., and Solomon, W. J., 2000. "The effects of blade count on boundary layer development in a low-pressure turbine". In 38th Aerospace Sciences Meeting and Exhibit, Reno, Nevada, January 10-13, Paper No. AIAA-2000-0742.

[14] Gerolymos, G. A., Michon, G. J., and Neubauer, J., 2002. "Analysis and application of chorochronic periodicity in turbomachinery rotor/stator interaction computa-

tions". *Journal of Propulsion and Power,* ***18***(6), November, pp. 1139–1152.

[15] Hall, K. C., Thomas, J. P., and Clark, W. S., 2002. "Computation of unsteady nonlinear flows in cascades using a harmonic balance technique". *AIAA Journal,* ***40***(5), pp. 879–886.

[16] McMullen, M., Jameson, A., and Alonso, J., 2006. "Demonstration of nonlinear frequency domain methods". *AIAA Journal,* ***44***(7), pp. 1428–1435.

[17] Arnaud, D., Ottavy, X., and Vouillarmet, A., 2004. "Experimental investigation of the rotor-stator interactions within a high-speed, multi-stage, axial compressor. part 2 - modal analysis of the interactions". In Proceedings of ASME Turbo Expo 2004, June 14-17, Vienna, Austria, ASME Paper No. GT-2004-53778.

[18] Courtiade, N., Ottavy, X., and Gourdain, N., 2011. "Modal decomposition for the analysis of the rotor-stator interactions in a high-speed multistage compressor". In 10th International Symposium on Experimental and Computational Aerothermodynamics of Internal Flows, Paper No. ISAIF-146.

[19] Lengani, D., Paradiso, B., Marn, A., and Göttlich, E., 2011. "Identification of spinning mode in the unsteady flow field of a LP turbine". In Proceedings of ASME Turbo Expo 2011, June 6-10, Vancouver, Canada, ASME Paper No. GT2011-46226.

[20] Moser, M., Tapken, U., Enghardt, L., and Neuhaus, L., 2009. "An investigation of low pressure turbine blade-vane interaction noise: Measurements in a 1.5-stage rig". *Proceedings of the Institution of Mechanical Engineers, Part A: Journal of Power and Energy,* ***223***(6), pp. 687–695.

[21] Dorney, D. J., and Sharma, O. P., 1997. "Evaluation of flow field approximations for transonic compressor stages". *J Turbomach,* ***119***, July, pp. 445–451.

[22] Santner, C., Paradiso, B., Malzacher, F., Hoeger, M., Hubinka, J., and Göttlich, E., 2011. "Evolution of the flow through a turning mid turbine frame applied between a transonic HP turbine stage and a counter-rotating LP turbine". In Proceedings of 9^{th} European Turbomachinery Conference, March 21-25, Istanbul, Turkey, Paper No. 110.

[23] Paradiso, B., Santner, C., Hubinka, J., Göttlich, E., and Hoeger, M., 2011. "Turning mid turbine frame behavior for different HP turbine outflow conditions". In Proceedings of ASME Turbo Expo 2011, June 6-10, Vancouver, Canada, ASME Paper No. GT2011-46506.

[24] Lengani, D., Santner, C., Spataro, R., Paradiso, B., and Göttlich, E., 2012. "Experimental investigation of the unsteady flow field downstream of a counter-rotating two-spool turbine rig". In Proceedings of ASME Turbo Expo 2012, June 11-15, Copenhagen, Denmark, ASME Paper No. GT2012-68583.

[25] Hubinka, J., Santner, C., Paradiso, B., Malzacher, F., Göttlich, E., and Heitmeir, F., 2009. "Design and construction of a two shaft test turbine for investigation of mid turbine frame flows". In 19^{th} International Symposium on Airbreathing Engines, September 7–11, Montreal, Canada, ISABE Paper ISABE-2009-1293.

[26] Hussain, A., and Reynolds, W., 1970. "The mechanics of an organized wave in turbulent shear flow". *Journal of Fluid Mechanics,* ***41***, pp. 241–258.

[27] Adamczyk, J. J., 1985. "Model equation for simulating flows in multistage turbomachines". In ASME Paper 85-GT-226.

[28] Holste, F., and Neise, W., 1997. "Noise source identification in a propfan model by means of acoustical near field measurements". *Journal of Sound and Vibration,* ***203***(4), pp. 641–665.

[29] Moser, M., Kahl, G., Kulhanek, G., and Heitmeir, F., 2007. "Construction of a subsonic test turbine facility for experimental investigations of sound generation and propagation for low pressure turbines". In ISABE conference Beijing, Paper No. ISABE-2007-1366.

[30] Hubinka, J., Paradiso, B., Santner, C., Göttlich, E., and Heitmeir, F., 2011. "Design and operation of a two spool high pressure test turbine facility". In Proceedings of 9^{th} European Turbomachinery Conference, March 21-25, Istanbul, Turkey, Paper No. 112.

[31] Persico, G., Gaetani, P., and Guardone, A., 2005. "Design and analysis of new concept fast-response pressure probes". *Meas. Sci. Technol.,* ***16***, pp. 1741–1750.

[32] Kupferschmied, P., Köppel, O., Gizzi, W. P., and Gyarmathy, G., 2000. "Time resolved flow measurements with fast aerodynamic probes in turbomachinery". *Meas. Sci. Technol.,* ***11***(7), pp. 1036–1054.

[33] Porreca, L., Hollenstein, M., Kalfas, A. I., and Abhari, R. S., 2007. "Turbulence measurements and analysis in a multistage axial turbine". *Journal of Propulsion and Power,* ***23***(1), pp. 227–234.

[34] Spataro, R., Santner, C., Lengani, D., and Göttlich, E., 2012. "On the flow evolution through a LP turbine with wide-chord vanes in an s-shaped channel". In Proceedings of ASME Turbo Expo 2012, June 11-15, Copenhagen, Denmark, ASME Paper No. GT2012-68178.

[35] ANSYS, 2010. *ANSYS CFX-Solver Modeling Guide*.

[36] Menter, F. R., 1994. "Two-equation eddy-viscosity turbulence models for engineering applications". *AIAA Journal,* ***32***(8), pp. 1598–1605.

[37] He, L., Chen, T., Wells, R. G., Li, Y. S., and Ning, W., 2002. "Analysis of rotor-rotor and stator-stator interferences in multi-stage turbomachines". *J Turbomach,* ***124***, October, pp. 564–571.

[38] Peters, A., and Spakovszky, Z. S., 2012. "Rotor interaction noise in counter-rotating propfan propulsion systems". *J Turbomach,* ***134***, January, p. 011002 (12 pages).

[39] Göttlich, E., 2011. "Research on the aerodynamics of intermediate turbine diffusers". *Prog Aerospace Sci,* ***47***(4), pp. 249–279.

Proceedings of ASME 2013 TURBO EXPO
GT2013
June 3-7, 2013, San Antonio Convention Center, San Antonio, Texas, USA

GT2013-95279

DEVELOPEMENT OF A TURNING MID TURBINE FRAME WITH EMBEDDED DESIGN - PART I: DESIGN AND STEADY MEASUREMENTS

Rosario Spataro, Emil Göttlich, Davide Lengani, Christian Faustmann, Franz Heitmeir
Institute for Thermal Turbomachinery and Machine Dynamics
Graz University of Technology
Graz, A-8010, Austria
Email: rosario.spataro@tugraz.at

ABSTRACT

The paper presents a new setup for the two-stage two-spool facility located at the Institute for Thermal Turbomachinery and Machine Dynamics (ITTM) of Graz University of Technology. The rig was designed in order to simulate the flow behavior of a transonic turbine followed by a counter rotating low pressure stage like the spools of a modern high bypass aero engine. The meridional flow path of the machine is characterized by a diffusing S-shaped duct between the two rotors. The role of turning struts placed into the mid turbine frame is to lead the flow towards the LP rotor with appropriate swirl.

Experimental and numerical investigations performed on the setup over the last years, which were used as baseline for this paper, showed that wide chord vanes induce large wakes and extended secondary flows at the LP rotor inlet flow. Moreover, unsteady interactions between the two turbines were observed downstream of the LP rotor.

In order to increase the uniformity and to decrease the unsteady content of the flow at the inlet of the LP rotor, the mid turbine frame was redesigned with two zero-lifting splitters embedded into the strut passage.

In this first part paper the design process of the splitters and its critical points are presented, while the time-averaged field is discussed by means of five-hole probe measurements and oil flow visualizations. The comparison between the baseline case and the embedded design configuration shows that the new design is able to reduce the flow gradients downstream of the turning struts, providing a more suitable inlet condition for the low pressure rotor. The improvement in the flow field uniformity is also observed downstream of the turbine and it is consequently reflected in an enhancement of the LP turbine performance.

In the second part of this paper the influence of the embedded design on the time-resolved field is investigated.

NOMENCLATURE

C	strut axial chord
C_{pT}	total pressure coefficient
C_p	static pressure coefficient
H	relative channel height
h/C	aspect ratio
HP	High Pressure
k	ideal gas specific heat ratio
LP	Low Pressure
LPV	low passage vortex
$m_{r,in}$	Reduced mass flow, stage inlet
M	Mach number
MAX	Maximum value in the local plane (in the embedded design case)
MID	midspan
$n_{r,in}$	Reduced rotational speed, stage inlet
p_T	total pressure
p	static pressure
P	normalized pitch
r	radial coordinate
Re	Reynolds number
TLV	tip leakage vortex
UPV	upper passage vortex
v	velocity
v_t	tangential velocity
x/C	normalized axial coordinate
α	Yaw angle (from meridional dir.)
γ	Pitch angle (from axial dir.)
η	efficiency
θ	circumferential coordinate
ζ	total pressure loss

Superscripts

$\wedge$	mass-weighted average in the local plane

INTRODUCTION

Modern civil aero engine companies have to face ambitious targets in terms of size and weight reduction. Therefore, over the last years a lot of research effort was put in getting beyond the standards of state-of-the-art propulsion systems.

In large engines, whenever it is required to maximize the pressure ratio at a fixed number of stages while keeping adequate rotational speeds, a conventional solution is to set up the system in multi-shaft configuration (up to 3 shafts in Rolls Royce TRENT engines family).

In order to increase the engine bypass-ratio and, therefore, the propulsion efficiency, the fan front section has to be enlarged. This is limited by structural and acoustic limits on the fan tip velocity. At the same time, the HP-shaft rotational speed should be increased whenever a higher cycle maximum pressure is required.

The resulting larger difference in the shafts rotational speeds leads to an increasing difference in the components diameters (compressors and turbines). Therefore, focusing on the turbine, the resulting S-shaped design of the transition duct between the HP and LP turbines is quite important for the optimisation of the overall engine aerodynamic performance and weight.

The fundamental work by Dominy et al. [1] on swan-necked diffusers identified the influence of the cross-passage pressure gradients in S-shaped ducts. In particular, experimental and numerical data clearly revealed the effects of the two bends on the generation of secondary flows as the flow develops through the diffuser. Swirl was found to influence the character of the flow [2] particularly through the skewing of the wakes.

In modern engines bulky struts are located within the transition duct in order to support the engine shaft and to lead service pipe lines. The flow through the inter turbine diffuser is then disturbed by the presence of these vanes which contribute to increase the level of losses. Recently Göttlich [3] published a review on the present state of the research of these components.

Among the different solutions aimed to shorten the transition duct, an integrated concept such as the turning mid turbine frame represents a remarkable example. Such architecture has been studied in a one-and-half-stage [4,5] and a two-stage [6,7] configuration. Here the idea was to replace the first LP vane row with aerodynamically optimised turning struts. The operation of such setups showed that the LP rotor inlet flow is characterized by large structures such as wakes and secondary flows generated by the struts. These structures on the one hand contribute to reduce the performance of the rotor, while on the other hand they represent a potential source of vibration for the rotor blades.

State of the art for the turbine center frame is non-lifting strut followed by separate first LP vane row. To the authors knowledge there is no serial commercial engine yet flying with a turning mid turbine frame architecture even if it is foreseen for the PW1000G [8] geared turbofan and in several future engine studies (i.e. Seda [9]).

A further problem in shortening the components is that the engine performance is highly affected by the blade row interaction. Aerodynamic performance, vibrations, acoustic emissions of LP turbines are sensibly influenced by the unsteadiness of the flow field propagating downstream the first LP blade row. Therefore, the stator-rotor interaction of the first LP stage needs a careful analysis.

Lengani et al. [10] showed by means of unsteady measurements performed downstream of a two-stage counter-rotating rig (with turbines connected via mid turbine frame) that the unsteadiness content observed downstream of LP rotor is considerably affected by the fluctuations generated by HP stage.

A step forward in the development of mid turbine frames could be represented by the application of an embedded design concept. The basic idea is to merge the strut and the LP vanes in one multisplitter component. Such a concept was already investigated by Lavagnoli et al. [11] and Yasa et al. [12] in the one and half stage short duration test facility located at the Von Karman Institute (VKI). In that facility, starting from a pre-existing LP vane row, the bulky struts were shaped extending every fourth vane, while the meridional flow path was kept the same. The authors observed that the struts cause an evident blockage effect and worsen the circumferential non-uniformity of the aerovane inlet flow field. The combined effect of multisplitter configuration and clocking was found to modify the spatial periodicity of the unsteadiness structure shed by the upstream stage. On the other hand no dramatic influence of the strut was found on the global unsteady performance.

In the present paper a novel and opposite to the VKI approach has been developed. This setup embeds two splitters into an existing turning mid turbine frame placed between two counter-rotating turbines. In this case, the baseline configuration uses turning struts with aft-loaded design. The reader interested in the experimental and numerical investigations conducted on the baseline configuration can refer to Santner et al. [6, 13], Spataro et al. [14, 15] and Lengani et al. [10, 16].

The new setup was designed and tested in the two-stage two-spool continuously operated facility located at the Institute for Thermal Turbomachinery of Graz University of Technology.

The design goal was to reduce the extension of the strut wakes and the secondary flows at the LP rotor inlet as well as to reduce the unsteady interaction observed in the time-resolved flow field downstream of the stage.

In the remainder it is shown that the operating points used to test the baseline and the embedded design provide comparable LP stage inlet conditions. Since the aim of this first part is to compare the time-mean flow of both setups the comparison is carried out by means of spanwise mass-averaged distributions.

A discussion about the influence of the splitters on the homogeneity of the flow field is presented, which lead to observation of a more suitable inlet condition for the LP rotor.

Part one of this paper concludes with a stage performance analysis, while in the second part of this paper (Spataro et

al. [17]) the influence of the embedded design on the unsteady fluctuation is investigated. In addition, the paper by Faustmann et al. [18] showed how such a concept influences the propagation of the acoustic field downstream of the stage.

EXPERIMENTAL APPARATUS AND METHODOLOGY

Facility

The transonic test turbine facility is a continuously operating two-stage cold-flow open-circuit plant, which consists of a transonic HP stage and a counter-rotating LP stage (a schematic drawing is shown in Fig. 1). This unique configuration allows the testing of rig inserts under engine representative conditions. Both turbines are designed with overhung-type turbine shafts and additionally the LP turbine is mounted on an axially movable frame. This allows easy disk assembly without dismantling the bearings and the simple application of transition ducts and integrated designs with different axial lengths. The facility is driven by pressurized air delivered by a separate 3 MW compressor station. The shaft power of the HP stage drives a three-stage radial brake compressor. The power of the LP turbine is absorbed by a water brake with a maximum power of 700 kW. Detailed information on the design and construction of the original single stage facility can be found in Erhard and Gehrer [19]. For the design of the LP-stage together with the integrated concept see Hubinka et al. [20] and for the operation Hubinka et al. [21]. Downstream of the test turbine a gas-turbine-driven suction blower was used to reduce the back pressure of the test setup and to increase the overall pressure ratio. Thus, with this device it is possible to run the test turbine facility with stable operating conditions without day-to-day variations. The suction blower uses a Rolls Royce Gnome helicopter engine via a flat belt drive as power source and allows a very precise adjustment of the turbine exhaust pressure by means of speed control.

Table 1 summarizes the main parameters for the HP stage and the LP stage (duct + LP rotor), and the operating condition.

Design of the splitters

The design process of the splitter vanes was based on a numerical investigation undertaken on the baseline configuration [14, 15]. The axial extension of the splitters as well as the splitter count represent a compromise between aerodynamic effectiveness and solid blockage, while the meridional flow channel was kept the same as for the baseline case. The two splitters axes have been located at $P = 0.33$ and $P = 0.67$ respectively in order to obtain equispaced wakes at the LP rotor inlet.

The generation and evaluation of several designs defined the final shape which was manufactured and tested.

For each splitter seven control sections located at different spanwise locations (H=0.00, H=0.05, H=0.25, H=0.50, H=0.75, H=0.95, H=1.00) were chosen. For each section, the same spanwise metallic angle and thickness distribution as the strut trailing edge was imposed. At the leading edge the splitter inlet blade angle was adjusted targeting to a zero-incidence condition.

Measurement techniques

The experimental investigation was conducted by means of 5 hole probes traversed in three measurement planes (Plane C, E and F in Fig. 1). Moreover, one of the strut passages was instrumented with pressure taps along five lines located at 10%, 25%, 50%, 75% and 90% over the vane span, and five lines located at 10%, 25%, 50%, 75% and 95% pitch over the hub and shroud endwalls (see Fig. 2). In Plane C the probe was traversed radially over 85% of the blade height and over one HP-vane pitch. At each measurement point the probes were turned into the flow to reach the highest accuracy and to ensure they were within the calibration range of the probe. Due to the variation in flow direction relative to the measurement location, in some planes specially developed five-hole-probes (IST, RWTH Aachen) with an inclined probe head of $2.5mm$ diameter were used. The probes were calibrated for Mach numbers between 0.1 and 0.8, yaw angles between -20 deg and +20 deg and pitch angles between -16 deg and +20 deg.

The correlation between the calibration characteristic and the value to be measured is given by a multi-parameter approximation.

The uncertainty of the Mach number is 0.005, while for the yaw and pitch angle the measurement error is ± 0.3 and ± 0.5 degrees respectively. Negative values of the yaw angle indicate a counter-rotating flow (with respect to the HP rotor circumferential speed) and negative values of the pitch angle indicate the flow direction towards the machine axis.

The measurement system consists of eleven multi channel pressure transducers PSI 9016 with a total amount of 176 channels and an accuracy of 0.05% full scale and four National Instruments Field Point FP-TC-120 eight-channel thermocouple input modules and one FP-RTD-122 resistance thermometer input module. The measurement uncertainties of the static pressure taps on the vane surface are $\pm 100Pa$.

A mixture of synthetic motor oil and titanium oxide is used to visualize the topology of the shear stress at the walls. The mixture has been uniformly painted in the whole passage surfaces of different struts in order to verify the periodicity of the flow and the reliability of the results. The applied oil film was

TABLE 1: Blading parameters and operating conditions.

Blading parameters						
		HP vane	HP blade	Struts	Splitters	LP blade
Vane/ blade no.		24	36	16	32	72
h/c_{ax}		1.15	1.37	0.53	3.5	2.94
Re(10^6)		2.38	1.1	1.86	0.4	0.46
Tip gap		-	unshrouded	-	-	shrouded
Operating conditions						
			HP stage		LP stage	
$n_{r,in}$ $[rpm/\sqrt{K}]$			524.4		195.3	
$m_{r,in}$ $[kg/s \cdot \sqrt{K}/(bar)]$			81.2		214.6	
Baseline	Stage p_t ratio		3		1.3	
Baseline	Power [kW]		1710		340	
with Splitters	Stage p_t ratio		2.83		1.36	
with Splitters	Power [kW]		1425		353	

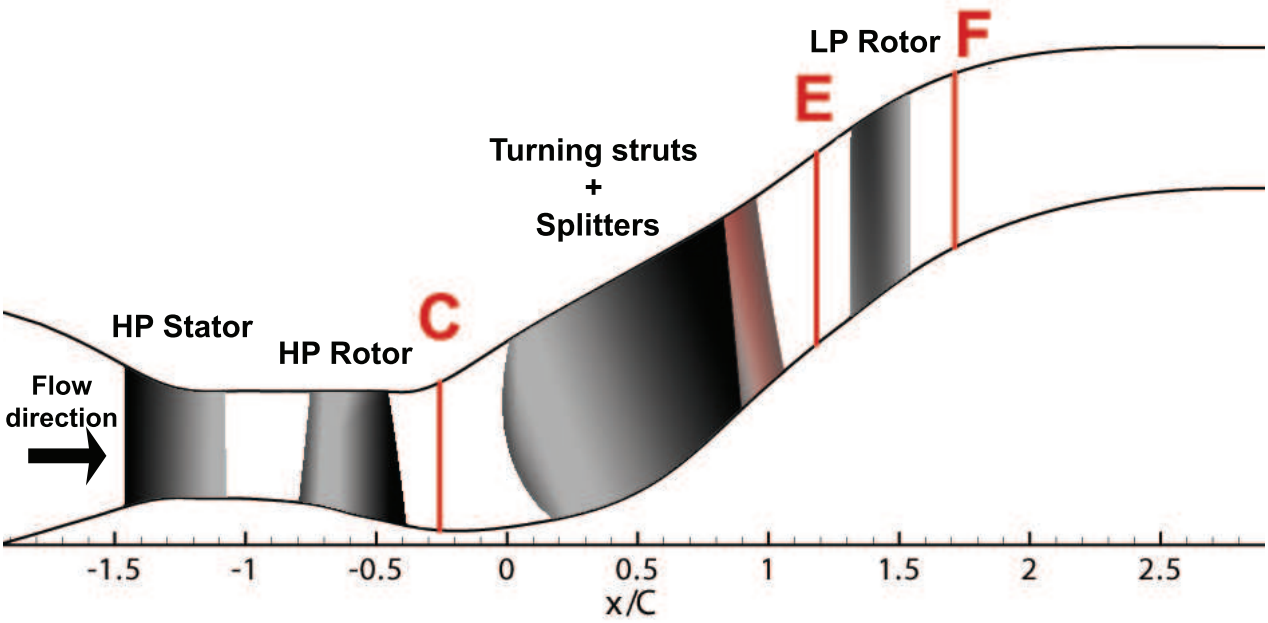

FIGURE 1: Two stage - two spool facility at the ITTM and measurement section

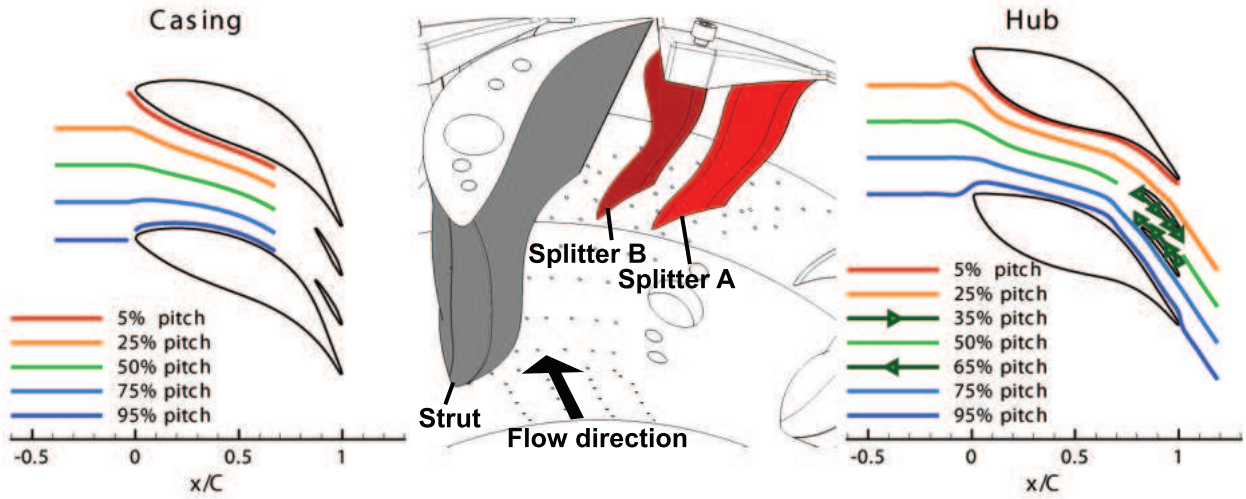

FIGURE 2: Pressure taps position at the hub and casing endwalls

exposed to the flow for approximately one hour after reaching the stable operating condition.

RESULTS AND DISCUSSION

In this section the steady measurements performed through the low pressure stage are presented. A special focus is on the comparison between measurements with and without splitters. The blockage induced by the splitters required a different pressure ratio than the baseline case. An assumption for the comparability between the two setups was necessary. The chosen matching condition was reached aiming for both the turbines to the same reduced speed and reduced mass flow (essential for the flow angle at the duct inlet) in order to have struts with the same inflow angle.

In the following the results from five hole probe measurements through the duct (Plane C, E and Plane F) will be presented and discussed. Static pressure measurements at the duct endwall and on the strut surfaces are also shown.

LP stage inlet flow

The HP turbine is a low aspect ratio stage with an unshrouded rotor, therefore secondary flows are predominant in the stator-rotor interaction [22, 23].

Figure 3 shows the time-averaged distribution of normalized Mach number (M/M_{MAX}), yaw angle (α), normalized total pressure (C_{pT}) and normalized static pressure (C_p) in Plane C, downstream of the HP stage. The contour plot shows the distribution of the total pressure and yaw angle over the measurement plane. The spanwise mass-averaged flow quantity distributions show the comparison between the baseline case and the multisplitter design. The spanwise location is plotted in terms of radial coordinate normalized with the channel height (H).

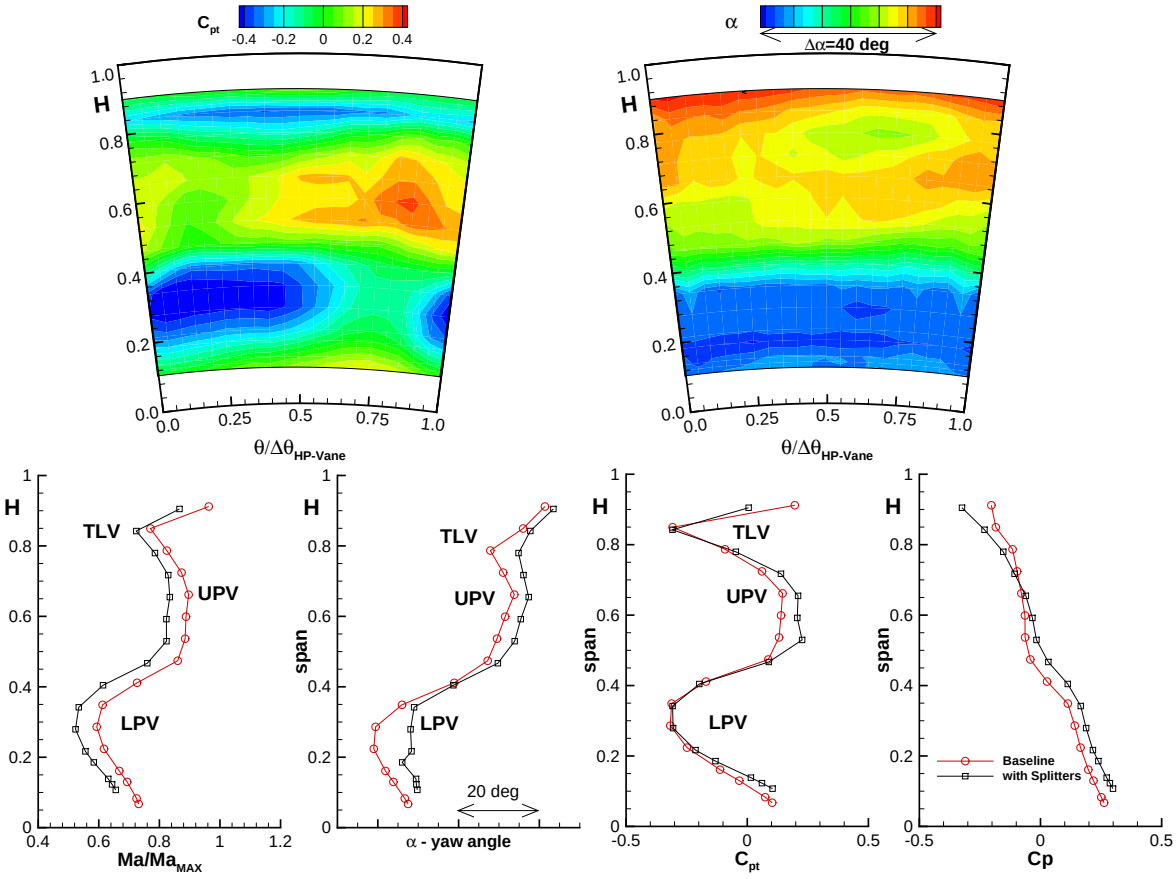

FIGURE 3: Plane C - Five hole probe measurements at the duct inlet (view from downstream)

The total pressure coefficient was defined as:

$$C_{pT} = \frac{p_T - \hat{p}_{T,C}}{\hat{p}_{T,C} - \hat{p}_C} \tag{1}$$

where $\hat{p}_{T,C}$ and $\hat{p}_C$ represent the mass-weighted total and static pressure on Plane C respectively.

In a similar way, the static pressure was normalized as:

$$C_p = \frac{p - \hat{p}_C}{\hat{p}_{T,C} - \hat{p}_C} \tag{2}$$

The value M_{MAX} used to normalize the Mach number represents its local maximum in the multisplitter case.

Downstream of this type of turbines, the main flow features which dominate the downstream time-resolved flow field are shocks and secondary flows (e.g. Denos et al. [24], Urbassik at al. [25], Schennach et al. [26]). Since these structures generate total pressure losses and induce changes in the mean flow angle, looking at the charts in Fig. 3, they can be identified with a spanwise trend variation of yaw angle, total pressure and Mach number. Therefore, it is possible to locate the consequences of the rotor tip leakage vortex at $H = 0.8$ (TLV), of the rotor upper passage vortex at $H = 0.65$ (UPV) and of the rotor lower passage vortex at $H = 0.3$ (LPV) (co-rotating with the TLV [27, 28]). Any visible circumferential variation of these features in the contour plots derives then from the stator-rotor interaction between the HP vanes and the HP rotor.

The comparison between the baseline case and the embedded design in Fig. 3 shows that for both cases the main structures are located at the same radial position and thus they appear to have the same influence on the flow field.

From Table 1 it is possible to see that it was not possible to reach the same pressure ratio for the HP stage due to facility limitations. This explains the slightly lower Mach number measured in Plane C, upstream of the splitters.

Nevertheless, the possibility to match the same reduced mass flow and reduced rotational speed allowed to have very similar flow angle distributions. Therefore the struts face a very similar flow ($\Delta\alpha_{MID} < 5deg$).

Flow within the strut passage

Figure 4 (a), (b) and (c) show the static pressure distribution measured on the casing, on the hub and on the strut surfaces respectively. The axial coordinate is normalized on the strut axial chord of each considered section. The static pressure at the endwalls are plotted along lines distributed at different pitchwise positions ($P = 0.5$, $P = 0.25$, $P = 0.50$, $P = 0.75$, $P = 0.95$ in Fig. 2). Two more tap rows were added in the splitter central passage in order to visualize the suction-to-pressure side gradient at the hub section ($P = 0.35$ $P = 0.65$ in Figure 4 (b)). The blade loading distribution is plotted at five different span positions ($H = 0.10$, $H = 0.25$, $H = 0.50$, $H = 0.75$, $H = 0.90$).

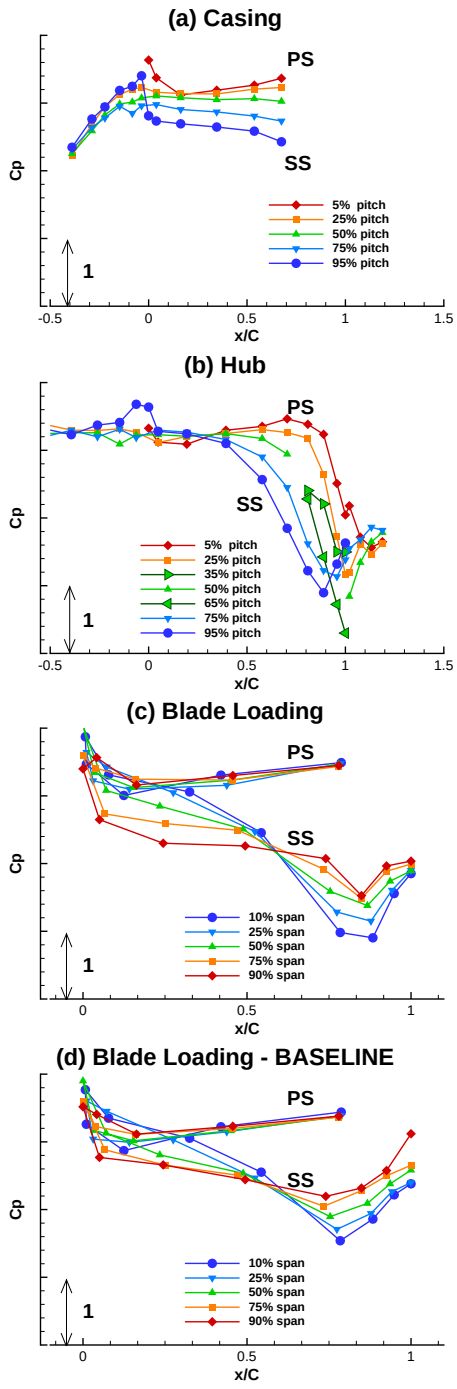

FIGURE 4: Static pressure measurements within the strut passage

Santner et al. [6, 13] and Paradiso et al. [7] already presented and discussed these distributions for the baseline setup. In particular, in that case it was observed the aft-loaded design of the strut and how this faces negative incidence at the lower half of the channel, zero-incidence at midspan and positive incidence at the upper part of the channel.

The distributions in Fig. 4 (a) and (b) show that at the front part of the strut channel ($0 < x/C < 0.2$), the suction-to-pressure side gradient is relevant just at the casing. At the hub endwall, the flow accelerates late in the passage $x/C \approx 0.3$. Moreover, the pressure taps located within the splitters passages show a maximum overspeed in the central channel.

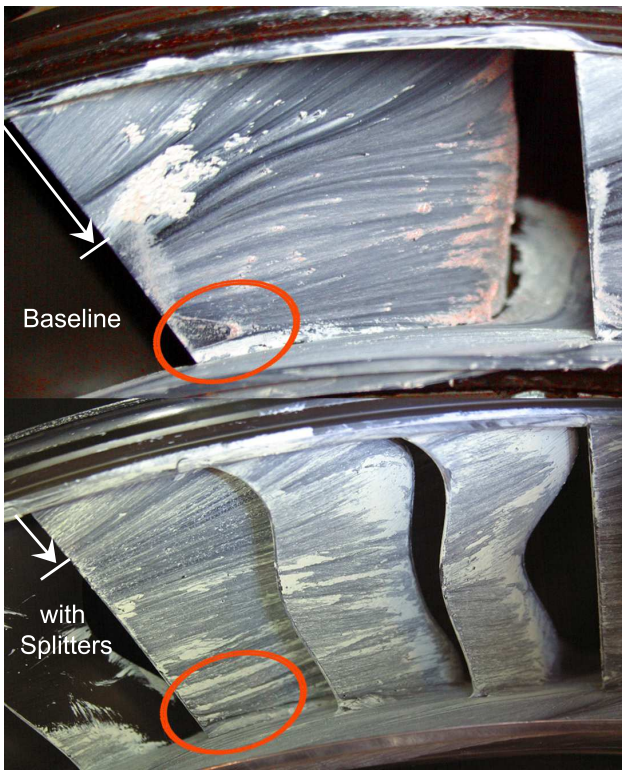

FIGURE 5: Comparison of oil flow visualizations on the strut suction side for baseline and multisplitter setups (view from downstream)

Looking at Fig. 4 (c), except for the rear part of the strut, the blade loading distribution over the strut shows a similar shape to the one already observed in the baseline setup (Fig. 4 (c)). This is due to the very similar incidence faced by the strut in both cases (as already observed in the comparison of the yaw angle distribution in Figure 3).

As already mentioned, the biggest difference between both setups in the blade loading distribution can be found in the rear part of the strut suction side exactly were the splitters are located ($0.8 < x/C < 1.0$). Because of the splitter blockage, a different flow area is distributed through the duct. Therefore, the flow is strongly accelerated into the splitter passages (note the underpressure on the strut suction side in Fig. 4 (c)).

This means that, in the design phase of such embedded concept, the engineer should take steps aimed to correct the splitter solid blockage. This could be carried out iterating the meridional flow path (known as area ruling and which also implies for each step a redesign of the strut), or applying 3D endwall contouring techniques.

Looking at the maximum overspeed point on the profile, it is interesting to notice that the hub-to-shroud gradient in the splitter passage is consistent with the baseline case.

1) the corner separation between the strut hub trailing edge and the hub endwall is reduced in the multisplitter design;

2) the strong downwash observed in the baseline configuration is also reduced with the consequence that the flow is better guided along the suction surface (white arrow in Fig. 5);

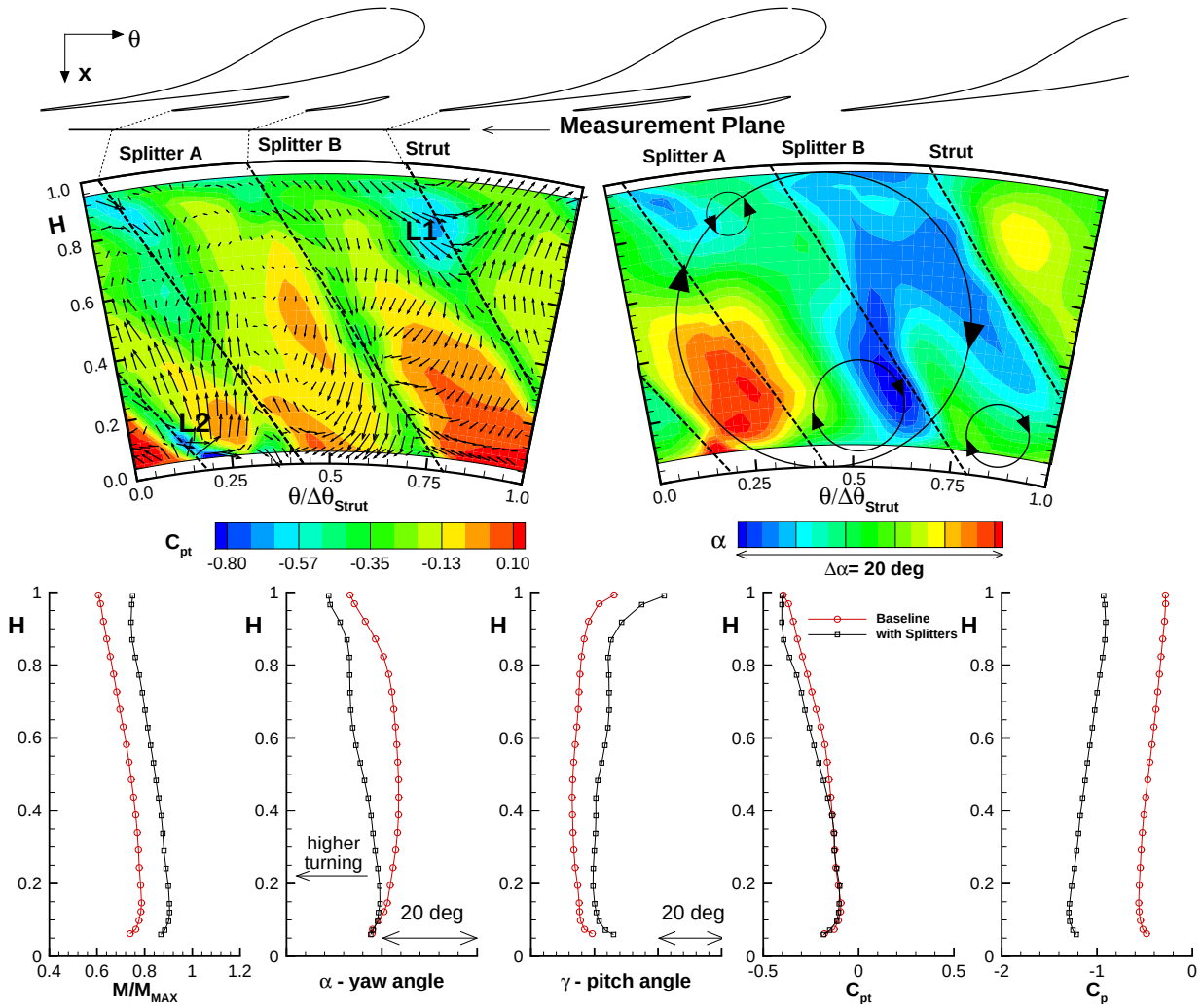

FIGURE 6: Plane E - Five hole probe measurements at the LP rotor inlet flow (view from downstream)

LP rotor inlet flow

Figure 6 shows five-hole probe measurements in Plane E which is located at $x/C = 1.28$. The contour plots show total pressure (on the left side) and yaw angle (on the right side) distributions. The yaw angle was defined positive in the direction of the HP rotor angular speed, which means that the blue color identifies area of higher turning, while the red color the ones of lower turning. The comparison between baseline and multisplitter setups in terms of spanwise distributions of mass-weighted Mach number, yaw angle, pitch angle, total pressure and static pressure is plotted at the bottom of the figure. The Mach number is normalized on its local maximum, while for the total and static pressure coefficient the definitions in Equation 1 and 2 were used respectively.

The contour plot of total pressure allows the identification of the position of the main structures such as strut and splitter wakes (dashed lines: Strut, Splitter A and Splitter B in Figure 6) as well as the main loss cores (L1, L2). L1 is representative of the strut shed vortex, while L2 is effected by the strut corner separation observed in the baseline case.

The secondary velocity vectors superimposed on the C_{pT} distribution are defined as the difference between the local velocity vector and a reference flow direction (see for example Chaluvadi et al. [29] and Persico et al. [30]). In the present case, the reference flow vector has been determined by subtracting from the local values the averages of the circumferential and radial velocity components in the radial and circumferential directions respectively. This procedure is necessary because of the very high velocity gradients that characterize the mean flow in both directions.

Focusing now on the flow angles, the effect of the splitter vanes in this plane is quite relevant since the mean turning and the pitch angles are enhanced by $5deg$ and $8deg$ respectively. Such a trend in the pitch angle is confirmed by the oil flow visualization in Fig. 5.

Moreover, looking at the yaw angle distribution in Fig. 6 a notable effect of the splitters can be seen on the shape of the yaw angle distribution. This is driven by the modified pattern of the secondary flow structures off the struts.

In order to better understand this effect, a simplified scheme is proposed in Fig. 7. The sketch shows the tangential velocities, where the contribution of a flow led through the vane without generating any vortices ("*vortex-free*" field) and the effect of secondary vorticities were separated. Finally, their combination is shown.

Regarding the *vortex-free* field, it has to be noticed that

the strut was designed to have, in first approximation, a linear spanwise variation of blade angle at the trailing edge (more turning at the shroud and lower turning at the hub). The result of this is the $vt(r)$ distribution in Fig. 7 (a).

For the baseline case in Fig. 7 it was found out that, due to a negative incidence at the lower half channel of the strut, no lower passage vortex is generated at the strut leading edge. Instead, a large passage vortex extending over the full span starts to develop at $x/C \approx 0.3$. On the other hand, the upper passage vortex was seen confined in the shroud endwall region. The yaw angle distribution in this plane was observed to be constant for $0.2 < H < 0.8$ (Fig. 6).

Figure 7 (b) clarifies how such a distribution can be explained by the major role played by the strut passage vortex. This vortex induces an overturning in the lower half channel and an underturning in the upper one, therefore leading to a roughly constant distribution in this region (Fig. 7 (c)). For $H < 0.2$ and $H > 0.8$ the spanwise variation in the mean angle distribution is driven by the strut shed vortices (not sketched in Fig. 7).

The velocity vectors and the vortices sketches in Fig. 6 reveal the presence of the vane passage vortex [13, 14, 16] extending over the full channel height and of small vortices (two at the hub and one at the shroud) that can be seen at the endwalls.

Referring to the multisplitter configuration in Fig. 7 (b) the extended passage vortex is cut and reduced by the splitters. On the other hand, whenever the splitters are designed as turning vanes, within each channel new upper and lower passage vortices are generated (UPVs and LPVs). The existence and the strength of such a vortices is related to the splitter deflection rate.

As a result, whenever an engineer faces the design of such component with splitter located in the rear part of the passage, he should be aware of two limit conditions which will define a trade-off for the performance optimisation:

Aft loaded strut The development of secondary vortices associated with the wide chord vane is delayed in the passage. The level of losses connected to the rolling up of these structures through the duct is lowered. With such a design the streamwise point of maximum suction-to-pressure side gradient is moved downstream in the passage. This means that the splitters would face a less uniform flow and therefore they have to be optimized by a highly 3D design in order to reach the zero-incidence condition for the whole span (profile losses minimization). Likely, this will lead to turning splitters, which implies on the one hand the need to optimise uneven flow passages, on the other hand the generation of new secondary structures that will be found at the inlet of the following rotor.

Front loaded strut Secondary vortices develop earlier in the passage but a more uniform pitchwise pressure gradient can be reached at the splitter inlet. The splitters design could be more easily optimised due to the reduced transverse pressure gradient in front of the vanes. The target would be to design the splitter vanes under zero-incidence zero-lift condition. Such a design would minimize the profile losses as well as avoid the generation of splitter secondary structures. It is necessary to point out that the three-dimensionality of a flow field confined in such a strut passage would need an unavoidable complex design of the splitters.

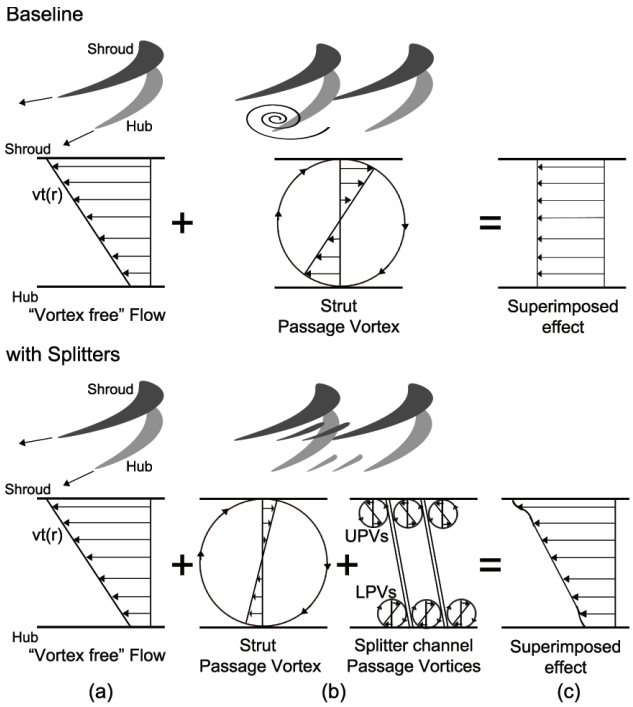

FIGURE 7: Embedded design concept: schematization of the strut secondary vortex suppression and splitter vortex generation mechanisms

LP rotor exit flow

Figure 8 shows five-hole probe measurements in Plane F which is located at $x/C = 1.71$ downstream of the LP rotor. Similar to Fig. 6, the contour plots show total pressure (left side) and yaw angle (right side) distributions. The yaw angle was defined positive in the direction of the HP rotor angular speed, which means that, referring to the LP rotor geometry, the blue color identifies the area of lower turning, while the red color the ones of higher turning.

The comparison between baseline and multisplitter setups in terms of spanwise distributions of mass-weighted Mach number, yaw angle, pitch angle, total pressure and static pressure is plotted in the lower charts. The Mach number is normalized on its local maximum, while for the total and static pressure coefficient the definition in Equation 1 and 2 were used respectively. The total pressure contour allows the identification of the trace of the strut wake convected through the rotor (dashed line in Fig. 8). L3 represents the loss core due to the strut passage vortex. This structure was already seen in the baseline design, but here, in the multisplitter setup, it is strongly reduced. L4 is a loss core due to the convection of the splitter B wake (see Fig. 6) through the rotor, which it can be better visualized in the time resolved flow field (Spataro et al. [17]).

Similar C_{pT} distributions are observed upstream of the rotor (Plane E in Fig. 6). A marked total pressure offset between

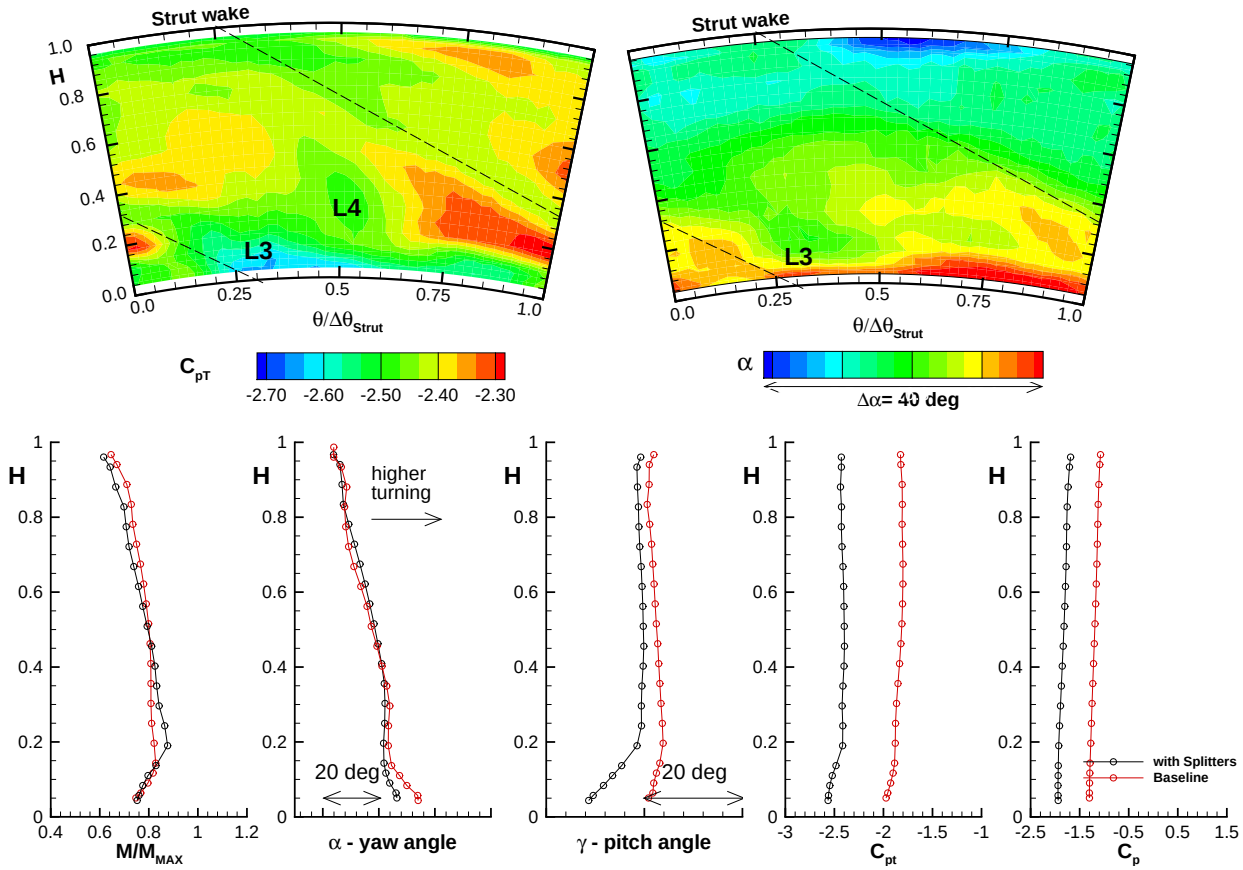

FIGURE 8: Plane F - Five hole probe measurements at the LP rotor exit flow (view from downstream). L3 loss core due to the strut passage vortex. L4 trace of the splitter B wake

baseline and multisplitter cases seen in this plane suggests that more work is extracted by the rotor in the splitter setup than in the baseline configuration. In the following section the two LP stage performances are presented.

Looking at the flow angle contour plot in Fig. 8, it is possible to see that the greatest non uniformities are located in the lower half channel. The comparison between the time-mean field measured in both setups shows that the multisplitter setup is more homogeneous in the both circumferential and radial directions (the interested reader can refer to [6, 10] for the five-hole probe measurements in the baseline case).

LP stage performance analysis

Before comparing the performance of both setups, it is important to notice that total and static pressure coefficient as defined in Eq. 1 and 2 respectively cannot be considered direct indicators of the stage performance, since the flow area through the duct is heavily affected, in this special case, by the splitter blockage.

Therefore, the following loss coefficient is used:

$$\zeta_{duct} = \frac{\hat{p}_{T,C} - \hat{p}_{T,E}}{\hat{p}_{T,C} - \hat{p}_{E}} \tag{3}$$

from which the definition of the duct efficiency follows:

$$\eta_{duct} = 1 - \zeta_{duct} \tag{4}$$

In Fig. 9 the spanwise ζ_{duct} distribution is plotted for Plane E. The comparison shows in general a lower level of losses generated through the duct for the splitter setup. In particular a strong reduction is visible in the shroud region, where the intense loss core due to the strut shed vortex plays a major role on the losses generation.

The stage efficiency was computed between Plane C (Stage inlet) and Plane F (Stage outlet), using the following definition:

$$\eta_{LPstage} = \frac{\frac{\hat{T}_{T,C}}{\hat{T}_{T,F}} - 1}{\left(\frac{\hat{p}_{T,C}}{\hat{p}_{T,F}}\right)^{\frac{\kappa-1}{\kappa}} - 1} \tag{5}$$

The efficiency difference for duct and stage was computed as:

$$\Delta\eta_i = \frac{\eta_{i,Splitter} - \eta_{i,Baseline}}{\eta_{i,Baseline}} \tag{6}$$

with $i = duct, LPstage$. The results of such a comparison are reported below:

$\Delta\eta_{duct}$	$\Delta\eta_{LPstage}$
$+3.71\%$	$+6.08\%$

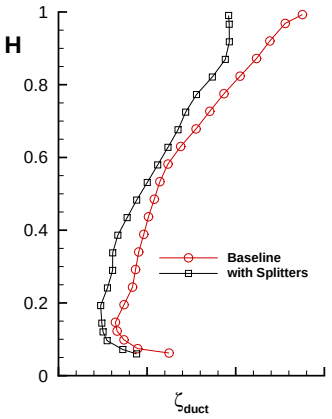

FIGURE 9: Losses through the duct for baseline and embedded design setups

CONCLUSIONS

The paper presented a new setup for a turning mid turbine frame where a novel approach to an embedded design was applied.

The discussion on the flow field is carried out by comparing steady measurements performed on a baseline case (no splitters within the strut passage) and the embedded setup.

Due to the increased blockage, a new operating point for the new setup is selected. At the LP stage inlet, five hole probe measurements performed in both cases show very similar distributions, while the stage pressure ratio is increased for the new setup.

Static pressure measurements within the channel show a similar trend between the two setups, though in the embedded design, a strong flow acceleration is seen as soon as the flow is guided into the splitter passage. The authors note the possibility to avoid this effect in the design phase reshaping the meridional flow path or applying 3D endwall contouring techniques.

For the embedded design, oil flow visualizations show a better distribution of the flow leading into the next rotor. This is also confirmed by five hole probe measurements performed in planes located upstream and downstream of the rotor. It turns out that the increased uniformity of the flow field (reduced strut wakes and secondary vortices) at the low pressure rotor inlet is responsible for the improvement of the overall LP stage performance.

Moreover, a scheme is proposed in order to help in understanding the mechanism by which the suppression of the strut secondary vortex enhances the flow turning and, in general, increases the homogeneity of the flow field downstream of the component.

A special focus in this paper is given to the design criteria for the turning mid turbine frame, whenever splitter blades have to be inserted within the strut passage. In the authors opinion the distribution of the strut blade loading along the chord is a critical design parameter for the aerodynamic optimisation of the component. A control of the suction-to-pressure side gradient would ease the splitter shaping in order to reach a zero-incidence (profile losses minimized) zero-lift (splitter secondary losses minimized) operating condition.

ACKNOWLEDGMENT

The authors would like to thank H. Peter Pirker, Cornelia Santner, Josef Hubinka and Berardo Paradiso (currently affiliated at Politecnico di Milano) for the important support during the experimental campaign. The research leading to these results has been partially founded by the European Union within the EU-project DREAM (contract No. ACP7-GA-2008-211861) as well as from the Austrian Ministry for Finance.

REFERENCES

[1] Dominy, R. G., Kirkham, D. A., and Smith, A. D., 1998. "Flow development through inter-turbine diffusers". *ASME Journal of Turbomachinery,* ***120***, January, pp. 298–304.

[2] Dominy, R. G., and Kirkham, D. A., 1996. "The influence of blade wakes on the performance of inter-turbine diffusers". *ASME Journal of Turbomachinery,* ***118***, January, pp. 347–352.

[3] Göttlich, E., 2011. "Research on the aerodynamics of intermediate turbine diffusers". *Progress in Aerospace Sciences,* ***47***, pp. 249–279.

[4] Miller, R. J., Moss, R. W., Ainsworth, R. W., and Harvey, N. W., 2004. "The effect of an upstream turbine on a low-aspect ratio vane". In Proceedings of ASME Turbo Expo 2004, June 14-17, Vienna, Austria, ASME Paper No. GT-2004-54017.

[5] Marn, A., Göttlich, E., Cadrecha, D., and Pirker, H. P., 2009. "Shorten the intermediate turbine duct length by applying an integrated concept". *ASME Journal of Turbomachinery,* ***131***, p. 041014 (10 pages).

[6] Santner, C., Paradiso, B., Malzacher, F., Hoeger, M., Hubinka, J., and Göttlich, E., 2011. "Evolution of the flow through a turning mid turbine frame applied between a transonic hp turbine stage and a counter-rotating lp turbine". In Proceedings of 9^{th} European Turbomachinery Conference, March 21-25, Istanbul, Turkey, Paper No. 110.

[7] Paradiso, B., Santner, C., Hubinka, J., and Göttlich, E., 2011. "Turning mid turbine frame behaviour for different hp turbine outflow conditions". In Proceedings of ASME Turbo Expo 2011, June 6-10, Vancouver, British Columbia, Canada, ASME Paper No. GT-2011-46502.

[8] Pratt-&-Withney. Pure power pw1000g geared turbofan engine. http://www.purepowerengine.com/.

[9] Seda, J. Aircraft engine with inter-turbine engine frame. united states patent 6708482 b2. http://www.freepatentsonline.com/6708482.html.

[10] Lengani, D., Santner, T., Spataro, R., Paradiso, B., and Göttlich, E., 2012. "Experimental investigation of the unsteady flow field downstream of a counter-rotating two-spool turbine rig". In Proceedings of ASME Turbo Expo 2012, June 11-15, Copenhagen, Denmark, ASME Paper No. GT-GT2012-68583.

[11] Lavagnoli, S., Yasa, T., Paniagua, G., Duni, S., and Castillon, L. "Aerodynamic analysis of an innovative low pressure vane placed in a s-shape duct". *ASME Journal of Turbomachinery,* ***134***.

[12] Yasa, T., Lavagnoli, S., and Paniagua, G., 2011. "Impact of a multi-splitter vane configuration on the losses in a 1.5 turbine stage". *Proceedings of IMechE Vol. 225,* ***225***, pp. 964–974.

[13] Santner, C., Göttlich, E., Wallin, F., and Hoeger, M., 2011. "Experimental investigation of turning mid turbine frame designs". In Proceedings of ISABE 2011, September 12-16, Gothenburg, Sweden, ISABE Paper No. ISABE-2011-1710.

[14] Spataro, R., Santner, C., Lengani, D., and Göttlich, E., 2012. "On the flow evolution through a lp turbine with wide-chord vanes in an s-shaped channel". In Proceedings of ASME Turbo Expo 2012, June 11-15, Bella Center, Copenhagen, Denmark, ASME Paper No. GT-2012-68178.

[15] Spataro, R., , Göttlich, E., Santner, C., and Heitmeir, F., 2013. "A numerical comparison on the aerodynamic performances of a two-stage two-spool turbine facility predicted by steady and unsteady simulations". In Proceedings of 10^{th} European Turbomachinery Conference, April 21-25, Lappenranta, Finland, Paper No. 39.

[16] Lengani, D., Selic, T., Spataro, R., Marn, A., and Göttlich, E., 2012. "Analysis of the unsteady flow field in the turbines by means of modal decomposition". In Proceedings of ASME Turbo Expo 2012, June 11–15, Copenhagen, Denmark, ASME Paper No. GT-GT2012-68582.

[17] Spataro, R., Göttlich, E., Lengani, D., Faustmann, C., and Heitmeir, F., 2013. "Developement of a turning mid turbine frame with embedded design - part ii: Unsteady measurements". In Proceedings of ASME Turbo Expo 2013, June 3-7, San Antonio, Texas, USA, ASME Paper No. GT-2013-95280.

[18] Faustmann, C., Lengani, D., Spataro, R., Marn, A., Göttlich, E., and Heitmeir, F., 2013. "Experimental investigation of the noise generation and propagation for different turning mid turbine frame setups in a two-stage two-spool test turbine". In Proceedings of ASME Turbo Expo 2013, June 3-7, San Antonio, Texas, USA, ASME Paper No. GT-2013-95698.

[19] Erhard, J., and Gehrer, A., 2000. "Design and construction of a transonic test turbine facility". In Proceedings of ASME Turbo Expo 2000, May 8–11, Munich, Germany, GT-48.

[20] Hubinka, J., Santner, C., Paradiso, B., Malzacher, F., and Göttlich, E., 2009. "Design and construction of a two shaft test turbine for investigation of mid turbine frame flows". In Proceedings of ISABE 2009, Montreal, Quebec, Canada, ASME Paper No. ISABE-2009-1293.

[21] Hubinka, J., Paradiso, B., Santner, C., Pirker, H. P., and Göttlich, E., 2011. "Design and operation of a two spool high pressure test turbine facility". In Proceeding of the 9th ETC conference, Instambul, Turkey, pp 1531-1540.

[22] Dénos, R., and Paniagua, G., eds., 2005. *Effects of Aerodynamic Unsteadiness in Axial Turbomachines*. VKI Lecture Series, LS 2005-03.

[23] Persico, G., Mora, A., Gaetani, P., and Savini, M., 2010. "Unsteady aerodynamics of a low aspect ratio turbine stage: modelling issues and flow physics". In Proceedings of ASME Turbo Expo 2010, June 14–18, Glasgow, UK, ASME Paper No. GT2010-22927.

[24] Dénos, R., Arts, T., Paniagua, G., Michelassi, V., and Martelli, F., 2001. "Investigation of the unsteady rotor aerodyanamics in a transonic turbine stage". *ASME Journal of Turbomachinery,* ***123***, pp. 81–89.

[25] Urbassik, R. M., Wolff, J. M., and Polanka, M. D., 2006. "Unsteady aerodynamics and interactions between a high-pressure turbine vane and rotor". *ASME Journal of Turbomachinery,* ***128***, pp. 35–42.

[26] Schennach, O., Woisetschläger, J., Paradiso, B., Persico, G., and Gaetani, P., 2010. "Three dimensional clocking effects in a one and a half stage transonic turbine". *ASME Journal of Turbomachinery,* ***132***, pp. 011019–1 (9 pages).

[27] Miller, R. J., Moss, R. W., Ainsworth, R. W., and Horwood, C. K., 2003. "Time-resolved vane-rotor interaction in a high-pressure turbine stage". *ASME Journal of Turbomachinery,* ***125***, January, pp. 1–13.

[28] Gaetani, P., Persico, G., Dossena, V., and Osnaghi, C., 2007. "Investigation of the flow field in a high-pressure turbine stage for two stator-rotor axial gaps-part 2: Unsteady flow field". *ASME Journal of Turbomachinery,* ***129***, July, pp. 580–590.

[29] Chaluvadi, V. S. P., I.Kalfas, A., Banieghbal, M. R., Hodson, H. P., and Denton, J. D. "An experimental study of the unsteady characteristics of the turbulent wake of a turbine blade". *AIAA Journal of Propulsion and Power,* ***17***.

[30] Persico, G., Gaetani, P., Dossena, V., D'Ippolito, G., and Osnaghi, C., 2009. "On the definition of the secondary flow in three-dimensional cascades". *I MECH E Journal of Power and Energy,* ***223***, pp. 667–676.

Proceedings of ASME Turbo Expo 2013
GT2013
June 3-7, 2013, San Antonio, USA

GT2013-95280

DEVELOPMENT OF A TURNING MID TURBINE FRAME WITH EMBEDDED DESIGN - PART II: UNSTEADY MEASUREMENTS

Rosario Spataro, Emil Göttlich, Davide Lengani, Christian Faustmann, Franz Heitmeir
Inst. f. Thermal Turbomachinery and Machine Dynamics
Graz University of Technology, Austria
Email: rosario.spataro@tugraz.at

ABSTRACT

The paper, which is constituted by two parts, presents a new setup for the two-stage two-spool facility located at the Institute for Thermal Turbomachinery and Machine Dynamics (ITTM) of Graz University of Technology. The rig was designed in order to reproduce the flow behavior of a transonic turbine followed by a counter rotating low pressure stage like those in high bypass aero-engines. The meridional flow path of the machine is characterized by a diffusing S-shaped duct between the two rotors. The role of wide chord vanes placed into the mid turbine frame is to lead the flow towards the LP rotor with appropriate swirl.

Experimental and numerical investigations performed on this setup over the last years showed that the wide chord struts induce large wakes and extended secondary flows at LP inlet flow. Moreover, large deterministic fluctuations of pressure, which may cause noise and blade vibrations, were observed downstream of the LP rotor. In order to minimize secondary vortices and to damp the unsteady interactions, the mid turbine frame was redesigned to locate two zero-lifting splitters into the vane passage.

While in the first part paper the design process of the splitters and the time-averaged flow field were presented, in this second part the measurements performed by means of a fast response probe will support the explanation of the time-resolved field. The discussion will focus on the comparison between the baseline case (without splitters) and the embedded design.

Nomenclature

BPF	Blade passing frequency
H	Relative channel height
HP	High pressure
LP	Low pressure
M	Mach number
p_t	Total pressure
PLA	Phase locked average
RSA	Rotor-synchronic average
t	time
T	Blade passing period
v	velocity
ρ	Flow density
θ	Circumferential coordinate
$<>$	deterministic periodic component

Subscripts

AVE	Circumferentially averaged properties, in the local plane
ax	Axial component
MAX	Maximum value, in the local plane
RMS	Root mean square

Superscripts

$\bar{}$	Time averaged properties
$\sim$	Phase locked properties
$'$	Stochastic fluctuating component

INTRODUCTION

The diffusing duct, which connects the HP with the LP turbine frame, has a critical impact on the overall performances of modern and future generation aero-engines. In fact, in high-bypass ratio turbofan and eventually in the new open rotor technology the diffusing duct may be a key component which could function as engine mount structure to the aircraft. This would lead to shorter and lighter engines. Furthermore, a new concept of integrated design, which combines the function of a strut with that of a LP-vane, has been recently developed according to these design trends (e.g., [1, 2]). In this configuration, the diffusing duct is provided with large vanes which have a structural function and have to properly lead the flow to the first LP rotor. The first LP stage is, then, constituted by the intermedi-

ate turbine diffuser provided with these turning vanes and an LP rotor at the outlet of the duct.

In such configurations the analysis of the unsteady flow features is critical for the understanding of the physical mechanisms that occur through the diffusing duct. This has been pointed out by a large amount of studies performed in the last 15 years. These works are too many to be exhaustively mentioned here, however, the interested reader may find a complete literature review in the paper of Göttlich [3]. Particularly, it has been shown that the unsteadiness generated by the HP stages influences the secondary flows of the turning vanes in the diffuser and hence its outlet flow. In fact, the pressure fluctuations, and hence the entropy waves, generated by the shock waves and velocity defects of the HP stages do not decay within the duct. The extent of the unsteadiness at the outlet of the duct, downstream of the first LP rotor, is critical for the aerodynamic performances, vibrations and acoustic emissions of the successive LP stages, and, then, need a careful analysis.

However, there is still a limited amount of openly published works that could present the impact on the aerodynamic performances of the diffusing duct together with up-and downstream components. This is due to manufacturing costs and design complexity of two-spool test turbines. Recently, results from a two-stage test turbine [4, 5] have shown that angle and velocity fluctuations of the first stage decay quickly in the former part of the diffusing duct. Whereas, the unsteady pressure perturbation from the stage upstream of the duct contributes considerably to the overall pressure fluctuations at the exit of the second stage. A non-negligible contribution to this unsteadiness is generated also by the interactions of the rotors even though there is a diffusing flow between them.

Flow control, duct and vane shape optimization, and endwall contouring are promising actions to optimize the flow at the outlet of duct and eventually reduce the extent of such unsteadiness at its outlet. A further solution is represented by merging the strut and the LP vanes in one multi-splitter component (e.g., Lavagnoli et al. [6] and Yasa et al. [7]). This embedded design approach has been designed and implemented in the counter-rotating two-spool facility of Graz University of Technology as documented in the first part paper [8]. This second part of the paper is aimed at the description of the unsteady effect and their propagation through the second stage of the facility. Time-resolved aerodynamic measurements have been performed on this research facility by means of fast response aerodynamic pressure probes. The sources of unsteadiness are identified considering the HP stage-strut-LP rotor interaction by means of the proper analysis of the time signal of the probe [5]. Thus, the deterministic fluctuations of the measured flow quantities and the stochastic fluctuations of total pressure are quantified. These results are discussed for the splitter configuration and compared with the baseline configuration without splitters [4].

EXPERIMENTAL APPARATUS AND METHODOLOGY

Facility

The transonic test turbine facility installed at the Graz University of Technology is a continuously operating two-stage cold-flow open-circuit plant, which consists of a transonic HP stage and a counter-rotating LP stage. This unique configuration allows the testing of rig inserts under aerodynamic conditions relevant for modern aero-engine. The part 1 paper [8] provides the description of the design parameters and operating conditions of the two configurations tested. This second part paper maintains the same nomenclature, particularly, the splitter vanes facing the suction and pressure side of the strut will be referred to as splitter "A" and splitter "B", respectively. Further details on the facility and on the baseline configuration, without splitters, may be found in Hubinka et al. [9, 10].

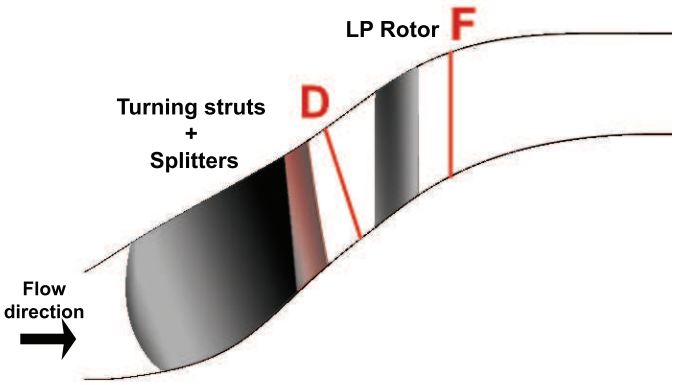

FIGURE 1: Schematic meridional section of the test setup with probe measurement planes (D, F).

For completeness, a sketch of the measuring planes adopted in the present paper is reported in Fig. 1. The plane F, downstream of the LP rotor, is the same plane employed for the investigation with the five hole prob in part 1 [8]. Whereas, the plane D, the plane immediately downstream of the struts and splitter vanes, differs from plane E of part 1 [8]. This inclined plane is, in fact, more suited for the fast response pressure probes adopted in the unsteady flow investigation. It helps reducing the region of out of calibration range of the probe because of the large radial component of velocity within the duct.

Measuring techniques

Unsteady flow measurements were performed by means of two different fast-response aerodynamic pressure probes. In the former studies with the baseline configuration [4, 5], a 2-sensor probe, operated as a virtual four sensor probe for 3D aerodynamic measurements [11], has been used. In the present paper a cylindrical one sensor probe has been used, see Persico et al. [12] for more details. Unsteady measurements with the one sensor have been repeated in the baseline setup and provided results in very good agreement with the 2-sensor probe. Limits of the one sensor probe have been observed in regions of the measurement plane with large radial components, where the error on static pressure increases when compared with the 2-sensor probe. It has to be noted that also the 2-sensor probe is at the limits of the calibration range in the same regions. Otherwise, for both probes, the extended uncertainty is in the order of $\pm 0.5\%$ of the kinetic head for the pressure measurements and of ± 0.3 deg for the flow angles.

The present paper describes the results obtained by the fast response probes in annular sectors in planes D and F (marked in Fig. 1). Plane D is a plane inclined by 110 deg to the horizontal direction and, at midspan, its distance from the vane trailing edge is 14% of the strut axial chord; whereas, plane F is perpendicular to the horizontal direction and is located at 77% of the LP rotor chord downstream of the LP blade trailing edge. The full area traverses were performed over one strut pitch (22.5 deg) up-and downstream of the LP rotor. The measurement grid consists, for both planes (D and F) and both configurations, of 19 positions along the blade span and of 46 positions over one pitch of the strut ($\Delta\theta_{strut}$).

Data reduction method

Data is acquired at 200 kHz for 2 seconds, it corresponds to more than 100 revolutions of the LP turbine and more than 350 of the HP turbine. The determination of the flow properties is made possible after phase averaging: the periodic fluctuations of velocity, pressures and flow angles are determined at each phase from the phase averaged values of the three rotations of the probe [13].

The 2S-FRAPP signals, and the two shaft encoders were acquired simultaneously, in order to provide the frequencies of rotation of the two shafts. Such measurement allows the decomposition of the flow with respect to the phase of one of the two rotors, hence, the effects of the two rotors on the flow may be observed separately. Furthermore, it allows also the reconstruction of a phase that takes into account the relative rotor-rotor positions (see Lengani et al. [5]).

Phase averaging was performed triggering the flow with the 2 shaft encoders according to the triple decomposition procedure [14], for a generic variable p:

$$p(t) = \overline{p} + < p > + p'(t) \tag{1}$$

where $< p >$ is the purely periodic component associated with a coherent periodic structure and $p'(t)$ is the random fluctuation associated mainly with turbulence. This decomposition is used to characterize a single source of periodic unsteadiness and, in the present case, allows isolating the effects of each rotor. However, considering the presence of two rotors (HP and LP rotor) at unrelated frequencies, the decomposition may be rewritten as [5]:

$$p(t) = \overline{p} + < p >_{HP} + < p >_{LP} + < p >_{HP,LP} + p'(t) \tag{2}$$

where the purely periodic components $< p >_{HP}, < p >_{LP}$, namely the coherent structures due to the HP and LP rotor respectively, have their own period and frequency. The term $< p >_{HP,LP}$ indicates the rotor-rotor interactions which generate energy content at the frequencies of the linear combination $i \cdot BPF_{LP} + k \cdot BPF_{HP}$ (with i and k integer and not zero), which are observed in two shaft facilities (e.g., [5, 15]). A particular phase averaging, rotor synchronic average (RSA), has been developed [4, 5] in order to provide the following time resolved distribution:

$$\tilde{p}_{RSA} = \overline{p} + < p >_{HP} + < p >_{LP} + < p >_{HP,LP} \tag{3}$$

Considering eq. 1, the stochastic fluctuating component is classically computed subtracting from the instantaneous value $p(t)$ the phase averaged value $\tilde{p} = \overline{p} + < p(t) >$. When two rotors are interacting, eq. 2 should be considered and hence the stochastic fluctuating component $p'(t)$ could be obtained as:

$$p'(t) = p(t) - (\overline{p} + < p(t) >_{HP} + \\ + < p(t) >_{LP} + < p(t) >_{HP,LP}) \tag{4}$$

However, as discussed in Lengani et al. [16], a faster solution to this problem is the use of Fourier filtering to determine the stochastic fluctuating component. This is based and extends the method of previous works (e.g., [17–19]). The fluctuating part of a variable directly measured from a probe, total pressure in the present case, may be determined with the following steps [16]:

1) FFTs are performed over sufficiently large blocks of samples in order to have a good frequency resolution;
2) the amplitude of the deterministic periodic components is digitally filtered out setting it to zero;
3) the "chopped" spectrum is transformed back into the time domain to provide directly the random fluctuating signal.

The final result of the post-processing procedure is the time resolved evolution of $p'_t(t)$. This data is further post-processed in order to provide the root mean square value $p'_{t,RMS}$ of its time or phase average. The time average is performed over ≈ 250000 samples, while the phase average is performed over ≈ 8500 samples (these numbers include the reduction of the original samples due to the post-processing procedures).

The stochastic fluctuations are further post processed computing their root mean square (RMS value, $p'_{t,RMS}$). The uncertainty on this quantity depends on the capability of the probe in measuring directly the instantaneous total pressure. This has been checked from the probe calibration. When the instantaneous flow direction exceeds the angle insensitivity range, the uncertainty on the phase averaged stochastic fluctuations can go up to 20% otherwise it remains within 8%. The areas with the highest uncertainty corresponds to the areas where the probe do not directly reads the total pressure. In these particular zones, the fluctuating part, because of the filtering procedure, may just underestimate the value of the stochastic fluctuations. Hence, the error on the stochastic fluctuations is higher in the regions of the minimum values.

RESULTS AND DISCUSSION

The results are presented in this section as contour plots in the absolute (stationary) reference frame. Time averaged distribution have been used for plane D, while time resolved distribution are displayed for plane F. The following plots represent views in the upstream direction on a sector covering one pitch of the struts. Consequently, the pictures cover 4 and 1/2 LP rotor blades and 2 and 1/4 blades of the HP rotor. In the plots the LP rotor has a clockwise sense of rotation while it is the opposite for the HP rotor.

The absolute Mach number and the stochastic fluctuations of total pressure are depicted in the following figures. These

quantities are plotted as non-dimensional coefficients. The Mach number is shown in terms of M/M_{MAX}, where M_{MAX} is the maximum value of the time averaged Mach number in the local measurement plane. Whereas, the stochastic fluctuations of total pressure $p'_{t,RMS}$ are made non-dimensional by $\rho v^2_{ax,AVE}$, the mass averaged axial velocity in the plane has been adopted in the definition in order to compare the two different setups. This term $(p'_{t,RMS}/\rho v^2_{ax,AVE})$ is used to provide a quantity as close as possible to the turbulence intensity. Particularly, the term $p'_{t,RMS}/\rho v^2_{ax,AVE}$ is proportional to the turbulence intensity (see for example [13, 20]) and it helps, indeed, identifying the causes of loss generation.

Furthermore, in order to provide information about the overall periodic unsteadiness, the root mean square (RMS) of the coherent periodic fluctuations of different flow quantities is provided in the following figures for both measurement planes. This quantity is computed as described by Tiedemann and Kost [21] and it represents an integral measure for the purely periodic component of the signal. Considering eq. 3, the periodic part obtained by the RSA ($< p >_{RSA}$), for a generic variable p, may be computed as $\tilde{p}_{RSA} - \overline{p}$:

$$< p >_{RSA} = < p >_{LP} + < p >_{HP} + < p >_{LP,HP} \qquad (5)$$

The RMS of this quantity is represented by one value for each measurement position. It estimates the amplitude of the temporal fluctuations induced by the unsteady interactions with the upstream blade and vane rows (similar considerations may be found in [21,22]). Furthermore, it may provide information for the design of the successive stage as it will be discussed in the followings.

Flow upstream of LP rotor

The detailed description of the time averaged flow downstream of the turning struts is provided in the part 1 of the paper [8]. The results of the FRAPP measurements provide more information on deterministic and stochastic stresses. Before discussing these results, since the FRAPP was used in a different plane than the five hole probe, the time averaged distribution of the Mach number in plane D is also reported in Fig. 2 and briefly discussed.

This contour plot of the non-dimensional Mach number distribution shows a large velocity gradient in the radial direction, which is mainly due to the diffusing channel. The regions at low momentum are associated to the wakes of the strut and of the two splitters vane as discussed in part 1 [8]. Furthermore, iso-countour lines of the RMS of the deterministic fluctuation of the flow angle are superimposed on the plot. The regions enclosed by these lines corresponds to the areas at low momentum and they help identifying the wakes of the three vanes. It has to be mentioned that these iso-contour lines represent the maximum value of the deterministic fluctuations of the flow angle. However, this fluctuating component is very low, it has a minimum to maximum angle variation that do not exceed 3 degrees and it is fluctuating just at the frequency of the HP rotor.

The term $p'_{t,RMS}/\rho v^2_{ax,AVE}$ (Fig. 3, on top) shows a similar result. The highest stochastic fluctuations are, in fact, identified in correspondence of the three vane wakes. Particularly, the strut wake and the pressure side splitter present the largest value. Whereas, the wake of the suction side splitter shows lower values with a local maximum in the tip region. The difference in the behaviour of the two splitters is due to the large vortical structures that characterize the strut passage which cause a region of high turbulence. This effect is clearly shown in the stochastic fluctuations plot of the baseline setup (Fig. 3, on bottom), which has been documented in Lengani et al. [16]. The strut passage without splitters present, in fact, a large region at high turbulence which is associated to the passage vortex. In the case of the splitter setup, the strength of this

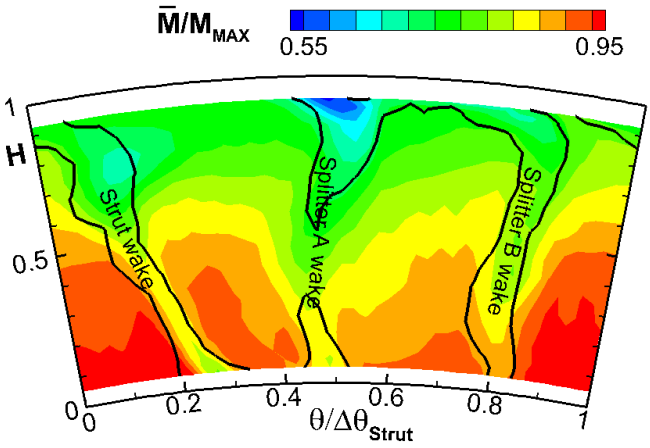

FIGURE 2: Time averaged distribution of Mach number in plane D, splitter setup.

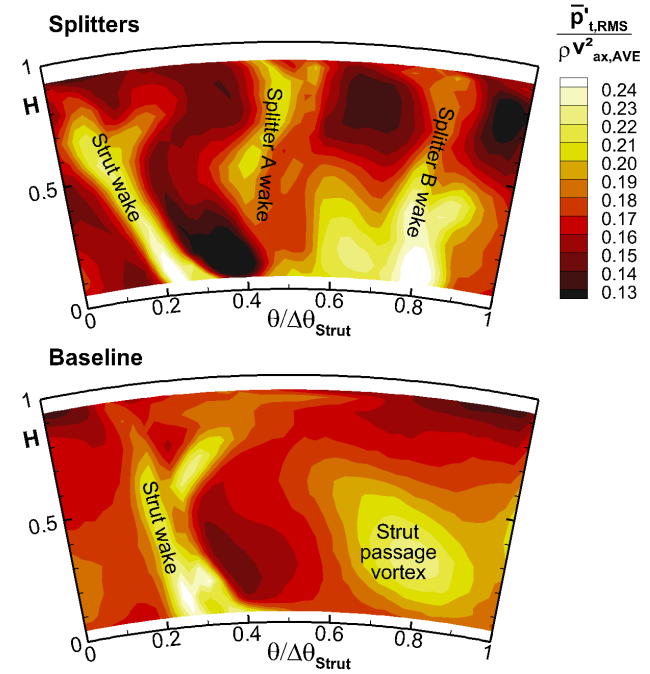

FIGURE 3: Time-averaged distributions of the RMS of the stochastic fluctuations of total pressure in plane D for the two configurations

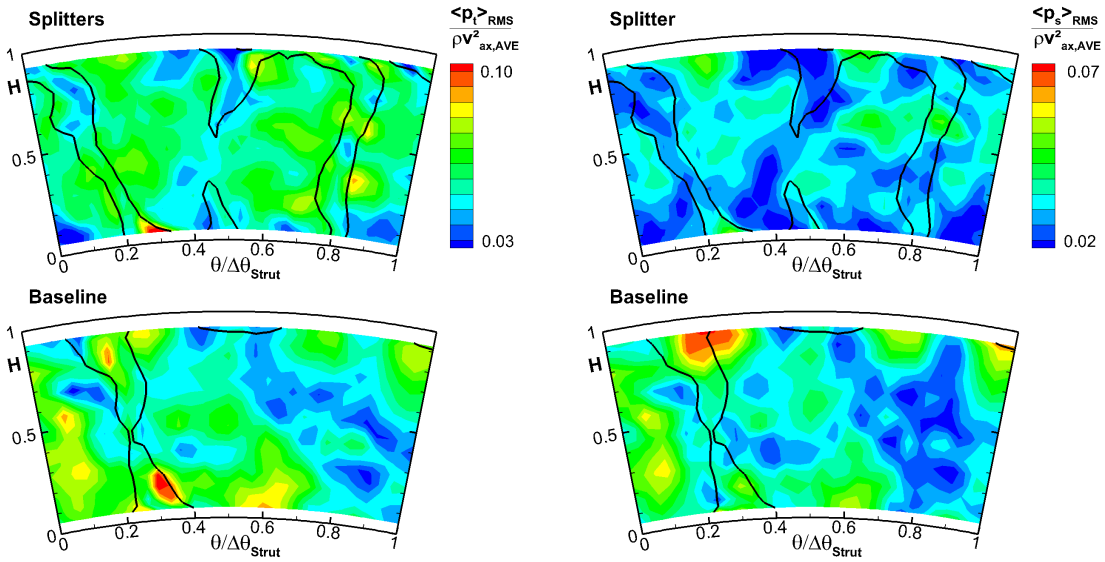

(a) Total pressure (b) Static pressure

FIGURE 4: Contour plots of the RMS of the deterministic fluctuations of pressure in plane D for the two configurations

vortical structure, and its associated turbulence, is reduced by the presence of the splitter vanes. However, the presence of the splitters leads to higher local turbulence in their wake, this is more noticeable for the splitter close to the strut pressure side (splitter "B", as marked over the plot). On the other hand, the level of turbulence intensity of the wake of the strut itself is reduced in the splitter configuration. This is probably because the growth of the boundary layers on the aft-portion of the strut is reduced by the presence of the splitters.

As also observed in Lengani et al. [16], these regions of high stochastic fluctuations are correlated to the mean flow structures of the exit flow of the vanes. In fact, there is a very low impact of the HP rotor unsteadiness on the generation of losses. The phase averaged map of the term $p'_{t,RMS}/\rho v^2_{ax,AVE}$ looks completely similar to the time averaged map shown in Fig. 3, and for this reason it is not shown.

A different behaviour is shown by the deterministic fluctuations of pressure which are depicted in Fig. 4. This picture reports the contour plots of the RMS of the total and static pressure periodic components computed from the HP rotor phase (in this plane there are no significant contributions from the LP related structures or rotor-rotor interactions). As for Fig. 2, iso-countour lines of the RMS of the deterministic fluctuation of the flow angle are superimposed on the plot to help identifying the vane wakes.

The RMS of total pressure for the splitter setup (Fig. 4a on top) shows an almost uniform distribution with local miminima in correspondence of the splitter "A" wake. However, it is difficult to associate the areas at high fluctuations to the structures of the flow emanated by the vanes. A similar consideration may be done for the baseline case (Fig. 4a on bottom). In this case the RMS of $< p_t >$ does not present an uniform distribution, and its largest values are shown in proximity of the strut wake. The comparison of the two setups reveals that the baseline case has the largest fluctuations in half portion of the plane, while the splitter case has lower fluctuations but uniformly distributed within the strut pitch. It has to be reminded that the deterministic fluctuations are due to the vane-rotor-vane interaction, which generates spinning modes (e.g., Tyler and Sofrin [23]). Furthermore, it is known that the circumferential modes with small spatial wavelength tends to decay whereas mode with small wavelength propagates (e.g., He et al. [24]). A map of the RMS of the fluctuation which is less uniform (baseline case) suggests that modes at small spatial wavelength characterize the flow and vice-versa for the splitter case. This suggests that the propagating pressure fluctuations will be reduced by the presence of the splitters, hence, low vibrations and low acoustic emission have to be expected with this former setup. The paper of Faustmann et al. [25], which deals with an aeroacoustic investigation on the two setups, confirms that dowsntream of the facility the noise emission at the HP blade passing frequency and its harmonics are reduced with the splitter. Figure 4b shows the RMS of the deterministic fluctuation of static pressure. The picture is reported for completeness but it has to be noted that the measurement error on the phase resolved static pressure is larger than the error on total pressure. The error on the static pressure is higher for the splitter configuration which presents an overall larger pitch angle (see part 1 [8]). However, this last picture confirms the trend discussed for the RMS of total pressure and it clearly shows the reduction in static pressure fluctuations, hence the lower vibrations and acoustic emissions due to the HP rotor with the splitter setup.

Flow downstream of LP rotor

LP rotor phase As previously discussed, the flow downstream of the LP rotor is characterized by multiple sources of unsteadiness (see eq. 2). In order to simplify the analysis of such complex flow the time resolved results are discussed at first considering the phase average based on the LP rotor. As previously mentioned (eq. 1), such phase averaging preserves just the coherent fluctuations due to the LP rotor. For the splitter case, three time snapshots are extracted from

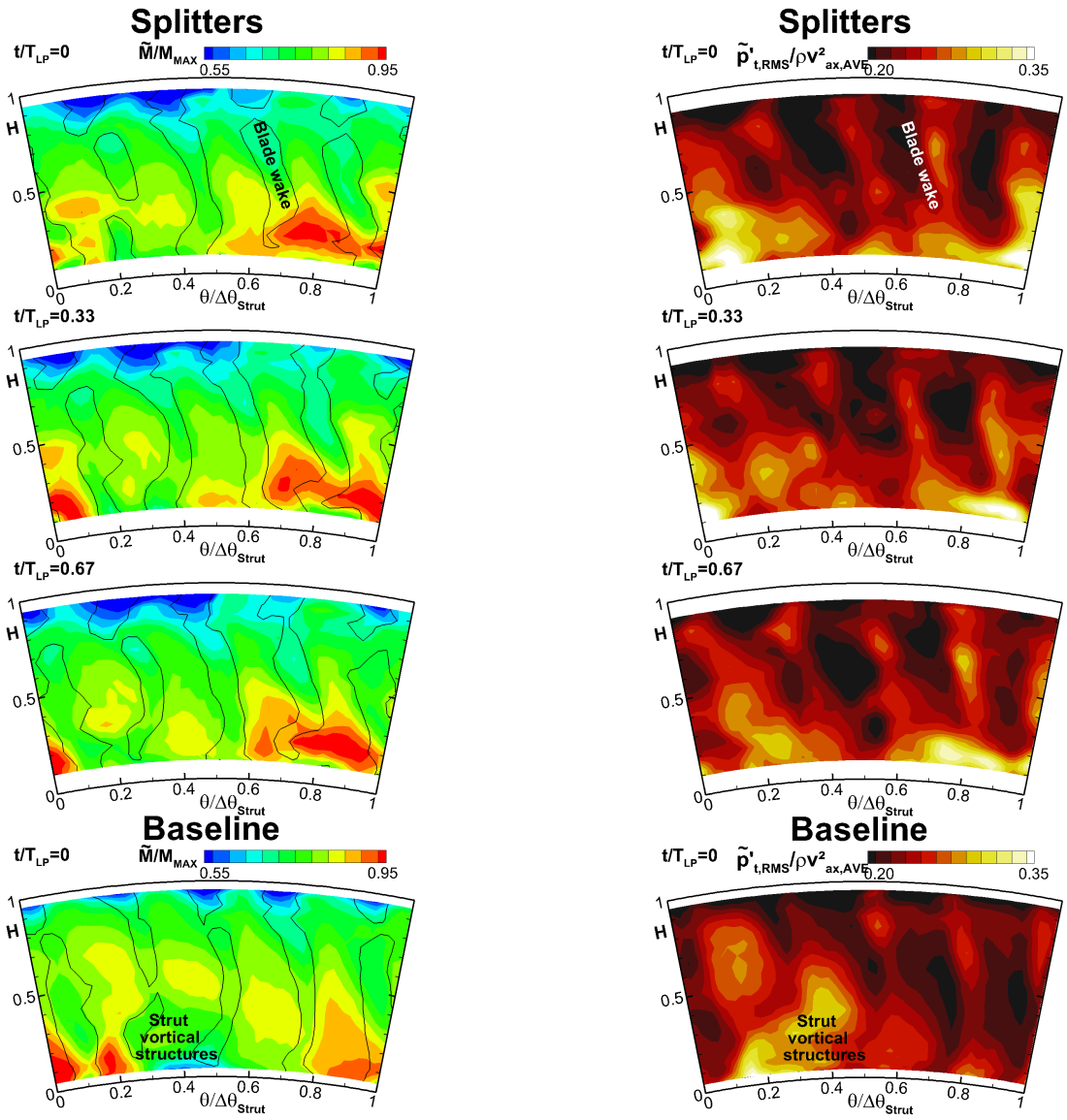

(a) Mach number

(b) Stochastic fluctuations

FIGURE 5: Time resolved distribution of Mach number and stochastic fluctuations of total pressure in plane F. LP rotor phase.

one averaged blade passing period in order to show the time resolved evolution of the Mach number, and of the stochastic fluctuations of total pressure (Fig. 5a and 5b, respectively). For completeness, on the bottom of the figures one time step for the same quantity is also shown for the baseline case, which was discussed in more details in [4]. To allow the identification of the blade wake positions, the iso-contour lines of the periodic fluctuations of the Mach number ($< M >= \tilde{M} - \overline{M}$) are superimposed on the plot of Fig. 5a. The position of one of the rotor wake is marked over the experimental results and it is enclosed by the iso-contour lines of $< M > /M_{MAX} = -2\%$, and, similarly, the other blade wakes may be identified enclosed within the iso-contour lines. Hence, a clear trace of the 4 and 1/2 blades of the LP rotor, which is moving in the counterclockwise direction, may be observed: alternately high and low velocity areas (the latter identified by the iso-contour lines) are representative of the blade passage flow and blade wake, respectively.

In the lower half of the channel ($H < 0.5$), the different blade passages present circumferential non uniformities which are due to the inlet condition. Particularly, in part 1 [8], it has been shown that the largest difference in the inlet yaw angle at the rotor is observed in the lower half portion of the channel. This variation in the incidence angle, which is caused by the vortical structures developing in the strut passage, leads then to the non-uniform flow observed along the circumferential direction. This effect is not relevant in the upper half of the channel ($H > 0.5$), where the only notable circumferential non-uniformities are due to the blade structures, namely their wakes and tip passage vortices.

The blade velocity defects, that may be identified within the iso-contour lines of $< M > /M_{MAX} = -2\%$, slightly change with the relative circumferential position of blade and struts (compare the different time steps of Fig. 5a). The largest difference within the time resolved evolution are shown close to the endwall regions. In particular at the hub, the iso-contour

lines of $< M > /M_{MAX}$ are bowed passing in particular circumferential positions (see for example the hub region at $0.7 < \theta/\Delta\theta_{Strut} < 0.9$ for $t/T_{LP} = 0.33$ or at $0.2 < \theta/\Delta\theta_{Strut} < 0.35$ for $t/T_{LP} = 0.67$).

This behaviour is different from what is classically observed in the open literature of LP turbines (e.g., [26, 27]). In fact, in conventional LP turbines, the flow at the outlet of adjacent blade passages is rather similar, the circumferential gradients are due to the blade loading. Moreover, the thickness and velocity defect of the blade wake depends on the vane wake-blade interactions (e.g., [28]). Such 2D interaction phenomenon is predominant in the generation of losses. In the present case, the rotor is interacting with a strut of completely different solidity and aspect ratio. However, the presence of the splitters improves the flow uniformity when compared with the baseline case. This aspect is clearly revealed when the time resolved evolution of the splitter setup is compared with the one of the baseline setup (bottom of Fig. 5a). For this time step the circumferential gradients of velocity are much larger in the lower half of the channel. Here, a large velocity defect is identified in the range $0.3 < \theta/\Delta\theta_{Strut} < 0.5$ which is due to the variation of incidence induced by the large strut passage vortex (the trace of which is marked over the picture as strut vortical structure). For the splitter case the intensity of such vortex is reduced and hence the LP outlet flow is more uniform. Furthermore, because of the large passage vortex of the baseline configuration, the regions within the blade passages at high velocity change their radial position according to the circumferential position. This effect is not visible in the splitter configuration, while it is clearly observed for the setup without splitters (the interested reader may consider the different time steps of the baseline configuration presented in Lengani et al. [4]).

A similar effect is observed in the time resolved evolution of the stochastic fluctuation RMS ($p'_{t,RMS}/\rho v^2_{ax,AVE}$) depicted in Fig. 5b. In the splitter setup (on top), the largest stochastic fluctuations are measured in the lower half of the channel. A local maximum is observed at the hub in the region $0.8 < \theta/\Delta\theta_{Strut} < 1.0$. This maximum value slightly depends on the time step, hence it is related to the structures of the upstream vanes, namely the wakes of the strut. Another local maximum of the stochastic fluctuations is detected around $0.2 < \theta/\Delta\theta_{Strut} < 0.4$ for the different time steps. This is originated by the interaction of the blade with the upstream splitter "B" (as marked over the plot). In the upper half of the channel, the stochastic fluctuations follow the iso-countour lines of low velocity regions of Fig. 5a. Hence, in this position, the local maxima of $p'_{t,RMS}/\rho v^2_{ax,AVE}$ are generated by the local shear layers of the blade wakes and tip passage vortex.

As observed for the velocity field, the distribution of the stochastic fluctuations is more uniform with splitters than without. The term $p'_{t,RMS}/\rho v^2_{ax,AVE}$ is shown for one time step of the baseline case measurements in the bottom plot of Fig. 5b. A large area at high random fluctuations is measured in the region $0.1 < \theta/\Delta\theta_{Strut} < 0.5$ and it characterizes the 80% of the channel height. Similar considerations were obtained in Lengani et al. [16] for the full time resolved evolution within one blade passing period. Hence, the analysis of the random fluctuations of total pressure leads to the same conclusion observed for the time resolved velocity distribution.

To summarize, for both setups similar phenomena are responsible for the random fluctuations and, therefore, for the loss generation. The first cause may be identified in the unsteady interaction of the vanes with the LP rotor, which generates the regions at the highest turbulence intensity. These are localized for the splitter setup in the lower half of the channel, whereas it influences a larger part of the channel in the baseline setup. A second cause may be identified within the structures of the LP rotor, such as its wake and secondary flows. This leads to areas at lower stochastic fluctuations and it is of comparable intensity between the two setups even though the LP rotor is more loaded for the splitter case.

Overall unsteadiness The flow field presented in the previous plot (Fig. 5) is related just to the structures (coherent and stochastic fluctuations) induced by the LP rotor. As observed in Lengani et al. [16], this is sufficient to describe the time resolved evolution of the stochastic fluctuations, which depend, for the largest part, on the LP unsteadiness. Similarly, the deterministic fluctuations of velocity and flow angle depend mostly on the unsteadiness induced by the LP rotor, as it has been shown by Lengani et al. [4] for the baseline setup. However, the deterministic fluctuations of pressure are related also to the HP rotor and to the rotor-rotor interactions (see eq. 5). The RSA was applied to all the measured quantities. Particularly, for the splitter setup the velocity and angle fluctuations have been found to depend mostly on the LP unsteadiness, since no significant differences where observed between RSA and the phase average based on the LP rotor. To provide a summary of these results, the RMS of the angle fluctuation is shown and discussed in the following considering the RSA.

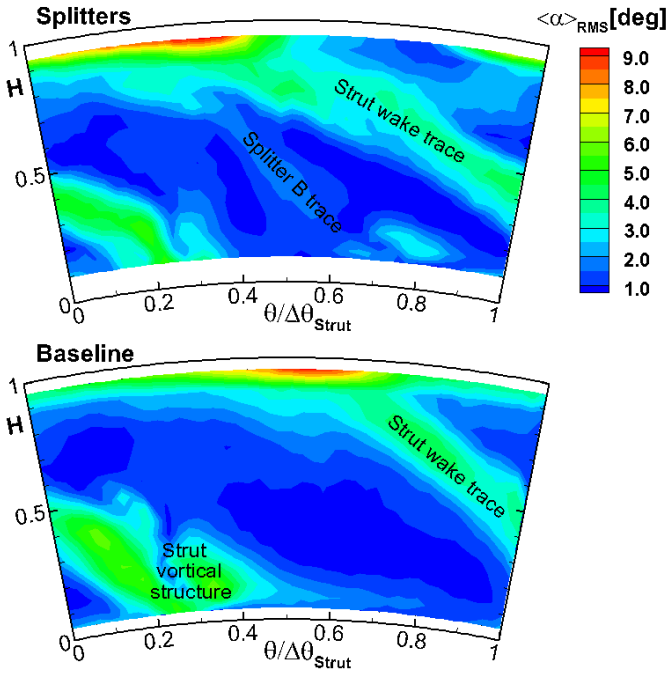

FIGURE 6: RMS of the coherent fluctuations of the flow yaw angle computed from the RSA, plane F.

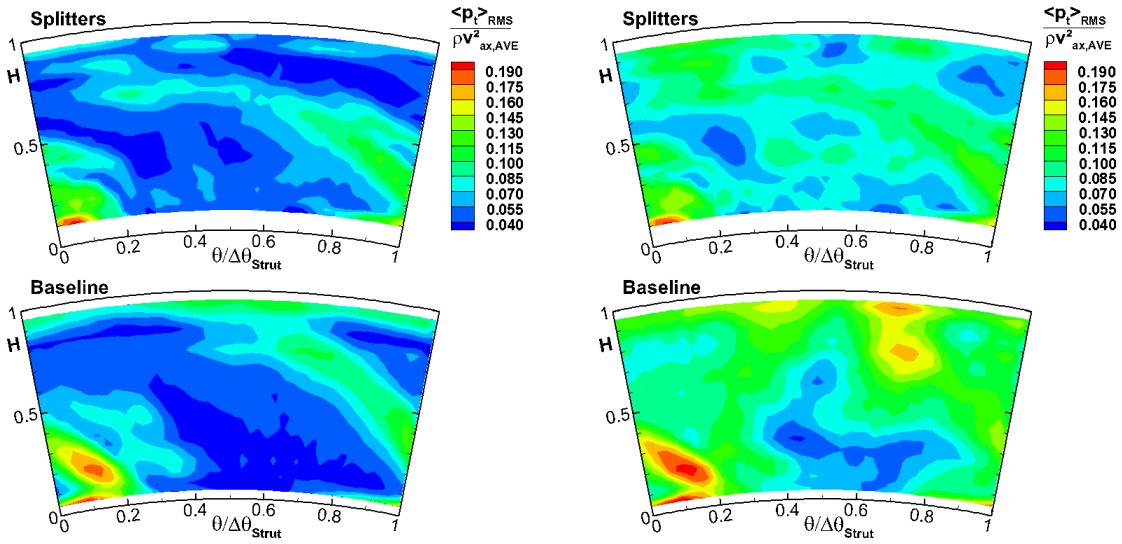

(a) LP phase (b) RSA

FIGURE 7: RMS of the coherent fluctuations of the total pressure in plane F.

The different behaviour of the pressure fluctuations is instead analyzed considering the two different phase averaging procedures (LP rotor phase and RSA).

Figure 6 shows the contour plot of the RMS of the flow angle periodic component ($< \alpha >_{rms}$) computed from the RSA. The largest fluctuations may be observed in correspondence of the trace of the strut wake and at the tip. The first region is the inclined line, which starts at $\theta/\Delta\theta_{Strut} \cong 0.2$ at the hub, and that, for periodicity, ends at $\theta/\Delta\theta_{Strut} \cong 0.4$ at the tip. The second region extends over the whole strut pitch for 20% of the blade height at the tip, and its maximum may be observed when it intersects the strut wake. This effect is due to the blade tip passage vortex which extends its fluctuations when it interacts with the strut structure coming from upstream. The wakes of the two splitters may be also identified as the 2 areas at relativily high fluctuations between the strut passage. However, the fluctuations induced by the interaction between the splitters and the LP rotor blades are of lower intensity than the ones induced by the interaction with the strut wake. The largest difference between splitter and baseline setup is observed in this area. In fact, the baseline setup (bottom of Fig. 6) shows higher fluctuation than the splitter setup at the hub for $0.1 < \theta/\Delta\theta_{Strut} < 0.4$. This is a further effect of the reduction of the large passage vortex of the baseline case because of the presence of the splitters. Furthermore, the trace of the strut wake presents slightly lower fluctuations in the case of the splitter setup. This is coherent with the slight reduction of the stochastic fluctuations in the strut wake for plane D observed in the splitter case (Fig. 3). In the rest of the area, particularly at the tip region, the two setups show very similar results.

It has to be noted that the term $< \alpha >_{rms}$, provided in this plot, is proportional to the variation of the incidence angle of the following vane row. Hence, in the lower half of the channel the vane following the first LP rotor would experience a lower unsteady loading in the case of the splitter vane. In the upper half of the channel the two different configurations show similar effects in terms of angle fluctuations. This is because, there, the angle fluctuations are mainly induced by the upper passage vortex of the LP blades.

As previously discussed the $< \alpha >_{rms}$ is shown just for the RSA, in order to discuss the overall unsteady effects on the flow angle. The term $< \alpha >_{rms}$ computed with the phase averaging based on the LP rotor shows a perfectly similar distribution with slightly lower values therefore it is not shown. The behaviour of the RMS of total pressure is instead different. For this reason, Fig. 7 shows the RMS of total pressure (made non-dimensional by the the term $\rho v^2_{ax,AVE}$) for the two configurations and for the two different decompositions. Figures 7a and 7b show the RMS of $< p_t >$ computed from the LP rotor phase and from the RSA, respectively. The splitter configuration is depicted on top of the pictures, and on bottom there is the baseline one.

The contour plot computed with the LP rotor phase clearly resembles the contour plot of $< \alpha >_{rms}$ (Fig. 6). The same areas at high fluctuations may be identified and they are mostly due to the strut and splitter wake for the splitter case and to the strut wake and the passage vortex for the baseline case. Rather low fluctuations of pressure are measured at the tip for both setups. The contour plot computed from the RSA show a different distribution with larger values of the RMS of $< p_t >$. The different regions with higher fluctuations are due to phenomena that are related to the HP rotor passing frequency and to the rotor-rotor interaction. In fact, the strong shock waves generated by the HP stator and rotor and by their unsteady interaction (e.g., [3, 29]), do not decay within the duct as shown in Fig. 4 upstream of the LP rotor. These pressure waves propagate further downstream and cause a significant contribution in the pressure fluctuations at the exit of the test section. It is then important to observe that the pressure fluctuations are reduced by the presence of the splitters up-and downstream of the LP rotor.

CONCLUSIONS

The paper described the time-resolved measurements performed in the second stage of a counter-rotating turbine for two different configurations of a mid turbine frame. The diffusing duct which connects the HP and LP rotor is operated at realistic aerodynamic conditions. Hence, the comparison between the two different designs of the mid-turbine frame is relevant for current two-spool aero-engines. This second part paper is focused on the characterization of the sources of unsteadiness and their relative influence for the two different configurations. The discussion have been classically carried on considering deterministic and stochastic stresses up-and downstream of the LP rotor.

Upstream of the LP rotor the time resolved measurements confirm the trend shown in the first part paper. The sources of losses in the baseline setup are due to the strut wake, passage vortex and shed vortices. This sources are identified as the region at high stochastic fluctuations of total pressure and their intensity is reduced in the splitter setup. However, new local maxima of stochastic fluctuations are induced by the splitter wakes, particularly by the pressure side splitter. Hence, the loss generation rate in this plane is not increased by the splitters. Moreover, the most important effect of the splitters have been observed on the coherent fluctuations of pressure. They have been identified to be due to the HP rotor unsteadiness, namely by the HP rotor shock system which propagates within the duct. The presence of the splitters reduces the maximum fluctuations at the blade passing frequency of the upstream rotor when compared with the baseline case.

In the first part paper, it has been shown that the splitter configuration leads to a different radial and circumferential flow angle distribution. With this distribution the LP rotor performs better than in the baseline configuration. As a consequence, downstream of the LP rotor, adjacent blade passages show lower circumferential gradients of velocity than the baseline case. A similar consideration may be done for the deterministic fluctuations of flow angle and the stochastic fluctuations which depend mostly on the interaction of the LP blade with the upstream vanes.

A different behaviour has been shown for the deterministic fluctuations of pressure. The total and static pressure fluctuations are also caused by the HP rotor unsteadiness which has not decayed and by the rotor-rotor interaction. The presence of the splitter reduces the extent of the pressure fluctuations propagating from upstream and, hence, reduces the overall unsteadiness. These reduction mechanism is particularly done on the HP rotor unsteadiness, which is among the largest contribution of pressure fluctuation. The damping out of this contribution leads then to a significant reduction of the aero-acoustic and vibrational problems.

ACKNOWLEDGMENT

The authors would like to thank H. Peter Pirker, Cornelia Santner, Josef Hubinka and Berardo Paradiso (currently affiliated at Politecnico di Milano) for the important support during the experimental campaign. The research leading to these results has been partially founded by the European Union within the EU-project DREAM (contract No. ACP7-GA-2008-211861) as well as from the Austrian Ministry for Finance.

REFERENCES

[1] Norris, G., Dominy, R. G., and Smith, A. D., 1998. "Strut influences within a diffusing annular s-shaped duct". In Proceedings of ASME Turbo Expo 1998, ASME Paper No. 98-GT-425.

[2] Marn, A., Göttlich, E., Cadrecha, D., and Pirker, H. P., 2009. "Shorten the intermediate turbine duct length by applying an integrated concept". *J Turbomach,* ***131***, October, pp. 041014–1–10.

[3] Göttlich, E., 2011. "Research on the aerodynamics of intermediate turbine diffusers". *Prog Aerospace Sci,* ***47***(4), pp. 249–279.

[4] Lengani, D., Santner, C., Spataro, R., Paradiso, B., and Göttlich, E., 2012. "Experimental investigation of the unsteady flow field downstream of a counter-rotating two-spool turbine rig". In Proceedings of ASME Turbo Expo 2012, June 11-15, Copenhagen, Denmark, ASME Paper No. GT2012-68583.

[5] Lengani, D., Santner, C., Spataro, R., and Göttlich, E., 2012. "Analysis tools for the unsteady interactions in a counter-rotating two-spool turbine rig". *Experimental thermal fluid science,* ***42***, October, pp. 248–257.

[6] Lavagnoli, S., Yasa, T., Paniagua, G., Castillon, L., and Duni, S., 2012. "Aerodynamic analysis of an innovative low pressure vane placed in an s-shape duct". *J Turbomach,* ***134***, pp. 011013–1–13.

[7] Yasa, T., Lavagnoli, S., and Paniagua, G., 2011. "Impact of a multi-splitter vane configuration on the losses in a 1.5 turbine stage". *Proceedings of IMechE,* ***225***, November, pp. 964–974.

[8] Spataro, R., Göttlich, E., Lengani, D., Faustmann, C., and Heitmeir, F., 2013. "Development of a turning mid turbine frame with embedded design - part i: Design and steady measurements". In Proceedings of ASME Turbo Expo 2013, June 3-7, San Antonio, Texas, USA, ASME Paper No. GT2013-95280.

[9] Hubinka, J., Santner, C., Paradiso, B., Malzacher, F., Göttlich, E., and Heitmeir, F., 2009. "Design and construction of a two shaft test turbine for investigation of mid turbine frame flows". In 19^{th} International Symposium on Airbreathing Engines, September 7–11, Montreal, Canada, ISABE Paper ISABE-2009-1293.

[10] Hubinka, J., Paradiso, B., Santner, C., Göttlich, E., and Heitmeir, F., 2011. "Design and operation of a two spool high pressure test turbine facility". In Proceedings of 9^{th} European Turbomachinery Conference, March 21-25, Istanbul, Turkey, Paper No. 112.

[11] Kupferschmied, P., Köppel, O., Gizzi, W. P., and Gyarmathy, G., 2000. "Time resolved flow measurements with fast aerodynamic probes in turbomachinery". *Measurement Science and Technology,* ***11***(7), pp. 1036–1054.

[12] Persico, G., Gaetani, P., and Guardone, A., 2005. "Design and analysis of new concept fast-response pressure probes". *Meas. Sci. Technol.,* ***16***, pp. 1741–1750.

[13] Porreca, L., Hollenstein, M., Kalfas, A. I., and Abhari, R. S., 2007. "Turbulence measurements and analysis in

a multistage axial turbine". *Journal of Propulsion and Power,* ***23***(1), pp. 227–234.

[14] Hussain, A., and Reynolds, W., 1970. "The mechanics of an organized wave in turbulent shear flow". *Journal of Fluid Mechanics,* ***41***, pp. 241–258.

[15] Peters, A., and Spakovszky, Z. S., 2012. "Rotor interaction noise in counter-rotating propfan propulsion systems". *J Turbomach,* ***134***, January, pp. 011002–1–12.

[16] Lengani, D., Santner, C., and Göttlich, E., 2012. "Evaluation and analysis of the stochastic unsteadiness in the last stage of a counter-rotating two-spool turbine rig". In Proceedings of Conference on Modelling Fluid Flow, September 4-7, Budapest, Hungary, paper No. 092.

[17] Camp, T. R., and Shin, H.-W., 1995. "Turbulence intensity and length scale measurements in multistage compressors". *J Turbomach,* ***117***, January, pp. 38–46.

[18] Oro, J. M. F., Díaz, K. M. A., Morros, C. S., and Marigorta, E. B., 2007. "On the structure of turbulence in a low-speed axial fan with inlet guide vanes". *Experimental Thermal and Fluid Science,* ***32***, pp. 316–331.

[19] Lengani, D., Paradiso, B., and Marn, A., 2012. "A method for the determination of turbulence intensity by means of a fast response pressure probe and its application in a LP turbine". *Journal of Thermal Science,* ***21***, pp. 21–31.

[20] Schüpbach, P., Abhari, R. S., Rose, M. G., Germain, T., Raab, I., and Gier, J., 2010. "Improving efficiency of a high work turbine using nonaxisymmetric endwalls-part II: Time-resolved flow physics". *J Turbomach,* ***132***, April, pp. 021008–1–10.

[21] Tiedemann, M., and Kost, F., 2001. "Some aspects of wake-wake interactions regarding turbine stator clocking". *J Turbomach,* ***123***, pp. 526–533.

[22] Persico, G., Gaetani, P., and Osnaghi, C., 2009. "A parametric study of the blade row interaction in a high pressure turbine stage". *J Turbomach,* ***131***, July, pp. 031006–1–13.

[23] Tyler, J. M., and Sofrin, T. G., 1962. "Axial flow compressor noise studies". *SAE Transaction,* ***70***, pp. 309–332.

[24] He, L., Chen, T., Wells, R. G., Li, Y. S., and Ning, W., 2002. "Analysis of rotor-rotor and stator-stator interferences in multi-stage turbomachines". *J Turbomach,* ***124***, October, pp. 564–571.

[25] Faustmann, C., Lengani, D., Spataro, R., Marn, A., Göttlich, E., and Heitmeir, F., 2013. "Experimental investigation of the noise generation and propagation for different turning mid turbine frame setups in a two-stage two-spool test turbine". In Proceedings of ASME Turbo Expo 2013, June 3-7, San Antonio, Texas, USA, ASME Paper No. GT-2013-95698.

[26] Arndt, N., 1993. "Blade row interaction in a multistage low-pressure turbine". *J Turbomach,* ***115***, January, pp. 137–146.

[27] Lengani, D., Paradiso, B., Marn, A., and Göttlich, E., 2012. "Identification of spinning mode in the unsteady flow field of a low pressure turbine". *J. Turbomach,* ***134***, pp. 051032–1–8.

[28] Hodson, H. P., and Howell, R. J., 2005. "The role of transition in high lift low pressure turbines for aero engines". *Progress in Aerospace Science,* ***41***(6), August, pp. 419–454.

[29] Dénos, R., Arts, T., Paniagua, G., Michelassi, V., and Martelli, F., 2001. "Investigation of the unsteady rotor aerodynamics in a transonic turbine stage". *J Turbomach,* ***123***, January, pp. 81–89.

Proceedings of ASME Turbo Expo
GT2013
June 3-7, 2013, San Antonio, Texas, USA

GT2013-95698

EXPERIMENTAL INVESTIGATION OF THE NOISE GENERATION AND PROPAGATION FOR DIFFERENT TURNING MID TURBINE FRAME SETUPS IN A TWO-STAGE TWO-SPOOL TEST TURBINE

C. Faustmann, D. Lengani, R. Spataro, A. Marn, E. Göttlich, F. Heitmeir
Inst. f. Thermal Turbomachinery and Machine Dynamics
Graz University of Technology, Austria
Email: christian.faustmann@tugraz.at

ABSTRACT

The paper deals with the investigation of the noise generation in the two-stage two-spool test turbine located at the Institute for Thermal Turbomachinery and Machine Dynamics (ITTM) at Graz University of Technology. The rig went into operation within the EU-project DREAM, where the target was to investigate the aerodynamics of interturbine flow ducts. The facility is a continuously operating cold-flow open-circuit plant which is driven by pressurized air. The flow path contains a transonic turbine stage (HP) followed by a low pressure turbine stage consisting of a turning mid turbine frame and a counter-rotating LP-rotor.

Downstream of the low pressure turbine a measurement section is instrumented with acoustic sensors. The acquisition system consists of a fully circumferentially traversable microphone array located at the outer casing, while at the hub endwall a stationary flush mounted microphone is placed as a reference.

Additionally a new embedded concept for the turning mid turbine frame was tested. Here, two zero-lift splitters were located into the vane passage.

In order to evaluate the noise emission of the turbine the facility was instrumented with a new acoustic measurement setup which is presented in the paper. Therefore the emitted sound pressure level and the microphones signal spectra are compared for both configurations. The acoustic field was characterized by azimuthal modes by means of a microphone array traversed over 360 degrees.

In the multisplitter configuration, the propagating modes due to the HP turbine are found suppressed by 5 dB, while the increase in amplitude of the modes related to the LP turbine is negligible. The overall effect is a reduction of the acoustic emission for the turning mid turbine frame with embedded design.

NOMENCLATURE

A	Fourier coefficient of the circumferential mode
B	Number of Blades
BPF	Blade passing frequency
c_{ax}	axial chord length
f	frequency
FWF	Austrian Science Fund
h	channel height
HP	High pressure
LP	Low pressure
m	circumferential mode
$m_{r,in}$	Reduced mass flow, stage inlet
n	Index of the harmonic of the BPF
$n_{r,in}$	Reduced rotational speed, stage inlet
n_c	number of circumferential points
p_t	total pressure
q	generic flow variable
r	radius
Re	Reynolds number
SPL	sound pressure level
STTF	Subsonic Test Turbine Facility
t	time
T	blade passing period
TTTF	Transonic Test Turbine Facility
V	Number of vanes
θ	Circumferential coordinate
Ω	Rotor angular velocity
< >	Deterministic periodic component
Superscripts	
-	time averaged properties
~	Ensemble-averaged properties
‘	stochastic fluctuating component

INTRODUCTION

Among the different sources of aerodynamic noise stemming from the flow around an airplane, the acoustic tonal emission generated by an aero engine provides the most significant contribution. Over the last years a lot of effort has been put in reducing the jet engine tonal emission, as for example replacing turbojets with turbofan engines, or adapting acoustic liners for the combustion chamber. Following, the targets declared in the document ACARE 2020 (Advisory Council for Aeronautics Research in Europe) the performance improvement in terms of fuel consumption (reduction by 50%) and NO_x-emissions (reduction by 80%) has to be followed by a decrease of 10 dB effective perceived noise level. To reach these targets researchers put high emphasis on the improvement of the intermediate turbine ducts guiding the flow from the HP to the LP turbine.

In modern engines bulky struts are located within the transition duct in order to support the engine shaft and to lead service pipe lines. These wide chord vanes induce an obstacle for the fluid flowing towards the LP turbine causing higher losses in this part of the machine. Recently Göttlich [1] published a review on the present state of the research of these components.

Among the different solutions aimed to shorten the transition duct, an integrated concept such as the turning mid turbine frame represents a remarkable example. Such architecture has been studied in one and a half stage [2, 3] and two stage [4, 5] configuration in the Transonic Test Turbine Facility (TTTF) located at Graz University of Technology. Here the idea was to replace the first LP vane row with aerodynamically optimized turning struts.

The facility is a continuously operating cold-flow open-circuit plant which is driven by pressurized air. The flow path contains a transonic turbine stage (HP) followed by a low pressure turbine stage consisting of a turning mid turbine frame and a counter-rotating LP-rotor.

The operation of such intermediate duct setups showed that the LP rotor inlet flow is characterized by large structures such as wakes and secondary flows generated by the struts. These structures on the one hand cause a performance reduction of the rotor, while on the other hand they represent a potential source of vibration for the rotor blades.

A further problem in shortening the duct is that the engine performance is highly affected by the blade-row-interaction. In particular, the extent of the unsteadiness at the outlet of the duct is critical for the aerodynamic performances, vibrations and acoustic emissions of the successive LP stages, and, therefore it needs a careful analysis. Additionally, the pressure fluctuations from the stage upstream of the duct contribute considerably to the overall pressure fluctuations at the exit of the second stage (Lengani et al. [6]).

Consequently, as a next step the two-spool facility at the Institute was instrumented with microphones placed downstream of the LP rotor in order to perform acoustic measurements. The acquisition system consists of a fully circumferentially traversable microphone array located at the outer casing downstream of the low pressure turbine, while at the hub endwall a stationary flush mounted microphone is placed as a reference. For the characterization of the azimuthal and radial modes, the microphone array has to be traversed over 360 degrees. In the TTTF Faustmann et al. [7] performed acoustic measurements, which were repeated for different HP vane-strut clocking position. The modal decomposition and Fourier analysis of the unsteady flow field showed that there is a small influence of the various clocking positions on the sound pressure level.

A step forward in the development of mid turbine frames could be represented by the application of an embedded design concept. The basic idea is to merge the strut and the LP vanes in one multisplitter component. The setup without splitters was redesigned embedding two zero-lift splitters in the strut passage in order to minimize secondary vortices and to damp the rotor-rotor interaction. The design process and the results of the aerodynamic measurements on the setup with splitters can be found in [8] and [9].

The aim of this paper is at first to present the acoustic measurement section and to discuss the comparison of the noise generated by the setup with and without splitters. It was observed that the mean value of the modes related to the HP rotor is reduced by 5 dB, whereas the mean value of the modes related to the LP rotor increases by 3dB in the setup with splitters. Moreover, the contribution of the predominant HP rotor is much higher than the one of the LP rotor. Hence, the increase due to the LP rotor in case with the splitters is negligible.

Adding splitter vanes between the struts in the mid turbine frame has not only a positive effect on the performance of the LP stage but also on the acoustic emissions.

EXPERIMENTAL SETUP AND METHODOLOGY

Facility

The Transonic Test Turbine Facility (TTTF) is a continuously operating two-stage cold-flow open-circuit plant, which consists of a transonic HPT stage and a counter-rotating LPT stage. This unique configuration allows the testing of rig inserts with a diameter up to 800 mm under engine-representative conditions. Both turbines are designed with overhung-type turbine shafts and additionally the LPT is mounted on an axially moveable frame. This allows easy disk assembly without dismantling the bearings and the simple rig modification between setups with transition duct and turning mid turbine frame designs of different axial lengths. The facility is driven by pressurized air delivered by a separate 3 MW compressor station. The shaft power of the HP turbine stage drives a three-stage radial brake compressor. This brake compressor delivers additional air mixed to the flow from the compressor station and increases the overall mass flow. The air temperature at turbine stage inlet can be adjusted by coolers between 40 °C to 185 °C. The maximum shaft speed of the HPT stage is limited to 11550 rpm. Depending on the stage

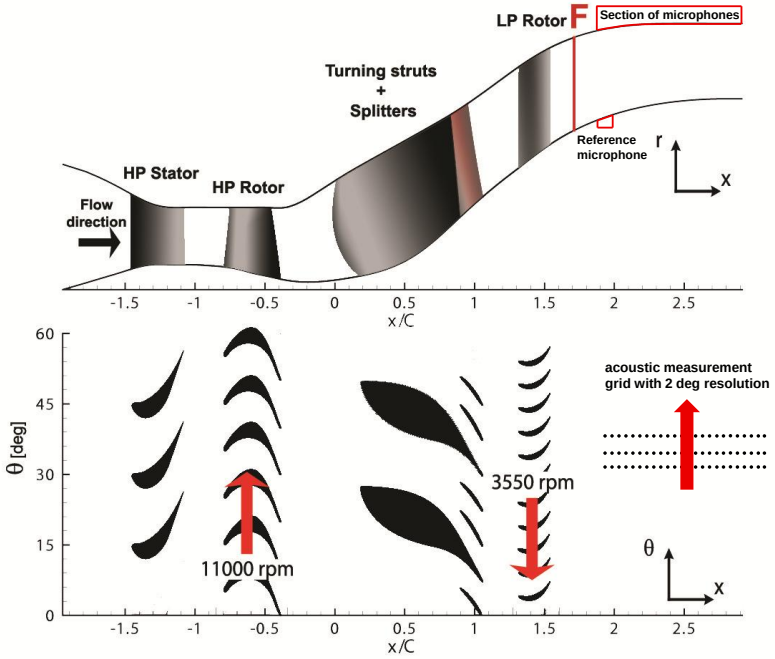

Figure 1: Meridional and blade to blade sections of the two-spool facility

characteristic a maximum coupling power of 2.8 MW at a total mass flow of 22 kg/s can be reached. The power of the LP turbine is absorbed by a waterbrake with a maximum power of 700 kW. Detailed information on the design and construction of the original single stage facility can be found in [10], on the operation in [11]. For the design of the LP-stage together with the turning mid turbine frame see [12]. Hubinka et al. [13] show first results from the rig behavior, whereas Santner et al. [14] discuss the results of an experimental investigation of the flow at the duct inlet and exit as well as downstream of the LPT.

Test setups

As already mentioned, the investigated test setups consists of a single-stage unshrouded transonic HP turbine, and an S-shaped turning mid turbine frame followed by a shrouded counter-rotating LP rotor. Figure 1 represents a meridional and blade to blade view of the test section. The incoming air flows at first through a transonic HP turbine with unshrouded rotor. Afterwards, the air is guided by turning struts towards the LP rotor with appropriate swirl angle. The HP turbine consists of 24 choked vanes and 36 blades. In the turning mid turbine frame 16 struts are chosen, while for the setup with splitters 32 splitter vanes were added (blading parameter see Table 1). The additional functions of the TMTF structures lead to constraints like a minimum required strut thickness leading to a maximum possible number of struts. Therefore a highly three-dimensional design of the airfoils and the duct, respectively, is necessary to reduce strong secondary flow effects and further to provide suitable flow angle and Mach number for the following low pressure rotor (LPT). A future area of application for mid turbine frames with turning struts, may be a geared turbo fan (GTF) engine. The LP rotor mounted in the test rig is shrouded and has 72 blades. Vane and blade count were chosen on one hand to have engine-like blade/vane ratios for the turbine components, while, on the other hand, to ease clocking effect studies [5] as well as rig modeling for CFD simulations. In fact the spacial periodicity of the whole machine is 90° and this allows to significantly reduce the computational cost whenever unsteady calculations have to be performed to investigate the full components interactions [6].

The HP vanes as well as the outer casing downstream of the struts are fully rotatable in circumferential direction. This allows to traverse circumferentially probes and microphones downstream of the low pressure turbine (Figure 1).

Operating conditions

Table 1 also displays the main parameters of the operating point. The HP vanes are operating under choked conditions. The absolute Mach number at the inlet of the turning mid turbine frame with a value of about 0.5 is representative for duct inlet conditions of modern jet engines with a single stage HP turbine at cruise operating point. Since the flow in the embedded design is changed by the splitter blockage, a new operating condition was selected in order to maintain the same reduced mass flow and the same reduced speed as for the setup without splitters. Due to facility limitations, it was not possible to reach a higher pressure ratio for the HP turbine. Nevertheless, measurement performed downstream of the HP stage showed good flow similarity between the two setups [8].

Measurement techniques

The microphone array, which was used to instrument the rig, consists of 24 microphones type 40DB from the company G.R.A.S.. This type of microphone is a ¼-inch prepolarized pressure microphone with a dynamic range upper limit of 170 dB and a frequency response from 10 Hz to 25 kHz (±1 dB). The preamplifier type 26AC has a very low inherent noise level as well as a dynamic range and a frequency response from below 2 Hz to 200 kHz (±0.2 dB). Pressure microphones have a so called sphere characteristic, which means, that every sound wave, independent from the angle of impingement on the diaphragm, has nearly the same intensity. There are two ways of mounting the microphones for acoustic investigations in flow ducts, either mount as microphone rake in the flow [15], or with flush mounted microphones on the wall [16]. A study was done for aligning the microphones behind the LP turbine in one of four exchangeable wall plates. The challenge was to design a microphone array, where the sensor accessibility and count as well as the spatial resolution would be optimized. In total 25 microphones are used, one as a reference microphone at the hub, which is fixed, and 24 microphones staggered and flush mounted at the outer casing downstream of the LP turbine, which are fully circumferentially movable. The angular displacement between the microphones is 6° and can be seen in Figure 2. The first 12 microphones are placed in the non-cylindrical part of the flow duct with an axial displacement of 6 mm with respect to the center of the diaphragm. The acoustic measurement data out of this region will be used to extend the post processing also to non-cylindrical ducts. Since the established acoustic post processing tools are developed for

Table 1: Blading parameters and operating conditions

Blading parameters					
	HP vane	HP blade	Struts	Splitters	LP blade
Vane/ blade no.	24	36	16	32	72
h/c_{ax}	1.15	1.37	0.53	3.5	2.94
Re(10^6)	2.38	1.1	1.86	0.4	0.46
Tip gap	-	unshrouded	-	-	shrouded

Operating conditions			
		HP stage	LP stage
$n_{r,in}[rpm/\sqrt{k}]$		524.4	195.3
$m_{r,in}[kg/s \cdot \sqrt{k}/bar]$		81.2	214.6
Baseline	Stage p_t ratio	3	1.3
Baseline	Power [kW]	1710	340
with Splitters	Stage p_t ratio	2.83	1.36
with Splitters	Power [kW]	1425	353

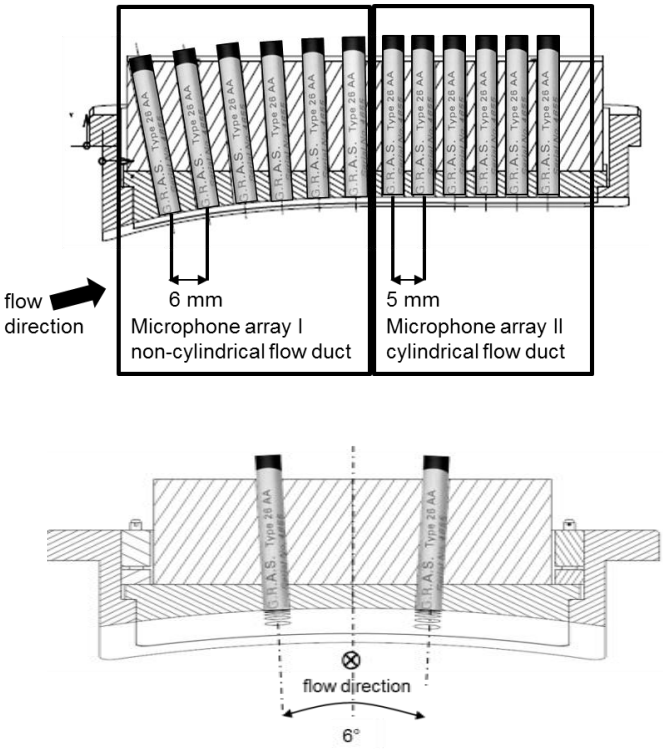

Figure 2: Meridional and axis-orthogonal views of microphone array I and II

flows in cylindrical ducts (e.g. [16] and [17]), it was important to maximize the microphone number in the straight part of the measurement section (Figure 2). The results presented in this paper are taken from microphone array II. Due to the desired frequency resolution and the space limitations the distance between the microphones is 5 mm (see Figure 2).

Data acquisition

For the data acquisition National Instruments equipment is used. The sampling frequency is 60 kHz. The post processing is done up to a frequency of 15 kHz. 26 of 32 channels are allocated to the 24 microphones plus 1 reference microphone as well as the HP- and the LP-trigger. The trigger signal was used to reconstruct the unsteady sound field by the rotors phase. The microphone array is traversed in steps of 2°. The signal from every channel is contemporary acquired and stored. The data acquisition period is 20 seconds per measurement point. It corresponds to more than 1000 revolutions of the LP turbine and more than 3500 of the HP turbine. In total 180 measurement positions are recorded in one and a half hours. During this time the operating condition is maintained perfectly stable.

Data reduction method

Azimuthal decomposition

In order to describe the sound generation mechanisms, Tyler and Sofrin [18] composed the pressure fluctuations at any circumferential position downstream of a compressor stage as a sum of harmonics. The theoretical model that they proposed has been verified by numerous aeroacoustic experimental investigations, and it is valid also for turbines (e.g. [16]). In particular, for an ideal rotor with identical blades the pressure fluctuations at a circumferential position θ are represented as the following Fourier series [19]:

$$p(\theta,t)=\sum_{n=0}^{\infty}\sum_{m=-\infty}^{\infty}A(m,n)e^{inB\Omega t-im\theta} \quad (1)$$

where *n* is the harmonic index (1 for the BPF, 2 for the 2 BPF, etc.), Ω the rotor angular velocity and *A(m, n)* a complex number defined for each circumferential mode *m* and for each harmonic *n*. Furthermore, Tyler and Sofrin [18] showed that the mode *m* of the spatial Fourier decomposition is restricted to some particular values:

$$m=nB+kV, with\ k=..,-1,0,1,.. \quad (2)$$

where a simple stator-rotor interaction is considered and B is the number of rotor blades and V the number of stator vanes. It is possible to consider the interactions of the rotor with a complete vane assembly by simply superimposing the effect of the single event. For example, in a turbine a mode m^* generated by a stator-rotor interaction will be scattered in the modes $m=m^*+kV_2, with\ k=..,-1,0,1,..$ by the following stator rows. Hence, for a stator-rotor-stator assembly the following modes are predicted:

$$m=nB+k_1V_1+k_2V_2, with\ k_1,k_2\ integer \quad (3)$$

where V_1 and V_2 are the number of vanes of the first and second stator row, respectively. A further extension of the present theory was provided by Holste and Neise [20]. They described the possible modes which may propagate in case of rotor-rotor interaction with different rotational speed, counter or co-rotating. The complex mode amplitude *A(m, n)* is computed from the pressure reading of the microphones performing the inverse operation of Eq. 1. Namely, in a first step a time to frequency domain transformation is applied to the time resolved pressure $p(t)_{x,\theta}$, for any circumferential position θ and any axial position *x*. Thereafter, a discrete Fourier transformation in the circumferential direction is applied to the complex pressure in the frequency domain $p(f)_{x,\theta}$:

$$A(m)_{x,f}=\frac{1}{N_c}\sum_{n_c}p(\theta)_{x,f}e^{-in_cm} \quad (4)$$

When this operation is applied to the raw signal it may result in a quite large error. Hence, in a first step the initial signal is phase averaged, in order to improve the noise to signal ratio removing the random fluctuations (as discussed in the following section). Then, in a second step, as suggested by Sijtsma and Zillmann [21], the complex modes $A(m)_{x,f}$ are computed considering a cross-correlation with a reference microphone (Eq. 17 of their paper).

Phase averaging

The determination of the flow properties is possible after phase averaging. Phase averaging is commonly performed in rotating machinery by means of a pulse per revolution obtained from a shaft encoder (e.g. [22] and [23]). This pulse is used to determine the beginning of each revolution, which represents also the end of the previous one. In the present paper phase averaging was performed triggering the flow with the two shaft encoders according to the triple decomposition procedure [24]:

$$p(t)=\bar{p}+<p>+p'(t) \quad (5)$$

where $<p>$ is the purely periodic component associated with a coherent periodic structure and $p'(t)$ is the random fluctuation associated mainly with turbulence. This decomposition is used to characterize a single source of periodic unsteadiness.

In the present paper each revolution is resampled to a fixed number of samples in order to correct the small speed variations of the two turbine shafts [25]. The phase averaged values are then computed as the average of the samples at the same phase. Such procedure is very well established and allows the identification of the structures correlated to the rotor rotational speed. The statistical error on the averaging procedure is below 1%. Since the two rotors are counter-rotating and their rotational speeds are uncorrelated, a phase locked average based on the phase of one of the two rotors removes completely the fluctuations of the flow quantities induced by the other rotor.

However, as highlighted by Lengani et al. [25], considering the presence of two rotors (HP and LP rotor) at unrelated frequencies, the complete decomposition may be rewritten as:

$$p(t)=\bar{p}+<p>_{HP}+<p>_{LP}+<p>_{HP,LP}+p'(t) \quad (6)$$

where the 2 distinct purely periodic components $<p>_{HP}, <p>_{LP}$ have their own period and frequency, and $<p>_{HP,LP}$ indicates the cross-interactions which generate energy content at the frequencies of the linear combination $i\cdot BPF_{LP}+k\cdot BPF_{HP}$ (with *i* and *k* integer and not zero). A particular phase averaging method has been developed by Lengani et al. [25] in order to provide the following time resolved distribution; rotor synchronic average (RSA):

$$\tilde{p}_{RSA}=\bar{p}+<p>_{HP}+<p>_{LP}+<p>_{HP,LP} \quad (7)$$

The RSA, as discussed in [25], preserves the frequency content of the coherent structures of the original signal improving its noise to signal ratio at any of the deterministic frequencies. In particular, the RSA has been used for the study of the rotor-rotor interaction frequencies $i \cdot BPF_{LP} + k \cdot BPF_{HP}$ (with i and k integer and not zero). Whereas, the classic phase averaging with one rotor shaft encoder has been used to study the blade passing frequency and its harmonics.

RESULTS AND DISCUSSION

This part of the paper presents the results of the investigation of noise generation and propagation for two different turning mid turbine frames. The results consist of two parts. At first, the frequency spectra generated by phase and rotor synchronic averaging are presented. Afterwards the azimuthal mode analysis is performed for the first and second BPF of the HP and the LP rotor as well as for the sum of the first BPF of the HP and LP rotor.

Frequency spectra analysis

After phase averaging of the raw signal over more than 3500 revolutions of the HP rotor, the mean frequency spectrum is calculated averaging the frequency spectra of each microphone (24) at each circumferential position (180). Figure 3 and Figure 4 report the comparison between the two setups in terms of mean frequency spectrum. Figure 3 shows that the highest amplitudes may be identified at the blade passing frequency of the HP rotor and its first harmonic. The red graph is shifted by 100 Hz for a better visibility

The frequency spectrum was cut off at 15 kHz. Both spectra are in good agreement to the level of the indicated harmonics h = 1, 2 of the blade passing frequency. Nevertheless, there is a difference up to 3 dB between the two different turning mid turbine frames at the BPF_{HP}. Moreover, the comparison shows that in the embedded design configuration the emitted tonal noise is lowered at 2 BPF_{HP}.
The frequency spectra obtained by triggering the time signal with the LP rotor (not shown in this paper, but matches with the results presented in Figure 4) show that the sound pressure level at BPF_{LP} and $2BPF_{LP}$ is 2 dB higher for the setup with splitters.

Further, the time signal was reconstructed by the use of the RSA. This post processing tool is used for the phase averaging as described in [25]. It allows in such special cases, as e.g. when the signal is acquired downstream of the LP rotor, to identify a new period synchronized with both the HP and the LP rotor. Therefore, the unsteady field phase resolved by the RSA (Eq. 7) correctly estimated the energy content of both rotors and of their interaction. In case of the RSA, in order to provide an accurate FFT, the phase averaging was performed changing the criteria in this way that three revolutions of the LP rotor are counted after coincidence (see Eq. 8 in [25]). Figure 4 represents the frequency spectra of the two different setups. The maximum sound pressure level detected at the sum of the blade passing frequencies of the two rotors ($BPF_{LP} + BPF_{HP}$) are in both cases nearly the same. Furthermore, the frequency spectra show that the highest amount of emitted noise is due to the HP rotor. Figure 4 also confirms the trend observed in Figure 3. At the BPF_{HP} the setup with the splitters shows a lower amplitude.

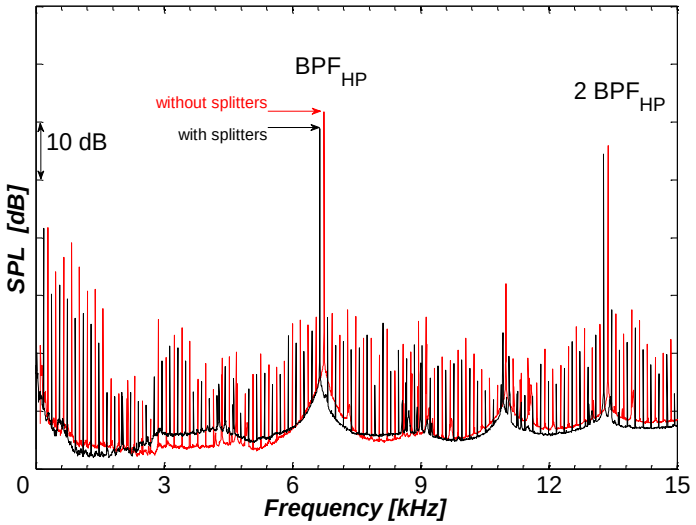

Figure 3: Frequency spectra of the time-signal reconstructed by the HP trigger for the setup without splitters (red) and with splitters (black)

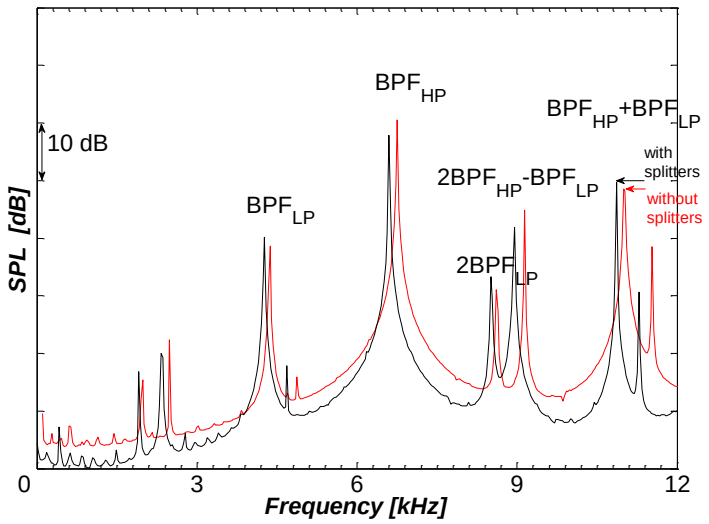

Figure 4: Frequency spectra of the microphone array for the sum of the BPF of the two rotors after rotor synchronic averaging; without splitters (red) and with splitters (black)

An opposite trend is observed at the $BPF_{LP} + BPF_{HP}$, where the amplitude is 10 dB lower than the one of the HP rotor alone. The amplitude at the frequency $2BPF_{HP} - BPF_{LP}$ is comparable in intensity to the sum of the two rotors. Almost 20 dB difference in the amplitude of the sound pressure level is observed between the HP and the LP rotor. At BPF_{LP} the pattern of the peaks of the two different setups is like the one at $BPF_{LP} + BPF_{HP}$.

Azimuthal mode analysis BPF

The second part of the results deals with the modal decomposition performed from the experimental data according to the post-processing procedure previously discussed. The results shown in the following refer just to the data of the last 12 microphones in array II (straight duct) because the microphones in the last portion of the duct are sufficient to reveal which of the modes are decaying or propagating. Furthermore, their propagation or decay nature has been theoretically predicted according to [19]. An overview about the propagating modes is given in Table 2 for the different blade passing frequencies. It has to be noticed that the modes marked in the
table present an asymmetric behavior, because the theoretical prediction taken into account for a swirl model (see Taddei et al. [17]). The main modes, as explained in the following, are scattered by 8 which is a result of the linear combination of the different vane and blade of the two stages.

Table 2: Range for the propagating modes dependent on the BPF

Propagating modes	range of the modes
BPF_{HP}	-44 : 8 : 36
$2BPF_{HP}$	-96 : 8 : 80
BPF_{LP}	-32 : 8 : 24
$2BPF_{LP}$	-64 : 8 : 48
$BPF_{LP} + BPF_{HP}$	-84 : 8 : 68

HP rotor noise

The discussion of the azimuthal mode analysis starts with the HP rotor. In order to provide an explanation of the complex pattern due to the vane/blade interactions the following scheme reports the modes predicted by equation 2 and 3 at the BPF_{HP} for the baseline setup (as also studied in Lengani et al. [6]):

HP stator-HP rotor interaction consists of the modes

$$36 + k \cdot 24 = .. -36; -12;\ 12; 36.. \quad (a)$$

HP rotor-LP stator interaction consists of the modes

$$36 + k \cdot 16 = .. -28; -12; 4; 20; 36.. \quad (b)$$

HP stator-HP rotor-LP stator interaction consists of the modes

$$36 + k_1 \cdot 24 + k_2 \cdot 16 = .. -44; -36; -28; -20;\ -12; -4;\ 4; 12; 20; 28.. \quad (c)$$

These modes may be identified in Figure 5 on the left for the baseline configuration. The picture shows the amplitude of the modal decomposition for the BPF_{HP} in dB, for the different circumferential mode order m plotted at the abscissa. In order to make the graph more readable the propagating modes are marked with black bars. It is clear that the propagating mode ranges from the mode -44 to 36. Modes lower than -44 and higher than 36 show a lower amplitude, hence they decayed within the duct. Furthermore, all the modes at higher amplitude belong to the linear combination of HP vane-HP blade-LP stator, and they are scattered by 8 (see also Table 2). Hence, the generation of noise coming from the HP rotor has to be attributed to its interaction with the up-and downstream vanes.

In case of the setup with splitters different modes may be predicted for the HP-rotor-LP stator interaction as well as for the HP stator-HP rotor-LP stator interaction. At a first approximation, the LP vane count may be considered equal to 48 because of the 32 additional splitters. However, it has to be reminded that the geometry of the splitters is not the same as the one of the struts (see Figure 1). Due to this reason, the theory of Tyler and Sofrin [18] is just partially fulfilled. Analyzing the interaction of HP stator-HP rotor-LP vanes the following modes may be predicted in the ideal case of 48 identical LP vanes:

$$36 + k_1 \cdot 24 + k_2 \cdot 48 = .. -36;\ -12; 12; 36; .. \quad (d)$$

Without this approximation, and considering that the number of vanes in case of the splitter is a multiple of the number of struts the modes were again, be obtained from this linear combination:

$$36 + k_1 \cdot 24 + k_2 \cdot 48 + k_3 \cdot 16 = .. -44; -36;\ -28; -20;\ -12; -4;\ 4; 12; 20; 28; 36 \quad (e)$$

The modes propagating in the case of the splitter setup are shown on the right side of Figure 5. The modes which change significantly between the two setups, are labeled in the picture (compare left and right plots of Figure 5). Particularly, the amplitude of modes -44 and -28 is reduced by almost 20 dB for the configuration with splitters. Similarly the mode +28 is reduced of about 10 dB. It is interesting to note that these modes are not predicted when the ideal LP vane number (48) is considered. Hence, the presence of splitter vanes changes the acoustic transmission through the LP vanes for modes which are instead propagating for the baseline case. To summarize, because of this cut-off effect, the modes mean value in the setup with the splitters is 5 dB lower than the one in the baseline setup.

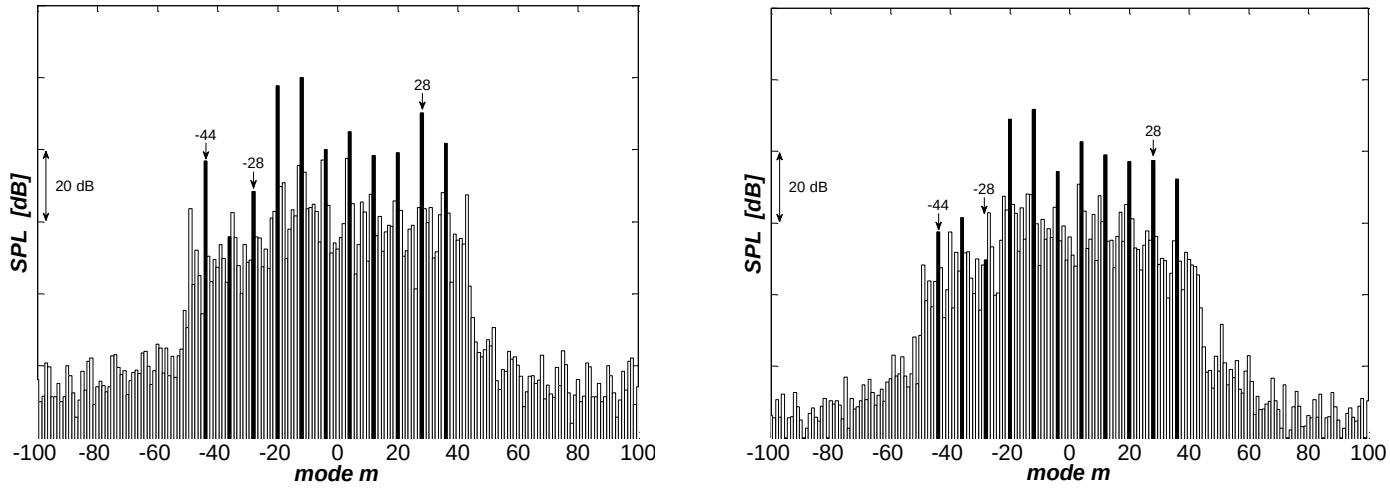

Figure 5: Azimuthal mode analysis of the flow with the HP trigger (BPF_{HP}); without splitters (left) and with splitters (right)

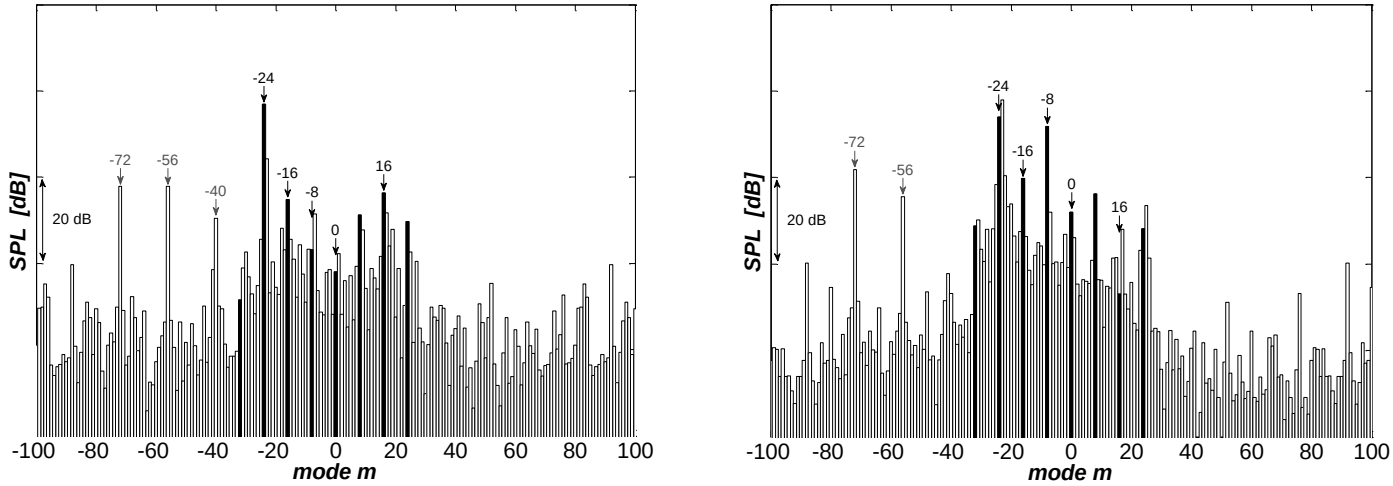

Figure 6:Azimuthal mode analysis of the flow with the LP trigger (BPF_{LP}); without splitters (left) and with splitters (right)

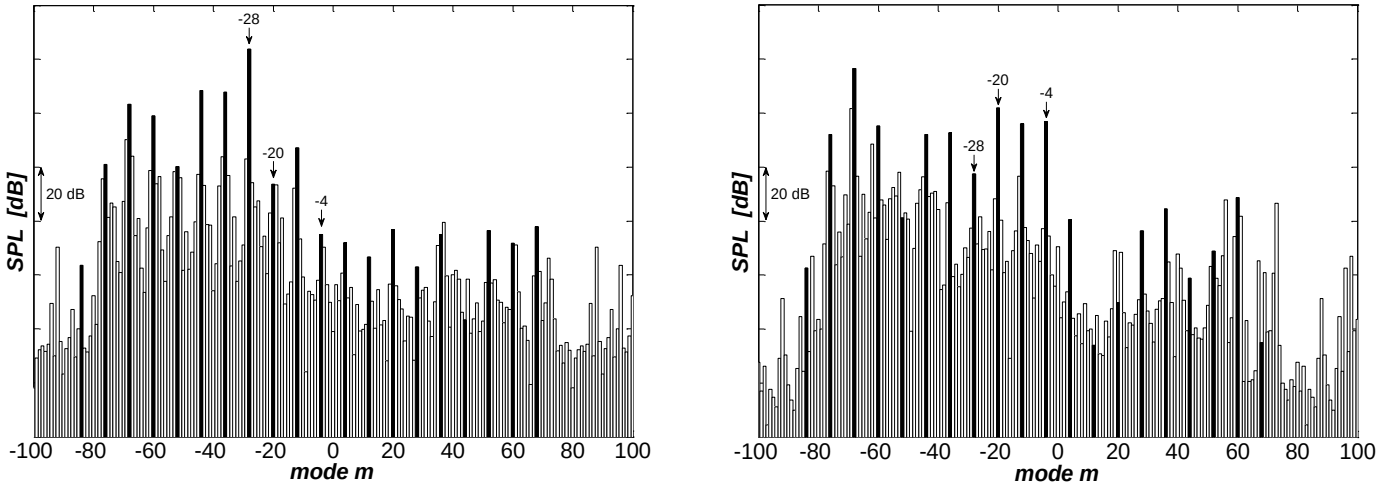

Figure 7: Azimuthal mode analysis of the flow with the two triggers (BPF_{LP}+BPF_{HP}); without splitters (left) and with splitters (right)

LP rotor noise

Figure 6 shows the amplitudes of the modal decomposition for the BPF_{LP}. This picture shows the results of the baseline configuration on the left side and the splitter configuration on the right side. The interaction between the LP vane and the LP blade generates the following modes:

$$-72 + k \cdot 16 = .. -72; -56; -40; -24; -8; 8; 24.. \qquad (f)$$

These modes may be clearly identified in the left side of Figure 6, marked as black bars. The highest amplitude is observed for mode -24. In the range -24<m<24 further modes are marked with black bars (such as -16, 0, +16) which may be computed when the linear combination of LP vane and blade is extended to the case of interaction with the HP vane $(-72 + k_1 \cdot 16 + k_2 \cdot 24)$. However, the interaction between the HP vane and LP blade is quite small (e.g., there is a difference of more than 20 dB between mode -24 and mode -16). It has to be noted that the modes -72, -56, and -40 can be still identified in the picture. They are generated by the LP rotor itself and by the LP stator-LP rotor interaction. These modes are cut-off, they show a lower amplitude than the propagating modes and decay further downstream of the duct.

In the case of the splitter setup (right side of Figure 6), a different LP vane count may be considered. Ideally, the LP vane-LP rotor interaction would consist of the modes:

$$-72 + k \cdot 48 = .. -72; -24; 24.. \qquad (g)$$

Mode -24 presents still the largest amplitude, however it is now of comparable intensity to mode -8. In the ideal case of the splitter setup, where the geometry of every LP vane is assumed to be the same, mode -8 should not be existing. However, as observed by Spataro et al. [23] the unsteady effects induced by strut and splitter vane wakes differ considerably downstream of the LP rotor. Hence, the modes generated by the interaction of the 48 LP vanes with the LP blades may be computed correctly when the modes are scattered by the number of the 16 strut (e.g., mode -8 is obtained subtracting the 16 vanes from mode -24). In the case of the splitter setup, the mode -8 is more than 20 dB larger than in the baseline case. Furthermore, also the amplitude of the modes generated due to the interaction HP vanes-LP vanes-LP-rotor (e.g., mode -16, 0, 16) is changed. Considering this interaction, the larger number of vanes in the splitter setup does not represent a cut-off design with respect to the LP rotor (the number of LP vanes is still lower than that of the LP blades). The splitter design tends to shift the significant modes towards lower modes (e.g., mode -8 which was hardly identifiable for the baseline setup). As observed from the mean spectrum (Fig. 4), the modes mean value is almost 3 dB lower for the baseline configuration.

Also for the splitter case it has to be noticed that the modes -72, -56 (that can be still identified in the picture) are cut-off as previously discussed for the baseline,. Particularly, mode -40 is reduced by more than 20 dB in the splitter configuration. The larger amplitude of the noise emission at the BPF_{LP} may be due to the effect of "shifting" the modes towards lower modes and not to an enhanced unsteady interaction. The unsteady measurements presented by Spataro et al. [9] performed with a fast response pressure probe traversed just downstream of the LP rotor, show that the unsteady pressure fluctuations, quantified for the LP rotor phase, are of comparable intensity for both setups.

In Figure 7 the modal decomposition is shown for the sum of the blade passing frequencies of the two rotors ($BPF_{LP} + BPF_{HP}$) for the baseline setup (left) and the setup with splitters (right). The modes mean value is nearly the same in both setups. On the other hand, there are some predominant modes with amplitudes changing up to 23 dB, which characterize the stator/rotor/stator/rotor interaction. Although mode -28 is dominant in the baseline setup, this is not true for the setup with the splitters. Despite this, in the case of the splitters, other modes like -20 and -4 occur, which are 20 dB and 14 dB, respectively, higher than in the baseline setup. That's the reason why the sound pressure level of both setups is nearly the same, looking at the sum of the blade passing frequencies of the two rotors.

Summary on propagating modes

The largest reduction of the modes mean value in the splitter case is associated to the HP rotor. The setup with the splitters has a 5 dB lower amplitude at the BPF_{HP} than the setup without splitters. At $2BPF_{HP}$ the results of the azimuthal mode analysis point in the same direction. A reduction of 4 dB was measured in case of the setup with the splitters.

Vice versa, the sound pressure level at BPF_{LP} and $2BPF_{LP}$ is smaller by 3 dB in case of the setup without splitters.

The sound pressure level at the $BPF_{LP} + BPF_{HP}$ is nearly the same in both cases.

CONCLUSIONS

The paper presented the results of an experimental campaign aimed to characterize the acoustic flied downstream of a transonic two-stage two-spool facility. A special focus is laid on the comparison between two setups of the mid turbine frame. The baseline case is designed with turning struts. The second design is characterized by the presence of two zero-lifting splitters embedded into the strut passage.

The design of a new fully rotatable measurement section located at the shroud endwall downstream of the LP turbine is presented.

The analysis of the frequency spectra and of the azimuthal modes were performed by phase averaging the signal by use of the HP and LP trigger as well as the adoption of a Rotor Synchronic Average (RSA).

In the frequency spectra, the peak of the BPF_{HP} is found to be 3 dB lower in the splitter setup. In the azimuthal mode analysis the difference is even higher. A reduction of 5 dB was observed at the BPF_{HP} in the setup with the splitters. This is also coherent with the result obtained from the unsteady aerodynamic measurements. The most important effect of the

splitters has been observed on the coherent fluctuations of pressure. They were found to stem from the HP rotor unsteadiness, namely the HP rotor shock system which propagates within the duct. The presence of the splitters reduces the maximum of the fluctuations at the blade passing frequency of the upstream rotor when compared with the baseline case. The addition of the splitters into the strut passage increases the number of the second stator vanes which leads to a cut-off configuration

The frequency spectra and the azimuthal mode analysis showed that the noise generated by the LP rotor is slightly higher in the setup with the splitters.

The analysis shows that the splitter design some modes are suppressed, while others are scattered or even more intensive than in the baseline configuration.

A special post processing tool called Rotor Synchronic Average which reconstructs the flow field using both spools triggers was used in order to investigate the rotor-rotor interaction. The frequency spectra after performing the FFT are very similar. Moreover, a similar behavior is seen in the sound pressure level of the propagating modes allocated to the different interaction phenomena. But there are differences in single modes of over 20 dB between both setups.

As a main result, the paper shows that unsteadiness content measured in the acoustic field downstream of the two-spool rig is highly affected by the HP rotor, whose fluctuations are found not to decay through the low pressure turbine. The addition of the splitters in the tuning mid turbine frame sensibly dumps the overall noise propagation by 5dB by acting as a cut-off filter for the HP stage rotor.

In addition to the acoustic benefit aerodynamic benefits are also observed. Steady and unsteady measurements showed that the increased homogeneity of the flow field (reduced strut wakes and secondary vortices) at the low pressure rotor inlet and behind the LP rotor enhances the performance of the LP stage.

ACKNOWLEDGMENTS

The authors would like to thank H.P. Pirker for operating the compressor station as well as MTU Aero Engines and Ulf Tapken from the DLR Institute of Propulsion Technology, Engine Acoustic Department, for the design of the alignment of the microphones in the acoustic measurement section.

REFERENCES

[1] Göttlich, E., 2011. “Research on the aerodynamics of intermediate turbine diffusers”. Progress in Aerospace Sciences, 47, pp. 249–279.

[2] Miller, R. J., Moss, R.W., Ainsworth, R.W., Harvey, N.W., 2004. “The effect of an upstream turbine on a low aspect ratio vane”. In Proceedings of ASME Turbo Expo 2004, June 14-17, Vienna, Austria, ASME Paper No. GT-2004-54017.

[3] Marn, A., Göttlich, E., Cadrecha, D., Pirker, H. P., 2009. “Shorten the intermediate turbine duct length by applying an integrated concept”. ASME Journal of Turbomachinery, 131, p. 041014 (10 pages).

[4] Santner C., Paradiso B., Malzacher F., Hoeger M., Hubinka J., Göttlich Emil, (2011), “Evolution Of The Flow Through A Turning Mid Turbine Frame Applied Between A Transonic HP-Turbine Stage And A Counter-Rotating LP-Turbine”, 9th European Conference of Turbomachinery Fluid Dynamics and Thermodynamics.

[5] Paradiso B., Santner C., Hubinka J., Göttlich E., Hoeger M., “Turning Mid Turbine Frame Behavior For Different HP Turbine Outflow Conditions”, Proceedings of ASME Turbo Expo 2011, paper no GT2011-46502

[6] Lengani, D., Santner, T., Spataro, R., Paradiso, B., Göttlich, E., 2012. “Experimental investigation of the unsteady flow field downstream of a counter-rotating twospool turbine rig”. In Proceedings of ASME Turbo Expo 2012, June 11-15, Copenhagen, Denmark, ASME Paper No. GT-GT2012-68583.

[7] C. Faustmann, D. Lengani, D. Broszat, A. Marn, E. Göttlich, F. Heitmeir, (2013), “Investigation on noise generation and propagation for different vane-vane positions in a two-stage two-spool test turbine”, submitted for 10th European Conference of Turbomachinery Fluid Dynamics and Thermodynamics

[8] Spataro, R., Göttlich, E., Lengani, D, Faustmann, C., Heitmeir, F., 2013. “Development of a Turning Mid Turbine Frame with Embedded Design - Part I: Design and steady measurements”. In Proceedings of ASME Turbo Expo 2013, June 3-7, San Antonio, Texas, USA, ASME Paper No. GT2013-95272.

[9] Spataro R., Göttlich E., Lengani D., Faustmann C., Heitmeir F., (2013), “Development of a Turning Mid Turbine Frame with Embedded Design - Part II: Unsteady Measurements”. In Proceedings of ASME Turbo Expo 2013, June 3-7, San Antonio, Texas, USA, ASME Paper No. GT2013-95280

[10] Erhard J., Gehrer A., (2000), “Design and Construction of a Transonic Test Turbine Facility”, ASME Paper 2000-GT-480.

[11] Neumayer F., Kulhanek G., Pirker H.P., Jericha H., Seyr A., Sanz W., (2001), “Operational Behaviour of a Complex Transonic Test Turbine Facility”, ASME Paper 2001-GT-489.

[12] Hubinka, J., Santner C., Paradiso B., Malzacher F., Göttlich E., Heitmeir F., (2009), “Design and Construction of a Two Shaft Test Turbine for Investigation of Mid Turbine Frame Flows”, ISABE Paper ISABE-2009-1293

[13] Hubinka, J., Paradiso B., Santner C., Göttlich E., Heitmeir F., (2011), “Design and Operation of a Two Spool High Pressure Test Turbine Facility”, 9th European Conference of Turbomachinery Fluid Dynamics and Thermodynamics.

[14] Santner C., Göttlich E., Wallin F., Hoeger M., (2011), "Experimental Investigation Of Turning Mid Turbine Frame Designs", ISABE Paper ISABE-2011-1710.

[15] Enghardt L., Tapken U., Neise W., Kennepohl F., Heinig K.: "Turbine Blade/Vane Interaction Noise: Acoustic Mode Analysis using In-Duct Sensor Rakes", 7th AIAA/CEAS Aeroacoustic Conference, May 28-30, 2001, Maastricht, Netherlands.

[16] Moser M., Tapken U., Enghardt L., Neuhaus L., (2009), "Investigation of LP Turbine Blade/Vane Interaction Noise Measurements in a 1.5 Stage Rig", 8th European Conference of Turbomachinery Fluid Dynamics and Thermodynamics.

[17] Taddei F., De Lucia M., Cinelli C., Schipani C., (2009) „Experimental Investigation of Low Pressure Turbine Noise: Radial Mode Analysis for Swirling Flows", ISUAAAT12 paper n° I12-S4-4

[18] Tyler, J. M., and Sofrin, T. G., (1962), "Axial flow compressor noise", SAE Transaction, 70, pp. 309–332.

[19] Rienstra, S. W., and Hirschberg, A., (2004), "An Introduction to Acoustics", Eindhoven University of Technology.

[20] Holste, F., and Neise, W., (1997), "Noise source identification in a propfan model by means of acoustical near field measurements", Journal of Sound and Vibration, 203(4), pp. 641–665.

[21] Sijtsma, P., and Zillmann, J., (2007), "In- duct and far-field mode detection techniques", In Proceedings of 13th AIAA/CEAS Aeroacoustic Conference, Rome, Italy, AIAA Paper 2007-3439.

[22] Sharma O.P., Butler T.L., Joslyn H.D., Dring R.P., (1985), "Three-dimensional unsteady flow in an axial flow turbine", AIAA J. Propul. Power 1 (1) 29–38.

[23] Suder K.L., Hathaway M.D., Okiishi T.H., Strazisar A.J., Adamczyk J.J., (1987), "Measurements of the unsteady flow field within the stator row of a transonic axial-flow fan: part 1-measurement and analysis technique", NASA Tech. Memorand. 88945.

[24] Hussain, A., and Reynolds, W., (1970), "The mechanics of an organized wave in turbulent shear flow", Journal of Fluid Mechanics, 41, pp. 241–258.

[25] Lengani, D., Santner, C., Spataro, R., and Göttlich, E., (2012 a), "Analysis tools for the unsteady interactions in a counter-rotating two-spool turbine rig", Experimental thermal fluid science, 42, pp. 248–257.